

Design of a magnetic field compatible, high-performance optical breast imaging system  
for MRI-guided optical spectroscopy

A Thesis

Submitted to the Faculty

in partial fulfillment of the requirements for the

degree of

Doctor of Philosophy

by

Fadi El-Ghussein

Thayer School of Engineering

Dartmouth College

Hanover, New Hampshire

Date

September 22<sup>nd</sup> 2014

Examining Committee:

Chairman \_\_\_\_\_  
Brian Pogue

Member \_\_\_\_\_  
Shudong Jiang

Member \_\_\_\_\_  
Keith Paulson

Member \_\_\_\_\_  
Sergio Fantini

---

F. Jon Kull  
Dean of Graduate Studies



## **Abstract**

Multimodality imaging is becoming the standard of care for research and clinical studies. Such an approach is able to provide complementary information which can detect and characterize tumors. Advancing instrumentation for diffuse near-infrared spectroscopy (NIRS) within a conventional magnetic resonance imaging (MRI) scanner requires careful choices to make a true hybrid imaging system. In this thesis, a series of system technology development studies were completed in order to analyze what was needed to prototype the next phase of this technology with detection being possible within the MRI. Initially in a breast imaging system, a set of parallel plates was used with a newly created frequency-domain and continuous wave source-detector array. The opto-electronic sub-system was created and deployed within a previously existing MRI-coupled spectroscopy approach, principally allowing incorporation of additional NIR wavelengths beyond 850nm, with interlaced channels of photomultiplier tubes and silicon photodiodes. This new sub-system improved the data quality and accuracy in recovery of all breast optical properties.

While the current system is highly functional, and was deployed in a large clinical trial of over 60 subjects, the usability was found to be limited due to the cumbersome nature of the fiber-breast geometry and adaptability of the system. Furthermore, there is a severe penalty for the lack of full breast coverage as the sensitivity of DOT to tumors drops. Full coverage of the breast was found to be a critical. Adding more fibers for full breast coverage is impractical due to the size of the fibers as well as the significant cost that would be incurred. In order to solve this challenge, we have built a system which places detectors in direct contact with the patient's tissue, thus, forgoing the long fiber optic

cables used with the hybrid system and improving light throughput.

The new modular design, which allows up to 64 detectors to be used, places the detectors' frontend electronics outside the MRI room without sacrificing the detectors sensitivity or dynamic range. Characterization and calibration of the system is described in detail.

## Acknowledgements

I would first like to thank my supervisor, Professor Brian Pogue for providing me with this incredible opportunity and allowing me to pursue my PhD degree with him. I am truly blessed to have been in his group. His driving force and support was a turning point when this work was overwhelming. I am sincerely grateful for his patience and for always finding the time to speak with me when I need his guidance. One can only be humbled to have met and been a student of such a great supervisor to whom I am deeply indebted.

I would also like to thank Professor Shudong Jiang who showed her enormous support and encouragement throughout my PhD. She engaged me in discussions and guided me through my first years as a graduate student. She went out of her way and displayed so much kindness and offered a great amount of help during our clinical trial in Xi'an, China. The success of the clinical trial and the completion of this PhD would have not been possible without her

It is hard to image where the optics in medicine group would have been if it wasn't for the tireless efforts and long vision of Professor Keith Paulson. Professor Paulson, the driving force behind this group at Dartmouth College, also was the key reason for getting the clinical trial off the ground. I am very thankful for his efforts and for his dedication to this group.

I would also like to thank Professor Sergio Fantini, a pioneer in his field, for being kind enough to serve as a member of my PhD committee. His work in this field played a key role in my understanding of optical tomography.

I must also thank my original mentor Professor Michael Kruger who has shaped me to the person I am today. He has engaged me, challenged me, motivated me, and helped me find the potential in myself. I am deeply indebted to him and will forever keep him in my thoughts.

Finally, I would like to thank my parents and my siblings, Amani and Feras for their love and support and my wife Shaimah for her love and support as well.

I dedicate this work to my mom and dad, Abeer and Mohammed. All the love of this world is not enough to repay them, but I will continue to love them more and more every day.

## Table of Contents

Abstract (times, regular, 12, double spaced).....	ii
Acknowledgements .....	iv
Table of Contents.....	v
List of Tables .....	viii
List of Figures.....	ix
List of Acronyms .....	xviii
1. Overview.....	1
1.1 Introduction to optical tomography and functional imaging .....	1
1.2 Aims of this thesis.....	3
1.3 Organization of this thesis .....	4
2. Background.....	6
2.1 NIR tomography/spectroscopy.....	6
2.2 Tissue Optics And Optical Contrast .....	7
2.3 NIR Instrument Types.....	12
2.4 Light Modeling and the diffusion approximation .....	17
2.5 Image Reconstruction .....	19
2.6 Photon Detectors.....	23
2.6.1 Light.....	23
2.6.2 Photomultiplier tube (PMT) detectors .....	25
2.6.3 Photodiodes/PIN photodiodes.....	29
2.6.4 Silicon Photomultiplier .....	32
2.6.5 Photon Counting .....	36
2.6.6 Detectors Comparison.....	41
3. Time-domain Imaging .....	44
3.1 Introduction - Background and Importance.....	44
3.1.1 TCSPC Building Blocks .....	48
3.1.1 Discriminators.....	49
3.1.1 Time-to-Amplitude (TAC).....	51
3.1.1 TCSPC Data Type.....	52
3.2 Small-Animal Time-Domain System Characterization .....	53
3.2.1 Control Flow Improvements .....	57
3.2.2 Calibration and Data Types .....	60
3.2.2.1 Laser Reference Calibration.....	60
3.2.2.2 Inter-detectors Calibration and Time-Referencing .....	62
3.3 Phantom/Animal Results.....	64
3.3.1 Phantom Imaging .....	64
3.3.2 Animal Imaging .....	66
3.4 Discussion and Conclusion.....	67
4. Design of a hybrid frequency domain/continuous wave system .....	69
4.1 Introduction - Background and Importance.....	69
4.2 Hybrid System Design .....	76

4.2.1	FD Detector Channels.....	79
4.2.2	CW Detector Channels.....	80
4.2.3	Rotary Mechanical Switch Array.....	81
4.2.4	Computer and data acquisition.....	83
4.3	System Characterization.....	85
4.3.1	Calibration.....	85
4.3.2	Detection linearity/limits.....	87
4.3.3	Gain settings.....	89
4.3.4	Cross talk.....	90
4.3.5	Stability and repeatability.....	91
4.3.6	Data acquisition duration and timing.....	92
4.4	Conclusion.....	93
5.	Hybrid FD/CW phantom and patients results.....	96
5.1	Introduction.....	96
5.2	Patient/Phantom Interface.....	96
5.3	Phantom Experiments.....	97
5.4	Healthy Subject Imaging.....	99
5.5	Patient Imaging.....	102
5.6	Discussion and Conclusion.....	105
6.	MRI Compatible Optical Detectors for In-Magnet Tissue Spectroscopy.....	107
6.1	Introduction.....	107
6.2	Solid State Detector System Design Approach.....	110
6.3	Detector Choice.....	111
6.3.1	Detector's Amplifier Circuitry.....	114
6.3.2	Dynamic Range.....	121
6.3.3	Phantom Testing.....	123
6.3.4	MRI Testing.....	124
6.4	Conclusion.....	126
7.	Design of a multichannel MRI compatible tomography system.....	129
7.1	Introduction.....	129
7.2	System Design.....	130
7.2.1	Detectors.....	130
7.2.2	Photodiode Circuit.....	134
7.2.3	PCB Design.....	141
7.2.4	Phantom Interface.....	143
7.2.5	Photodiode packing.....	144
7.2.6	Calibration.....	145
7.2.7	Cross talk.....	150
7.2.8	Phantom Experiments.....	150
7.2.8.1	Ink Phantom Results.....	151
7.2.8.2	Blood Phantom Results.....	156
7.3	Discussion and Conclusion.....	157
8.	Conclusion and Future Directions.....	158
8.1	Completed Work.....	158
8.2	Future Directions.....	159
8.2.1	EMI Interference.....	160

8.2.2 Cables.....	162
8.2.3 Synchronizing MRI/NIRS Acquisition.....	163
8.2.4 Patient Interference .....	166
8.2.5 Simultaneous Breasts Acquisition .....	167
8.2.6 Scattering and absorption information.....	168
Appendices.....	169
Appendix A: Noise Sources.....	169
Appendix B: Programs Flowcharts.....	172
Appendix C: PCB Circuits.....	180
Appendix D: Detectors.....	180
References.....	181

## List of Tables

Table 2.1: Comparison of DOT techniques .....	17
Table 2.2: Photon detectors summary.....	43
Table 4.1: A breakout of the time spent on the main sections of the acquisition process .	93
Table 5.1: Chromophore concentration of two representative cases of the breast cancer clinical trial .....	105
Table 6.1: Showing some of the key available specification parameters for the two detectors, a silicon photodiode and avalanche photodiode related to sensitivity of detection. ....	112, 113
Table 6.2: Photodetector evaluated . ....	112, 113
Table 7.1: Polarity and input ranges of the signals that can be used with the NI-PGIA of the PCI-6031E data acquisition card.....	137

## List of Figures

Figure 2.1: Different paths photons travel through tissue. Path A: specular reflection, Path B: Ballistic photons (direct transmission), Path C: diffuse reflection, Path D: diffuse transmission, Path E: diffuse transmission (snake photons), Path F: absorption. ....	9
Figure 2.2 (a): Absorption spectrum of the four main chromophores found in breast tissue, (b) scattering spectrum of tissue. ....	11
Figure 2.3: Light input/output of optical signal for the three instrument types used in DOT. (a) Time-domain, (b) frequency-domain, (c) steady-state. ....	13
Figure 2.4: the transmission of a light pulse through tissue is illustrated where broadening due to multiple scatter is illustrated along with attenuation of the broadened pulse due to absorption. The temporal bands detected have traversed different average paths, as illustrated in the bottom row. ....	16
Figure 2.5: the detection of light in an electron-vacuum tube is illustrated at left, where electrons are generated from a photocathode and travel through vacuum to the anode where current is generated. On the right, the electron multiplication is illustrated by sequential collision at each of the charged dynodes in a photomultiplier tube. ....	25
Figure 2.6: a. Diversity of PMT output pulse heights (b) PMT output pulses and pulse height distribution of the pulses. ....	27
Figure 2.7: PMT operation modes: (a) analog (b) photon counting. ....	28
Figure 2.8: Schematic of Si Photodiode Cross Section. ....	29
Figure 2.9: (a) photons illuminating an ideal reverse-biased p-n photodiode, (b) PIN photodiode operation, (c) forward-biased (photovoltaic) operation of a photodiode, (d) reverse biased operation of a photodiode. ....	31

Figure 2.10: SiPM detector showing SPAD array. ....	33
Figure 2. 11: Pulse waveform for different number of photoelectrons. ....	34
Figure 2.12. Dark count rate of a 1mm, 35um microcell SPM as a function of discriminator threshold for different over-voltage levels. ....	35
Figure 2.13: Basic building blocks of a photon counting system. ....	37
Figure 2.14: PHD curve of light and dark signals from a PMT detector. ....	38
Figure 2. 15: Cause of pileup effects in photon counting. ....	40
Figure 2.16: Pileup effect on data acquisition. ....	41
Figure 3.1: Building blocks of a typical TCSPC system. ....	48
Figure 3.2: Data types in a time-domain measurement. ....	53
Figure 3.3: The schematics of the system are shown in (a) with the optical hardware including laser diode (LD), lenses for delivery and pick up (CH1 – CH5), and photomultiplier tubes (PMTs). The electronics and control systems are shown in(b), with single photon counting (SPC) cards and direct current control (DCC) cards feeding the PMT detectors, a laser driver (Sepia), and USB control of the linear filter stages and the rotating gantry stage. ....	54
Figure 3.4. Panels showing the main options presented to users for optical data acquisition. ....	57
Figure 3.5: Panel showing some advanced options presented to users for controlling the single-photon counting components. ....	58
Figure 3.6. The program flow is shown for part of the internal workings of the LabVIEW user interface.....	60

Figure 3.7: A reference channel is used to monitor the laser as a function of scan time. An impulse-response function (IRF) is acquired each time a measurement is made. A time correction and an amplitude correction is to time-domain data based on variations of IRF mean-time and total photon count. ....	62
Figure 3.8. Semi-cylindrical phantom insuring diffused light field seen by each detector is equivalent. Calibration factors and timing for each detector are computed and used to correct raw time-domain data. ....	63
Figure 3.9: Impact of inter-detector calibration and time-referencing shown for the central detector (left) and for all detectors (right). ....	64
Figure 3.10: Wedge phantom used in system characterization. ....	65
Figure 3.11: Evaluation of signal-to-noise ratio (SNR) for wedgen phantom experiments. ....	65
Figure 3.12 (a) Image of the mouse phantom used in system characterization, (b) microCT image of the mouse phantom, (c) time-domain optical reconstruction results overlaid on the microCT image .....	66
Figure 3.13 (a) Contrast-enhanced magnetic resonance images of mouse head injected with U251 orthotopic glioma tumor in the left cerebral hemisphere as indicated by the red arrow, (b) fluorescence reconstruction of the time-domain system overlaid with co-registered microCT images of the head of the mouse. ....	67
Figure 4.1: The concept of homodyne detection is illustrated in terms of in-phase and quadrature (I&Q) detectors with low pass filters (LPF), producing a pair of signals (I & Q) for each measurement .....	71

Figure 4.2: Heterodyne detection illustrated here is useful for optical signals in the MHz range because these signals are electronically mixed with an offset frequency that results in the signal being shifted to a lower frequency for direct detection. ....	74
Figure 4.3: An example of a frequency-domain system. ....	75
Figure 4.4: FD/CW hybrid imaging system. A photo of the complete system is shown in (a). The system diagram is shown in (b). A photo of human subject being imaged using the system.....	78
Figure 4.5 switch array: Solidworks drawing of the array is shown in (a) and photos of the actual assembly are shown in (b) and (c). ....	83
Figure 4.6: (a) Flowchart used in programming the (b) LabVIEW program which controls the hybrid system .....	84
Figure 4.7: Standard deviation of the natural log of the amplitude (In AC) (a) as well as the standard deviation of the phase (b) of the photomultiplier tube (PMT) as a function of incident light power. The blue marks represent the results for the new system while the red marks represent the results for the system built by McBride et al. ....	88
Figure 4.8: Photodiode (PD) response as a function of incident light power for the two available gain settings of the PD. ....	89
Figure 5.1: Schematic of two different breast interface geometries: circular (a) and the new pentagonal interface (b). ....	97
Figure 5.2: Bilateral axial images of all healthy volunteers imaged in this study arranged by cup size. The NIRS/MRI breast coil was able to accommodate all sizes, densities, and compositions in the group. ....	97

Figure 5.3: Reconstruction values on a gelatin phantom with 2 cm inclusion. The inclusion was filled with varying concentrations of blood. MRI images of the phantom are shown with the 2 cm inclusion overlaid (a+b). A photo of the actual phantom is shown in (c). Reconstruction as a function of true total-hemoglobin values are shown for total hemoglobin, oxygen saturation, water, lipids, scatter power, and scatter amplitude in (d). Blue circles are for the background while red circles are for the inclusion. ....99

Figure 5.4: Representative healthy volunteer imaging by combined optical system and MRI. Different axial MRI slices are shown with overlays of total hemoglobin (a), oxygen saturation (b), water (c) and lipid (d) fraction, scatter amplitude (e) and power (f). In each case, the region with the lowest value is removed and the region with the highest value is made slightly opaque to visualize overlaid MRI. A bilateral axial image (g) shows little degradation of MRI image quality. ....101

Figure 5.5: a representative case of a NIRS imaging showing a benign tumor for patient #46. ....103

Figure 5.6: a representative case of a NIRS imaging showing a malignant tumor for patient #58 as confirmed by biopsy. ....103

Figure 5.7: Total concentrations of HbT, StO<sub>2</sub>, water, lipid, SA, SP, and TOI of NIRS results of patient #46.....104

Figure 5.8: Total concentrations of HbT, StO<sub>2</sub>, water, lipid, SA, SP, and TOI of NIRS results of patient #58. ....105

Figure 6.1: Images of 3 breast lesion cases are shown, with DCE-MRI scans shown as maximum intensity projection (MIP) images in the top row, and the overlay of the light sensitivity patterns in the bottom row for each corresponding case, along with the

suspected lesion shown segmented in blue. If placement of the fibers is ideal ,then there is good overlap over the lesion as shown in the two left cases, however the right case is an example of nearly no overlap for NIRS with the tumor. ....109

Figure 6.2 Basic simple TIA circuit for the two detectors, based upon a single amplification stage. ....115

Figure 6.3 Output Current vs. illuminance for different reverse voltage values, illustrating the higher VR can lead to higher dynamic range. ....117

Figure 6.4: Illustration of the source-detector electronics with coupling into the MRI (a). Electrical schematics of the optimized amplifier circuits used at the distal end of the cables to the SiPM (b) and PD (c) detectors are shown.....119

Figure 6.5 In (a) the responsivity of the SiPM detector connected via a long cable is shown at different amplifications from bias voltages. The low, medium and high amplification values correspond to bias values of 28V (triangles), 28.5V (circles), and 30.5V (squares). The solid (blue) symbols denote the 661nm wavelength response while the open (red) denote 948nm. In (b) the response of the PD detector is shown using different amplifications, by varying the feedback resistance. Low gain was produced with feedback of 100K  $\Omega$  (circles) and high gain at a feedback of 100M  $\Omega$  (squares). .122

Figure 6.6 Tissue phantom measurements using the PD, SiPM, and a fiber-optic coupled PMT for the 661nm laser (a) and PD and SiPM for the 948nm laser (b). Note the PMT used cannot detect light at 948nm, so was not included. Photo (top) and MRI scan (bottom) of the detectors mounted on the silicon phantom is also shown (c). ....124

Figure 7.1: S5107 Hamamatsu Photodiode Detector is shown with design schematics of the packaging. ....131

Figure 7.2: PDB-V609-3 Photodiode by API Advanced Photonics, Inc, along with package schematic at right. ....	132
Figure 7.3 (top row) 3D MRI surface rendered images of the API and Hamamatsu detectors using (a) thrive MRI sequence, (b) FFE MRI sequence, (c) T2 – TSE MRI sequence, (d) T1 – TSE MRI sequence, (bottom row) MRI coronal view of the API and Hamamatsu detectors using (e) thrive MRI sequence, (f) FFE MRI sequence, (g) T2 – TSE MRI sequence, (h) T1 – TSE (MRI sequence. ....	133
Figure 7.4 (a) programmable gain functionality implemented using a dedicated programmable gain amplifier (PGA), (b) or by varying feedback network (Rf and Cf). ....	135
Figure 7.5: Schematic diagram of the photodiode circuit showing implementation of the gain changing mechanism via the SPDT relays. ....	136
Figure 7.6 (a) Saturation of photodiode output at high gain setting sue to the 60 Hz frequency signal caused by power line interference for the photodiode circuit shown in Figure 6.2, (b) Photodiode output at high gain setting for the same input signal but for the modified circuit shown in Figure 7.5.....	139
FIGURE 7.7: The design is shown for varying the gain of the photodiode transimpedance amplifier circuit using a single relay (a) and dual relays (b). ....	140
Figure 7.8: Photodiode performance characteristic is shown for a single relay (orange) and a dual relay (blue) configuration.....	140
Figure 7.9: The schematic of the digital multiplexer circuitry used to expand the number of available outputs is shown, as needed to control the 64 photodiode relays .....	142

Figure 7.10: A photograph of the final electronic prototype is shown, as used to interface to the photodiode detectors via the ribbon cable (lower left), and coupling to the DAQ card (upper left) .....143

Figure 7.11: Diagram of interface built using Solidworks and used for testing the new multiple-detector array. ....144

Figure 7.12 (a) photodiode detector packaging, (b) and (c) are two types of interfaces that are used to hold the detectors into contact with phantoms. ....145

Figure 7.13 (a): The calibration phantom holder is shown, as designed with a laser fiber at the center of the holder and one photodiode detector snapped into one of the available slots. In (b) the diagram of calibration setup is shown. ....146

Figure 7.14 The response of the low and high gain settings of the photodiode amplifier are shown, for calibrated input light powers. Measureable signal was seen down to 1pW on the high gain, and 1 nM on the low gain. ....147

Figure 7.15 In (a) the calibrated output of a phantom experiment is shown, and (b) shows the raw output of the same phantom experiment, while (c) shows the normalized calibrated and raw output of the same phantom experiment, showing minimal need for calibration. ....149

Figure 7.16: The crosstalk behavior of two neighboring channels is shown, with signal recorded in the blue data, and crosstalk in the orange data shown, exhibiting minimal increase over the noise floor. ....150

Figure 7.17: Phantom and phantom inclusion molds as printed, allowing a hole to be created for an inclusion in the gelatin phantom. ....151

Figure 7.18 Image of phantom showing location of the inclusion as seen in the NIRFAST display. ....	152
Figure 7.19 (a) image of the phantom holder showing the detector array, (b) image of the phantom showing an empty inclusion (c) mesh of the phantom showing the location of sources and detectors around the phantom .....	152, 153
Figure 7.20 Reconstructed ink concentration of the phantom inclusion for a large range of contrasts recovered. ....	154
Figure 7.21 Reconstructed ink concentration of the phantom inclusion from 1 up to 5 times the background absorption value. ....	154
Figure 7.22: (a) mesh of the phantom showing the inclusion along with the location of sources and detectors around the phantom. This inclusion only intersected two out of the four source/detector planes used for data acquisition. (b) Reconstructed ink concentration of the phantom inclusion up to 5 times the background absorption value. ....	155
Figure 7.23 2D reconstruction of the four acquisition planes was done, and the recovered contrast is shown as a function of increasing input contrast in the inclusion. ....	156
Figure 7.24 Total blood concentration reconstruction of the phantom inclusion from 1 up to 5 times the background absorption value. ....	157
Figure 8.1: (a) An example of a single trace connecting different points on a circuit board (b) star connection implementation is shown where wires (black) shown in the figure are connected to IC circuits on one end and soldered together on the end.....	161
Figure 8.2: 3M™ Shielded/Jacketed, Flat Cable used to transport the photodiode signals to the amplifier circuitry outside the MRI room .....	162

Figure 8.3: An example of a photodiode output dominated by RF pulses of the MRI during a simultaneous MRI/NIRS acquisition .....163

Figure 8.4: An example of a photodiode output during a simultaneous MRI/NIRS acquisition showing intervals that can be used to collect NIRS data after the MRI RF pulses settle .....164

Figure 8.5: An example of a photodiode output under high gain setting during a simultaneous MRI/NIRS acquisition showing no intervals for acquiring NIRS data during MRI imaging .....165

Figure 8.6: An example of a photodiode output under high gain setting during a simultaneous MRI/NIRS acquisition showing possible NIRS acquisition intervals during the beginning of an MRI sequence .....166

Figure 8.7 Possible breast interface for full breast coverage based on previous breast interface design .....167

*List of Acronyms (times, 14, italics)*

Continuous Wave	CW
Frequency Domain	FD
Magnetic Resonance Imaging	MRI
Total Hemoglobin	HbT
Tissue Optical Index	TOI
Oxygen Saturation	StO <sub>2</sub>
Scatter Amplitude	SA
Scatter Power	SP
Deoxy-Hemoglobin	Hb
Oxy-Hemoglobin	HbO
Finite Element Method	FEM
Near-Infrared	NIR
Near Infrared Spectroscopy	NIRS
Graphical User Interface	GUI
Radiative Transport Equation	RTE
Signal to Noise Ratio	SNR
Photomultiplier Tube	PMT
Photodiode	PD

# CHAPTER ONE

## Overview

### 1.1 Introduction to optical tomography and functional imaging

Medical imaging is a field that uses technology in order to create images from inside human body. This noninvasive form of diagnosis has experienced a rapid growth during the past quarter century with advances in technologies that enable it. Many imaging systems can be divided into two main categories: anatomic and functional imaging systems. Anatomic imaging is most commonly performed via systems such as x-ray, x-ray CT, MRI, and US. This form of imaging produces detailed static images of the interior structures of the body. However, this form of imaging is often unable to identify early stages of pathology or other active processes until very large numbers of cells become involved, allowing detection of larger structural changes in the images. Anatomical imaging can be complemented by functional imaging techniques, which look at the biological activity or function of the organ or tissue of interest. Examples of functional (or molecular) imaging are monitoring of physiological changes in tissue such as blood flow, oxygen saturation, hemoglobin concentration, and cellular metabolism; parameters that are effected by tumor angiogenesis and tissue abnormalities. Clinical functional imaging includes PET, angiography, Doppler US, NM, SPECT, contrast-enhanced MRI, and optical imaging. Due to its low spatial resolution, functional imaging systems are often not intended to compete with the superior resolution of anatomical imaging systems. However, multi-modality imaging systems such as PET-CT, PET/MRI, SPECT/CT, and MRI/optical have combined both forms of imaging into a single system in order to obtain anatomic as well as metabolic information about tissue and are becoming the standards-of-care in different clinics.

One disadvantage of functional imaging systems based on PET and SPECT is that they require the injection of a radioisotope in the blood which limits their use as well as the number of times a patient may be imaged. Optical imaging is another functional imaging technique which uses low-energy visible or near infra-red light between the wavelengths of 600 to 1000nm and has proven to be able to detect concentrations of natural chromophores in the body including oxygenated hemoglobin, deoxygenated hemoglobin, water and lipids (fat). Diffuse optical imaging (DOT), also may be known as near-infrared spectroscopy (NIRS), is used to reconstruct spatial maps of the optical scattering coefficient and the absorption coefficient in order to reveal tissue properties that can be used to medical prognosis. DOT has been combined with contrast-enhanced MRI in previous systems and has shown promising results in increasing the sensitivity and specificity of breast cancer detection.

DOT provides a significant advantage over other functional imaging methods. It uses non-ionizing radiation, which eliminates radiation exposure and allows for repeated imaging without any harm to the patient; it could potentially be used on younger women as compared to x-ray; it could be lower cost; it is simple to implement compared to systems like MRI and X-ray CT; it is able to differentiate between soft tissues due to differences in absorption and scattering of tissue; benign and malignant tumors show different patterns and therefore can be distinguished; it is able to utilize various contrast mechanisms (endogenous and exogenous); and it could be built as a portable system which would enable use as a point-of-care technology.

Similar to all imaging modalities, DOT has a few disadvantages, including the need for trained expert users, difficulty for combining the results from one imaging modality to DOT, and poor spatial resolution which limits tumor size detection.

DOT has evolved a great deal due to advancement in development of computing technologies, optical hardware, and light propagation modeling. The combination of this within structural imaging modalities such as X-ray or MRI has been shown to provide a data set that with their NIRS information is overlaid on the anatomic map. While DOT/NIRS alone may not replace existing imaging modalities, it is a safe methodology that can provide functional information that may otherwise be difficult or harmful to obtain using conventional imaging modalities. Applications are primarily in functional imaging of the brain[1] [2] [3, 4], monitoring of tissue after surgery[5], and combined with other imaging modalities yields an increase in sensitivity and specificity of breast cancer detection[6, 7] [8] [9] [10].

## **1.2 Aims of this thesis**

The overall aim of this PhD was to understand the technology used in diffuse optical tomography imaging in order to design and build a system that can perform functional imaging of the breast while coupled to MRI for simultaneous MRI-NIRS imaging. In order to do so, first, a small-animal fluorescence tomography system was used to understand and improve a time-domain based optical tomography system. In this work, the system was reprogrammed in order to remove many bugs that caused intermittent problems that prohibited data acquisition. The system was also calibrated and characterized by imaging phantoms as well as small animals. Next, the work of Wang et al[1] [2] [3] was extended where a new and efficient hybrid system coupling frequency-domain and continuous-wave measurements was designed and built for non-invasive breast imaging that was able to perform optical spectroscopy of the breast using wavelengths between 600 and 950 nm. This MRI-coupled system was tested on phantoms, volunteers, and was also used to perform a clinical trial on patients in Xi'an, China. The clinical trial demonstrated the importance and need for full breast coverage for achieving accurate results.

Therefore, the third aim of this thesis was to find a cost effective solution which can cover the entire breast volume of the breast without sacrificing data quality or budget. Since our applications involves coupling MRI with NIRS, photon detectors that can be placed directly on the breast while the patient is inside the MRI were tested. This method disregards costly and bulky fiber optic cables that deliver and collect light in typical DOT setups. The final aim of this thesis was to present the design and development of a 64-channel cost efficient system which used the detector solution investigated.

### **1.3 Organization of this thesis**

Chapter 2 presents a brief background of diffuse optical tomography and functional imaging. NIR instrument types are discussed along a brief introduction of the mathematics behind image reconstruction. Three of the most important photon detectors that are used in DOT (photomultiplier tubes, photodiodes, and silicon photomultiplier) along with photon counting techniques are discussed.

Chapter 3 presents a background of time-domain DOT along with the building blocks and technology behind time-correlated single photon counting. A summary of a small-animal imaging fluorescence tomography system is presented along with the work performed in order to reprogram, calibrate, and test the systems. Results of phantom testing along with a small-animal imaging experiment are shown. Chapter 4 describes the work done to design and build a hybrid frequency-domain and continuous-wave breast imaging system. System characterization is discussed in detail including calibration, sensitivity, crosstalk, stability, and data acquisition and timing. Phantom testing along with in-vivo results of volunteers and cancer patients are presented in chapter 5. Chapter 6 explains the work done to test MRI-compatible photon detectors for in-magnet use. The results of this chapter was used to build a 64-channel system

which allows detectors to be placed directly on the breast tissue for simultaneous MRI and NIRS imaging while in-magnet as described in chapter 7. This chapter covers the characterization of the system as well as presents results performed on phantoms. Finally, chapter 8 discusses conclusions learned from this thesis along with future investigations and improvements.

## CHAPTER TWO

### Background

#### 2.1 NIR tomography/spectroscopy

Diffuse optical tomography is a unique noninvasive imaging modality where light in the near infrared (NIR) region (600-1000nm) is delivered to tissue while the transmitted/reflected portion of the light is acquired and analyzed. Implementation of non-linear tomographic algorithms enables reconstruction of functional information where changes in molecular compositions, such as oxyhemoglobin, deoxyhemoglobin, water, and lipids are recorded. The data then reveals physiological activity in the body that may be used to improve diagnostic accuracy since benign and malignant tumors have different vascular features.

A set of light sources and detectors that are placed on the surface of the tissue make up the transmittance measurements in diffuse optical tomography. Therefore, measurements are performed on tissue that partially transmits light. In DOT, light is delivered to tissue at one or more locations and the transmitted/reflected light exiting the tissue is collected at one or more locations, with delivery and collection commonly implemented using optical fibers. The intensity of the light is attenuated as the light photons travel inside of the tissue. The attenuation of light carries information pertaining to tissue composition and detectors at different locations are used to record the light as it exits. This attenuation is caused by mechanisms which may have either absorbed the light photons or which may have scattered the light photons from their initial direction. By separating the contribution of absorption and scattering, one is able to gain insights to the composition of tissue such as the absorbers previously described.

Measurements at multiple wavelengths are used in spectroscopic separation of the effects of individual chromophores in tissue. The minimum number of wavelengths necessary depends

on the number of chromophores that need to be quantified. For example, if only two chromophores need to be quantified, then, a minimum of two wavelengths are necessary to separate the effects of each chromophore. Furthermore, depending on properties of the tissue, it is possible to image tissue up to 10 to 12 cm thick. Although it is possible to increase this depth by increasing the optical power (intensity) of the light source used, the ANSI standards limits are imposed on the amount of optical power that are allowed to be used on living tissue.

After passing through tissue, the remaining light is registered by detectors at various locations around the tissue. Advanced algorithms are then used to estimate the complex pathways light has traveled through tissue and thereupon reconstruct images showing the spatial distribution of absorption and/or scattering of light in tissue [11, 12] [13] [14] [15]

Significant progress has been made over the past decade as instrumentation, inversion theory, and computing have matured, and so many prototype systems have been set-up for clinical trials.

## **2.2 Tissue optics and Optical Contrast**

Optical imaging relies on the interaction between photons and tissue, and therefore, the contrast provided by optical imaging is different than that provided by other functional imaging modalities such as PET and SPECT. As photons of light propagate through tissue, they encounter different particles that may either absorb the photons or scatter them in a different direction from their initial direction of propagation. Scattering and absorption both cause the light intensity to be attenuated as the remaining photon flux exits the tissue. Absorption causes annihilation of the photon as the photon transfers its full energy to the absorbing. Scattering alters the direction of the photon causing the photon to travel a complex and random path that

may lead to absorption of the photon or to exiting the tissue at a random location from the direct line-of-sight between the light source and the light detector.

Absorption of photons in tissue is due to natural chromophores which include oxyhemoglobin, deoxyhemoglobin, water content, lipids, melanin, collagen, etc. The relative concentrations of these values can be used to identify tumors and other abnormal tissues [16]. Scattering of photons in tissue is due to scatters such as cell nuclei and mitochondria.

While DOT relies on the natural endogenous chromophores of tissue, another form of optical imaging known as fluorescence diffuse optical tomography (FDOT), or diffuse fluorescence tomography (DFT), relies on exogenous contrast agents that are injected into the body. Exogenous contrast agents are able to enhance the contrast between normal healthy tissue and suspected tissue as well as provide an increase in detection sensitivity allowing pico-molar and even femto-molar contrast concentrations to be recovered [17]. These agents can target molecules that are specific to the type of cancer, such as breast cancer, and provide a robust signal-to-background ratio compared to imaging endogenous contrast alone [18]. FDOT enables signals to be detected at depths of 7-14 cm [19]. As will be shown below, tumors normally cause an increase in light attenuation as the photons are absorbed by the vascular structure of the tumor. However, with FDOT, when the contrast agents accumulate at the tumor site, photons that are absorbed by the contrast agents will be reemitted at a different wavelength where it can be filtered out in order to detect the fluorescent signal and isolate the tumor [20] [21]. The contrast in FDOT is due to fluorescence as opposed to absorption as in DOT. The drawback of this technique of course comes from causing the modality to become invasive (or minimally invasive) as compared to the non-invasive nature of DOT. However, there have been indications

where DOT imaging alone without contrast agents is insufficient for clinical applications which is in part why DOT is usually combined with other imaging modalities [22].

Regardless of the technique, photons follow different and complex paths as they migrate through tissue. Representative paths are shown in Figure 2.1. A photon incident on tissue may reflect from the surface of the tissue (paths A and C), diffuse through tissue (paths B, D, and E), or be completely absorbed (path F). When a photon is absorbed, it transfers its energy to the tissue. Photon reflection may be divided further into specular reflection (Path A) where the photons are reflected immediately as they hit the surface of the tissue, or diffuse reflection (Path C) where photons diffuse through tissue scattering multiple times until they reach the same plane the photons had entered. Transmission may also be divided further into direct transmission (path B) where photons may exit the tissue without experiencing any scattering, and diffuse transmission (paths D and E) where photons are scattered multiple times before they exit the tissue.

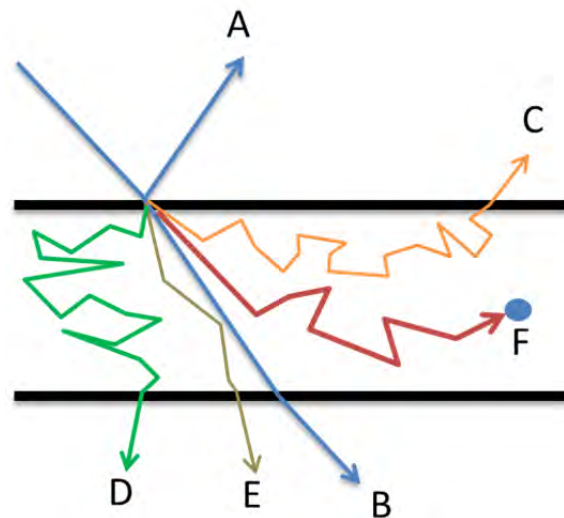


Figure 2.1: Different paths photons travel through tissue. Path A: specular reflection, Path B:

Ballistic photons (direct transmission), Path C: diffuse reflection, Path D: diffuse transmission, Path E: diffuse transmission (snake photons), Path F: absorption.

Photons that do not experience any scattering as shown in path B are known as ballistic photons. These photons carry the most amount of spatial information because of the fact that they have traveled the shortest path between the source and detector and have no information about the tissue other than the direct path it has followed between the source and the detector. While these photons carry the most amount of spatial information, only very few photons make it without scattering. Furthermore, ballistic photons decay with very high exponential attenuation as the thickness of the medium increases, making them unrealistic for any appreciable tissue thickness [23].

Photons which may have scattered very few times are sometimes referred to as snake photons (path E). These photons carry partial information about the nature of the original photons such as their initial direction and polarization. The majority of photons, however, are diffuse photons (paths C and D) where they diffuse through tissue scattering enough times to completely lose any information about the original nature of the photons. Imaging systems that utilize snake photons have a great spatial resolution, but low SNR due to the number of photons. On the other hand, imaging systems that use diffuse photons have a great SNR, but low spatial resolution as these photons would have traveled a complex tortious path before arriving to the detector.

The idea of DOT, or NIR spectroscopy, is to illuminate tissue with several wavelengths at one or more source locations, then observe the emerged light with detectors at one or more locations, and then to recover the concentrations of the tissue chromophores. Chromophores that absorb photons have a strong dependence on the wavelength of light used. The absorption

spectrum of the four main chromophores is shown in Figure 2.2. There are two main points that are illustrated in the figure. First, it is clearly shown that each chromophore has a distinct spectral shape. Second, one may note the reduced absorption at wavelengths between 600 and 1000 nm.

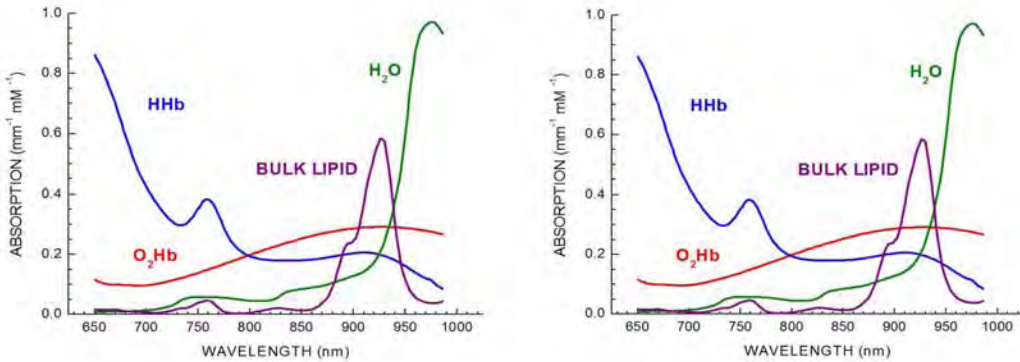


Figure 2.2 (a): Absorption spectrum of the four main chromophores found in breast tissue, (b) scattering spectrum of tissue.

The first point explains why multiple wavelengths are used in DOT. Since each chromophore has a distinct spectral shape, by using enough wavelengths, one is able to separate the effects of each chromophore and thus, obtain the concentration of each chromophore. The second point explains why DOT uses the narrow spectral window of the electromagnetic spectrum. Light below 650 nm is strongly absorbed by hemoglobin while light above 1000 nm is strongly absorbed by water. Since contrast in DOT is mainly due to chromophores absorbing the photons, complete absorption of photons will result in no or very little contrast. Therefore, the 650-1000 nm spectral window is used with optical imaging which enables imaging to be performed at centimeter depths. Unlike absorption, scattering of photons in tissue is weakly dependent on the wavelength of light as shown in Figure 2.2 (b).

By analyzing the absorption and scattering of tissue, one is able to distinguish between normal and abnormal tissue. For example, in general, tumors have high vascular features than the surrounding tissue leading to an increase in photon absorption. Furthermore, by looking into the scattering, one may be able to discriminate between benign and malignant tumors and cysts. While tissue does exhibit properties other than absorption and scattering (i.e. fluorescence, inelastic scattering, etc. [24] [25]), these interactions are smaller when compared to absorption and scattering and are usually ignored in intrinsic NIRS.

### **2.3 NIR instrument Types**

Three different measurement types are used with DOT/NIRS methods: 1) steady-state (SS) [also known as continuous-wave, CW], 2) frequency-domain (FD), and 3) time-domain (TD). These types differ in their complexity as well as the amount of tissue information that may be retrieved from the measurements. The light input and measured output signal for the three different techniques is depicted in Figure 2.3.

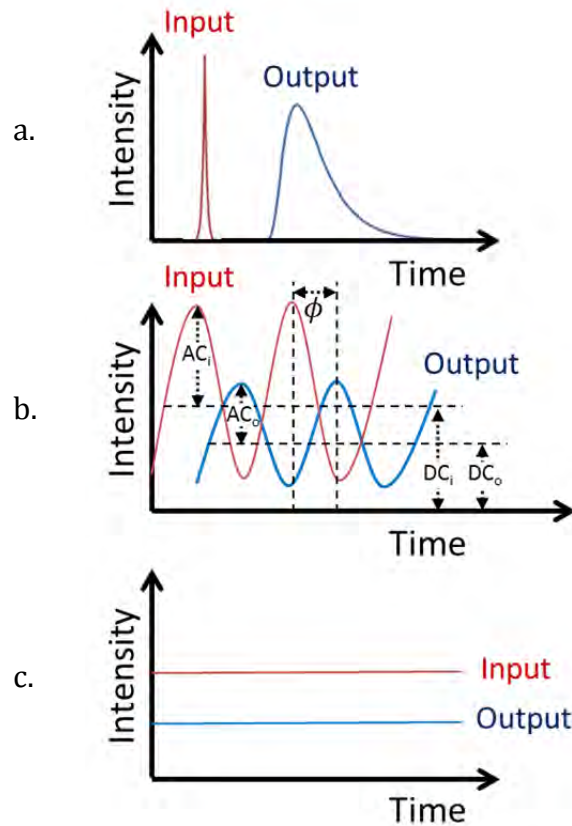


Figure 2.3: Light input/output of optical signal for the three instrument types used in DOT. (a) Time-domain, (b) frequency-domain, (c) steady-state.

The simplest approach to optical tomography is the steady-state technique. In this approach, a constant intensity light source (white light, LED, or laser) is incident on tissue while the attenuated reflected and/or transmitted light is measured. The light source may be modulated at low frequency (from DC up to a few MHz) to increase the signal-to-noise ratio (SNR). Modulating the light source and measuring the attenuated light at the same frequency as the source improves SNR by allowing the measurement to lock onto the correct signal while suppressing sources that are not correlated with the modulated measurement such as background light. Modulation of the source also permits multiple sources and/or multiple wavelengths to be used simultaneously by modulating sources and/or wavelengths at difference modulation

frequencies. Steady-state measurements provide relative changes to optical contrast (Hb, HbO) and not absolute measurements. A drawback of steady-state imaging is that the absorption and scattering of tissue cannot be determined simultaneously as intensity measurements alone cannot separate the effects of each [26]. One way to solve this problem is to assume a constant scattering throughout tissue (homogeneous tissue) and then derive the absorption information using intensity measurements [27]. Another approach is to use multiple source/detector positions to image tissue.

Frequency domain spectroscopy employs a modulated light source (50 MHz to 1 GHz) where the phase and amplitude of the transmitted/ reflected output signal is measured with respect to the input light as shown in Figure 2.3 (b). Different methods are used to measure the phase and amplitude including homodyne detection, heterodyne detection, and single-side band detection. These methods are detailed in Chapter 4.

Time domain systems can provide the most information about the nature of the diffuse photons and thus the tissue composition. In TD systems, a narrow laser pulse illuminates the tissue and the light flux on the boundary is measured. As the laser pulse travels through tissue, it is attenuated, delayed, and gets broadened with respect to the original pulse. Absorption and scattering coefficients may be determined by measuring the time it takes for the pulse to reach the detector and the shape of the pulse. For example, photons in a high scattering medium will take longer to exit the tissue as they keep scattering, which will lead to a broadening of the input laser pulse as shown in Figure 2.4. Photons in a high absorption medium will be attenuated and only photons with a relative short pathlength will make it through the tissue which will result in a lower pulse intensity while somewhat preserving the width of the input pulse as shown in Figure

2.4. Figure 2.4 also shows the banana patterns photons create as they are scattered in tissue showing the arrival of early, diffuse, and the late photons associated with the banana patterns.

Streak cameras, time-correlated photon counting systems (TCSPC), and time-gated intensified CCD imagers are used with TD measurements and are able to generate images with improved image quality [28]. Furthermore, TD systems can be used with FDOT where images of fluorescent yields and lifetimes of multi-components can be obtained to further enhance DOT[29]. TCSPC systems are discussed further in Chapter 3.

The advantage of time-resolved techniques (TD and FD) over SS is that these methods are able to measure the distance a photon travels in addition to the number of photons that exit the tissue (i.e. light intensity). FD provides an average pathlength of the photons while TD systems provide a precise measure of the pathlength. This additional data adds to the uniqueness of the solution to recovering the absorption and scattering coefficients and enables a better image reconstruction.

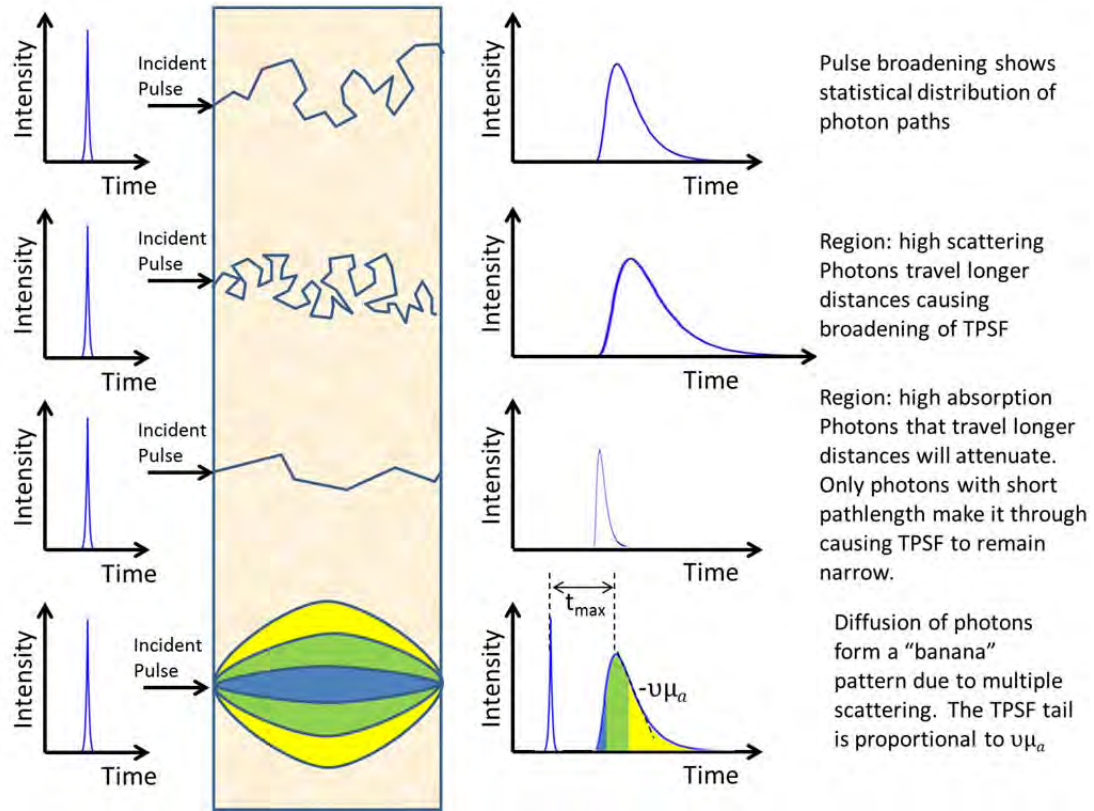


Figure 2.4: the transmission of a light pulse through tissue is illustrated where broadening due to multiple scatter is illustrated along with attenuation of the broadened pulse due to absorption. The temporal bands detected have traversed different average paths, as illustrated in the bottom row.

A summary of the three methods is shown the table below.

	Steady-State	Frequency-Domain	Time-Domain
Cost	Cheap	Moderate	Expensive
Complexity	Low	Medium	High
Measurement	High SNR	Medium SNR	Low SNR

Table 2.1: Comparison of DOT techniques.

## 2.4 Light Modeling and the diffusion approximation

Light photons in biological tissue can be modeled by the radiative transfer equation (RTE). The RTE describes the propagation of radiation through a medium (e.g. tissue for example). It is a differential equation that describes the change in light intensity  $L(\vec{r}, \hat{s}, t)$  with respect to time in a medium where photons do not interact with one another and are subjected to absorption and scattering events. The RTE is given by:

$$\frac{1}{c_m} \frac{\partial L(\vec{r}, \hat{s}, t)}{\partial t} = -\hat{s} \cdot \nabla L(\vec{r}, \hat{s}, t) - (\mu_a(r) + \mu_s(r))L(\vec{r}, \hat{s}, t) + Q(\vec{r}, \hat{s}, t) + \frac{\mu_s + \mu_s}{4\pi} \int_{4\pi} L(\vec{r}, \hat{s}', t) P(\hat{s}' \cdot \hat{s}) d\Omega'$$

, where:

$L(\vec{r}, \hat{s}, t)$  = the light intensity (number of photons per unit volume) at position  $r$  in direction  $\hat{s}$

$P(\hat{s}' \cdot \hat{s})$  = the normalized scatter phase function which gives the probability of scattering from direction  $\hat{s}'$  to direction  $\hat{s}$

$S$  = the source distribution

$\mu_a$  = the absorption coefficient (0.002 to 0.01 mm<sup>-1</sup> for breast tissue; 1/ $\mu_a$  represents the average distance a photon would travel before experiencing an absorption event)

$\mu_s$  = the scattering coefficient (0.1 to 10 mm<sup>-1</sup> for breast tissue ; 1/ $\mu_s$  represents the average distance a photon would travel before experiencing a scattering event)

$c_m$  = the speed of light in the medium ( $c_m = c_o/\eta$  where  $c_o$  is the speed of light in vacuum and  $\eta$  is the index of refraction of the medium)

The RTE states that the change in the light intensity with respect to time is effected by the flow of photons in the  $\hat{s}$  direction ( $\hat{s} \cdot \nabla L(\vec{r}, \hat{s}, t)$ ), the scattering and absorption events that occur ( $(\mu_a(r) + \mu_s(r))L(\vec{r}, \hat{s}, t)$ ), by the source of light ( $Q(\vec{r}, \hat{s}, t)$ ), and by photons that scatter from other directions into the  $\hat{s}$  direction ( $\frac{\mu_s + \mu_s}{4\pi} \int_{4\pi} L(\vec{r}, \hat{s}', t) P(\hat{s}' \cdot \hat{s}) d\Omega'$ ).

The RTE equation can be solved numerically via Monte Carlo simulations or analytically. Analytic solutions can be found for problems with simple geometries and cannot usually be found for complex geometries. Monte Carlo simulations are a great tool for analyzing the RTE. This method simulates the path of individual photons as they scatter and get absorbed in tissue. However, this method is stochastic in nature where the variance of the resulting photon fluence depends on the number of photons simulated. Therefore, this method requires a large number of photons to be simulated in order to arrive at the correct results and, thus, is very computationally expensive. An approximation to the RTE known as diffusion approximation is used to simplify the modeling of photons in tissue and is more computationally efficient. The diffusion approximation in time domain is given by:

$$\frac{1}{c_m} \frac{\partial \phi(r, t)}{\partial t} + \mu_a(r) \phi(r, t) - \nabla \cdot D(r) \nabla \phi(r, t) = q_o(r, t)$$

, where:

$\phi$  = the fluence rate (photon density) at position  $r$

$D(r)$  = the diffusion coefficient and is defined as:  $D(r) = \frac{1}{3(\mu_a(r) + \mu'_s)}$  where  $\mu'_s$  is the reduced scattering coefficient defined as  $\mu'_s = (1 - g)\mu_s$  where  $g$  is the anisotropy factor which describes the relative directional bias of optical scattering ( $g \sim 0.7-0.9$  for tissue)

Here, an isotropic source  $q_o$  delivers photons through the media. The first term in the diffusion approximation is the flow of photons out of the volume with respect to time. The second term is the total absorption per volume. The third term is the product of the photon density and diffusion coefficient. The right hand side of the equation is the source term. The frequency-domain equivalence of the time-domain diffusion approximation can be found by Fourier transforming the time-domain equation and is given by:

$$\frac{j\omega}{c_m} \phi(r, w) + \mu_a(r)\phi(r, w) - \nabla \cdot \mathbf{D}(r)\nabla\phi(r, w) = q_o(r, w)$$

, where  $\omega$  is the modulation frequency.

In order to arrive at the diffusion approximation, few assumptions were made which include: 1) scattering events dominate over absorption events ( $\mu_a \ll \mu_s$ ), 2) source term is isotropic, 3) phase function is independent of absolute angle, 4) photon flux changes very slowly. All such approximations are valid for tissue measurements. Assumption 2 may seem plausible with highly directional sources such as laser light. However, due to the high scattering of tissue, even highly directional light can be modeled as an isotropic light source after one reduced scattering distance ( $\sim 1\text{mm}$ ). Assumption 4 limits light modulation to less than 1 GHz.

## 2.5 Image Reconstruction

Image reconstruction is beyond the scope of this thesis. However, a brief introduction follows. There are two problems that are related to image reconstruction in diffuse optical tomography: the forward problem and the inverse problem. In the forward problem, one is interested in finding the light intensity at the boundary of tissue with known optical properties for a known source input. The solution to this problem is simply found by solving for the light intensity term in the diffusion approximation equation. In the inverse problem, light is delivered to tissue and light detectors measure the light output at the tissue boundary. In this problem, one is interested in finding the tissue optical properties that have caused the measured data.

Both problems are best solved using numerical methods which include Monte Carol, finite element methods (FEM), or finite difference methods (FDM). Image reconstruction in this thesis was implemented using NIRFAST, which uses FEM methods to solve diffusion approximation problem.

In FEM, the tissue is modeled by finite number of elements where each element has nodes at its corners. The goal of this method is to estimate the photon density of the diffusion approximation ( $\phi$ ) at each of these nodes. The location of each node is defined in a mesh.

It can be shown that applying FEM to the forward solver becomes a simple matrix problem of the form [30]

$$\begin{bmatrix} A_{bb} & A_{bl} \\ A_{lb} & A_{ll} \end{bmatrix} \begin{bmatrix} \Phi_b \\ \Phi_l \end{bmatrix} = \begin{bmatrix} S_b \\ S_l \end{bmatrix}$$

, where A components are elements of the diffusion approximation equation,  $\Phi$  is the photon density and S is the source intensity [30].

In the inverse problem, the numerical way of finding a solution to the light intensity at the boundary is through minimizing the difference between the measured fluence  $\phi^m$  and

between the calculated fluence data  $\phi^c$  obtained from the forward solver. This minimization is given by:

$$\chi^2 = \sum_{i=1}^{NM} (\phi_i^c - \phi_i^m)^2$$

, where NM is the number of measurements.

Another approach to minimization, known as the Tikhonov approach, adds an extra term that can be thought of as a damping term which keeps the current optical property estimate from wandering off too far from the initial estimate.

$$\chi^2 = \sum_{i=1}^{NM} (\phi_i^c - \phi_i^m)^2 - \lambda \sum_{j=1}^{NN} (\mu_j - \mu_o)^2$$

, where  $\lambda$  is a weighing factor of the difference between the current estimate of the optical property at each node subtracted from the initial estimate  $\mu_o$  and NN is the number of FEM nodes.

Minimizing the  $\chi^2$  function is done by setting the first derivative to 0:

$$\left(\frac{\partial \phi^c}{\partial \mu}\right)^T (\phi^c - \phi^m) - \lambda(\mu_j - \mu_o) = 0$$

The derivative matrix above is known as the Jacobian matrix J. Using this linear approximation and solving the problem as an iterative scheme gives [11]:

$$(J^T J + \lambda I) \delta \mu = J^T \delta \phi - \lambda(\mu_j - \mu_o)$$

, where  $\delta \mu$  is the update for the optical properties,  $\delta \phi$  is the data-model misfit at the current iteration, and I is the identity matrix. In NIRFAST, this equation is iterated until the update ( $\delta \mu$ ) from one iteration to the next is less than 2%.

After solving for the optical properties at each wavelength, the chromophore concentrations are calculated using a constrained least square fit to the Beer's law,  $\mu_a = [\epsilon]C$ , where  $\epsilon$  is the molar absorption spectra of the tissue's absorbing chromophores and C is the

concentration of the chromophores. Also, the scatter power (b) and scatter amplitude (a) are also calculated using an approximation to Mie's scattering theory:  $\mu'_s = a\lambda^{-b}$ . The scattering power and amplitude reflect variations of the tissue composition and maybe used to enhance image reconstruction and differentiation between tumors.

The Beer's law and Mei's scattering law that are used to find the chromophore concentrations and scattering information can be incorporated directly into the reconstruction. This spectral constraint method reduces the number of unknown parameters ( $\mu_a$  and  $\mu'_s$  at each wavelength) to 6 parameters (oxy-hemoglobin, deoxy-hemoglobin, water, lipids, scattering amplitude and scattering power). The spectral constraint image reconstruction reduces the parameter space by coupling together the measurements at all wavelengths along with the Beer's law and Mei's scattering law. This approach is faster, more accurate, and more robust to noise [31] [32]

Finally, another approach that simplifies the inverse problem and increases the speed and accuracy is to include a priori information. A priori information ... During reconstruction,

Breast image reconstruction in this thesis is implemented in NIRFAST which automates and simplifies the process of image reconstruction. The steps needed to perform image reconstruction are as follows: a mesh based on the MRI results is created for each patient. Each mesh is then segmented into three regions: adipose, glandular, and tumor which serves as a priori information for image reconstruction. Sources and detectors are then placed on the mesh. The location of sources and detectors is obtained through the MRI stack by use of MRI fiducial makers that are placed at known location with respect to the detectors/sources. In other cases, the sources/detectors may be known in advance for simple cylindrical or circular geometries. Forward data is then simulated on the mesh. Next, the optical properties of the mesh is estimated

though an iterative Levenberg-Marquardt style iterative update with a modified Tikhonov regularization. All these steps are handled via two open source software packages NIRFAST and NirVIEW.

## 2.6 Photon Detectors

Photon detection in DOT experiments demand high performance detectors as tissue absorption may reduce optical signals by approximately 10-fold per centimeter of tissue for light in the red to near-infrared part of the spectrum[17]. The transmitted optical power through tissue in optical tomography depends on the tissue type, source strength, and source-detector separation and may range from milli-watts up to femto-watts for a total dynamic range of  $10^{12}$ . The purpose of this section is to review and compare photon detectors that are used in the projects of this thesis. Specifically, photomultiplier tube, photodiodes, and silicon photomultiplier are discussed in detail. Photon counting is also discussed as it pertains to diffuse optical tomography and is one of the most sensitive techniques that yields the highest signal-to-noise ratio.

### 2.6.1 Light

Light consists of a stream of particles called photons. The role of a light detector is to convert photons (photon flux [photons/second]) into a signal that can be measured. In order to appreciate their role, it is useful to calculate the energy of a single photon. The energy of a photon depends on the wavelength. For a red photon with a wavelength of 600nm, its energy can be calculated using the following formula:

$$E_{\text{photon}} = h\nu = h \left( \frac{c}{\lambda} \right) = 6.62 \times 10^{-34} \frac{(3 \times 10^8)}{(600 \times 10^{-9})} \approx 3 \times 10^{-19} \text{ joules}$$

, where:

$h$  = Planck's constant [joule-seconds],

$\nu$  = frequency of light ( $\nu = \frac{c}{\lambda}$ ) [Hz]

$c$  = speed of light [m/s]

$\lambda$  = wavelength of light [m]

Power is equal to the energy per unit time and for a 600 nm photon, the power associated with a single photon per second is  $\sim 3 \times 10^{-19}$  Watts. In order to further appreciate photon detectors, one can calculate the number of photons that are emitted by a weak laser signal. A typical hand-held laser pointer emits a laser beam with a power of  $\sim 1$  mW at a wavelength around 600 nm. The number of photons that are emitted by the laser diode per each second can be calculated using the following formula:

$$n = \frac{P\lambda}{hc} = \frac{(1 \times 10^{-3}) \times (600 \times 10^{-9})}{(6.62 \times 10^{-34}) \times (3 \times 10^8)} \approx 3 \times 10^{15} \text{ photons/second}$$

, where

$P$  = incident light power [watts].

Photons striking a detector could range from a single photon up to millions of photons and even more. A detector that is able to accommodate such a large dynamic range does not exist and one has to take into consideration the working principles and limitations of photon detectors that are used for light detection.

Finally, the speed of light is  $3 \times 10^8$  m/s in vacuum. This speed is reduced as light travels in different mediums. For example, light travels at a speed of approximately  $2.2 \times 10^8$  m/s in tissue[33]. Thus, in one picosecond, light travels a distance of 300  $\mu$ m in free space but only 220  $\mu$ m in tissue. Although this is a very small difference, systems such as time-correlated single photon counting essentially utilize extremely fast detectors and electronics in order to detect photons down to 1 picosecond ( $1 \times 10^{-12}$  s) resolution. Even higher time resolutions may be

reached using streak cameras which can reach a resolution down to the femtosecond ( $1 \times 10^{-15}$  s) range.

### 2.6.2 Photomultiplier tube (PMT) detectors

To this day, PMT detectors are the gold standard among the most sensitive detectors. A single photon striking a PMT detector generates anywhere between  $10^6 - 10^9$  electrons. With the proper resistor terminated at the output of the PMT, this current pulse is converted to voltage in the mV range which can easily be measured. A simplified schematic of a typical PMT is shown in Figure 2.5 below.

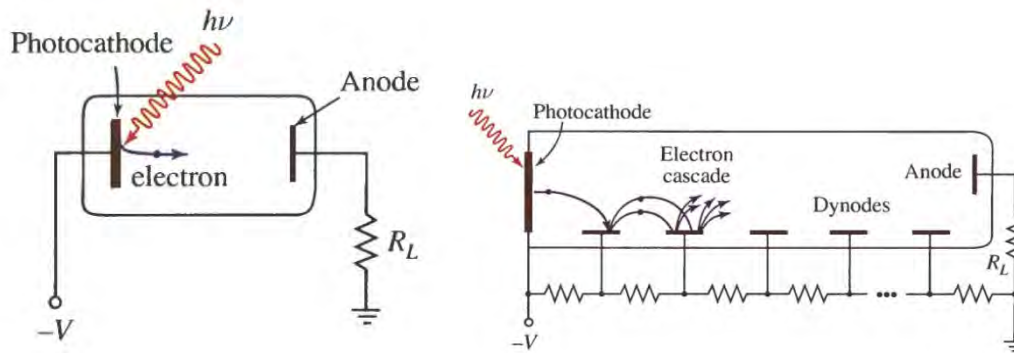


Figure 2.5: the detection of light in an electron-vacuum tube is illustrated at left, where electrons are generated from a photocathode and travel through vacuum to the anode where current is generated. On the right, the electron multiplication is illustrated by sequential collision at each of the charged dynodes in a photomultiplier tube [34].

A PMT consists of a photoemissive cathode (photocathode), focusing electrode(s), electron multiplier (dynodes) and electron collector (anode). The entire apparatus is housed inside a vacuum tube. When a photon strikes the photocathode, an electron is generated (photoelectron). The focusing electrodes direct the photoelectron to the dynode chain where each dynode is then used to multiply the number of electrons through the process of secondary emission. The first conversion process, the photoelectron conversion, has a rather poor

efficiency (typically below 30%). In fact, some of the emitted photoelectrons do not find their way to the first dynode and thus cannot be multiplied. The collection efficiency of a PMT varies with wavelength and is between 60 and 90%. The remaining electron multiplication activity after the first dynode has very little noise associated with this process and is usually very efficient.

As the electrons are multiplied by each consecutive dynode in the chain, the number of electrons grows larger and larger until all the electrons are collected at the anode. The output signal therefore is a current signal consisting of a large number of electrons. By connecting the anode to the ground through a resistor, the current signal induces a voltage drop across the resistor which can be measured by electronic circuitry. Each dynode in the dynode chain contributes to the electron multiplication. The multiplication due to each dynode is not constant and exhibits some variance. Therefore, one considers only the mean value of the secondary emission factor for each dynode ( $\delta$ ). In an n-dynode chain PMT, a single electron is multiplied by  $\delta^n$  and results in a pulse at the anode. This gain mechanism associated with the photomultiplier tube detectors makes it one of the most sensitive devices to date.

Due to the variance of secondary emission, the generated output pulse has a large variance. Thus, for the same number of photons striking the PMT, output pulses with varying heights are generated. Figure 2.6 (a) shows an example of PMT output pulses with varying heights that may result from the same number of incident photons. Figure 2.6 (b) shows a histogram of the pulse height distribution. As expected, the pulse height distribution shows a Poisson characteristic except for a slight deviation at the low pulse heights side of the curve due to dark counts which will be explained later in this chapter.

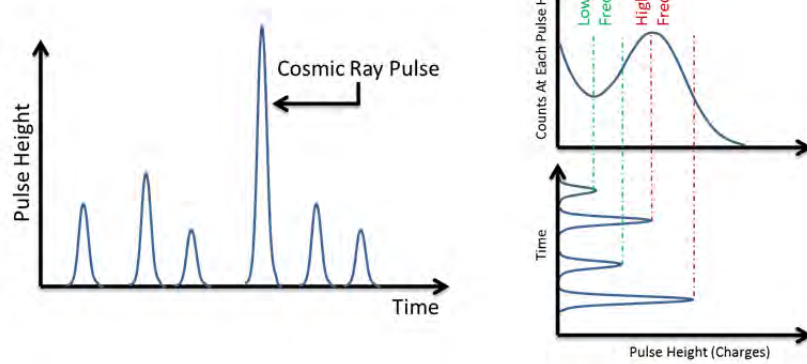


Figure 2.6: a. Diversity of PMT output pulse heights (b) PMT output pulses and pulse height distribution of the pulses.

A PMT detector may be operated in an analog (DC) or digital (photon counting) mode. In an analog mode, the detector is unable to resolve the effect of individual photons due to the large number of photons striking the detector. The contribution of individual photons cannot be measured, but rather the sum of contributions of all photons is summed. This mode is depicted in Figure 2.7 (a).

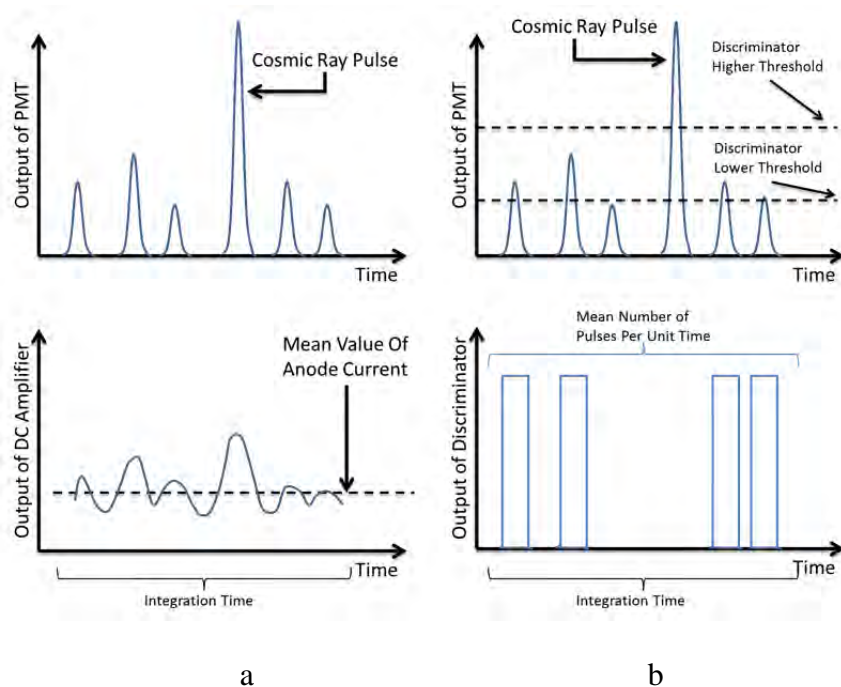


Figure 2.7: PMT operation modes: (a) analog (b) photon counting.

As shown in part a, even though photons generate pulses, the pulses end up overlapping each other. In this mode, the mean value of the analog current, which is proportional to the intensity of the light flux input, is measured. Due to the statistical characteristics and variance of the amplitude of the output pulses, the noise of the mean value of the anode current is larger than the photon (shot) noise. SNR is lower in the analog mode than photon counting operation mode.

In digital (photon counting) mode, the detector receives photons that are separated from each other by at least the width of the single electron response (SER) of the detector. This mode allows the individual pulses to be counted and summed, regardless of the pulse amplitude. The number of pulses counted per unit time is proportional to the light flux intensity. An immediate advantage can be seen here where the noise associated with the output pulse variation no longer contributes to the noise of the output signal. There are several advantages to using PMTs in digital (photon counting) mode instead of the analog mode which are discussed in more detail in the photon counting section in this chapter.

Typical NEP values for a bandwidth of 1 Hz for a PMT are between  $10^{-15}$  and  $10^{-16}$  Watts [35]. This translates to detection of 400 to 4000 photons per second for a 800 nm photons. Cooling the PMT can improve the NEP value by reducing dark current. Cooled PMT detectors are able to reach NEP values of  $10^{-21}$  W/Hz<sup>-0.5</sup> [36]. Including shot noise in the calculation above will reduce the NEP value slightly. The difference, however, will increase with increasing bandwidth.

### 2.6.3 Photodiodes/PIN photodiodes

A Photodiode is a fast, highly linear photon detector with high quantum efficiency. It is a semiconductor device where a P-layer and N-layer regions form a p-n junction which is the basic element of a photodiode. By controlling the thickness of these layers as well as the dopant concentration in the layers, the spectral and frequency response of the photodiode can be controlled to fit various applications. Figure 2.8 shows a schematic of the cross section of a typical photodiode.

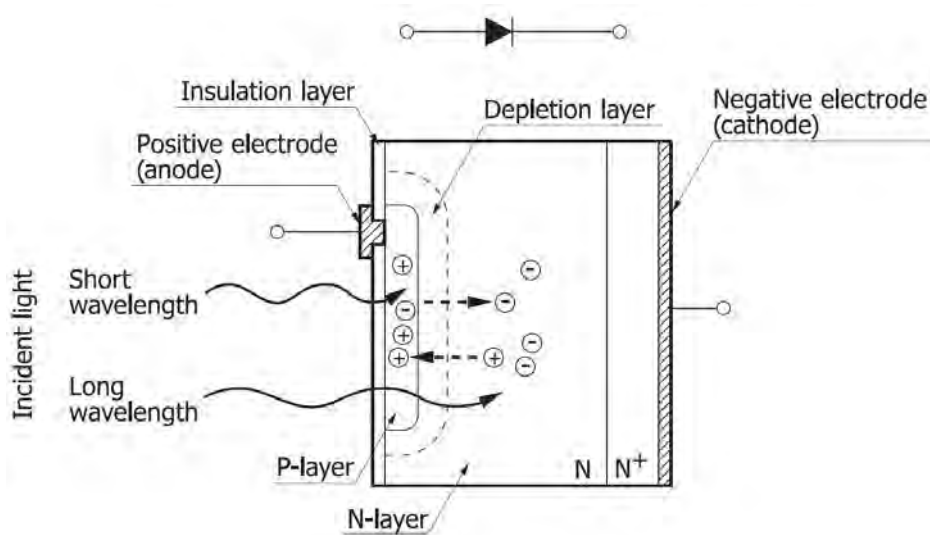


Figure 2.8: Schematic of Si Photodiode Cross Section [37].

Light (with sufficient energy) incident on a photodiode generates electron-hole pairs throughout the photodiode in proportion to the light level. Due to the dopant concentration which

offers excess electrons in the n-layer and excess holes in the p-layer, the electron-hole pairs distribute themselves in such a manner which results in an accumulation of positive charge in the P-layer and a negative charge in the N-layer. If connected to a circuit, electrons will flow away from the N-layer side and holes will flow away from the p-layer type resulting in an electric current in the circuit.

While the electrons and holes rearrange themselves in the PN junctions, a depletion region that is free of excess carriers (no holes or electrons) is created. Adding a voltage potential across the PN junction of the device creates an additional electric field which in turn, enables a larger depletion region and aids in transporting the carriers to their respective terminals; holes are transported to the anode side (p-layer) and electrons are transported to the cathode side (n-layer).

A PIN photodiode, shown in Figure 2.9 (b), is similar to an ordinary photodiode except it has an additional intrinsic (un-doped) layer sandwiched between the p and n layers and is thus called p-i-n or PIN photodiode. This region provides better and smoother depletion region which has advantages over ordinary photodiodes and will be discussed later in this section.

When light is incident on the photodetector, photons that are absorbed in the depletion region or the intrinsic region in a PIN photodiode create electron-hole pairs, most of which contribute to the photocurrents. These electron-hole pairs are swept from the junction by the electric field where holes move toward the anode and electrons move toward the cathode, thus, generating a photocurrent.

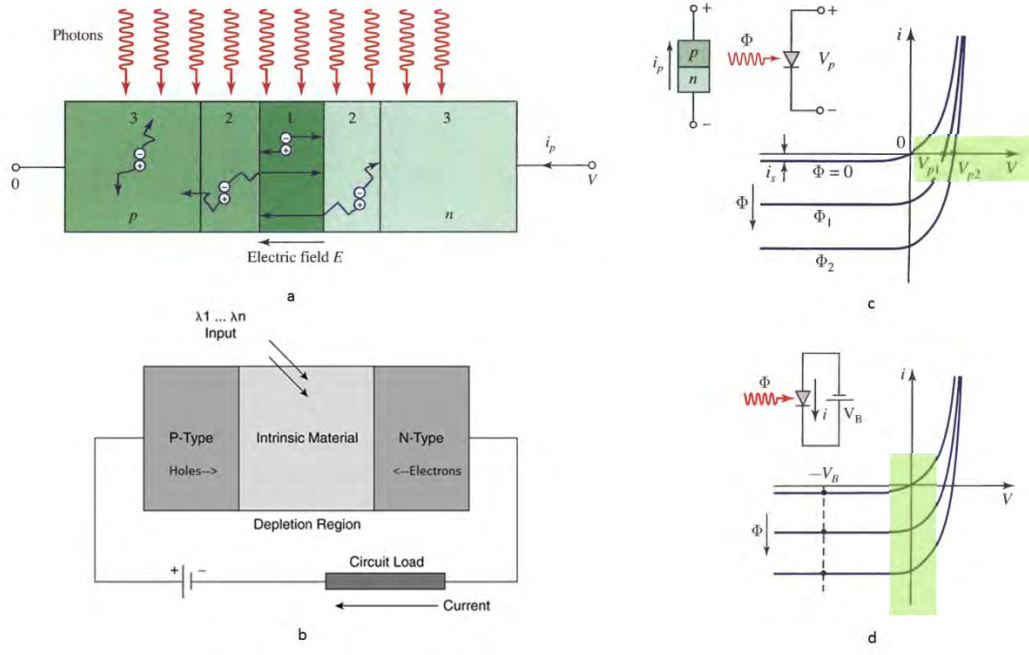


Figure 2.9: (a) photons illuminating an ideal reverse-biased p-n photodiode, (b) PIN photodiode operation, (c) forward-biased (photovoltaic) operation of a photodiode, (d) reverse biased operation of a photodiode.

A p-n junction allows current to flow easily in one direction (forward biasing) but hardly at all in the other direction (reverse biasing). In forward biasing mode depicted in Figure 2.9 (c), also may be known as zero-bias mode, the detector generates current as light is absorbed by the detector. This mode of operation requires no biasing voltage and it is said that the detector is operating in the photovoltaic region. This mode has the advantage that the dark current is kept at a minimum. However, the maximum speed is not achieved.

In reverse biasing mode, as shown in Figure 2.9 (d) an external reverse voltage bias is applied, which increases the width of the depletion region, resulting in an increase in responsivity and a decrease in junction capacitance which leads to an increase in the response time of the detector. Detectors operating in reverse bias mode are said to operate in the photoconductive mode. The output signal in this mode is highly linear. The dependence of the

photocurrent on the light power can be very linear over six or more orders of magnitude of the light power, e.g. in a range from a few nanowatts to tens of milliwatts for a silicon p-i-n photodiode with an active area of a few  $\text{mm}^2$  [48]. However, this mode has a higher dark current contribution to the output signal resulting in a slightly less sensitive detector compared to the forward (zero) biased mode.

One of the disadvantages of photodiodes is that they provide no internal gain mechanism. One photon generates a single electron-hole pair. Therefore, these detectors must use an amplifier circuit in order to amplify the output signal and detect low light levels. Furthermore, in order to detect a signal, the incident light must be larger than the inherent noise of the detector. With photodiode, noise limits the sensitivity of these detectors in room-temperature to several hundred photons [38].

For a  $1 \text{ cm}^2$  active area detector, a typical value of NEP is around  $10^{-12} \text{ W/Hz}^{-0.5}$  [36]. The NEP value is a strong function of temperature due to the direct temperature dependence and due to the dependence of the shunt resistance  $R_{\text{sh}}$  on the temperature. Also, smaller area detectors can reach a higher NEP value of around  $10^{-15} \text{ W/Hz}^{-0.5}$ . Adding a bias voltage may slightly increase the sensitivity of the photodiode but will also increase the dark current, thus, decreasing the NEP value.

#### **2.6.4 Silicon Photomultiplier**

The silicon photomultiplier is a novel semiconductor detector which consists of an array of SPAD detectors in parallel as shown in Figure 2.10. Each SPAD represents one pixel (also referred to as a microcell) of the SiPM detector that is capable of detecting single photons. SiPM detectors are known by many names in the literature where some of the common ones include multipixel photon counter (MPPC), pixelized photon detector (PPD), multipixel Geiger-mode

avalanche photodiode (MPGM APD), Geiger-mode avalanche photodiode (G-APD), solid state photomultiplier (SSPM), etc. These detectors overcome the weakness of the smaller size of SPAD detectors

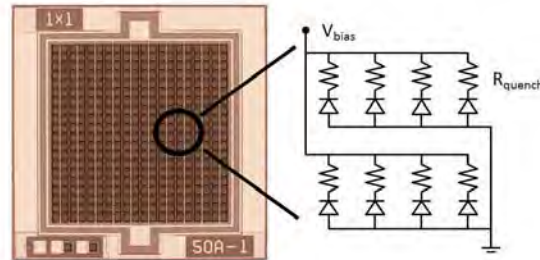


Figure 2.10: SiPM detector showing SPAD array[39].

When the photon flux is low and photons arrive at intervals longer than the recovery time of a pixel, the output of a SiPM detector will be pulses that are equal to a single photoelectron and photon counting can be used to count the number of photons and deduce the intensity of light. Note that all the pixels are connected to a single readout channel. When the photon flux is high or the photons arrive in short pulses with intervals less than the recovery time of a pixel, the output pulses from the pixels will overlap each other and create a larger pulse as shown in figure 2. 11 below for 2 and 3-photoelectron pulses [40]. This pseudo-analog output can measure the number of photons per pulse which is not possible with SPAD detectors. By measuring the height or by integrating the area of each pulse, the number of photons detected can be estimated and the photon flux can be measured.

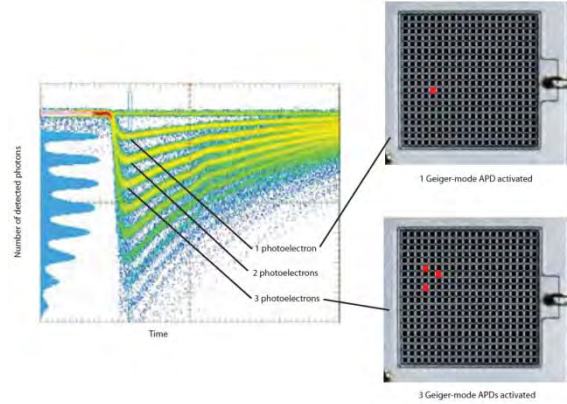


Figure 2.11: Pulse waveform for different number of photoelectrons [41].

In order to calculate the efficiency of SiPM detectors, the photon detection efficiency takes the fill factor into consideration and is defined as:

$$PDE(\lambda, V) = QE(\lambda)\epsilon(V)GE$$

, where QE is the quantum efficiency,  $\epsilon$  is the avalanche initiation probability, and GE is the geometrical efficiency (fill factor) which reflects the fraction of photosensitive surface of the device due to the fact that each pixel is surrounded by some strip of insensitive material separating the pixels from each other.

Typical pixel size varies between 20-100um with a pixel density between 100 and 1000 per  $\text{mm}^2$  (highest density achieved so far is around 1600 pixel per  $\text{mm}^2$ ). Typical active areas range between 1x1 to 3x3  $\text{mm}^2$ . SiPM detectors have numerous advantages: they are solid state devices, compact, rugged, durable, require low bias voltage (<100V) and low power consumption, low cost (<\$300), easy to use, high photon detection efficiency (PDE ~ 20% and increasing with a potential of reaching 70%), high gain ( $10^5 \sim 10^6$ ), good speed response (300 – 900 nm), good time resolution, have a wide spectral response range, have no burn in phenomena that might occur due to light saturation, they tolerate accidental illumination, and can be used for photon counting. Also, these detectors are insensitive to magnetic fields up to 15 Tesla.

The dark count rate is high for SiPM detectors. Dark counts are caused by thermally generated electrons afterpulsing, and optical cross talk where thermally generated electrons are the dominant continuator for SiPM detectors. At room temperature, typical dark count rates are  $10^5$ - $10^6$  counts per second per  $\text{mm}^2$  [42] The dark pulses have a Poisson distribution in time and so the noise contribution is the square root of the dark count rate. Reducing the volume of the detector or cooling the detector will reduce the dark counts significantly. Another method that combats dark counts is to use a discriminator and set its threshold value above the single electron level which improves the dark count rate substantially. Figure 2.12 below shows effect of setting different discriminator threshold values. However, reducing the temperature further may enhance dark counts caused by afterpulsing. Afterpulsing is a phenomenon where phantom pulses are generated some time after the generation of the primary pulse. This is due to electron charges being trapped in the semiconductor dopant during the avalanche caused by the primary pulse. These trapped charges themselves cause an avalanche which results in a false pulse which may be regarded as a true pulse.

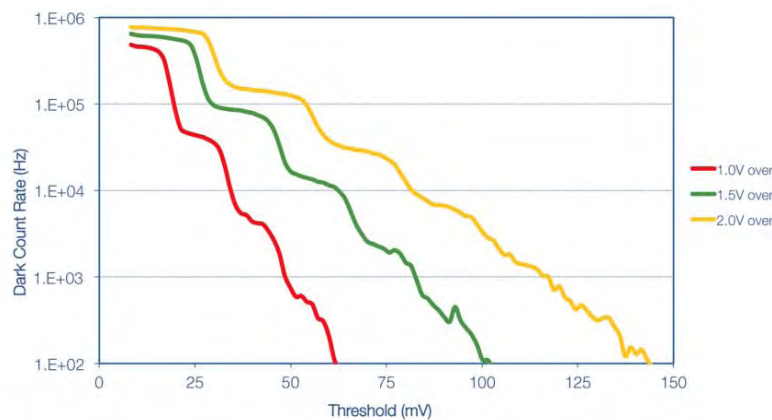


Figure 2.12. Dark count rate of a 1mm, 35um microcell SPM as a function of discriminator threshold for different over-voltage levels [43].

Optical cross talk is another issue that plagues SiPM detectors where an avalanche in one pixel will initiate another avalanche in a neighboring pixel. During avalanche multiplication, carriers near the junction emit photons as they are accelerated by the high electric field. Three photons with energy higher than 1.14 eV are emitted for  $10^5$  carriers during an avalanche breakdown [44]. Increasing the discriminator threshold reduces the dark count rate including dark counts due to optical cross talk.

The breakdown voltage and the dark count rate are both a function of temperature. Temperature stabilization may be required for some applications using these detectors. Finally, NEP values for SiPM can reach as low as  $0.5 \times 10^{-15} \text{ W/Hz}^{0.5}$  [45]

### **2.6.5 Photon Counting**

As discussed above, a PMT detector may be used in analog mode or digital (photon-counting) mode. Advantages of using a PMT detector in analog mode include:

- 1- Analog mode is better suited for high intensity signals where the dark noise component is small enough that it can be neglected.
- 2- Analog mode is cheaper than the photon-counting mode since it does not require advanced components normally needed to perform photon-counting operations.

For low light level applications, light measurement is no longer a continuous stream of particles but rather discrete photons. For such applications where the light flux is extremely low, the signal to noise ratio (SNR) approaches 1. In this regime, photon counting detection techniques are superior to analog detection techniques.

Photon counting can be implemented with detectors that offer a high enough gain to distinguish individual photons. For example, photodiode detectors have no internal gain and therefore cannot be used to detect single photons. APD detectors have gain, but not high enough

to detect single photons. APD can register 10-20 photoelectrons, but not lower. PMT, MCP-PMT, SPAD, and SiPM detectors are in fact able to register single photoelectrons. Their high internal gain allows the detector to output electrical pulses corresponding to individual single photons.

A simple photon counting system is shown in Figure 2.13. The basic blocks in a photon counting systems are a detector, a discriminator, and a counter. A preamplifier/amplifier combination may be used prior to the discriminator. The pulses from the detector are fed into a discriminator where pulses higher than a user-defined threshold are counted. Those pulses are referred to as photon counts. The counter is used to keep track of the number of pulses that correspond to these photon counts. A more advanced concept of photon counting is the time-correlated single photon counting (TCSPC). TCSPC is discussed in more detail in Chapter 3.

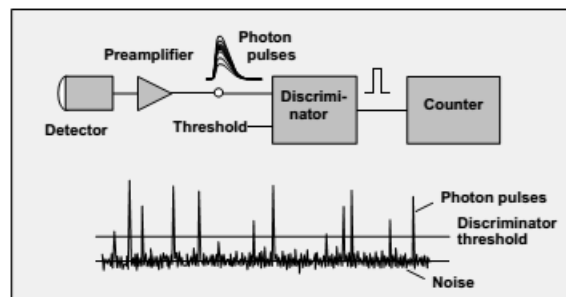


Figure 2.13: Basic building blocks of a photon counting system [46].

The noise in photon counting systems is due to dark count and shot noise. Shot noise is a fundamental type and cannot be eliminated. Shot noise is due to the stochastic nature of the photoelectric process variation. This noise is the major noise source whenever light intensity and count rates are very low as in photon counting. Dark counts are due to thermally released electrons and cannot be distinguished from electrons that were released from photon bombardment. These counts are present even in the absence of light.

In order to understand the advantage of using photon counting systems, and with PMT detectors in particular, the noise sources associated with PMT will be detailed. Dark counts in a PMT can be divided into two types: thermal emissions from the photocathode and thermal emissions from dynodes. Electrons that are released due to thermal fluctuations from the photocathode cannot be distinguished by electrons released due to light striking the photocathode. The pulse-height distribution (PHD) curve of these dark counts shows a Poisson distribution similar to the PHD curve of the actual light signal as shown in Figure 2.14. However, electrons that are thermally released from dynodes have an exponential pulse height distribution. Therefore, in order to disregard this type of dark counts, thresh holding technique maybe used to only allow pulses that are higher than a certain threshold to be counted, which results in improvement of the signal-to-noise ratio. Reducing the other type of dark counts caused by electrons released from the photocathode may be implemented via proper design and cooling of the PMT.

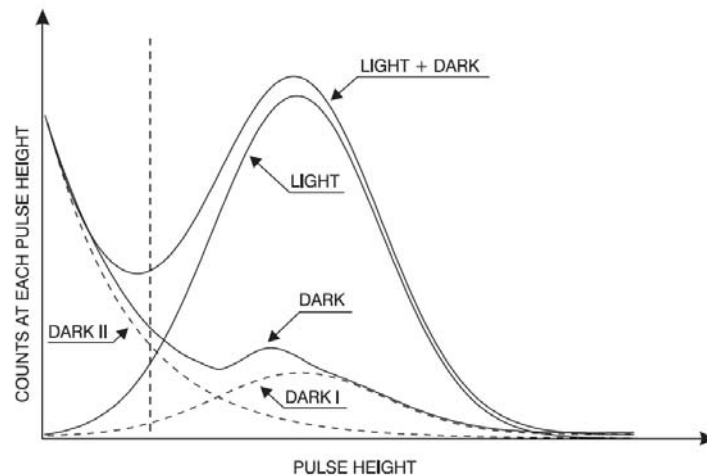


Figure 2.14: PHD curve of light and dark signals from a PMT detector [47].

The dark signal is the superposition of these two components. Note that in a Poisson distribution, the dispersion of the distribution is equal to the mean value. In order to obtain the correct PHD of the light signal, the dark signal must be subtracted from the PMT measurements. Single photon counting offers significant advantages compared to its analog counterpart.

Advantages of photon counting over analog DC methods [47] [48]:

- 1- Single photon counting is not subject to the detector gain fluctuation
- 2- Single photon counting reduces part of the dark signal, thus, increasing SNR of the data. The PHD figure shows that if the discriminator's threshold level is on the "valley" of the PHD, we can eliminate pulse counts that are due to thermal emission from dynodes, which constitute a major noise component. In analog mode, this noise gets added directly to the signal and cannot be removed.
- 3- Single photon counting systems have improved stability. A small change in the supply voltage of photon counting detectors will change the gain of the detector. This will affect the pulse height output in analog mode but will not affect the pulse count in photon counting mode. Single photon counting also displays a better stability against electric sensitivity of the electronics used especially of the amplifier-discriminator test [47].
- 4- Due to the RC circuits inherent to analog systems, a signal reaches its final value exponentially. Photon counting systems are unaffected by the RC time constant that is inherent part of analog systems' electronics.

One of the drawbacks of single photon counting systems is that as the light level increases, the response of a photon counting system becomes nonlinear: the recorded counting rate

(counts/second) underestimates the true counting rate and the output is no longer proportional to the incident light flux.

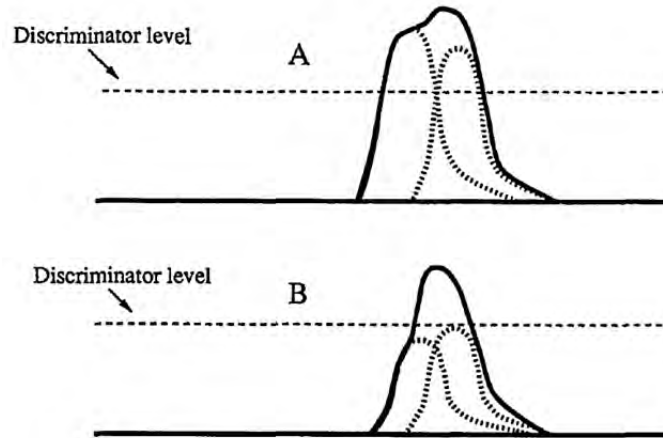


Figure 2. 15: Cause of pileup effects in photon counting[49].

Nonlinearity in a photon counting system, also known as pulse pileup, is due to overlapping of pulses as well as the dead time of the detector/electronics. Depending on the pulse height distribution and the discriminator level, pulse pileup might cause count loss or even count gain as shown in Figure 2.15. When two photon pulses are too close to each other, the system is unable to resolve the pulses and will ignore the second photon which causes a count loss. Also, if two pulses due to dark counts are below the discriminator level but are too close to each other, their values add and an a pulse that exceeds the threshold level appears instead, which causes a gain with pulse counts.

While pulse pileup is especially true for high counting rates where the probability of more than one photon striking the detector in a short period of time is higher, it is also true even for low counting rates since there still exists a probability of a multi-photon event. Also, after the detection of a photon event, the detector/electronics must wait some time before another pulse is detected. This time interval is known as the dead time of the system and causes non linearity of photon detection.

Figure 2.16 below shows the effect of pileup on the time-domain and CW measurements. Curve **a** is the correct curve in both figures while curves **b** and **c** show the corresponding measurements as the intensity of light increases thereby causing pulse pileup errors. Pulse pileup in time-domain systems causes the signal profile to be skewed to earlier times. In steady state measurements, pulse pileup causes a decrease in the apparent intensity of the light source.

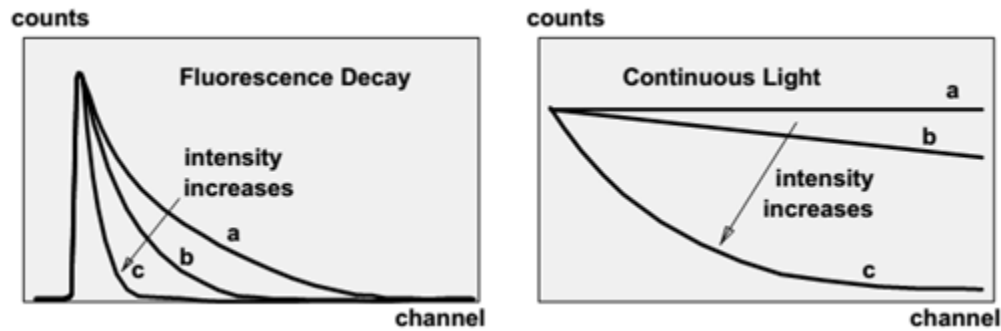


Figure 2.16: Pileup effect on data acquisition [46].

### 2.6.6 Detectors Comparison

There are many different kinds of photon detectors and a comprehensive list of these detectors along with their properties is beyond the scope of this thesis. However, table 2.2 below presents a summary of essential properties of the most sensitive detectors that are used in photon detection of visible and near-infrared photons. There are many different selection criteria and areas of comparison. These properties were considered when choosing the proper photon detector for projects discussed in this thesis. The selection criteris shown in the table below are:

- Quantum efficiency: probability that a single photon will generate a charge carrier that will contribute to the detectors' final output
- Collection efficiency: a measure of how efficient the detector is in transferring the primary photoelectrons or electron-hole pair charge carriers to the output terminal

- Wavelength: the spectral range of the electromagnetic spectrum that can be registered by the detector
- Bandwidth: the operating frequency of the detector at which the response of the detector drops below 3dB of the DC output
- ENF: Excess noise factor – a measure of the noise added to the signal due to the inherent internal gain mechanism of a detector
- NEP: the input radiant power that produces a signal value equal to the noise value produced in the detector
- Gain: ability of the detector to turn a single photon into multiple charge carriers that can contribute to the final detector output
- Minimum Detectable Signal: this measure is similar to the NEP. It is the minimum number of photons needed to register an output which exceeds the noise of the device
- Operation Voltage: Voltage needed to enable detector
- Miniaturization: ability to manufacture the detector with small a small sensitive size
- Large Area: ability to manufacture the detector with a large sensitive area
- Mechanics Robustness: robustness of the detector
- Insensitivity to Mag. Field: the effect of an external magnetic field on the detector
- Ambient Exposure: ability of the detector to be exposed to ambient light
- Noise: Inherent noise of the device
- Dynamic Range: the ratio between the largest and smallest possible intensity that can be detected by the detector
- Production Costs: cost to produce the detector
- Temperature Sensitivity: Sensitivity of the detector to change in temperature

## Summary of photon detectors properties

	Ideal	PD/PIN	APD	PMT	SiPM	CCD	ICCD	EBCCD	EMCCD
Quantum Efficiency	1	... 80%	... 80%	10% ... 50%	... 80%	... 80%	... 80%	... 50%	... 80%
Collection Efficiency	1	1	1	0.9	0.4	1	0.7	0.85	1
<b>Wavelength (nm)</b>	300-1200	300-1100	300-1700	115-1700	300-900	300-1100	300-1100	300-1100	300-1100
Bandwidth	High	~ 100kHz	~ GHz	~ 100 MHz	~ MHz	< 1MHz			
ENF	1	1	2	1.3	1.3	1	1.6-4	1	1.3-2
NEP ( $fW/\sqrt{Hz}$ )		100	10	0.1	0.5				
Gain	$10^6$	1	10 - 1000	$10^4 - 10^9$	$10^5 - 10^7$	1	$10^4$	$10^3$	$10^3$
Minimum Detectable PE	1 pe	100-300 pe	10-20 pe	1 pe	1 pe				
Operation Voltage (V)	<10V	10-100	100 - 500	1k – 3k	< 100				
Miniaturization	Yes	Yes	Yes	No	Yes	No	No	No	No
Large Area	Yes	Yes	No	Yes	Yes	Yes	Yes	Yes	Yes
Mechanical Robustness	High	High	Medium	Low	High	No	No	No	No
Insensitivity to Mag. Field	Yes	No*	No*	No**	Yes	No	No	No	No
Ambient Exposure	Yes	No Impact	No Impact***	No	No Impact	Yes	No	No	No
Noise	None	Low	Medium	Low	High	Medium	Low	Low	Low
Bandwidth	High	~ 100kHz	~ GHz	~ 100 MHz	~ MHz	< 1MHz			
Dynamic Range	Single photon	Good	Good (4-5)	Great (4 – 6)	Determined by pixel # (2 – 5)				
Production Costs	Free	Low	Low	Medium	Potentially Low	Low	High	High	High
Temperature Sensitivity	No	Low	High	Low	Low	High	Medium	High	High

**Table 2.2: Photon detectors summary**

## CHAPTER THREE

### Time-Domain Imaging Systems

#### 3.1 Introduction - Background and Importance

A time domain system operates by precisely measuring the time it takes for photons to propagate through tissue. It relies on illuminating tissue with an ultra-short laser pulse, with a typical width from few femtoseconds up to few nanoseconds, and recording the shape of the pulse as it exits the tissue. Scattering and absorption of photons affect the shape of the laser pulse as it exists, and by measuring the shape of the broadened pulse, one is able to quantify the scattering and absorption features of the tissue.

The temporal distribution of the photons in a time-domain system is known as the temporal point spread function (TPSF). The width of a TPSF signal after it exits the tissue depends on the type and thickness of tissue photons, but may extend anywhere from hundreds of picoseconds to hundreds of nanoseconds. The fast decay in the TPSF profile requires specialized systems in order to measure a TPSF. A TPSF profile may be acquired directly or indirectly. Direct time-domain technologies that are able to record such TPSF measurements include streak cameras, fast photon detectors and oscilloscopes, and time-correlated single photon counting (TCSPC) systems. Indirect methods for acquiring the TPSF are typically not used to record an entire TPSF profile. Instead, they are used to isolate and record part of the TPSF signal. Indirect methods include time-gating, correlation, phase shift methods, etc.

Time-gating methods typically measure early photons which have traveled the shortest path from the source to the detector and thus, have experienced the least

scattering. Early photons provide higher spatial resolution for optical imaging since these photons propagate closest to a straight line between the source and the detector. Gating techniques record these early photons and reject the remaining photons which have undergone a tortuous path due to multiple scattering and have arrived later in time compared with early photons. Gating removes these late photons which contain little scattering and absorption information in the direct path between the source and detector. Late photons, however, have the advantage of improving the image contrast [50] [51] since unlike early photons which may be affected by both absorption and scattering, late photons are primarily affected by absorption [52]. Gating methods include gated image-intensified CCD, optical Kerr gate, parametric amplifiers [53, 54], stimulated Raman amplification [55], second-harmonic generation [56] [57], and cross-correlation [58]

In order to achieve the best results with gating techniques, the gating window must be very small. Experimental studies that evaluated spatial resolution as a function of gating time have shown that a spatial resolution of  $\sim 2$  mm is achievable for gating times of the order to tens of picoseconds [59]. While gating techniques may be able to acquire a full TPSF, they are inefficient. In order for gating methods to acquire a full TPSF, the small gate width must shift across the entire TPSF so that it may be recorded fully. This acquisition technique is extremely inefficient since the majority of the photons are not collected during each gate acquisition. Also, the time gating approach for measuring early photons is limited by the number of available photons. As mentioned before, ballistic photons decay exponentially fast as the thickness of the medium increases making them unrealistic as the tissue thickness increases.

The other technique used with time-domain measurements acquires a full TPSF. This technique can be divided further into analog and digital TPSF recording methods. Analog TPSF recordings rely on streak cameras or fast detectors and oscilloscopes (or digitizers) while digital TPSF use time correlated single photon counting techniques which rely on the statistical nature of photons.

A synchroscan streak camera is able to record the time-decay profile of the signal in a single shot. The working principle behind streak cameras was explained in Chapter 2. One of the greatest advantages of streak cameras is their temporal resolution which is in the ps range. Streak cameras, however, are not suitable for NIR tomography as they have several disadvantages. They have a low quantum efficiency that is typical of vacuum based photon detectors (<30%), bulky, very expensive, have a small detection area, have a low dynamic range, and they require a long acquisition time. Furthermore, a streak camera may not be able to sample the signal profile time-decay accurately for very weak signals consisting of only few photons per pulse [60]. For such weak signals, it is possible to increase the number of photons simply by increasing the input laser power, but there may be limitation imposed on the power which may prohibit such an increase. The discrete nature of such weak signal prohibits the use of analog measurement techniques. The solution in this case is to use time-correlated single photon counting (TCSPC) technique.

TCSPC technique is the gold standard in time domain measurements. In a TCSPC system, the time-of-flight of individual photons relative to a reference signal derived directly from the source is measured and recorded. This technique relies on registering the arrival times of single photons precisely in reference to the main excitation

pulse. Many excitation pulses are used and the photons that are detected for each pulse are registered. A histogram representing the distribution of the photons arrival per time bin is built up over many excitation pulses which results in a TPSF profile that is equivalent to the single-shot TPSF profile captured by the streak camera technique.

Compared to streak cameras, TCSPC systems offer great advantages: they offer very high dynamic range, excellent temporal linearity and large collection area (since TCSPC may employ large area detectors such as PMT or MCP-PMT). While their temporal resolution was inferior to streak cameras, advances in technologies made these systems a great competitor to streak cameras with all the benefits of the streak cameras and none of the drawbacks.

In order to detect single photons, single photon sensitive detectors such as photomultiplier tube (PMT), micro channel plate (MCP) or single photon avalanche photodiode (SPAD) detectors must be used. Due to the limitation of virtually all detectors as well as electronics, TCSPC measurements require detection of no more than a single photon per input pulse. It is recommended that the number of photons per cycle reaching the detector is 0.1 to 0.01 photons (i.e. 1 photon for every 10 to 100 cycles, respectively). Only, 1% to 10% of the incident pulses generate a single photon. Most of the pulses do not generate any photons, and more importantly, the probability of two photons striking the detector simultaneously is very low (enter actual value here). The reason behind this requirement is that after a single photon detector senses a single photon, there is a “dead” time after which the detector/electronics are not able to respond to additional photons. Therefore, for an input laser pulse, if multiple photons were to strike the detector, the first photon would be registered while the rest of the photons

would fail to register, until the dead time of the detector/electronics has elapsed. The photons which were not registered would have been lost. Since a TCSPC system builds a histogram of photons that were registered, those unregistered photons, which are part of the actual measured signal, will distort the TPSF profile and skew the histogram results more toward early photons.

### 3.1.1 TCSPC Building Blocks

The main building blocks of a basic single photon counting system includes a detector, a discriminator, and a counter. The classic TCSPC setup adds a time-to-amplitude converter and replaces the counter with a combination of analog-to-digital converters and memory. Amplifiers may be used throughout the system. The building blocks of a TCSPC system is shown in Figure 3.1.

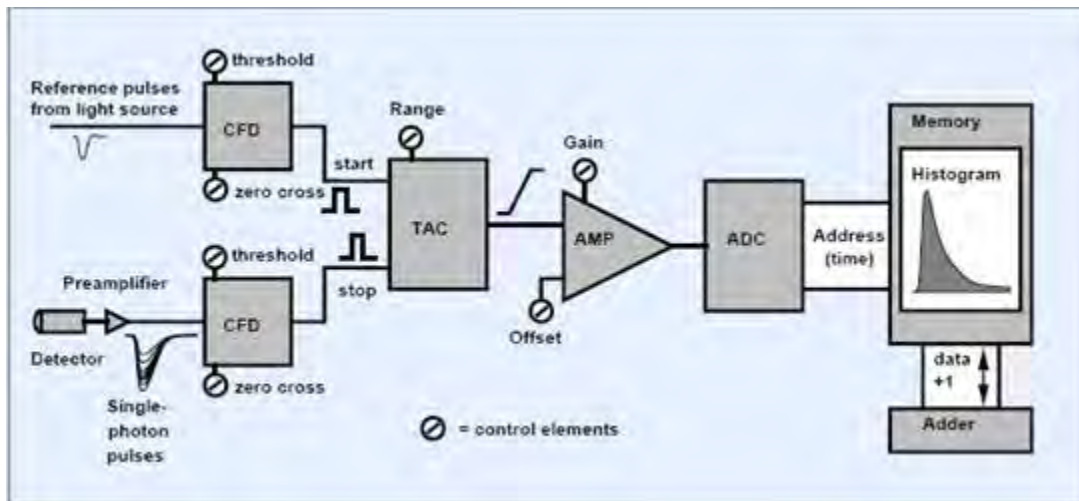


Figure 3.1: Building blocks of a typical TCSPC system [46].

As is shown in the Figure, the output of the detector is connected to the discriminator. The detector delivers pulses which correspond to individual photons. A preamplifier may be used in order to convert the detector's output to the proper signal to be used by the discriminator. The discriminator triggers when a valid pulse is detected.

It is imperative that the discriminator deliver the trigger at the exact time the pulse was detected. There is no room for timing errors as any timing errors introduced in this block will lead to a much distorted output. Therefore, the discriminator used must deliver the trigger at the exact time a valid pulse is received. Furthermore, since detectors may produce pulses with slightly different heights and pulse shapes for the same photon, the discriminator must be able to compensate for the variances in the pulses height and trigger at the same time regardless of the pulse height. The output of the discriminator is connected to a time-to-amplitude converter and is used to stop (or start) a timer that calculates how much time has elapsed between the arrival of the photon and the reference excitation pulse which caused the photon. The other pulse which delivers the stop (or start) signal to the TAC comes from the reference signal. The reference pulse signal might be electronic and directly connected from the light source to the TAC input or may come from another detector/discriminator combination that monitors the output of the light reference source.

Finally, the output TAC signal (which may be amplified) is sent to an analog-to-digital (ADC) converter where the output of the ADC is equivalent to the photon detection time. The digital output of the ADC is then connected to some type of memory.

### **3.2.2 Discriminators**

There are two main types of discriminators: leading edge and constant fraction discriminators. A leading edge discriminator looks at the leading edge of the detector pulse. If the pulse reaches a user-predefined threshold, the discriminator emits a logic pulse. The problem with this type of discriminators is that pulses from detectors such as PMT's and APD's have a considerable amplitude jitter due to the gain mechanism. This

amplitude jitter causes a jitter in the rise time of the pulses. This amplitude inconstancy will trigger the leading edge discriminator at slightly different times depending on the amplitude of the pulse. This is known as “time-walk”. Signals with large pulse amplitude are steeper and reach discriminator’s level threshold faster than signals with smaller pulse amplitude. This issue is not critical for single photon counting systems that are only interested in the presence of photons and ignore the photon arrival time. However, for TCSPC based systems, photon arrival times and accumulation of the statistics needed to build of a TCSPC profile is the main goal of such systems and trigger time dependence on the pulse’s peak amplitude is unacceptable.

A constant fraction discriminator is able to solve the time-walk problem of leading edge discriminators by triggering only when the input pulse reaches a user-predefined fraction of the peak value. CFD doesn’t just look at the edge of the pulse, but it looks at the entire pulse to determine if the pulse has reached a fraction of a user-defined value. The CFD discriminator is triggered at the same time regardless of the pulses’ amplitudes. Therefore, a CFD is used to extract valid detector pulses as well as obtain the exact timing of these pulses.

The CFD works by comparing the original signal with an attenuated and delayed version of itself. A CFD generates an attenuated and inverted replica of the original signal and then sums this signal to a delayed version of the original signal. The original unipolar input signal has now transformed into a bipolar signal which crosses the zero axis and changes polarity exactly when a constant fraction of the input pulse amplitude is reached. The zero crossing time of this signal is independent of the amplitude of the

input signal. By adjusting the attenuation and the delay of the split signals, one is able to choose the pulse constant fraction.

The CFD is responsible for many of the advantages of photon counting. First, the output pulses are counted independent from their amplitude at the detector output. For detectors such as the PMT detector, this is a great advantage that solves many issues which contaminate PMT measurements including the large statistical variance of pulse amplitudes due to the PMT gain mechanism as well as high voltage supply dependence.

Another advantage is that by setting the discriminator's threshold level at the 'correct' point, one can eliminate lower pulses that are due to the thermal emission from the dynodes, which will suppress part of the dark current and increase the signal to noise ratio. .

### **3.1.3 Time-to-Amplitude (TAC)**

The second major block of a TCSPC system is the time-to-amplitude (TAC) converter. A TAC acts like a stop watch where one input initiates the start of the count while the other input stops it. The output of the TAC therefore is a voltage (or current) signal which corresponds to the time difference between these two events. For TCSPC, one of the inputs to the TAC is obtained directly from the CFD while the other input is obtained from the reference. The reference sync pulses may be provided electronically by certain systems such as mode-locked lasers or other laser systems or by feeding the input laser source to a detector and then using a separate discriminator circuit to detector the start of the reference pulse.

A TAC is simply a current source and a capacitor. One pulse turns on the current source which charges the capacitor and another pulse turns off the current source which

stops charging of the capacitor. When the current source turns off, the capacitor retains its voltage value which represents the time difference between the start and the stop pulses. Very accurate and stable time differences can be obtained with TACs.

### 3.1.4 TCSPC Data Type

A TPSF recorded at fixed optode spacing can be used to obtain values for  $\mu_a$  and  $\mu_s'$  by fitting the TPSF to a light transport model [61]. The whole TPSF could in theory be used in image reconstruction. However, this is very computationally intensive.

Different data types may be extracted from a TPSF measurement that can be used to simplify image reconstruction. These data types include the mean flight time, integrated intensity (equivalent to a CW measurement), variance, etc. Frequency domain data is simply the Fourier transform of the time domain TPSF measurement except that the time-domain measurements include much more frequency components than a typical frequency domain system. For example, a typical frequency domain measurement uses a single modulation frequency of 100 MHz, whereas a typical time domain system uses a light pulse of 100 ps. The Fourier transform of the ps light source yields a frequency range from 0 to GHz.

The main data types extracted from TPSF measurements are intensity, mean photon flight time, and variance all of which are shown in Figure 3.2 below.

$$Intensity [y(t)] = \sum_t y(t)$$

$$Meantime [y(t)] = \frac{\sum_t y(t) \times t}{\sum_t y(t)}$$

$$Variance [y(t)] = \frac{\sum_t y(t) \times [t - \langle t \rangle]^2}{\sum_t y(t)}$$

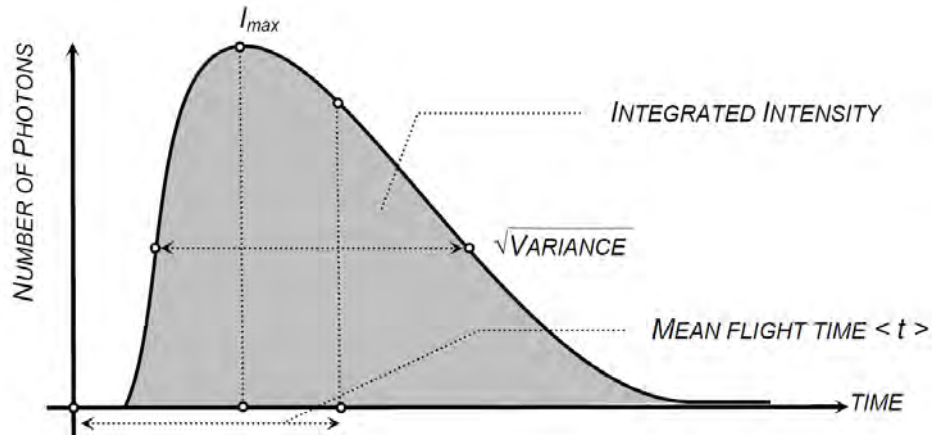


Figure 3.2: Data types in a time-domain measurement [62].

Intensity measurements are equivalent to the measurements obtained from a steady-state based imaging system and corresponds to DC signal measurements (0 MHz). This data type is sensitive to surface coupling [26]. The intensity and meantime calculated from the TPSF are almost equivalent to the amplitude and phase of a frequency-domain system [63]. Other data types may also be used to enhance the separation between  $\mu_a$  and  $\mu_s$  but may be more sensitive to noise [64]. These additional data types do not have an equivalent type in frequency domain [15]

### 3.2 Small-Animal Time-Domain System Characterization

Small-animal imaging systems have become an important translational tool between research and clinical applications. Small-animal fluorescence tomography system development varies widely in their technologies and capabilities, but the key goal of most systems is to allow visualization or quantification of the emitted intensity from fluorophores. A small-animal microcomputed-guided time-domain fluorescence tomography instrument shown in Figure 31 was built by our research group [65] [66] [67]. The system has a subject bed that couples to a commercial microCT system, and thereby allows sequential x-ray CT and fluorescence tomography imaging. The data sets also

allow either image fusion or image synergy, where the x-ray structure is used to enhance the recovery of the fluorescence image.

The system schematics are shown below in Fig. 3.3 showing the optical design (a) and the electronic control design (b).

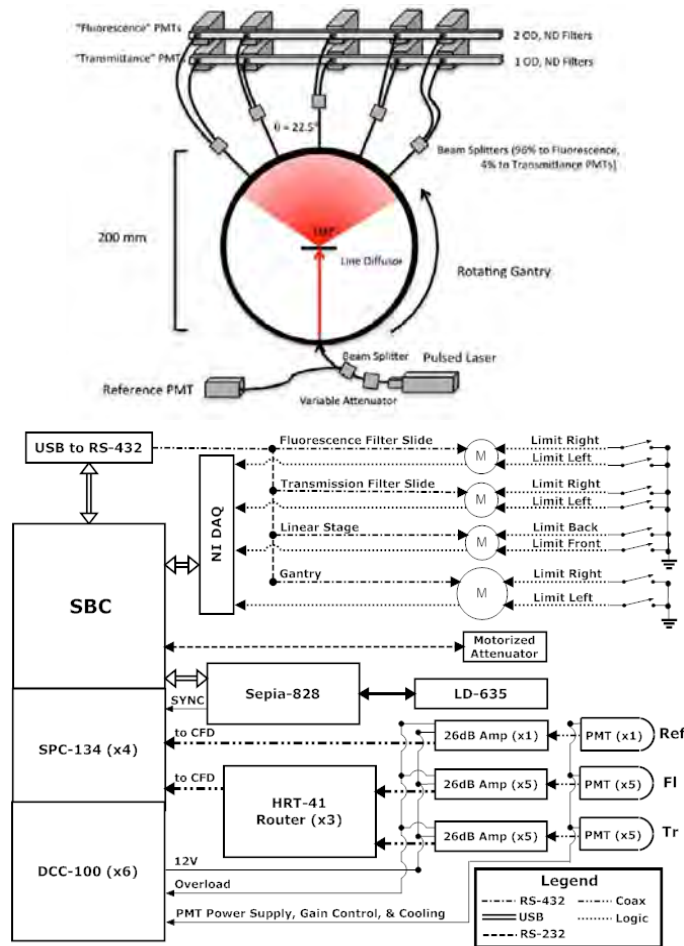


Figure 3.3: The schematics of the system are shown in (a) with the optical hardware including laser diode (LD), lenses for delivery and pick up (CH1 – CH5), and photomultiplier tubes (PMTs). The electronics and control systems are shown in(b), with single photon counting (SPC) cards and direct current control (DCC) cards feeding the PMT detectors, a laser driver (Sepia), and USB control of the linear filter stages and the rotating gantry stage.

A specimen is placed on a motorized stage in the middle of a motorized rotating gantry. The rotating gantry enables a single source with a fan beam configuration of detectors that rotate around the surface of the specimen. Fully non-contact excitation and detection is achieved and a flexible number of measurements can be obtained. A 635nm laser diode is used to excite the fluorophores within the animal. Five optical channels (CH1 through CH5) use focalized detection to collect the diffuse transmission of excitation, due to tissue scattering, and fluorescence signals, due to fluorophores, at the surface of the specimen. Each channel separates the scattered signal and the fluorescence signal using appropriate filters. Once the signals are separated, they are measured by photomultiplier tube (PMT) detectors. The signals from all detectors are routed to time-correlated single photon counting (TCSPC) modules which provide sequenced binning of each count, into a time histogram. The TCSPC measurement is driven by the pulsed laser diode (80 MHz), which is controlled by a Sepia-828 multichannel diode laser driver. All controls of the laser driver including pulse rate and laser power are controlled by software. The diode is coupled to a 50  $\mu\text{m}$  fiber optic beam-splitter that delivers 5% of the signal to a reference channel and the other 95% toward a collimated source fiber directed at the specimen. A computer controlled motorized attenuator in line with the source fiber can be dynamically adjusted to ensure that the detected transmission and fluorescence signals fall within the linear range of the photomultiplier tubes (PMTs).

A custom-built single board computer (SBC) is used to control all the components of the system. The computer houses 6 PCI-DCC-100 direct current control modules, which are used to supply power to the photomultiplier tube detectors. The DCC modules are also used to control the cooling and the gain of all detectors as well as provide an

overload current protection. There are 11 PMT's in the system - five detectors are used to measure signal fluorescence and five detectors are used to measure signal transmission (scattering of tissue). The remaining detector is used to measure the pulsed laser reference signal in order to initiate the photon counting measurements. The computer also houses four SPC-134 time-correlated single photon counting modules. Each SPC-134 module consists of 4-channel single photon counting units. All modules work in parallel allowing for simultaneous photon counting measurements.

A HRT-41 router is used to connect up to four separate detectors to a single SPC-134 module. Three routers are used to route the signal from ten detectors to three separate SPC-134 modules. The reference detector does not use a router and is connected directly to a separate SPC-134 module. Each detector uses a distinct channel of the SPC-134 module. The photons from individual detectors are routed into different curves in the SPC memory, and thus, the system is able to acquire data simultaneously from all detectors.

Different motorized stages are connected to the computer via USB connections. These stages are used to position filters, attenuate the laser signal, rotate the gantry and move the sample. Feedback from the filter stages is monitored by USB-6009 National Instruments data acquisition hardware.

Current work on the tomography system has focused on updating the control software in order to provide a more logical flow of use as well as improve the needed automatic control of filters and calibration which is essential for the data to be reconstructed accurately [67]. The automatic exposure control has also been improved which resulted in a reduction the acquisition speed time. Finally, an additional laser at a different wavelength was added to the tomography system in order to enhance and

improve the contrast-to-background ratio for better image reconstruction. This system control flow and the laser enhancement are outlined and the performance of the system is demonstrated.

### 3.2.1 Control Flow Improvements

The control of the subsystems presented above is implemented through a newly developed LabVIEW interface, as shown in Figure 3.4. This interface gives users a complete control over data measurement and system parameters. The software automates all steps necessary to acquire data and also provides advanced control functions to manipulate the TCSPC, DCC, and the laser parameters, as shown in Figure 3.5.

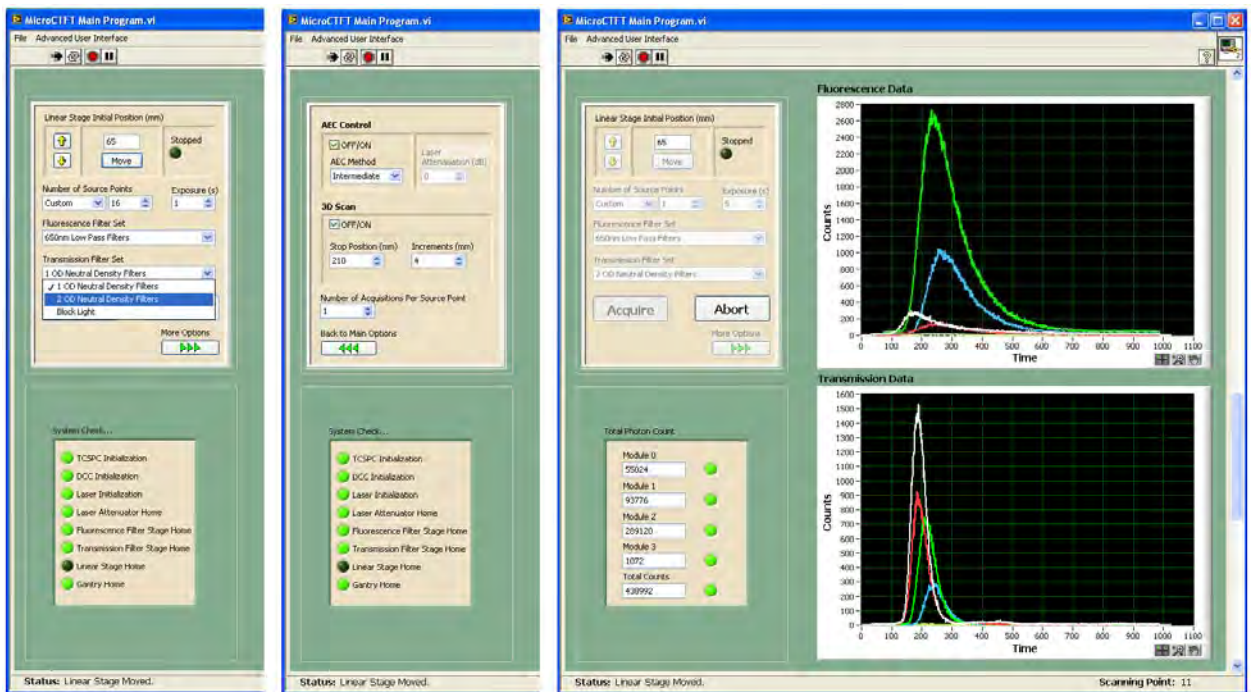


Figure 3.4. Panels showing the main options presented to users for optical data acquisition.

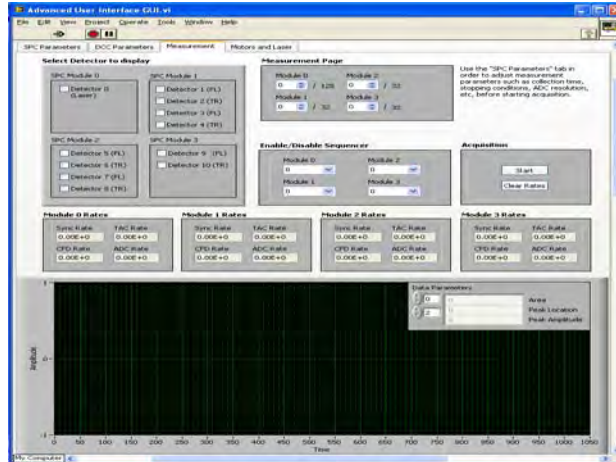


Figure 3.5: Panel showing some advanced options presented to users for controlling the single-photon counting components.

The software has been redesigned and built from the grounds up in order to improve the functionality and allow the data acquisition to be as user-friendly as possible. The software allows researchers and students alike to operate the software with minimum number of steps. The GUI is simple yet enables the user to access advanced options in order to customize data acquisitions to fit the subject being imaged. A partial list of the parameters which can be controlled by the user includes:

- Number of sources ( $N_s = 1$  to 360)
- Number of acquisitions per point for increased SNR
- Number of tomography slices and axial scan increments
- Attenuation filters for transmission channels (blocked, 1dB, 2dB)
- Choice of different fluorescence filters
- Laser integration time per measurement ( $\Delta T = 0.01s$  to 5s)
- Laser attenuation value (1 to 50 dB)

Moreover, the automatic gain control has been tweaked in order to speed up data acquisition. Automatic gain control is an essential step in data acquisition. It controls the laser intensity attenuation that may be incident on the surface of the subject while ensuring that the detectors receive the maximum light and maximize the count rate detected by each channel of the 10 PMTs without being saturated or suffer pileup effects. [67]

In order to perform automatic gain control, the TCSPC signal is acquired as a test in a low light setting, and then again in a higher light setting. The change in counts versus input light level then allows the laser intensity to be increased to a level that allows maximal count acquisition for actual tissue imaging. This exposure control approach is done automatically, allowing all animals and tissue phantoms to be imaged with maximal accuracy in fluorescence and transmission intensity in manner that is transparent to the user.

Finally, the entire architecture of the graphical user interface was designed from the grounds up in order to create a code that is modular, expandable, and professional. Flow charts were designed through the programming process in order to aid in developing a user interface with these criteria. Figure 34 shows a sample flow chart that was used to design the main GUI screen. Each box in the flowchart diagram controls a procedure and had a similar flowchart that controlled its internal workings.

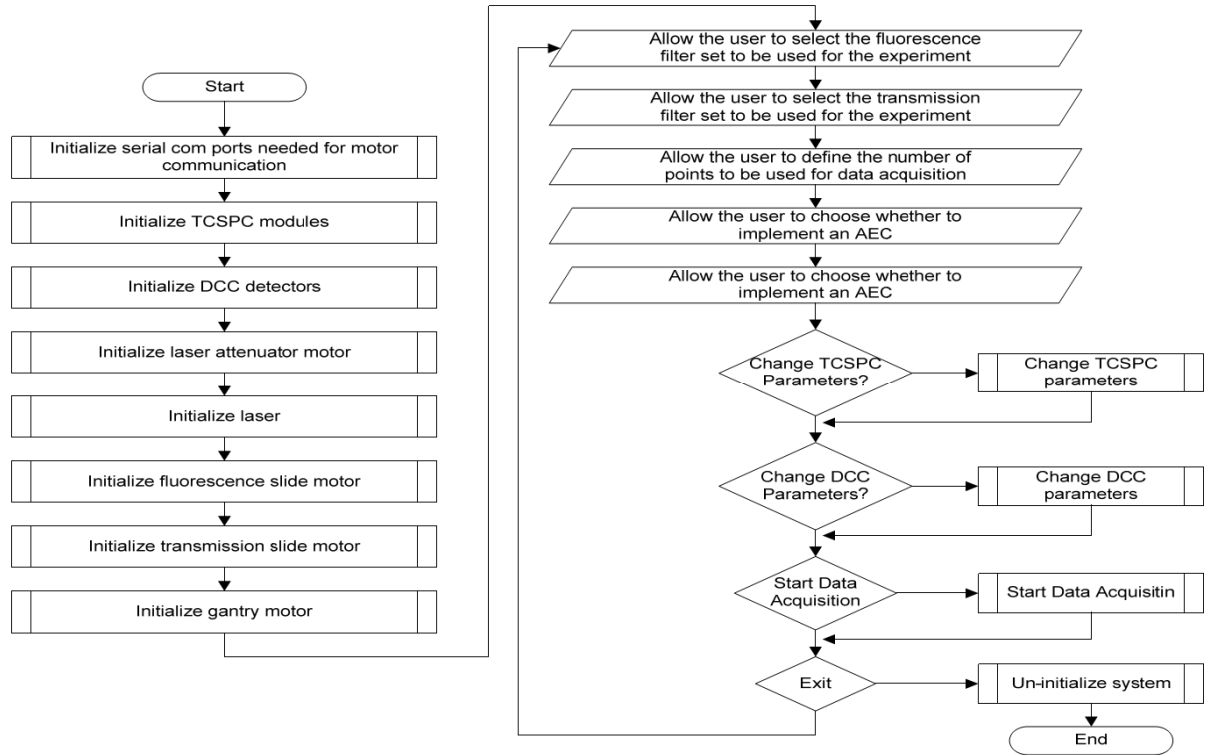


Figure 3.6. The program flow is shown for part of the internal workings of the LabVIEW user interface.

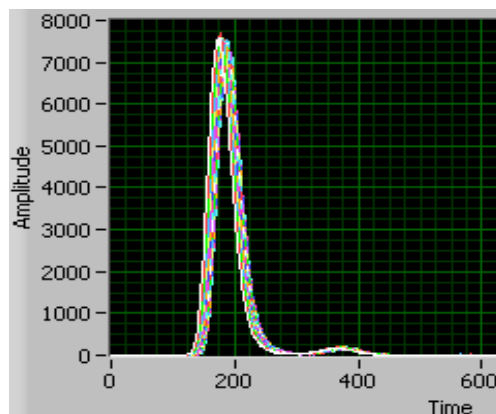
### 3.2.2 Calibration and Data Types

Calibration is an important step that accounts for detector differences with respect to signal intensity, filter efficiency, pulse delay and temporal dispersion of the signal. Full calibration of a time-domain optical imaging system requires accounting for detector channel differences with respect to not only signal intensity and filter efficiency, as with continuous-wave systems, but also with respect to pulse delay and temporal dispersion of signal. The intrinsic sensitivity, pulse dispersion, and time delay properties of each detector were determined with a single calibration experiment that can be easily repeated before system use.

#### 3.2.2.1 Laser Reference Calibration

Pulsed lasers may not emit pulses that are exact replica of each other. In fact, if the laser is not given enough time to warm up prior to an experiment, the laser intensity will fluctuate from one pulse to the other. There also might be a slight offset between the delays of one pulse to the next. Therefore, monitoring the laser pulses is essential in time-domain experiments.

Figure 3.7 shows 20 reference laser pulses superimposed on top of each other. As can be seen from the figure, the pulses do not exactly overlap. Figure 3.7 (b) shows a plot of the mean time vs. the pulse number. Also, as can be seen from the figure, there is a shift in the mean times of the laser pulses. This shifting continues for a period of time until the laser pulse stabilizes. Figure 3.7 (c) shows a plot of the total photon count vs. laser pulse number. Again, there is slight variance in the total photon count (which is directly related to the intensity of the laser). As the laser is allowed to warm up for about 30 minutes, it gets more stable where its intensity remains constant within few percent and the time-delay stabilizes.



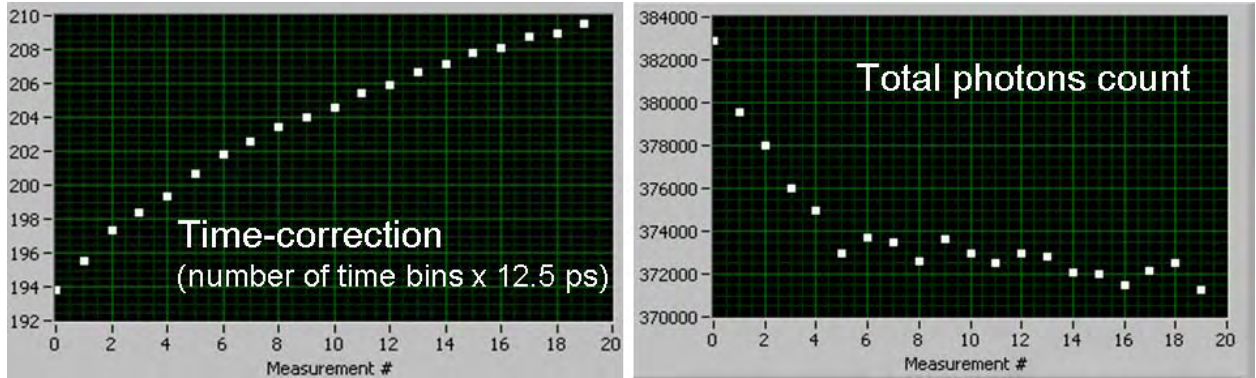


Figure 3.7: A reference channel is used to monitor the laser as a function of scan time. An impulse-response function (IRF) is acquired each time a measurement is made. A time correction and an amplitude correction is to time-domain data based on variations of IRF mean-time and total photon count.

Therefore, the laser pulses were monitored in order to correct for pulse instability and variance during data acquisition. The intensity and the time delay of all the laser pulses were normalized with respect to the first laser reference pulse. The scaling and time delay factors were then multiplied and added to the signals from the ten detectors.

### 3.2.2.2 Inter-detectors Calibration and Time-Referencing

In order to calibrate the detectors with respect to each other, a semi-cylindrical phantom, shown in Figure 3.8 (b), was designed which insured that the diffuse light field seen by each detector is equivalent. As the laser light hits the center of the phantom, the light detected by all detectors should in theory be the same, including the light intensity as well as the temporal delay. However, due to differences in the detectors, fibers, and other factors, there will be differences in both the intensity and the time delay of the signal received by the different PMTs. Scaling factors as well as timing corrections for each detector were computed and used to correct raw time-domain data.

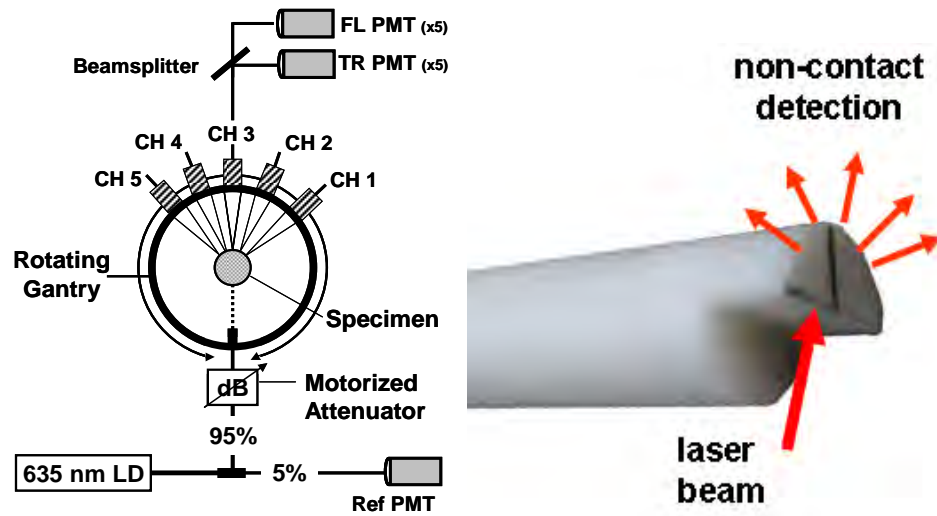


Figure 3.8. Semi-cylindrical phantom insuring diffused light field seen by each detector is equivalent. Calibration factors and timing for each detector are computed and used to correct raw time-domain data.

As can be seen from Figure 3.8 below, calibration plays a crucial step in the quality of the data. Figure 3.9 (a) shows 10 acquisitions collected from the semi-cylindrical phantom. As can be seen, there is a slight shift of the data with respect to the time axis. This shift arises from fluctuations of the laser power which was discussed earlier. The calibrated data is shown in Figure 3.9 (c) which shows the same data set in Figure 3.9 (a) after applying the calibration coefficients. Figure 3.9 (b) shows ten acquisitions from five different detectors. The calibrated data is shown in Figure 3.9 (d).

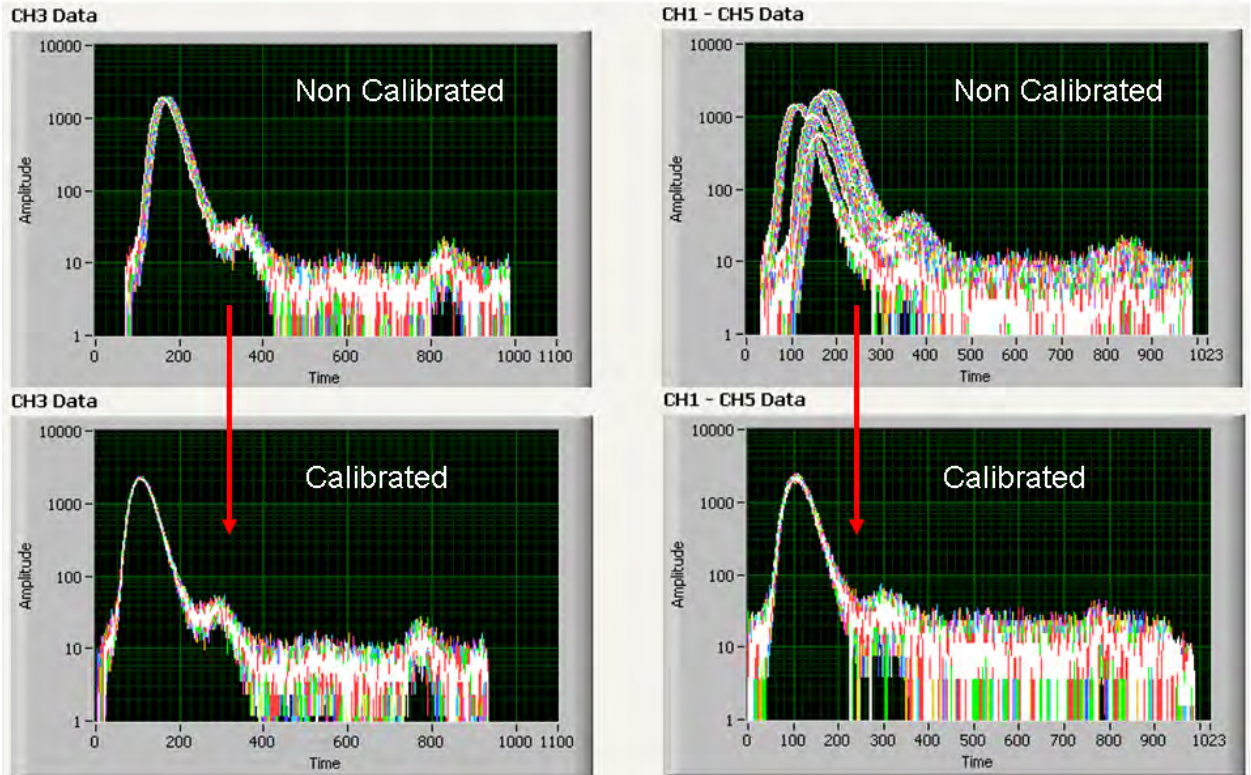


Figure 3.9: Impact of inter-detector calibration and time-referencing shown for the central detector (left) and for all detectors (right).

### 3.3 Phantom/Animal Results

#### 3.3.1 Phantom Imaging

Characterization of the system has been performed to determine its sensitivity to detect different concentrations of the Alexa Fluor 647 dye in tissue having different depths.

The figure-of-merit used to quantify sensitivity is the signal-to-noise ratio:

$$SNR = \sqrt{N}$$

where  $N$  is the peak amplitude of the detected time-domain fluorescence signal. A tissue-mimicking phantom shown in Figure 3.10 is used to evaluate the sensitivity of the tomography instrument to small levels of fluorophore concentrations and to varying tissue thicknesses

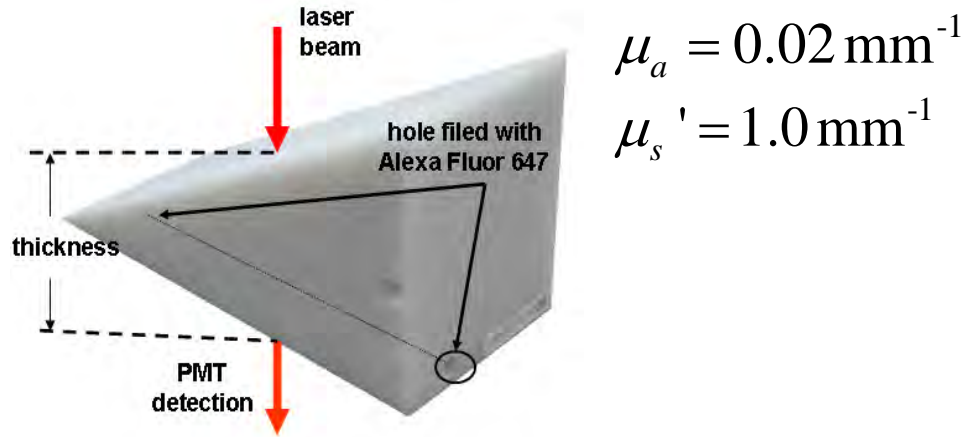


Figure 3.10: Wedge phantom used in system characterization.

Figure 3.11 (a) shows SNR as a function of thickness for different laser integration times and for a fixed AF647 concentration ( $C_F=0.001 \mu\text{g/ml}$ ). Tissue thickness sensitivity is increased up to 65 mm (SNR=2) for an integration of  $\Delta T=5\text{s}$ . Figure 3.11 (b) and (c) show SNR curves as a function of AF647 concentration for tissue thicknesses varying from 19 mm to 50 mm. (b) shows the sensitivity curves for  $\Delta T=0.1\text{s}$  while (c) shows the corresponding curves for  $\Delta T=5\text{s}$

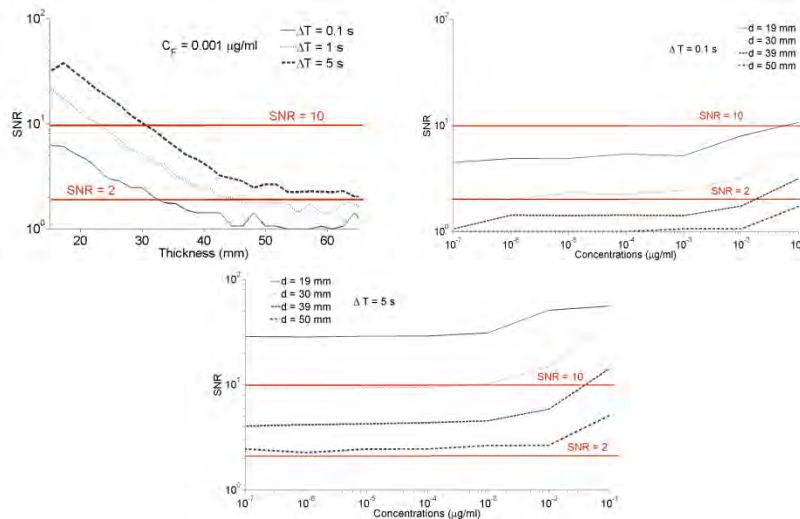


Figure 3.11: Evaluation of signal-to-noise ratio (SNR) for wedge phantom experiments.

A mouse phantom (Caliper Life Sciences, Hopkinton, MA) shown in Figure 3.12 (a) was used for further characterization of the system. microCT image of the phantom was acquired which provided structural information of the phantom showing two cylindrical inclusions as shown in Figure 3.12 (b). Both inclusion were filled with 100nM solution of the AlexaFluor 647 fluorescent dye mixed with 1% Intralpid in water. Once the phantom was imaged using the microCT system, it was then moved to the fluorescence tomography system where it was imaged. The data was then reconstructed using NIRFAST and the fluorescence image reconstruction is shown in Figure 3.12 (c).

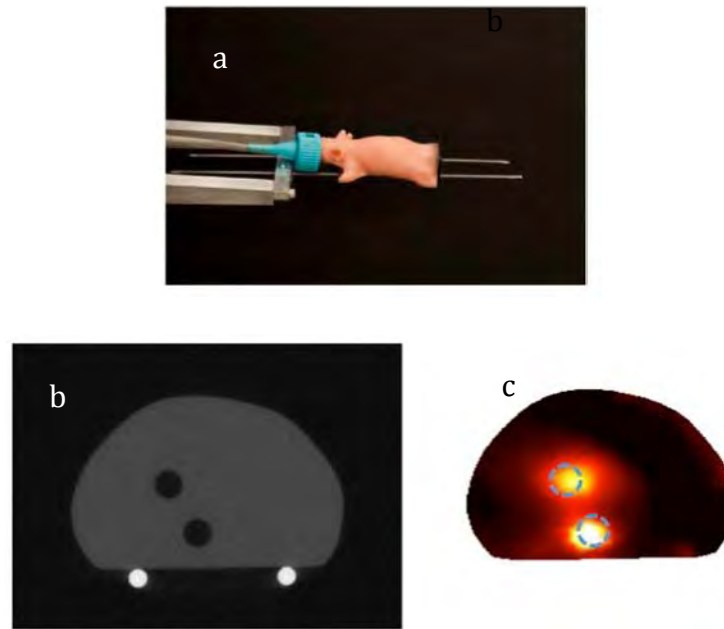


Figure 3.12 (a) Image of the mouse phantom used in system characterization, (b) microCT image of the mouse phantom, (c) time-domain optical reconstruction results overlaid on the microCT image.

### 3.3.2 Animal Imaging

Finally, a nude-type mouse was injected orthotopically with a U251 human glioma cell line. The animal was then injected with a 1 nanomole of IRDye 800CW-EGF

and 1 nanomole of Alexa Fluor 647 in 100 ul of phosphate buffer solution, 12 hours prior to imaging the subject. The mouse was then anesthetized then imaged using an MRI system in order to identify the location of the tumor. The mouse was then imaged using the microCT and the time-domain fluorescence tomography system sequentially. The MRI and microCT-overlaid fluorescence images are shown in Figure 3.13.

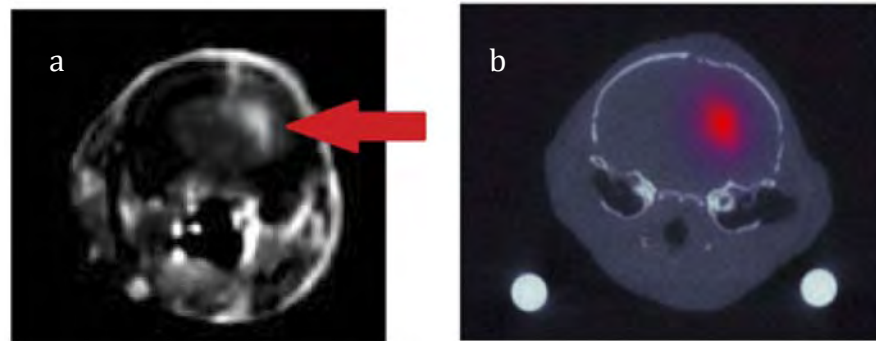


Figure 3.13 (a) Contrast-enhanced magnetic resonance images of mouse head injected with U251 orthotopic glioma tumor in the left cerebral hemisphere as indicated by the red arrow, (b) fluorescence reconstruction of the time-domain system overlaid with co-registered microCT images of the head of the mouse.

The tumor absorbs more contrast agent than the normal brain. Its location can be seen in the left cerebral hemisphere of the MRI image as indicated by the red arrow. The microCT image of the mouse is shown in Figure 3.13 (b). The fluorescence reconstruction of the TCSPC system is overlaid on the microCT image and is within 1 mm of the tumor center of mass as determined by the MRI image.

### 3.4 Discussion and Conclusion

Although TD techniques are more expensive compared to frequency domain and steady state measurements, they offer a rich data set that contains more information

compared to the other techniques. By measuring a TPSF with high accuracy and resolution, a great deal of information can be extracted from the shape of the TPSF [68].

Subsystems for non-contact preclinical fluorescence tomography instruments need to be automated and carefully designed. This includes the control of motors (animal positioning, filter positions, gantry motion) as well as laser and light detection subsystems. In particular, without automatic exposure laser control the acquisition of data can be sub-optimal, and the reconstruction of the fluorescence tomography images is less accurate. The design of the software workflow presented here allows this automated exposure control to be implemented in a manner that is transparent to the user in order to further facilitate the routine use of fluorescence tomography for biological studies.

Calibration is also an essential part in time-domain systems. Laser calibration was performed in real time by acquiring laser pulses in real-time during data acquisition and correcting for laser pulse strength and timing variations. Inter-detectors calibration was performed using a specialized semi-cylindrical phantom which simplified detector calibration and enabled accurate adjustments of the differences of all detectors.

Finally, phantoms were used to characterize the system prior to animal studies. A wedge phantom proved that the system can be used to image animals up to 50 mm in diameter although acquisition time would have to increase in order to increase the signal-to-noise ratio of the results. A mouse phantom with two inclusions also was used to further show the system's sensitivity. The system was also used in an animal study and showed a great potential for imaging tumors in small animals.

## CHAPTER FOUR

### Design of a hybrid frequency domain/continuous wave system

#### 4.1 Introduction - Background and Importance

Frequency domain (also known as phase modulation) is another technique that is used in optical tomography. Both time domain and frequency domain measurements aim at measuring the time it takes for photons to pass through a medium. Frequency measurements measure the average path a photon travels as opposed to the actual precise path measured with the time domain techniques. TD and FD are related to each other via Fourier transform. For example, a 100 ps laser source has harmonics which extend in the frequency domain from DC up to 10 GHz. The repetition rate of the pulses gives the fundamental frequency, whereas the pulse width determines the width of the power spectrum band [69]. A frequency domain measurement may use a single frequency or may use several discrete frequencies. FD is typically limited to frequencies below 1 GHz which corresponds to a temporal resolution of a few nanoseconds [70] [63]. However, FD technique can still accurately measure the mean time from the phase shift data. While time-domain techniques are capable of higher sensitivity and yields a more thorough data set, FD techniques are more economical and are easier to incorporate into clinical settings [71].

In a frequency-domain (FD) system, the intensity of the light source is modulated. The modulation frequency that is used depends on several factors including tissue thickness, detectors, and imaging method (transillumination vs. reflectance). In order to obtain the highest SNR and avoid phase-wrapping problems, it is required that the product  $\omega \tau = 1$  where  $\omega$  is the angular modulation frequency of the laser source and  $\tau$  is

the time it takes a light source to travel through tissue[72]. The angular modulation frequency ( $\omega$ ) is equal to  $2\pi f$  where  $f$  is the modulation frequency of the source (in Hz). For a source-detector separation of few centimeters,  $\tau$  is around 1 ps in tissue. Therefore, typical modulation frequencies used in FD tomography is around 100MHz. For smaller source-detector separation, or smaller tissue (such as in animal studies), the modulation frequency must be increased.

In a frequency domain measurement, both the amplitude and the phase of the attenuated signal relative to the source may be measured. While amplitude and phase are both important in frequency domain measurements, phase plays a more crucial role and determining the phase accurately is crucial. In fact, phase measurements alone are sufficient to calculate optical properties of tissue in multiwavelength systems [73]. FD measurement techniques can be divided into analog and digital. The analog measurements utilize homodyne detection, heterodyne detection (also known as cross correlation detection), or single-sideband (SSB) detection in order to measure the phase and amplitude of the signal [73]. The signal can be coupled to digital electronics afterwards. Digital techniques aim at digitizing the signal and using digital signal processing techniques to process the amplitude and phase information.

In homodyne detection, the signal at the detector end is fed to an in-phase and quadrature (I&Q) demodulator where the phase and the ac amplitude of the signal are measured. A heterodyne detection uses mixers in order to down convert the high frequency detector output into a lower frequency signal that can be processed easier. The single-sideband (SSB) method differs from the heterodyne method by generating a

sideband signal as the second RF signal. Both heterodyne and SSB methods require phase coherence and frequency stability between the input and reference signal.

Homodyne detection uses local oscillator signal with the same carrier frequency as the measured signal. This technique may be implemented with optics such as a laser beam, beam splitters, and interferometers or with non-linear electrical devices such as I&Q demodulators. Converting the light signal into an electrical signal and then using devices such as I&Q demodulators is easier and less prone to error than using optics to demodulate the signal. The schematic diagram of an I&Q demodulator used with homodyne detection is shown in Figure 4.1. The demodulator consists of two double-balanced mixers. The two inputs of the demodulator are the detected signal and a reference signal, both of which are modulated at the same frequency.

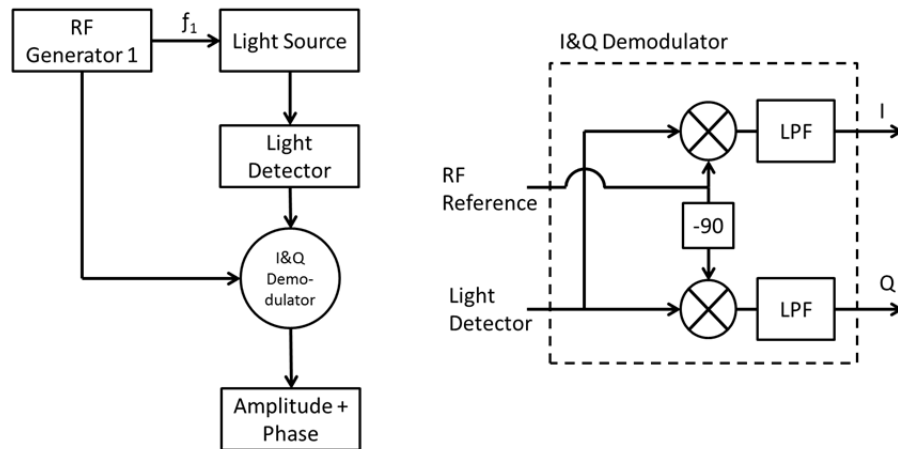


Figure 4.1: The concept of homodyne detection is illustrated in terms of in-phase and quadrature (I&Q) detectors with low pass filters (LPF), producing a pair of signals (I & Q) for each measurement.

The mixers act as signal multipliers. If the reference signal has the form  $A \sin(\omega t)$  and the output signal from the detector is  $B \sin(\omega t + \phi)$ , the I&Q

demodulator splits the detector and reference signals into two parts, in which one part of the split reference is multiplied by the corresponding part from the split detector signal while the other part of the detector signal is multiplied by a 90°-shifted version of the reference signal. The output signals then include in-phase and quadrature components where the in-phase, I, becomes

$$\begin{aligned} I(t) &= \left(\frac{A}{2}\right)\left(\frac{B}{2}\right) \sin(\omega t + \phi) \sin(\omega t) \\ &= \left(\frac{AB}{8}\right) \cos(\phi) - \left(\frac{AB}{8}\right) \cos(2\omega t + \phi) \end{aligned}$$

, and the quadrature signal, Q, is

$$\begin{aligned} Q(t) &= \left(\frac{A}{2}\right)\left(\frac{B}{2}\right) \sin(\omega t + \phi) \cos(\omega t) \\ &= \left(\frac{AB}{8}\right) \sin(\phi) + \left(\frac{AB}{8}\right) \sin(2\omega t + \phi). \end{aligned}$$

A low pass filter (LPF) eliminates the high frequency components of both the I and Q outputs, and the amplitude and phase simply becomes the geometrical sum of both outputs, i. e. amplitude =  $\sqrt{I^2 + Q^2}$  and phase =  $\tan^{-1}\left(\frac{Q}{I}\right)$ . While the homodyne technique is simple and inexpensive to implement, its output is a DC signal that is affected by 1/f noise discussed in chapter 2. The heterodyne detection technique is similar, but improves on the signal-to-noise ratio of the homodyne approach.

Heterodyne detection uses local oscillator signal with a slightly different carrier frequency with reference to the measured signal. This technique may be implemented with optics such as a laser beam, beam splitters, and interferometers but it is easier and

more economical to demodulate the signal electronically either at the detector or by using non-linear electrical devices such as mixers.

The key feature of heterodyne detection is to translate signals from one frequency band to another frequency band thereby allowing the input signal to be processed more effectively. An example of this non-linear process is shown in the figure 4.2 below where signal A at frequency  $f_1$  is mixed with signal B at frequency  $f_2$  which results in waveform C which has two frequency components  $f_1+f_2$  and  $f_1-f_2$ . Mathematically, mixing is equivalent to multiplying the two signals (a non-linear process) in order to generate two other signals at frequencies equal to the sum and the difference of the original signals. For example, if we represent the reference signal by  $A \sin(\omega_1 t)$  and the detector output signal by  $A_2 \sin(\omega_2 t)$ , then, after mixing both signals, the output becomes

$$\begin{aligned} &= A_1 \sin(\omega_1 t) \times A_2 \sin(\omega_2 t) \\ &= A_1 A_2 \frac{1}{2} [\cos(\omega_1 - \omega_2) t - \cos(\omega_1 + \omega_2) t] \end{aligned}$$

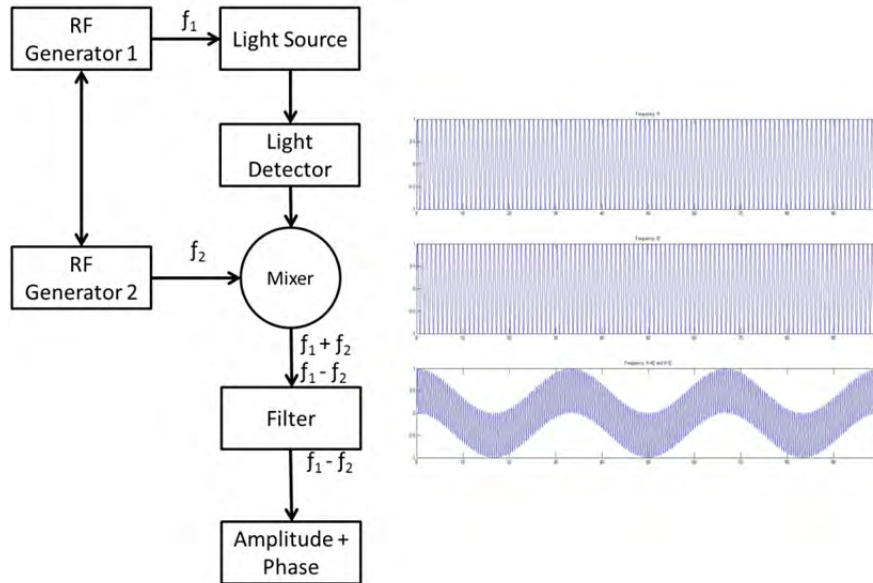


Figure 4.2: Heterodyne detection illustrated here is useful for optical signals in the MHz range because these signals are electronically mixed with an offset frequency that results in the signal being shifted to a lower frequency for direct detection.

Heterodyne detection can be accomplished electronically in two different ways. The first method uses RF mixers in order to electronically mix the detector output signal at  $f_1$  with a reference signal at  $f_2$  which will generate two signals. The high frequency component is filtered out and the low frequency signal is input to the data acquisition system. The other method relies on internally modulating the detector in order to produce the cross-correlation frequency. Internal down conversion in a PMT, for example, is accomplished by modulating one of the dynodes (usually the second dynode). A network analyzer can also be used to perform frequency domain measurements through heterodyne principle at a wide frequency range. [74] [75]

With FD systems, a single modulation frequency is usually used. As explained previously, a 100 MHz signal is typically used for tissue imaging. As the modulation frequency increases, the sensitivity of the detector and electronics shows a decrease.

However, one advantage of using a higher modulation frequency is the increase in phase shift difference between the normal and tumor tissue due to the increase in the absorption. Some systems utilize multiple modulation frequencies. Gulsen et al [75] found that multifrequency image reconstruction provides a better image quality compared to a single modulation frequency systems.

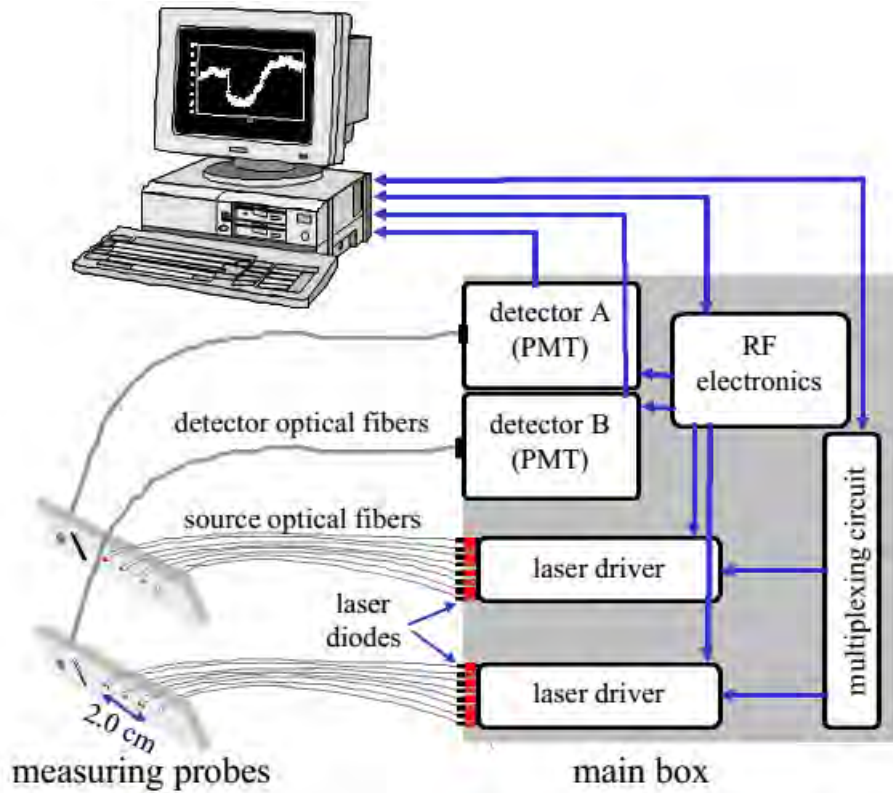


Figure 4.3: An example of a frequency-domain system [72].

Several frequency domain systems have been built. Some FD techniques only measure the phase at one or two fixed frequencies [76]. Other systems measure phase and amplitude at fixed source-detector separations [77]. Other systems measure phase and amplitude at a broad range of frequencies [78] [79] [74].

Both FD and TD techniques aim at measuring the propagation delay of photons traveling through tissue from the source to the detector, thus, enabling quantification of

the absorption and scattering information of the tissue media. While TD provides precise timing of the photons from the source to the detector, FD technique provides the average time it took the photons to travel from the source to the detector [73].

FD systems are more economical compared to TD systems since FD measurement can afford less sensitive, slower rise time (smaller bandwidth) detectors. Steady-state techniques can be combined with frequency domain/time-domain systems if the optical pathlength (or differential pathlength factor (DPF)) is determined by the FD/TD systems[73].

## **4.2 Hybrid System Design**

The challenge in NIR breast imaging is to provide a robust system which has appropriate wavelength coverage with appropriate dynamic range capability for the discrete sizes and attenuations possible between women breasts imaged. Most DOT systems operate at 2 – 4 wavelengths [80] and, due to the limited sensitivity of PMT detectors, use light between 650nm and 850nm [81] [82] [83]. Later systems have evolved to include additional wavelengths. However, the larger lipid and water absorption peaks both lie at 930nm and 975nm respectively [84]. Recovering the water and lipid content is not that accurate without coverage in this range. Adding these wavelengths has been shown to improve the recovery of both chromophore concentrations in breast spectroscopy [85] [86] as well as NIR breast tomography in an earlier version of the system [84] [87]. This earlier attempt was not on a compact system but rather utilized a large spectrometer array which was for initial prototype testing. In the current rendition, a more compact system prototype was engineered to test the ability to measure these signals and quantify water and lipid.

Frequency domain measurements using intensity-modulated sources, are extremely stable and cost effective, but have the inherent limitation that most high dynamic range FD systems are based upon photomultiplier tube (PMT) detection. PMT detectors in general have low photon detection efficiency. The highest gain PMTs have wavelength response curves that fall off dramatically above 825nm, and so while these systems provide excellent separation of  $\mu_a$  and  $\mu_s'$ , they do not provide for the best wavelength coverage for optimal spectroscopy. The use of steady-state CW (or low frequency modulated) light to measure the attenuation of light at longer wavelengths can supplement frequency domain measurements, if combined in a manner which utilizes the known spectral shapes as prior estimates of the key molecules to be quantified [83] [87]. The system developed here was designed with the idea of sequential illumination for FD followed by CW, allowing the widest spectral range possible for MRI-guided NIR spectroscopy of breast cancer.

In this work, a new NIR optical parallel detection system of both frequency and continuous wave domains was developed to improve the data quality and accuracy in recovery of all breast optical properties. In order to extend the measurements to longer wavelengths while maintaining the system in a compact and mobilized manner, rather than using CCDs for each detector as previously tried, solid-state silicon photodiode (PD) detectors with a large active area (10 mm x 10 mm) were used.

The hybrid imaging system, shown in Figure 4.4 (a), was designed to accommodate (4.2.1) frequency-domain (FD) and (4.2.2) continuous-wave (CW) measurements. All the FD/CW imaging components along with the (4.2.3) rotary switch array and the (4.2.4) data acquisition and control software are housed inside a single

portable rack. Fiber optic bundles held into thick cables connect the light detectors to the (4.2.5) patient breast interface.

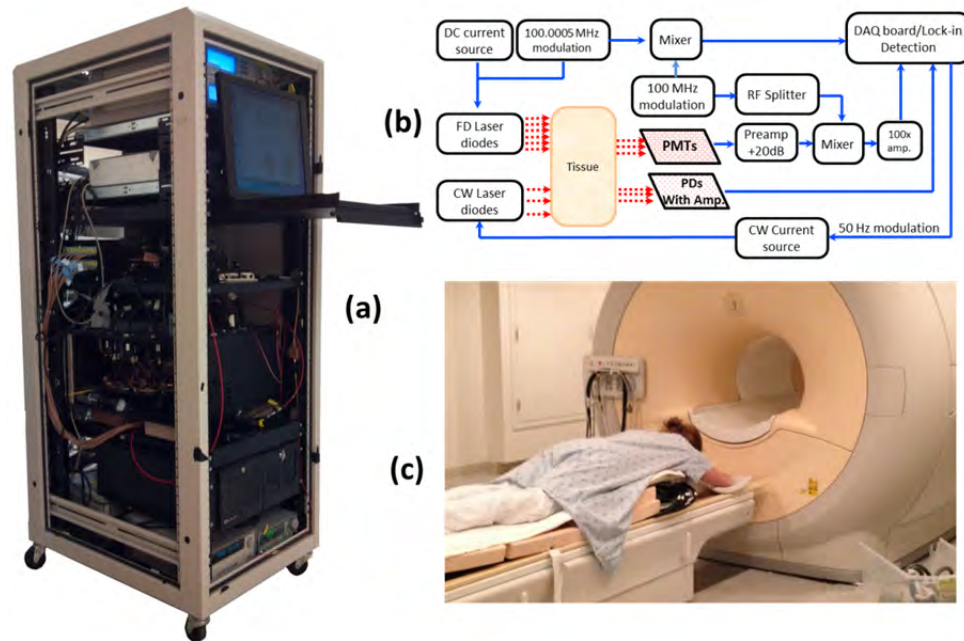


Figure 4.4: FD/CW hybrid imaging system. A photo of the complete system is shown in (a). The system diagram is shown in (b). A photo of human subject being imaged using the system.

A diagram of the internal details of the hybrid system is shown Figure 4.4 (b). Detailed description of the components and their interconnection is described below. In brief, a bias-tee combines DC current along with an RF signal ( $f = 100.0005$  MHz) in order to drive the FD laser diodes, while a laser current module drives the CW laser diodes. The output of the lasers is directed to the tissue via fiber optic cables. The transmitted signal is recorded using photomultiplier tube (PMT) detectors for FD measurements and then followed by photodiode modules for the CW measurements that are used with the longer wavelengths. The output of the PD modules is connected directly to the data acquisition (DAQ) board while the output of the PMT detectors is

converted to voltage, amplified, and then heterodyned to a lower frequency signal using mixers. The output of the mixer is amplified further and then is read by the DAQ board

#### **4.2.1 FD Detector Channels**

The PMT modules were used with wavelengths below 850nm for frequency domain measurements. The instrumentation for this portion, illustrated in the schematics shown in figure 4.4 (b), is nearly identical to our previously published system [82], with two important upgrades, including: (1) a 20dB amplifier that was added after each PMT, and (2) a programmable gain amplifier on the data acquisition (DAQ) card. The light source consists of six intensity-modulated (100MHz) laser diodes that cover the main spectral range of the four chromophores under study (660, 735, 785, 808, 826, and 849nm). A bias-T combines DC bias current from an ILX Lightwave laser driver with a 100MHz AC signal from a Marconi function generator in order to drive the laser diodes. The modulation depth of the lasers is 25-40%. The lasers are activated one at a time by digitally controlling a 6-way RF switch which passes the biased current to the selected laser diode. Each laser diode is mounted on a fiber launch module (Thorlabs, Princeton NJ) where the output of each laser is directed into the input of a 6x1 fiber optic combiner (Fiberguide, Stirling, NJ). The output fiber is then directed to the rotating stage, discussed in section (c,) where it acts as the source fiber in the system.

PMT (H9305-3, Hamamatsu, Japan) detectors with a 1.4ns rise time are used to acquire the attenuated laser light that is transmitted through tissue. The spectral response range of the PMTs is 185 to 900nm with peak sensitivity at 450nm. The sensitivity of the photomultiplier tube decreases rapidly at wavelengths longer than 850. Power to all PMTs is supplied from a single power supply. Thin film filters (Kodal Wratten Red 25,

Edmund Optics) are installed on the detectors window in order to block visible light below 600 nm from entering the PMTs.

The RF output of the PMT detectors is amplified using a 20dB RF low-noise preamplifier (Minicircuits) which also filters out the DC component of the signal. Adding this amplifier has increased the S/N ratio by a factor of 100. The output of the preamplifier is then heterodyned with a local oscillator (LO) reference signal (100.0005MHz) in order to down convert the 100MHz PMT output and produce an intermediate frequency (IF) signal (500Hz) that can be processed more easily by the DAQ cards. The IF output of the mixer is then amplified (100x) and filtered by a differential-amplifier/3-pole Butterworth low-pass filter circuit in order to reduce high frequency noise before it is measured by the data acquisition card. The resulting output signal is read by the DAQ card where it is phase-locked with a reference signal in order to obtain the phase and amplitude of the attenuated signal detected by the PMT.

The LO signal is obtained by dividing the power of a 13dBm 100MHz function generator output into 15 signals using 1x16 RF splitter. Each output of the RF splitter is then connected to the LO input of the mixers. One output is terminated via a 50 Ohm terminator since only 15 mixers are used. The two signal generators are synchronized and the reference signal used for the phase-lock detection is obtained by mixing a portion of the output of each signal generator. This reference signal is then connected to the data acquisition card where the phase from all channels is compared with the phase of the reference signal.

#### **4.2.2. CW Detector Channels**

The CW measurement system extends the range of wavelengths used to image the breast in order to better quantify the chromophore concentrations. The system consists of three laser diodes (903, 912, and 948nm) and 15 silicon photodiode (PD) modules that are housed in the same enclosure as the FD components. The output of the laser diodes is intensity-modulated at 50Hz in order to obtain better signal-to-noise ratio through software-based lock-in detection as shown in Fig.4.4 (b).

The detectors used are high-precision silicon photodiode modules which incorporate a current-to-voltage amplifier within the module (C10439-03, Hamamatsu, Japan). These modules have an active area of 1 cm<sup>2</sup> and a large spectral response range (190 to 1100nm) with peak sensitivity at 960nm. The sensitivity of the PD modules is switchable between a low and a high range. The two photodiodes nearest to the laser source are set to low sensitivity in order to avoid light saturation of the modules while the remaining modules are set to high sensitivity. Thin film filters (Kodak-87 Wratten, Edmund Optics) are installed on the detectors' window in order to block light below 800nm. All PDs are driven by a single dual-output power supply. CW measurements only extract the change in amplitude of the light through tissue. Therefore, unlike the FD measurements, no additional components were needed to connect to the PD modules. The output of the PD's is connected directly to the data acquisition cards.

#### **4.2.3 Rotary Mechanical Switch Array**

A portable rack contains all the FD and CW components including laser diodes, signal generators, computer, and the detectors array. The detectors array is housed inside a custom mechanical switch as shown in Figure 4.5, which was designed using SolidWorks and built in-house using 1/4" aluminum sheets. The assembly (21" x 21") was

designed to accommodate both PD and PMT modules. The PD and PMT modules are mounted on the top circular plate while the RF splitter and mixers are mounted on the bottom circular plate. Both circular plates rotate via a high precision motor mounted on the bottom circular plate as shown in Figure 4.5 (a). This allows multiplexing of the laser source and detectors to 16 different positions, giving a total of 240 measurements (16 sources x 15 detector measurements) for each wavelength. The detectors position is always fixed relative to the source position. Fiber optics cables connect the patient interface to the top square plate of the switch assembly. A small gap exists between the top square plate and the circular plate holding the detectors which allows the circular plate to rotate. Light from the fiber optics cables is multiplexed to all detectors through holes in both the square and circular plates that align with each other as the circular plates rotate. The fibers remain fixed and thus, the same fiber that was used for the source is also used for detection.

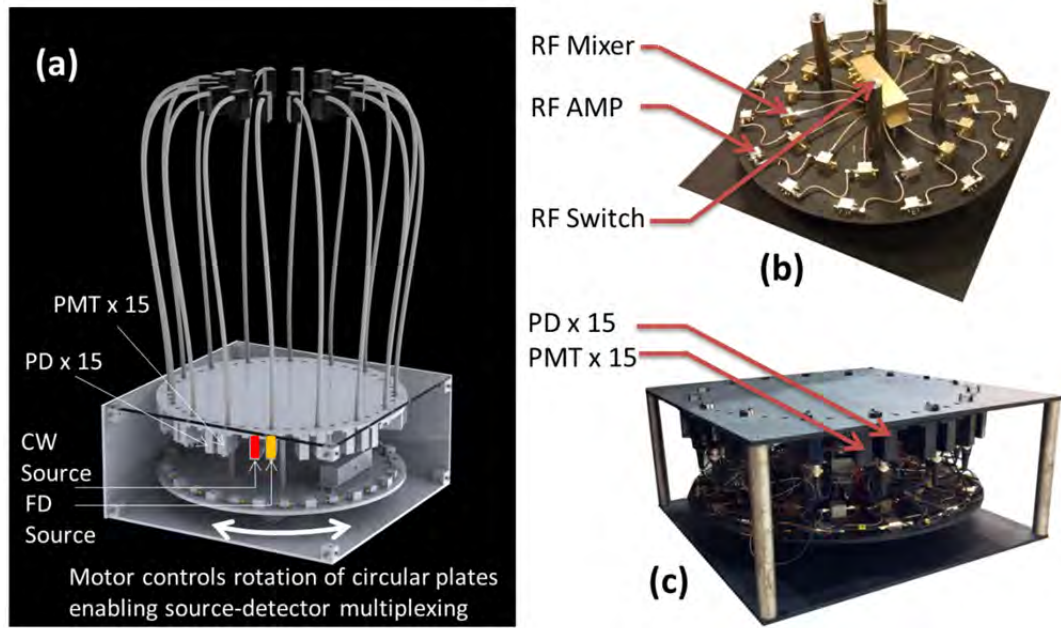


Figure 4.5 switch array: Solidworks drawing of the array is shown in (a) and photos of the actual assembly are shown in (b) and (c).

#### 4.2.4 Computer and data acquisition

A computer running custom LabVIEW software controls the system components and enables automation of the entire system. The program allows the user to select the lasers to be used for imaging and provides advanced options that enable the user to run different customizable scans. The LabVIEW software controls the signal generators via GPIB, the rotary stage through RS232, and two PCI data acquisition cards. The code was programmed by following proper software development methods and the code architecture was documented with flow charts as shown in Figure 4.6 (a). The main graphical user interface which enables control of the hybrid system is shown in Figure 4.6 (b).

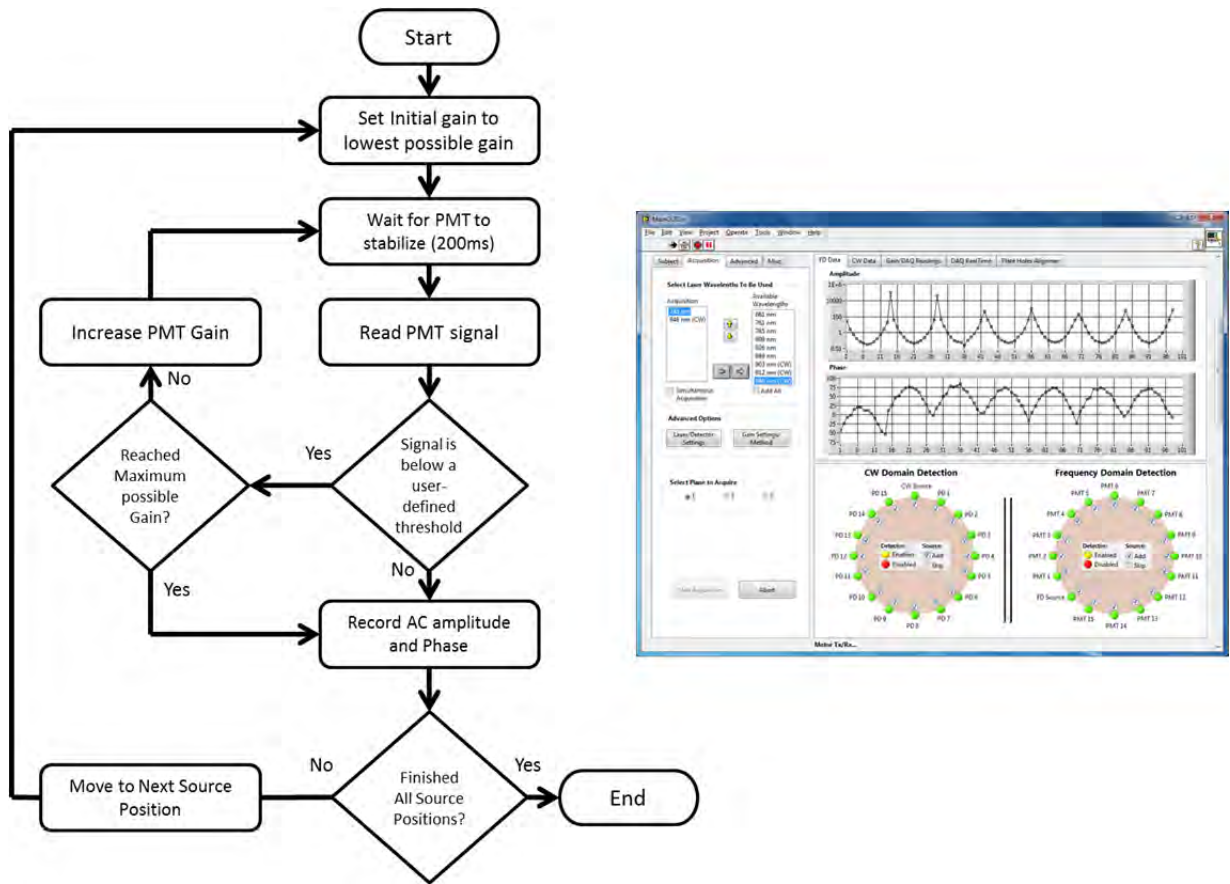


Figure 4.6: (a) Flowchart used in programming the (b) LabVIEW program which controls the hybrid system.

A 16-bit 64-channel multifunction DAQ card (NI-PCI 6031E, National Instruments) is used for acquiring the data from the PMT. The FD signals are sampled at 4KHz and 1000 samples/channel are acquired. The signal from each FD measurement is then phase-locked with a reference signal that is also connected to the same DAQ card. The phase and amplitude of each channel is analyzed and recorded. The CW data is sampled at 4KHz and 2000 samples/channel are acquired.

The multifunction DAQ card used has a programmable gain amplifier. The use of this digitally controlled amplifier ensures that the analog FD/CW signals use the maximum resolution of the analog-to-digital converter of the DAQ card which improves

the signal's accuracy. Using this amplifier has increased the S/N ratio by a factor of 10. During acquisition, data from each channel is sampled for 100ms in order to find the maximum and minimum of each channel. Once this range is found, the appropriate gain is selected for each individual channel and the signals are acquired again.

The gain of the PMT detectors is controlled by a 16-bit 16-channel static analog voltage output card (NI PCI-6703, National Instruments). The gain is set by applying voltages between 0.3-1.1V in increments of 0.1V.

## **4.3 System Characterization**

### **4.3.1 Calibration**

Calibration is a critical step needed in order to get meaningful linear response of voltage data from the PD/PMT detector optical measurements. This takes into account amplitude losses and phase delays that result from differences in detectors response, optical fiber losses, and RF components performance. The goal of the calibration process is to produce the same response (amplitude and phase measurements) for equivalent inputs across the entire dynamic range of the detectors. Three types of calibration were used as described below:

#### a) Individual PMT & PD Responsivity Correction

Detector responsivity calibration was used to account for the differences in PMT responses to the same optical signal. The relative sensitivity of each optical detector was quantified using a single light source which was placed in the radial center of a cylindrical homogenous phantom. The response of all the detectors was measured and a scaling factor was obtained which corrects for slight differences of the intensity detected. However, the signal detected is affected not only by differences in the detector response

and associated RF-circuitry, but also by differences in the dispersion properties of the fiber bundles. Since the detectors rotate while the fiber bundles remain fixed, the scaling factors were obtained for each of the 16 different source positions in order to correct for fiber bundles differences.

#### b) PMT Gain Calibration

Different light levels reach the PMT detectors depending on their position from the source fiber. In order to account for this difference, the PMT offers a large dynamic range. The large dynamic range of a PMT is in part due to the ability to manipulate gain, which affects the light level that can be detected over many orders of magnitude. But critically, the response of the PMTs at different gain levels must be calibrated if the signal is to be interpreted in a linear manner across these orders of magnitude. The calibration process that was used is similar to the calibration process that was described by Mastanduno et al [88].

#### c) Homogenous calibration

Homogenous calibration is used to compensate for optical fiber losses and any small errors that might develop during the detector calibration process, and also allows a better match of the data to the forward diffusion model in the image reconstruction process. This calibration also needs to account for the two different detectors used. Prior to each experiment, a phantom with optical properties similar to the breast (or to a heterogeneous phantom) is imaged with both types of detectors using all available wavelengths. The data set consisting of the logarithm of the intensity and phase shift from the homogenous phantom experiments are subtracted from a calculated diffusion model of the same phantom region, and this is then added onto future measurements of heterogeneous

phantoms or tissues that were imaged. This provides a fiber-by-fiber small correction, assuming additive errors can be fixed this way.

#### **4.3.2 Detection linearity/limits**

In order to determine the sensitivity and linearity of each detector, a fixed optical signal along with neutral density (ND) filters were used to look at the detectors response as a function of incident light power. The light power was increased incrementally by removing the ND filters from the path of the laser beam while the AC amplitude and phase response of the PMTs and the AC amplitude of the PDs were recorded. The AC signal error and phase error as a function of incident power for one of the PMTs for this system is shown in Figure 4.7. The results are compared to the previous generation system built in our lab [82] in order to demonstrate the improvement of the new system over the older one. The full dynamic range of the PMT's was about  $1 \times 10^5$  with the lowest signal detected at around 10 pW using the highest gain setting. Adding the RF amplifiers to the system has helped in increasing the S/N ratio of the FD measurements.

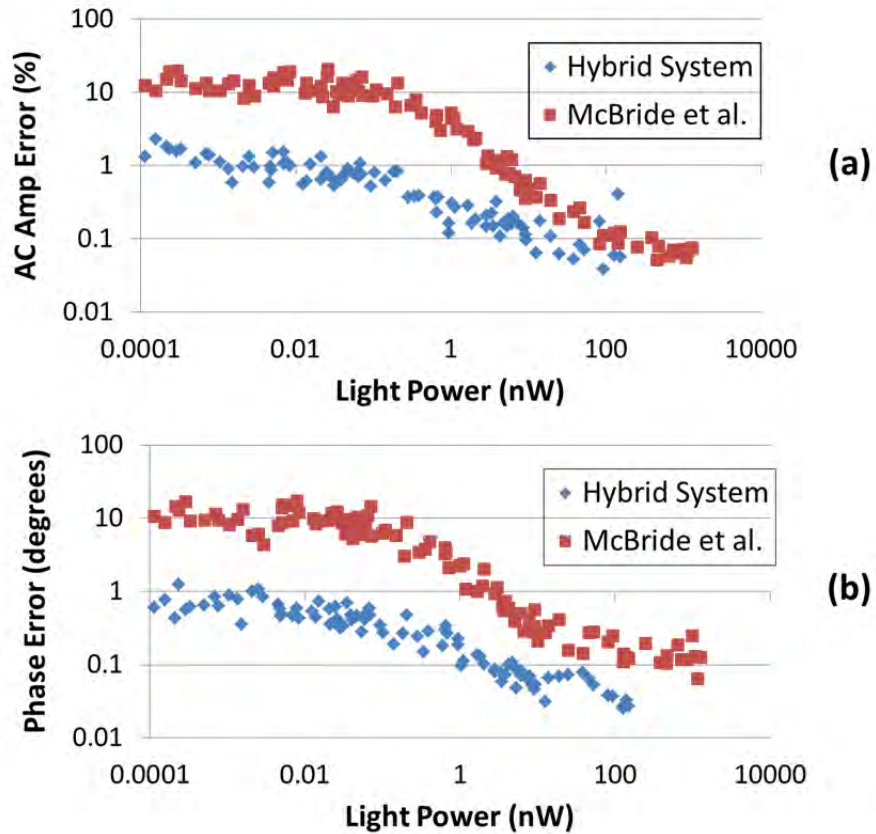


Figure 4.7: Standard deviation of the natural log of the amplitude (In AC) (a) as well as the standard deviation of the phase (b) of the photomultiplier tube (PMT) as a function of incident light power. The blue marks represent the results for the new system while the red marks represent the results for the system built by McBride et al.

Figure 4.8 shows the response of one of the PD's as a function of light power for the two gain settings of the PD. The low range exhibits linearity over the range of 0.1nW up to 2uW while the high gain setting exhibit linearity over the range of 1pW up to 20nW. Thus, the full dynamic range of the PDs is  $2 \times 10^6$ .

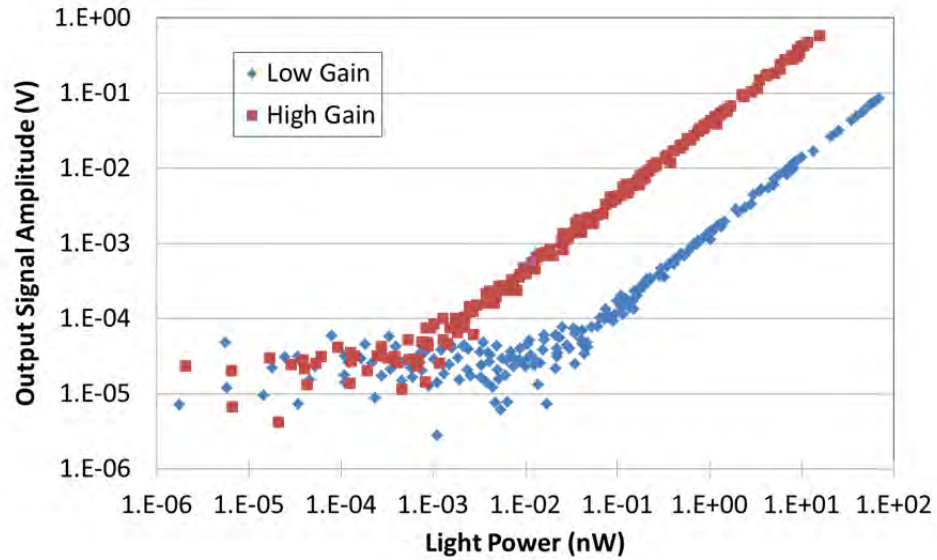


Figure 4.8: Photodiode (PD) response as a function of incident light power for the two available gain settings of the PD.

### 4.3.3 Gain settings

PMT detectors nearest to the light source receive orders of magnitude more light than detectors farther away. In order to account for this variability, the gain of the PMT detectors must be adjusted accordingly. The gain of the PMT detectors is adjusted by adjusting an analog control voltage input which is controlled via a static analog voltage output NI-6073 card from National Instruments.

Prior to acquisition, the PMT would be set to the lowest gain possible (0.3V). The gain of each PMT is then increased in 0.1V increments while monitoring the PMT output AC signal. Once the AC signal reaches a user defined threshold, the gain of that particular PMT is set. The process continues until all PMT gain values have been set or until the gain reaches a maximum user-defined value. The system waits for 100ms during the process of finding the proper gain before acquiring and analyzing the AC

signal. However, once the gains have been set for all PMT's, the system waits for an additional 1000ms to ensure a better stability of all PMTs.

As mentioned previously, the sensitivity of the PD modules is switchable between a low and a high range using a switch on the back of the PD module. The two photodiodes nearest to the laser source receive much more light than the remaining modules and therefore had to be set to low sensitivity range in order to avoid detector saturation. A high sensitivity setting was used for the remaining modules since the amount of light received by these detectors is below the saturation point of the high sensitivity range.

In order to improve the performance of the system even further, a programmable amplifier on board the DAQ card was used. During acquisition, data from each channel (FD and CW) is sampled for 100ms in order to find maximum and minimum of each channel. Once this range is found, the appropriate gain is selected for each individual channel and the signals are acquired again. This ensures that the maximum ADC resolution is used while acquiring all signals.

#### **4.3.4 Cross talk**

There are two types of cross-talk that may affect the results of the system. The first type is an inherent property of the PMT where increasing the light intensity of a signal while maintaining the phase influences the phase readout. This is due to space charge effects of the PMT. In order to minimize this cross-talk, we start the PMT at the lowest possible gain and increase the gain in discrete steps until the signal is above the noise floor of the system, but well below the saturation level of the PMT. Once the signal level reaches a user-defined minimum value which is approximately the middle of

the dynamic range of the PMT, the gain is set. This method ensures that the PMT anode current does not reach large values that may disturb the electric field inside the PMT and cause the phase to change.

The other type of cross talk that may affect the measurement is interchannel cross talk from the DAQ card. This type of cross talk may be improved if differential-measurements are used. However, due to system limitations, our system had to use the single-ended termination where all the signals share the same ground point. This causes cross-talk between channels if one channel detects a larger signal compared to its neighboring channels. However, the same method that improves the space charge cross-talk affect also improves the interchannel cross-talk. By increasing the gain of each PMT until the signal is in the middle of the dynamic range for all PMTs, the voltage read by the DAQ device is roughly the same for all channels.

#### **4.3.5 Stability and repeatability**

The repeatability of the system was determined by repeating a phantom measurement continuously while keeping all the parameters in the experiment the same. The phantom used is a silicon phantom with diameter of 86 mm. The laser light was directed to the center of the phantom. The phantom experiment was run five times and the standard deviation of the phase as well as the standard deviation of the natural log of the amplitude (In AC) was calculated. It was found that the average repeatability of the phase and In AC is 0.2 degrees and 0.5% respectively, as compared to 0.4 degrees and 0.5% for our previous system.

In order to measure the stability of the system, the same repeatability experiments were performed over an entire week ensuring that the system is turned on and off prior to

the experiments. It was found that the average stability of the phase and In AC is 0.44 degrees and 1.2% respectively.

#### **4.3.6 Data acquisition duration and timing**

Experiment duration is very important when patients are involved in imaging. Several improvements were implemented in order to shorten the duration of the full 9-wavelength acquisition including optimizing the way PMT gains are calculated for different source position as well as refining software procedures.

Different breast/phantom interface geometries and different gain-fixing algorithms effect the duration differently. During FD acquisition, for gain routine A, the first laser is activated and the rotary stage moves until the source and detectors are aligned with the first source position. The gain finding routine sets the PMTs to the proper gain and then data from all PMTs are acquired. Next, the rotary stage moves to the next source position, sets the proper gain and acquires the data. This continues until every source position have been acquired. Once the results from the first wavelength are obtained, the system repeats the same process above for the remaining wavelengths.

Another variation to the routine above is used to reduce the acquisition time. The second routine (routine B) reduces the time required for calculating the PMT gain by adjusting how the gains are calculated. It is identical to routine A above during the acquisition of the first wavelength. However, for the remaining wavelengths that are used in the acquisition, the gain values that were found for the first wavelength are used as the initial starting values for the remaining wavelengths. In both gain finding routines, once the FD acquisition is finished, the system performs a similar process for the CW wavelength measurements. The only difference is that no gain finding routine is needed

while acquiring data with the PD modules since PD module gains cannot be adjusted using software.

Running an acquisition with all 9 wavelengths takes anywhere from 9 to 20 minutes depending on what geometry and which gain finding routine is used during the acquisition. The total data acquisition time for each wavelength is shown in table 1. The acquisition shown used a pentagon interface that was designed by Mastanudno et al that accommodates all breast sizes. In addition to the total data acquisition time at each wavelength, table 1 shows the average time it takes the system to determine the gain for the PMTs (column: “Gain”); for movement of the rotary switch array (column: “Motor”); and for miscellaneous steps which include toggling the lasers, setting up the function generators, etc (column: “Misc”). Gain routine B approach has cut down the time of a full 9-wavelength scan from 19 to about 12 minutes

	<b>Gain (s)</b>	<b>Motor (s)</b>	<b>Misc (s)</b>	<b>Total Time/</b>
<b>FD – Routine A</b>	85	30	20	135 (~2.25 min)
<b>FD – Pentagonal geometry Routine B</b>	40	30	20	90 (1.5 min)
<b>CW</b>	N/A	30	26	56 (~ 1min)

Table 4.1: A breakout of the time spent on the main sections of the acquisition process.

#### 4.4 Conclusion

Imaging water and lipid concentrations poses a problem since the ideal FD or time-resolved systems are PMT based, and so limit their response to wavelengths that are below the main spectral features of water and lipids. The ability to accurately image water and lipid concentrations enables better characterization of malignant and benign tissue as well as provides better characterization of cysts and is also critical to recovering accurate hemoglobin and oxygen saturation values. The new hybrid system presented here has extended the wavelength range in order to include these spectral features and

thus improves the data available for separation of chromophore contributions. However, since pure CW measurements do not accurately decouple chromophore concentrations and scattering, our system combines FD and CW measurements. Admittedly this technological solution is a complicated coupling of two detection technologies; however it is presented here in a design which not only allows simultaneous sampling but fast source switching. The design is also extendable to more channels and faster speeds, however is slightly configuration dependent in terms of timing.

A key advantage of the system is the integration of all components into a portable standalone prototype, allowing wider optical bandwidth of detection. The previous system used 16 spectrometers which used CCD's to measure the light signal. The system was a prototype extendable to different types of spectroscopy including fluorescence and Raman, but not ideal for extending into highly parallel acquisition in a cost effective manner. The current hybrid system contains all imaging components inside a single rack, and is a logical prototype of how to combine FD and CW detection in a package that is compact, cost effective, and extendable.

The addition of +20dB amplifier after each PMT has increased the signal-to-noise ratio of the FD measurements. However, while changing the gain of the PMTs provides a high working range of linearity, the FD system was not able to detect light signal levels as low as detectable in the CW system. This is likely due to the relatively low S/N ratio of the phase measurement by PMT. The PD modules used with the CW measurements proved to be excellent detectors with a very high dynamic range of  $2 \times 10^6$  and detection limit at 1 pW. And unlike the PMTs, the PD modules did not require any additional electronics or RF components in order to accurately measure the light signal, so they can

be easier to integrate into a massively parallel system. While the PD displayed better linearity and no space-charge effect cross-talk, FD measurements of phase and amplitude cannot be acquired due to the lower temporal bandwidth of the PDs.

Another advantage of the hybrid system is that it has a bandwidth between 50 – 800MHz allowing multiple modulation frequencies to be used. Since an MRI scan takes a little over 30 minutes while an optical exam takes 12 minutes, it is possible to run multiple optical scans with different modulation frequencies during a single MRI scan, or the higher frequencies could be used when the tissue volume is smaller. A disadvantage of our current breast interface is that a 3D scan is not possible without having to reposition the patient; however the current hybrid array can be used with a larger number of channels, in a serial manner, if a better breast interface was developed.

## CHAPTER FIVE

### Hybrid FD/CW phantom and patients results

#### 5.1 Introduction

In order to test and validate the hybrid FD/CW system, first experiments with gelatin phantoms were performed. While phantoms are a great tool to test a system, they cannot completely characterize the system performance as phantoms are not able to mirror the oxygen saturation and lipid contents of a real breast. Therefore, human volunteers were used to further test the system and get a more complete picture of all chromophores (hemoglobin, oxy-hemoglobin, water and lipids). Finally, the hybrid system was shipped to Xi'an, China where a clinical trial in collaboration with Dr. Junqing Xu was performed on 61 patients. The results of the hybrid system was combined with MRI results in order to assess the advantage combining both modalities.

#### 5.2 Patient/Phantom Interface

Figure 5.1 shows the schematic of two different breast interface geometries. Instead of the circular patient interface (Fig 5.1 (a)) that have been used with our previous generation imaging system [82], a pentagonal patient interface (Fig. 5.1 (b)) was designed to accommodate various breast sizes to be imaged inside the MR room [89]. One end of each of the sixteen long fiber bundles is coupled into a breast MR coil and contact the breast with limited pressure for simultaneous MR and optical imaging of patients/phantoms. The other end of each of these sixteen fiber bundles are passed through a conduit in the wall and connect the source and detectors in the imaging assembly located outside the MR room. More details about this new interface are discussed elsewhere [89].

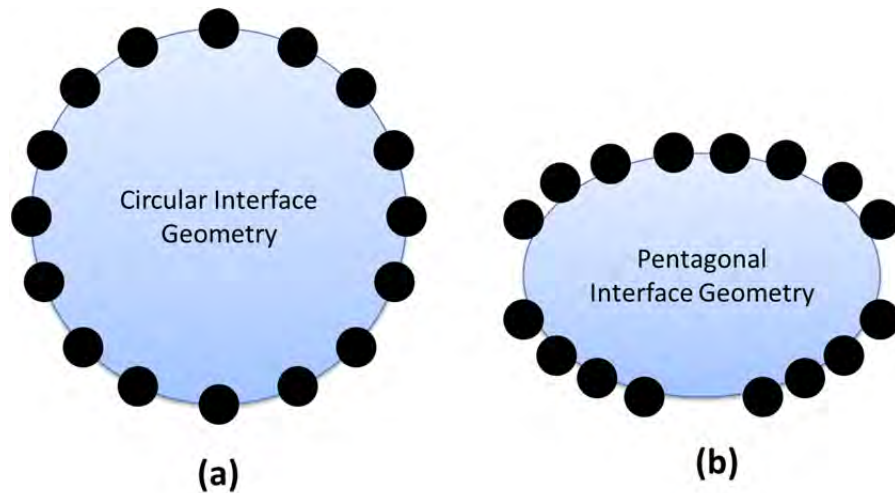


Figure 5.1: Schematic of two different breast interface geometries: circular (a) and the new pentagonal interface (b).

The primary goal of the interface is to accommodate different breast sizes and it was successfully used in imaging breast sizes ranging from A to D as shown in Figure 5.2 which shows breast MRI images of healthy volunteers.

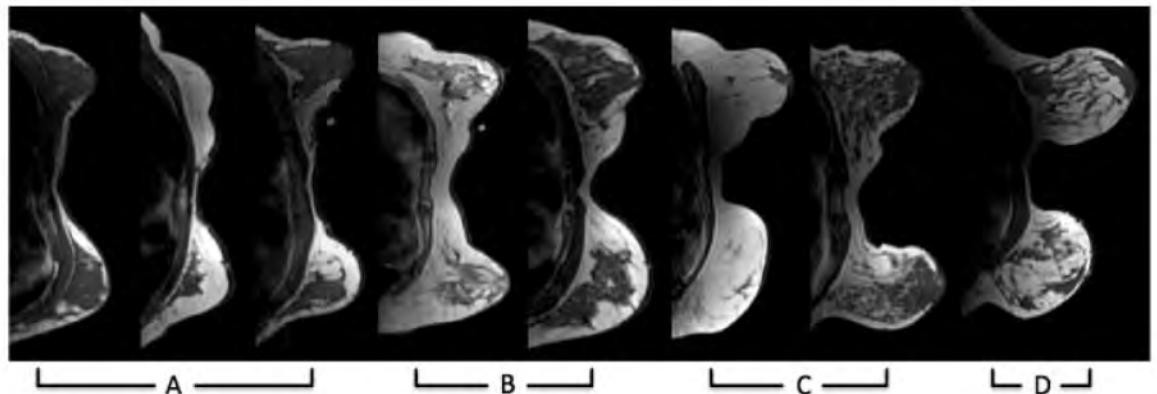


Figure 5.2: Bilateral axial images of all healthy volunteers imaged in this study arranged by cup size. The NIRS/MRI breast coil was able to accommodate all sizes, densities, and compositions in the group

### 5.3 Phantom Experiments

In order to study the system in detail, tissue phantom experiments were performed on a gelatin phantom mimicking breast tissue. The blood gelatin phantom was prepared

as described by Mastanduno et al by mixing water, type 1 Agarose, 1% Intralipid, and whole porcine blood. The hematocrit level of the blood was measured by a Hemocue device to be 8 g/dL and the blood concentration of the phantom was set 15 $\mu$ M which is approximate to what is found in healthy breast tissue. The phantom was constructed with a hollow 2 cm cylindrical inclusion. The inclusion was filled with different porcine blood concentrations starting from 0  $\mu$ M up to 45  $\mu$ M in 5  $\mu$ M increments in order to vary the absorption systematically (15  $\mu$ M concentration was not used). With each concentration, the phantom was imaged with all FD/CW measurements and data was acquired at 9-wavelengths. The blood concentration was recovered using Nirfast software [11] to determine the accuracy in recovery of the blood concentration of each run as compared to the expected concentrations. Briefly, the difference between measured data and a diffusion-based model of light propagation through the medium [90] [91] [9] is minimized to yield estimates of the optical properties of the tissue of interest. The three-dimensional reconstruction algorithm was designed to employ a priori information gained from MRI to guide the optical solution as outlined in previous work by Carpenter et al [92] [93]. This technique makes the assumption that each of the segmented regions defined from the MR, adipose and fibroglandular, have similar optical properties throughout. We simplify the image reconstruction problem computationally by completely eliminating variation within regions, and thus, are able to quantify optical properties between regions but not within them [93]. We also use spectral priors in the reconstruction, solving directly for tissue chromophores rather than absorption ( $\mu_a$ ) and scattering ( $\mu_s'$ ) coefficients at each wavelength as outlined in previous work [91] [9] [92]

[94]. These methods were applied to both phantom and human subject image reconstruction.

Figure 5.3 shows reconstruction results as a function of the actual blood concentration used. Hemoglobin recovery in the background was 25  $\mu\text{M}$  compared to the actual 15  $\mu\text{M}$  concentration. The background values were very stable across concentrations, with the norm of the residuals being 0.0054. Recovered HbT values from the inclusion showed a linear increase (norm of the residuals = 0.0066) with an average recovery of 71% of the true blood concentration.

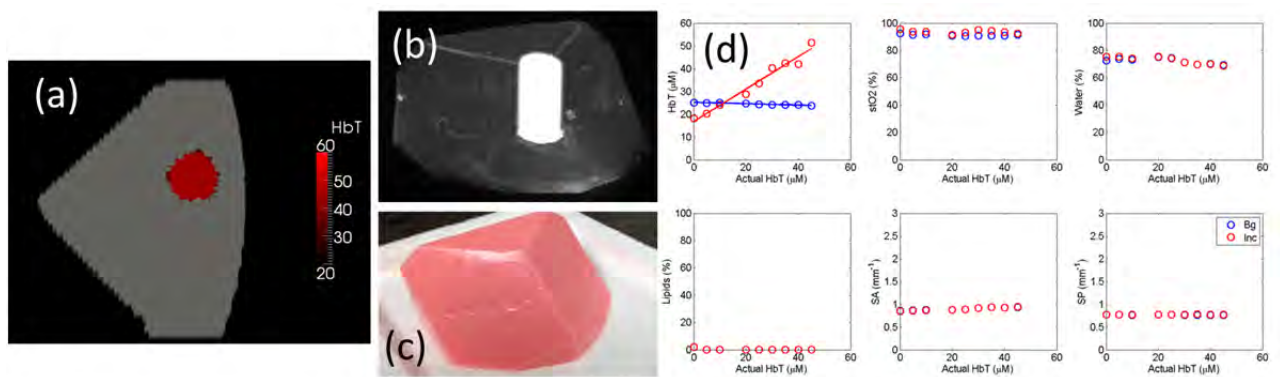


Figure 5.3: Reconstruction values on a gelatin phantom with 2 cm inclusion. The inclusion was filled with varying concentrations of blood. MRI images of the phantom are shown with the 2 cm inclusion overlaid (a+b). A photo of the actual phantom is shown in (c). Reconstruction as a function of true total-hemoglobin values are shown for total hemoglobin, oxygen saturation, water, lipids, scatter power, and scatter amplitude in (d). Blue circles are for the background while red circles are for the inclusion.

#### 5.4 Healthy Subject Imaging

All human subjects imaging has been carried out under an Institutional Review Board (IRB) approved protocol, #11487, and have been given informed consent prior to entering the study. Imaging protocol for the human subject examination was approved by

the Committee for the Protection of Human Subjects at Dartmouth-Hitchcock Medical Center. The subjects were positioned into the clinical MR breast coil and optical fibers were moved into contact with the breast tissue. If a fiber was unable to contact the breast, data from that fiber was omitted. Co-registration between optical and MR images was done using MR fiducial markers in the plane of the fibers and bilateral MR images in the axial geometry. Optical and MR data were collected concurrently, with data collections taking 12 and 30 minutes, respectively and reconstructed using the methods outlined above

The combined FD/CW system and pentagonal interface has been used to successfully image nine healthy volunteers at Dartmouth Hitchcock Medical Center. A representative case is shown in Figure 5.4. The volunteer was positioned such that her breasts were centered in the MR coil to minimize image artifact and then lightly compressed by the fiber optic cables to ensure good coupling. Optical data was collected in approximately 9 minutes for FD and 3 minutes for CW, totaling 12 minutes. MRI acquisition took approximately 30 minutes, and a second optical scan was performed during the remaining time. Data from one fiber was removed due to poor coupling with the breast tissue.

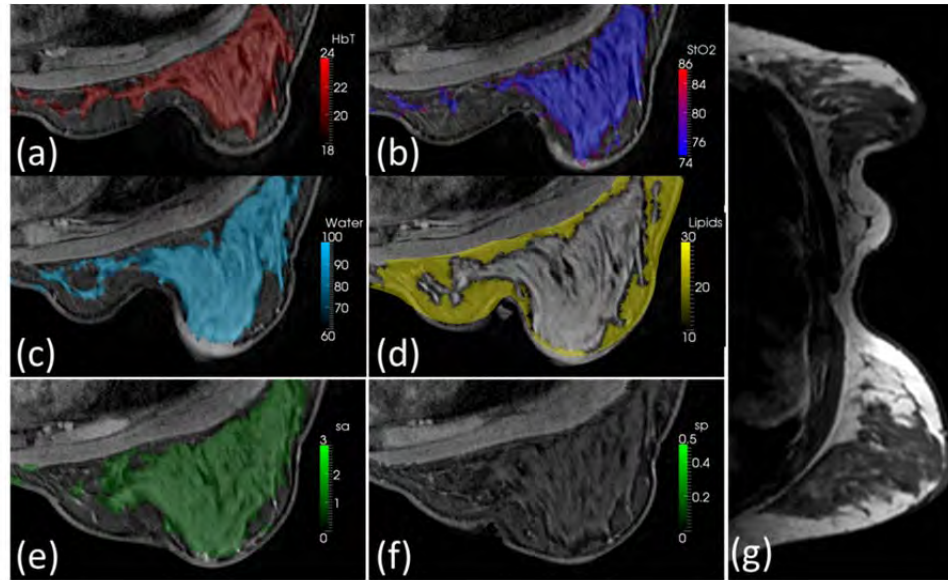


Figure 5.4: Representative healthy volunteer imaging by combined optical system and MRI. Different axial MRI slices are shown with overlays of total hemoglobin (a), oxygen saturation (b), water (c) and lipid (d) fraction, scatter amplitude (e) and power (f). In each case, the region with the lowest value is removed and the region with the highest value is made slightly opaque to visualize overlaid MRI. A bilateral axial image (g) shows little degradation of MRI image quality.

A 3D finite element mesh of approximately 40k nodes was created specific to the patient based on the MR scan and segmented into adipose and fibroglandular regions. Optical data was co-registered to the MRI using fiducial markers in line with the optical fibers and the data was calibrated absolutely versus the model. A hard priors approach was then used to reconstruct for oxygenated hemoglobin, deoxygenated hemoglobin, water and lipid fraction, scatter amplitude, and scatter power [11]. This volunteer showed total hemoglobin concentration of  $18 \mu\text{M}$  in the adipose region and  $22 \mu\text{M}$  in the glandular region with high oxygen saturation (74-86%) as well. Water content was higher in the glandular region while lipid content was higher in the adipose region. MRI image

quality was not affected by the optical image acquisition aside from a slight distortion of one breast from the optical fibers. The volunteer reported no discomfort due to the procedure.

### **5.5 Patient Imaging**

The hybrid system was shipped to Xi'an, China in order to perform a clinical trial in collaboration Xijing Hospital. The imaging protocol for human subject examination was approved by the Committee for the Protection of Human Subjects at Dartmouth-Hitchcock Medical Center and at Xijing Hospital. There, MRI-guided near infrared spectroscopy using our hybrid system was delivered to 3 healthy volunteers and 61 patients. Out of the 61 patients, 44 patients went through surgical resection where 16 patients were diagnosed as benign and 28 where diagnosed as malignant.

Data analysis of the NIRS results are described in detail in Mastanudo et al. Two representative cases are shown below for patient #46 showing a benign tumor (Figure 5.5) and for patient #58 showing a malignant tumor as confirmed via biopsy (Figure 5.6).

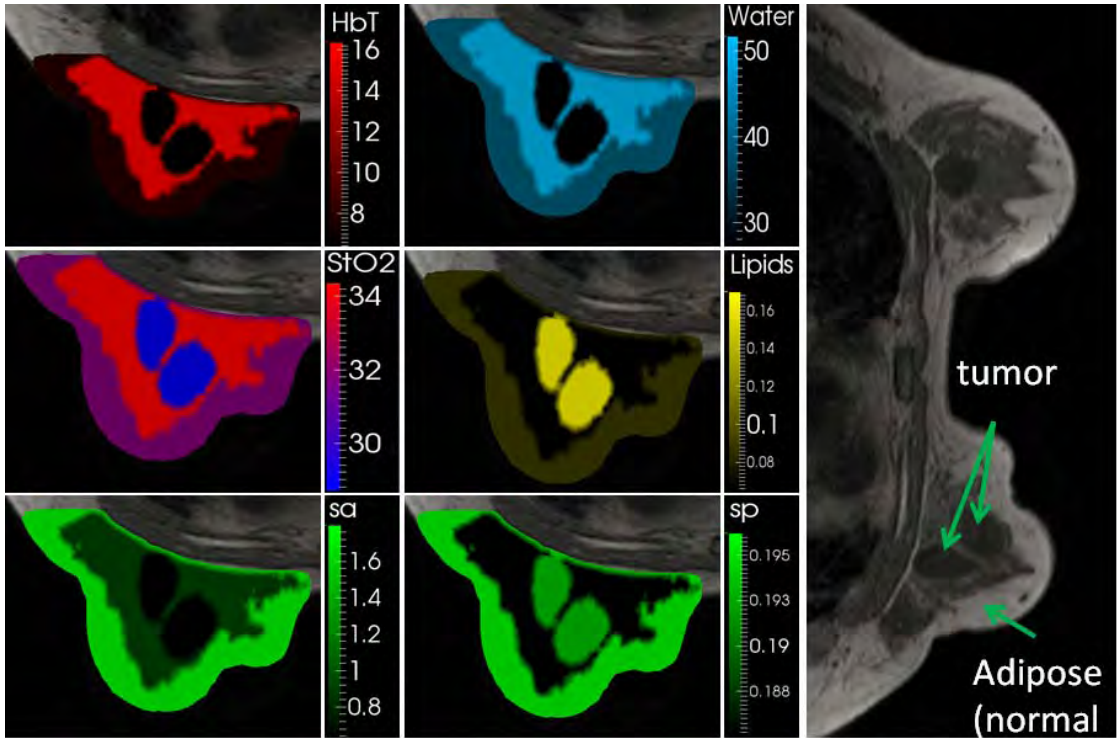


Figure 5.5: a representative case of a NIRS imaging showing a benign tumor for patient

#46.

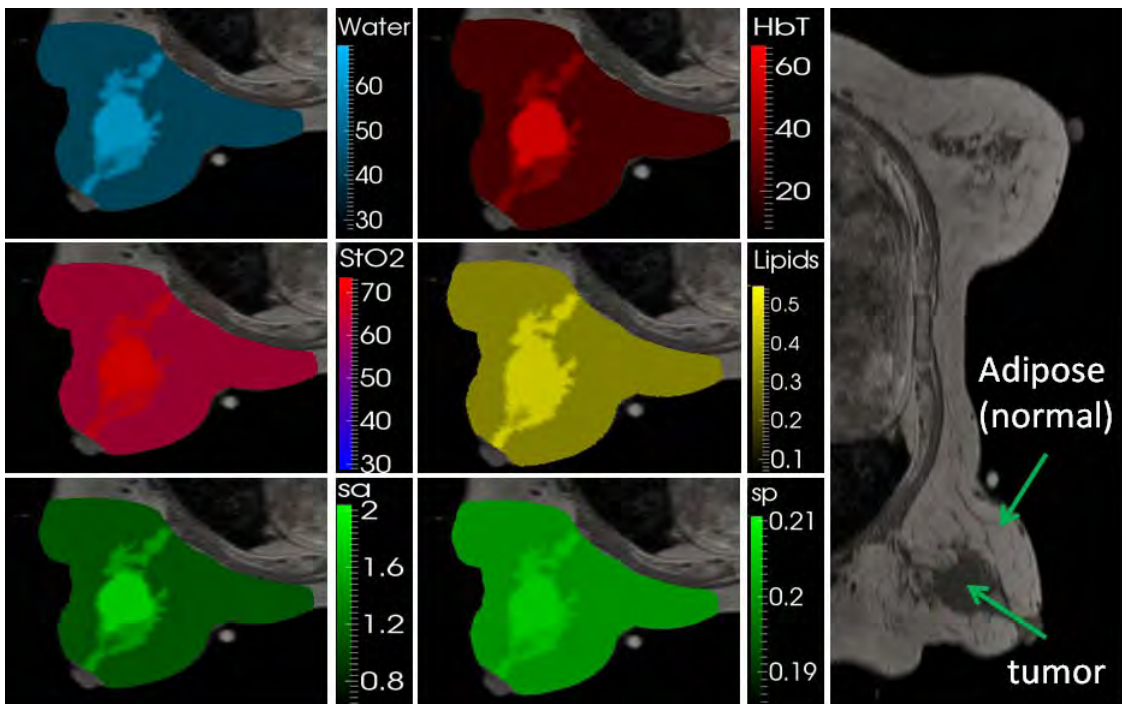


Figure 5.6: a representative case of a NIRS imaging showing a malignant tumor for patient #58 as confirmed by biopsy.

The plots in Figures 5.7 and 5.8 shows the chromophore values of the tumor and the normal tissue of patient #46 and patient #58 respectively. Table 5.1 below shows the contrast of these chromophores (tumor chromophore concentration/normal tissue chromophore concentration). HbT is simply the total hemoglobin defined as the concentrations of oxy-hemoglobin and deoxy-hemoglobin combined ( $HbT = HbO + Hb$ ), oxygen saturation is defined as the ratio of deoxy-hemoglobin divided by the total hemoglobin concentration ( $StO_2 = \frac{HbO}{HbT}$ ), the tissue optical index is defined as  $TOI =$

$$\frac{HbT * Water}{Lipid}$$

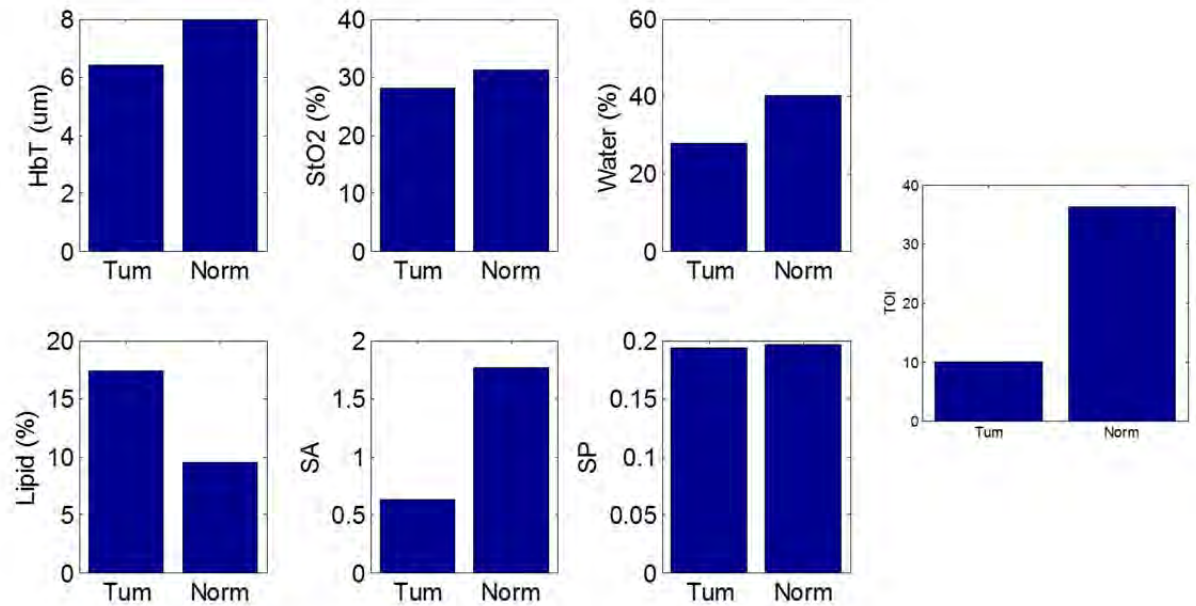


Figure 5.7: Total concentrations of HbT, StO2, water, lipid, SA, SP, and TOI of NIRS results of patient #46.

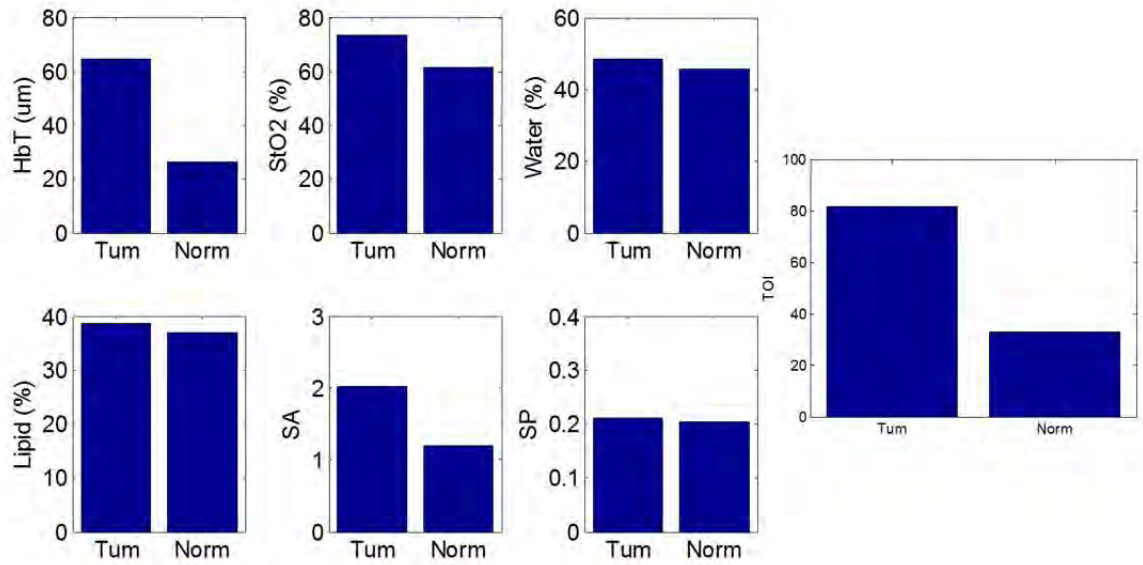


Figure 5.8: Total concentrations of HbT, StO<sub>2</sub>, water, lipid, SA, SP, and TOI of NIRS results of patient #58.

Chromophore	HbT	StO <sub>2</sub>	Water	Lipid	SA	SP	TOI
Patient #46 (benign)	0.8	0.9	0.68	1.82	0.35	0.98	0.28
Patient #58 (Malignant)	2.5	1.2	1.1	1.1	1.7	1	2.5

Table 5.1: Chromophore concentration of two representative cases of the breast cancer clinical trial.

## 5.6 Discussion and Conclusion

The hybrid frequency-domain continuous-wave system was validated using gelatin phantom experiments that were able to track the linear increase of blood inside a 2 cm inclusion in a pentagonal phantom that is specific to our clinical NIR-MRI breast coil. We found that contrast recovery was slightly lower than expected, but this is a known problem in diffuse optical tomography, and likely due to crosstalk between absorption and scatter [95] [96]. We found that the system displayed linear contrast recovery over a

wide range of hemoglobin concentrations with stability in the background. Our system was most accurate through the lowest concentrations, which have contrasts similar to what we expect to see in malignant breast lesions [95]. Several healthy volunteers have been imaged using this system and reconstructed with results consistent with past work and literature values[97] [98] [99]. The presented case shows elevated hemoglobin, oxygen saturation, water, and scattering parameters in the glandular tissue likely due to the higher cellular metabolism in the more complex tissue. Lipid content was higher in adipose region, consistent with our expectations [100].

Finally, the system was validated with cancer patients during a clinical trial that was performed in Xi'an, China. The results were very promising and demonstrated the validity of the system.

## CHAPTER SIX

### MRI Compatible Optical Detectors for In-Magnet Tissue Spectroscopy

#### 6.1 Introduction

Magnetic Resonance Imaging (MRI) is used to image soft tissue structure, functional blood flow parameters and vascular leakage patterns in patients. It has high sensitivity to malignancy but slightly lower specificity in the task of breast imaging [101]. In recent years, there has been interest in additional ways to increase the specificity of the MR information by adding optical absorption and scattering spectroscopy to the scanner. This hybrid approach would be similar to the way PET has been added to CT scanners as an option, and now PET can be added to MRI systems[102]. In particular, the added-value of optical spectroscopy would be in terms of the addition of hemoglobin, water and lipid sensing, which is especially important to the understanding of newer biological therapies[103]. One of the major technical challenges in combining MRI with optical spectroscopy is signal detection over the very wide dynamic range which is required with a source-detection configuration that is compatible with routine clinical use[104, 105], and an optical system coupling which is not overly sensitive to the tissue boundary. The challenge is made even more demanding by the intense magnetic field that exists as well as the electromagnetic interference that occurs from the radiofrequency (RF) pulses involved, such that special attention to system design is required in order to avoid performance degradation of either the MRI and Diffuse Optical tomography (DOT) imaging results.

MRI-guided near-infrared spectroscopic tomography (NIRST) for breast imaging has been investigated in a few pilot trials, and appears to have potential value in terms of

increasing the specificity of characterizing lesions[105-107]. The conceptual framework for the breast exam would be to deploy the standard MRI scan for its anatomic and blood flow leakage (dynamic contrast) images, which are then used as prior information for NIRST quantification of total hemoglobin, oxygen saturation, water and lipid content[107]. Simultaneous MRI/DOT measurements enable data sets to be directly coregistered and analyzed, and is technologically similar to designs of fNIRS studies which use multiple source-detector fibers placed on tissue in the scanner[108, 109]. Essentially all of the MR-compatible systems developed to date have relied on optical spectroscopy interfaces which use long fiber optic cables, similar to the system described in the previous chapter, to carry the light signal to and from the tissue of interest. Due to their bulk size, fragility, weight, and cost, the use of long fiber optic cables present a subtle but important impediment to a system design that is clinically practical.

In fact, the main disadvantage of the system described in the previous chapter is the lack of full breast coverage due to the nature of the fiber optic cable bundle. Complete breast coverage is essential since it is not feasible to image lesions outside the volume of projections of the measurements[110]. The breast interface described in the previous chapter, however, has 16 fiber optic cable bundles which are used to image a single plane of the breast as shown in figure 6.1.

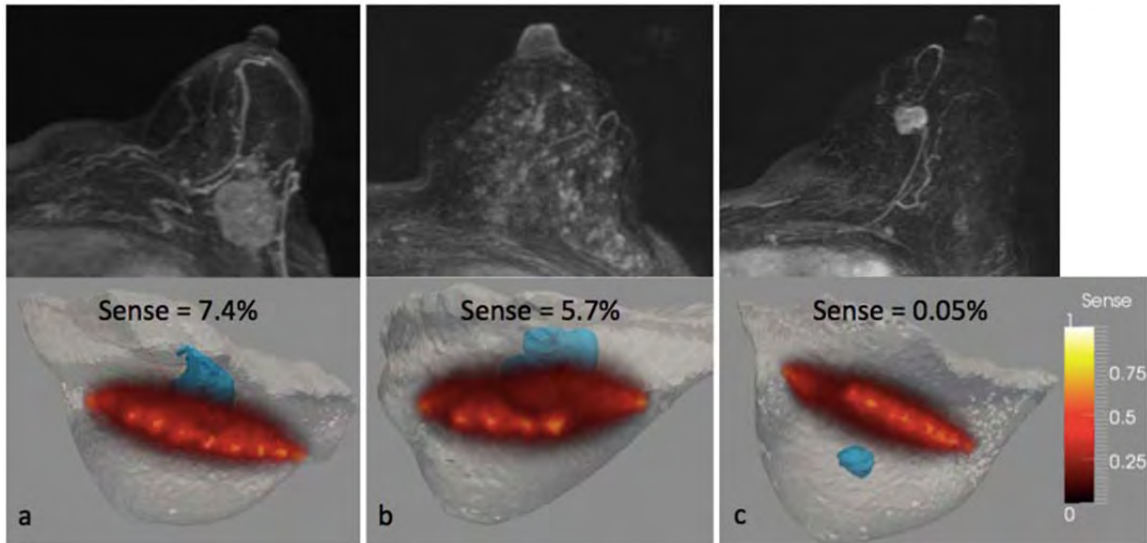


Figure 6.1: Images of 3 breast lesion cases are shown, with DCE-MRI scans shown as maximum intensity projection (MIP) images in the top row, and the overlay of the light sensitivity patterns in the bottom row for each corresponding case, along with the suspected lesion shown segmented in blue. If placement of the fibers is ideal, then there is good overlap over the lesion as shown in the two left cases, however the right case is an example of nearly no overlap for NIRS with the tumor.

Size and cost of the fiber optic cable bundles impose restrictions on the number of fibers that can be used. Aside from the cost factor, appending additional fiber optical cables creates a very large interface making handling and system set-up more challenging. While previous studies have examined ways to translate a single set of fibers along the breast in a parallel plate fashion [111], this process is not ideal, as it still requires the set of fibers, but also requires an extended compression of the breast in the MRI, which is thought to be undesirable for both comfort and blood flow concerns. Having numerous large fiber optics cables in multiple plans would also be unappealing from a workflow function perspective in the MRI suite. This is true even for our 16 fiber bundles where one patient decided against examination due to the discomfort brought by the large fiber

bundles that are connected to the breast interface. Taken together, these issues demanded us to consider a different design approach to NIRS measurement.

## **6.2 Solid State Detector System Design Approach**

A technological solution which would place sources and detectors directly on the tissue and utilize electrical (rather than optical) signal transfer through MRI compatible wires would be more desirable from a clinical perspective. One approach is to place detector modules directly inside the MRI, such as those built for the existing hybrid PET-MRI systems, which are not clinically available [112] [113] [114]. These detector modules include the light sensitive detector after the scintillator, as well as the associated front-end electronics for detector control and output signal amplification and shaping. However, due to the limited space of the MRI bore and the accompanying large size of detector modules, this approach is not ideal for building a system that has a large number of detectors for full breast coverage.

A slight modification to the approach above is to only place the detector inside the MRI while keeping the front-end electronics outside the MRI. This approach will simply tether the detector to the electronics via long electrical cables that will transmit the detector readout signal to the electronics located outside the MRI. The frontend electronics are necessary for the operation of these detectors. For example, as discussed in Chapter 2, the gain of a photodiode detector is one as it does not offer a way of multiplying the generated charge carriers. In order to fully exploit the sensitivity of a photodiode, it must be connected to an amplifier circuit that is optimally designed to amplify the generated current. Highly sensitive detectors, such as those used for low light level detection, require electronics to be as close as possible to the detectors in order

to avoid any degradation of signal-to-noise ratio [115]. While tethering of the electronics to the detectors via long electrical cables may be unorthodox and cause degradation of the signal-to-noise ratio, this approach enables the design of a system with a large number of detectors yet with a small overall footprint while keeping the system design simple and modular. Therefore, this approach was tested to determine the effect of tethering on the signal-to-noise ratio.

### **6.3 Detector Choice**

The intense magnetic field inside an MRI machine presents a challenge to the type of detector and/or electronics that may safely be allowed inside the MR bore. Typical human MRI magnets range from 1.5 to 7 Tesla, with most research based systems for breast imaging now being 3T. The choices of detectors is then governed by this, and specifically, ferrous-based materials such as iron, cobalt, nickel alloys, and most stainless steel materials are not compatible with these environments. Aside from causing image artifacts, these materials can be pulled toward the magnet source even at modest concentration, causing mechanical damage and/or harm to patients and staff. However today many solid state detectors have an active area which is largely silicon based and can be developed with non-ferrous leads.

In this development, vacuum-tube based sensors such as PMTs were eliminated from the choices, as the altered path of the generated charge carriers inside of the dynode chain eliminates the detector's function [116]. Instead, solid state semiconductor photon detectors are inherently MRI compatible and are the ideal choice [117]. The range of reasonable options includes 1) photodiodes (PDs), 2) avalanche photodiodes (APDs), 3)

charged coupled devices (CCDs), 4) single photon avalanche photodiodes (SPADs), and 5) silicon photo-multipliers (SiPMs).

The challenge with these types of detectors is their packaging, frontend electronics, and module housing – all of which is not usually MRI compatible. Electronic and amplifier circuits are typically made of silicon, iron, nickel and cobalt which are attached to the main body of the chip via silver-brazing. Frontend electronics is not a concern since the approach used here was to place the electronics far away from the MRI bore. Detector packaging, however, may be custom ordered or machined to maintain MRI compatibility. Since the goal here was a configuration with detectors placed inside the MRI and amplifier electronics placed outside the MRI, it was possible to eliminate CCD and SPAD detectors, leaving PDs, APD's, and SiPMs as the only viable options.

Using the equations from Appendix D regarding the signal to noise and NEP calculations for photodiodes and avalanche photodiodes, one can calculate the NEP for PD and APD detectors. The table below compares a PD and an APD with similar size. A bandwidth of 100 Hz was used along with a feedback resistor of 1 G, amplifier bias current of 1 pA and an amplifier input noise voltage of  $15\text{nV}/\text{Hz}^{1/2}$ .

<b>Parameter</b>	<b>Si Diode #1</b>	<b>Si APD</b>
<b>Sensitivity (S)</b>	0.6 A/W @ 960 nm	30 A/W @ 960 nm
<b>Dark Current (I<sub>dark</sub>)</b>	10 pA	1 nA
<b>Shunt Resistance (R<sub>sh</sub>)</b>	1 GΩ	N/A
<b>Shunt Capacitance (C<sub>sh</sub>)</b>	65 pF	40 pF
<b>Excess Noise Factor (ENF)</b>	1	3.7
<b>Gain (M)</b>	1	60

<b>NEP Detector</b>	$7 \times 10^{-14} \text{ W}_{\text{rms}}$	$8.6 \times 10^{-14} \text{ W}_{\text{rms}}$
<b>NEP Detector + Amp</b>	$1 \times 10^{-13} \text{ W}_{\text{rms}}$	$8.6 \times 10^{-14} \text{ W}_{\text{rms}}$

Table 6.1: Showing some of the key available specification parameters for the two detectors, a silicon photodiode and avalanche photodiode related to sensitivity of detection.

If one were to make a choice on the basis of NEP due to the combination of the detector and amplifier circuitry combined, one may consider the APD to be the ideal choice. However, as discussed in Appendix D, the APD requires a high-voltage ultra-stable power supply in order to bias the detector. Furthermore, the APD is very temperature sensitive. APD's also have a lower dynamic range compared to photodiodes and they cost much more. In fact, excluding the noise due to amplifiers, the NEP of photodiodes is slightly better than that of APDs due to the excess noise factor associated with APD detectors. If one were to include all these factors, a photodiode becomes the only clear option. Therefore, most work performed in this testing was with photodiodes and silicon photomultiplier detectors.

The aim of this chapter is to report on the performance of these two options MRI compatible detectors: PDs and SiPMs, when placed inside the scanner bore, while being connected via a long electrical cable to frontend electronics located outside the MRI room. Both detectors, which offer a compact form factor with high dynamic range, were directly compared with optimized amplifier designs, and their performance for tissue spectroscopy was compared. The usable dynamic range of these detectors was measured while they were tethered to an optimized amplifier circuit at the distal end of a transmission line. The effect of the long separation between the detector and frontend electronics was evaluated by comparing the dynamic range of the detectors when

connected directly to the frontend electronics relative to when connected through a long electrical cable. Phantom experiments were also performed in order to evaluate the performance of the detectors inside the MRI more fully.

### **6.3.1 Detector's Amplifier Circuitry**

Both detector types, the photodiode and the silicon photomultiplier, are silicon-based semiconductor detectors that generate a photocurrent as they are illuminated. Both detectors require an external amplifier to obtain the maximum signal to noise ratio and reach the highest sensitivity limits. As explained in Appendix D, a SiPM requires reverse biasing in order to operate. A photodiode, on the other hand, can be zero (forward) biased or reverse biased with each configuration yielding different advantages as will be explained below. In order to maximize the signal to noise ratio and obtain the highest sensitivity, a transimpedance amplifier (TIA) was used to amplify the detectors output.

A transimpedance amplifier is an amplifier configuration that is used to translate a current output signal into a voltage signal. This amplifier type is essential for circuits and instruments that can only accept a voltage input and must generate a voltage signal as an output.

A TIA can be built in several configurations and each configuration is marked by its own set of tradeoffs. Figure 6.2 shows the basic circuit where the gain is controlled by the feedback resistor,  $R_f$ .

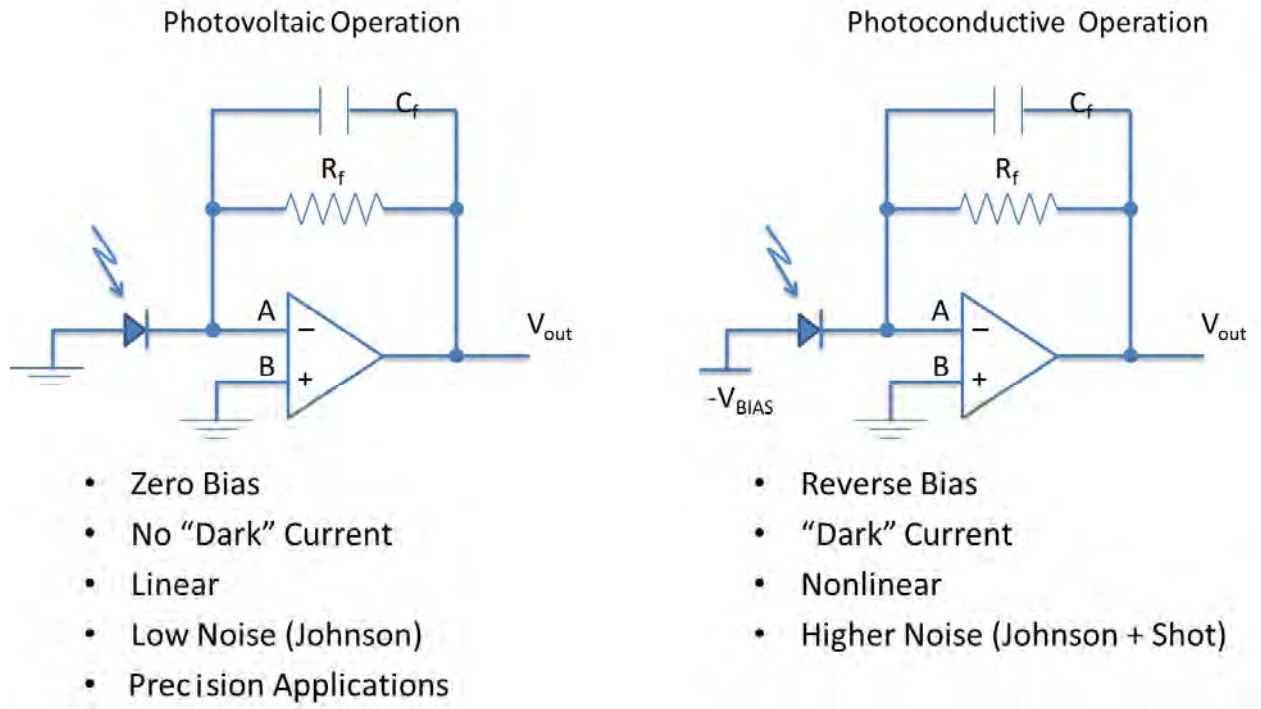


Figure 6.2 Basic simple TIA circuit for the two detectors, based upon a single amplification stage.

By connecting the photodiode as shown in figure 6.2(a), the photodiode operates in the photovoltaic mode. In this configuration, points A and B are forced to the same potential (0V) by the operational amplifier forcing the photodiode to be zero biased and thus, eliminating the possibility of dark current. In reality, however, the dark current does not completely disappear as the amplifier's input offset voltage will result in small error across the photodiode's terminals. This issue can be partially solved by selecting an amplifier with a very low input offset voltage.

By connecting the photodiode as shown in Figure 6.2(b), the photodiode operates in the photoconductive mode. In this mode, the photodiode is reversed biased via the voltage  $-V$ . This mode improves the bandwidth by lowering the junction capacitance of

the photodiode as explained in chapter XYZ. In both biasing schemes, the bandwidth of the setup can be calculated using:

$$f(-3dB) = \sqrt{\frac{\text{Amplifier Gain Bandwidth Product}}{4\pi * R_f * C_d}}$$

, where the amplifier gain bandwidth product is usually specified for a detector,  $R_f$  is the feedback resistance and  $C_d$  is the sum of the junction capacitance and the amplifier (common-mode + differential input) capacitance.

In the above circuit,  $C_f$  is used to prevent gain peaking of the amplifier. At low frequencies, the TIA inverting input is forced to be at the ground potential (point A = point B) and the current flows through  $R_f$ . At higher frequencies, the capacitor will affect the circuit response. A capacitor is necessary to prevent peaking of the amplifier. Selecting a large capacitor value results in better stability at the expense of a lower signal bandwidth. However, in this project, bandwidth is not critical as the photodiode is detecting light from a continuous-wave laser source operating at 0 or low frequency (<1 KHz). A low frequency modulation is possible, and even recommended in order to increase the signal-to-noise ratio as long as the modulation frequency is much lower than the 3dB cutoff frequency of the photodiode circuit. Modulation at frequencies higher than the 3dB cutoff frequency causes the amplifier to oscillate which may damage the amplifier and/or lead to wrong results.

$$C_f > \sqrt{\frac{C_s + C_i}{2 \cdot \pi \cdot R_f \cdot f_{opamp \ crossover}}}$$

Ideally, all the photodiode current flows through the feedback network. However, in reality, all op amps have input bias current that introduces error to the output.

Therefore, it is critical to choose an op amp with the lowest values possible for bias current and input offset voltage. The output voltage signal in the configuration above is simply:  $V_{OUT} = I_{Photodiode}R_F$

Dark current in a photodiode arises when the photodiode is reverse biased (voltage is applied across the photodiode). This dark current approximately doubles for every  $10^0\text{C}$  increase in temperature [118].

Operating in the photoconductive mode allows for higher speed operations compared to photovoltaic mode. However, even at such higher speeds, the photodiode bandwidth remains much lower than the bandwidth required for frequency domain DOT measurements ( $\leq 50\text{MHz}$ ). Also, with photoconductive mode, the dark noise becomes a big factor in decreasing the sensitivity of the photodiode. There is an additional advantage to operating in the photoconductive mode. Applying a reverse voltage is sometimes effective in enhancing the upper limit of linearity as shown in Figure 6.3.

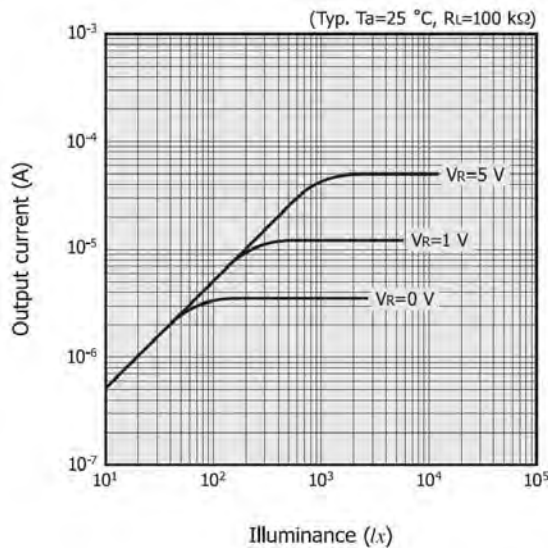


Figure 6.3 Output Current vs. illuminance for different reverse voltage values, illustrating the higher  $V_R$  can lead to higher dynamic range. [37]

The lower limit of the linearity of a photodiode is determined by the noise equivalent power (NEP) while the upper limit depends on the load resistance, reverse voltage, etc., and is given by the equation [37]:  $P_{sat} =$

$$\frac{V_{Bi} + V_R}{(R_s + R_L) * S_\lambda}$$

, where

$P_{sat}$  = the input energy at the upper limit of linearity in Watts ( $P_{sat} \leq 10mW$ )

$V_{Bi}$  = the contact voltage [V] (~0.2 to 0.3V)

$V_R$  = the reverse voltage [V]

$R_L$  = the load resistance [ $\Omega$ ]

$S$  = the photo sensitivity at wavelength [A/W]

$R_s$  = the photodiode series resistance [ $\Omega$ ]

However, NIRS applications suffer from lack of photons and require higher sensitivity for low light level detection. Since sensitivity is critical in NIRS, the photodiode was configured in a photovoltaic operation with zero bias, in order to minimize the noise and increase the sensitivity of the photodiode configuration. The SiPM detector, on the other hand, was operated in reverse bias configuration due to the working mechanism of the SiPM detectors.

The dynamic range of SiPM and PD detectors was measured while the detectors were placed inside the bore of the MRI magnet and the preamplifier circuitry was placed outside the MRI room. An eight meter cable was used to connect the detectors to the preamplifiers through a conduit in the MRI room wall. The detector was placed inside a light-tight box which had a small window that enabled the laser light to enter. A fiber optic cable was used to deliver the laser light to the detectors inside the MRI bore. The

detectors were evaluated using 661 and 948nm CW laser wavelengths. Different neutral density filters were placed in front of the laser source in order to attenuate the laser light. The detector output at each filter setting was recorded with a 16-bit 100KS/s PCI-6031E (National Instruments) data acquisition card. A schematic of the setup is shown in Fig. 6.4(a).

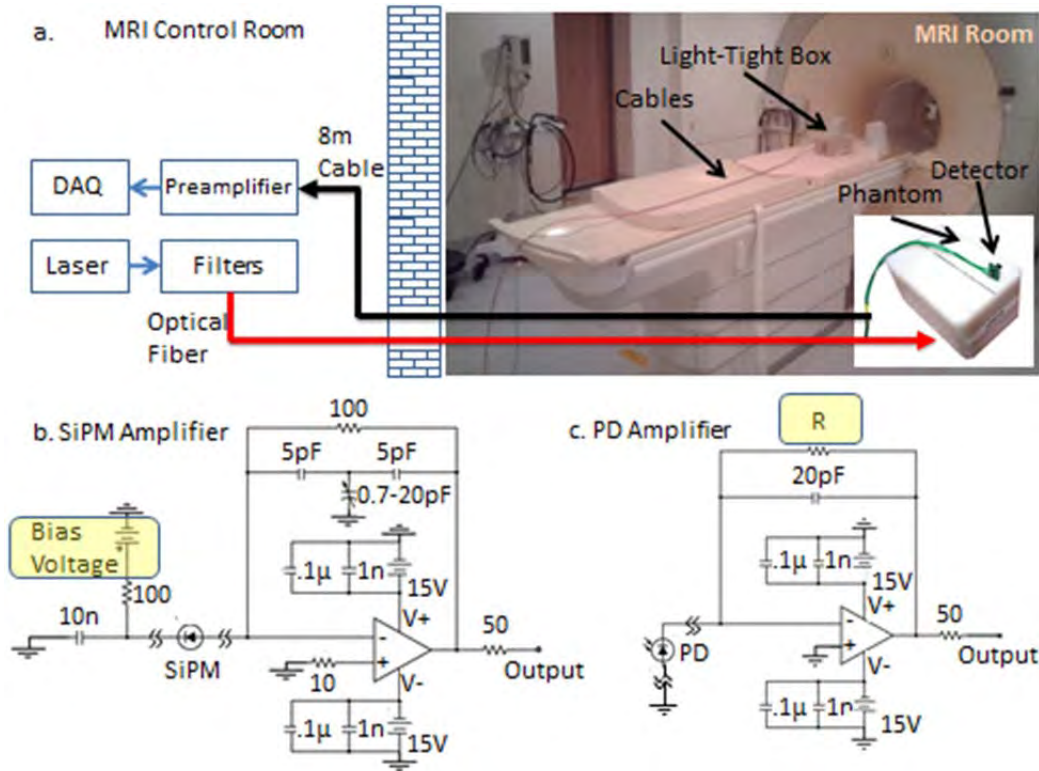


Figure 6.4: Illustration of the source-detector electronics with coupling into the MRI (a).

Electrical schematics of the optimized amplifier circuits used at the distal end of the cables to the SiPM (b) and PD (c) detectors are shown.

The SiPM detector used in this study was a  $3 \times 3 \text{ mm}^2$  sensor from AdvansID (ASD-RGB3S-P-50) with 3600 cells and a cell size of  $50 \times 50 \mu\text{m}^2$  with a 45% fill factor. The detector package was plastic with no ferromagnetic parts ensuring that the detector was MRI compatible. The SiPM detector was mounted on a surface-mount (SMT) to pin

converter socket (ASD-EP-S-3) to simplify prototyping. The photodiode detector was a PIN type photodiode from Hamamatsu Inc. (S5107-1369) with a  $10 \times 10 \text{ mm}^2$  active area. The detector was a surface mount type placed on a ceramic package and custom ordered through Hamamatsu Inc. to ensure MRI compatibility.

The SiPM detector was connected as shown in Fig. X.4(b). A variable power supply was used to bias the SiPM detector through a  $100 \Omega$  resistor at several bias voltages: 28 to 30.5V in 0.5V increments. A dual supply ultralow distortion, ultralow noise operational amplifier (AD797) was used in the inverting configuration to convert the detector current into an amplified voltage signal which was measured by the data acquisition board. The AD797 has a bias current of 250pA, very low noise of 0.9nV, low offset voltage of  $80 \mu\text{V}$ , a dual supply operating range from  $\pm 5\text{V}$  to  $\pm 15\text{V}$ , and a gain bandwidth product of 110MHz. The length of the wire (cable) between the SiPM (inside MRI magnet) and other electronics (in MRI console room) was 8 meters.

The photodiode detector was operated in a zero bias configuration for excellent linearity and low dark current as shown in Fig. X.4(c). The amplifier chosen for this task is the OPA827; a JFET operational transimpedance amplifier with a low bias current of 3pA, very low noise of  $250\text{nV}_{\text{pp}}$ , low offset voltage of  $150 \mu\text{V}$ , a dual supply operating range from  $\pm 4\text{V}$  to  $\pm 18\text{V}$ , and a gain bandwidth product of 22MHz. The amplifier does not require symmetrical power supplies as it only requires a minimum supply voltage of 8V, thus, increasing the performance of the amplifier against fluctuations and spikes due to the power supply.

The gain of the amplifier circuit was set by using different feedback resistor values: 10K, 100K, 1M, 10M, 100M, and 1G $\Omega$ . The laser power was measured via a calibrated Hamamatsu power meter.

### **6.3.2 Dynamic Range**

The dynamic range as a function of incident light power for the SiPM is shown in Fig. x.5(a). The blue markers represent the 661nm laser light while the red markers represent the 948nm counterpart. Three different bias voltages are shown: 28 (triangles), 28.5 (circles), and 30.5 V (squares). These results were obtained by placing the detector inside the MR and connecting it to the preamplifier circuitry outside the MRI room using the 8 meter electrical cable. Depending on the bias voltage, the dynamic range extended from  $\sim 10$  pW to  $\sim 100$   $\mu$ W. The results for measuring the dynamic range of the detector when connected directly to the operational amplifier were identical to the results using the long cable. The cable length between the detector and the preamplifier did not affect the sensor sensitivity or its dynamic range.

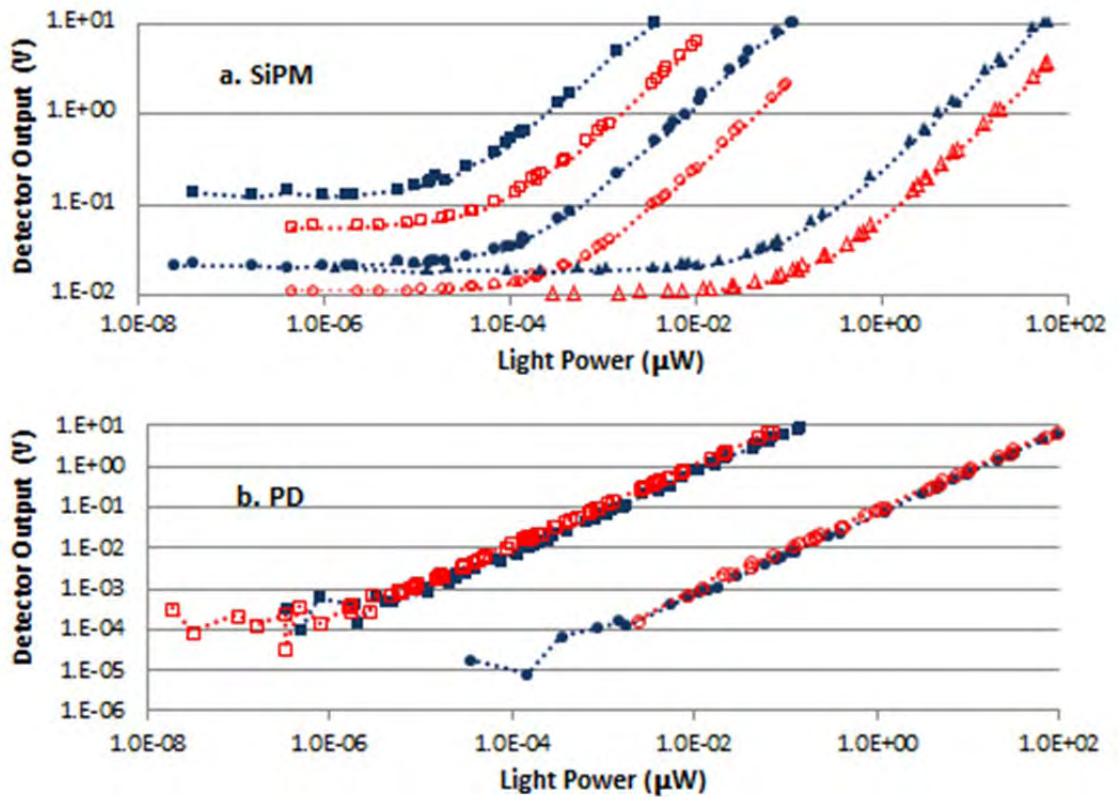


Figure 6.5 In (a) the responsivity of the SiPM detector connected via a long cable is shown at different amplifications from bias voltages. The low, medium and high amplification values correspond to bias values of 28V (triangles), 28.5V (circles), and 30.5V (squares). The solid (blue) symbols denote the 661nm wavelength response while the open (red) denote 948nm. In (b) the response of the PD detector is shown using different amplifications, by varying the feedback resistance. Low gain was produced with feedback of 100K  $\Omega$  (circles) and high gain at a feedback of 100M  $\Omega$  (squares).

The dynamic range for the photodiode detector is shown in Fig. 6.5(b) where the PD was located inside the MRI scanner and was tethered to the amplifier circuitry outside the MRI room using the long electrical cable. Two wavelengths are shown: 661 (blue) and 948 nm (red). The dynamic range of the setup depends on the gain of the amplifier

circuit and extends from  $\sim 1$  pW to  $\sim 100$   $\mu$ W. The circles in Fig. X.5(b) represent a feedback resistor gain of  $100\text{K } \Omega$  while the squares show data for a feedback resistor gain of  $100\text{M } \Omega$ . The dynamic range results of the detectors tethered via the 8 m cable matches the results of the detector directly coupled to the amplifiers for all feedback resistor gain values up to  $100\text{M } \Omega$ .

### **6.3.3 Phantom Testing**

A rectangular silicon phantom was used to simulate a breast optical tomography experiment. The laser light was incident on the bottom surface of the phantom and the photon detectors were placed one-at-a time on the top surface of the silicon phantom at nine different source-to-detector distances. We also used our existing PMT-based MR-compatible imaging system, which uses 12 m fiber optic cables to carry the light signal from the phantom to the detector, in order to evaluate and compare the results of the solid state detectors to those of the PMT. The phantom experiment was carried out with two different laser wavelengths – 661nm and 948 nm – in order to study the effect of the longer wavelengths on the photon detectors. The results using the PD, SiPM and PMT detectors for 661 nm laser light are shown in Fig. X.6(a). Fig. X.6(b) shows the attenuation of the 948 nm laser light as a function of distance for the PD and SiPM detectors.

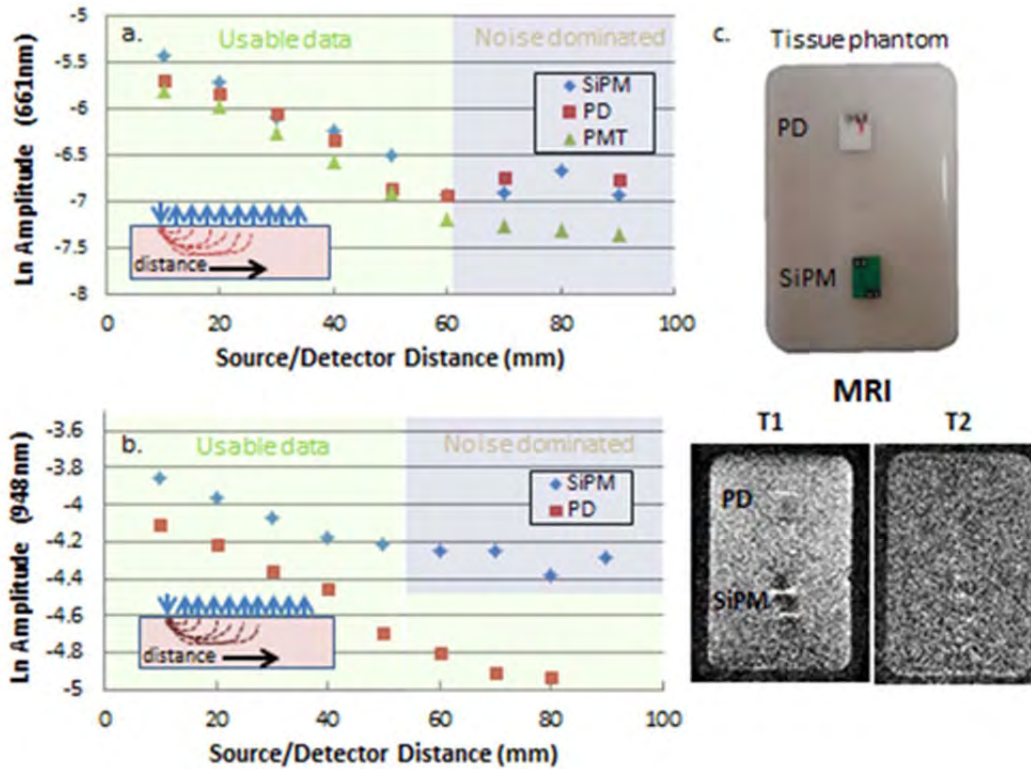


Figure 6.6 Tissue phantom measurements using the PD, SiPM, and a fiber-optic coupled PMT for the 661nm laser (a) and PD and SiPM for the 948nm laser (b). Note the PMT used cannot detect light at 948nm, so was not included. Photo (top) and MRI scan (bottom) of the detectors mounted on the silicon phantom is also shown (c).

#### 6.3.4. MRI Testing

T1 and T2 MRI sequences of the silicon phantom were obtained with and without the detectors mounted in order to study the effect of the detectors on the quality of the MRI signal. The phantom was placed inside a RF head coil in the MR room. A T1 MRI sequence with detectors mounted on the phantom showed minor artifacts for the SiPM detector (SNR = 2.6 dB) compared to the PD (SNR = 3.4 dB) whereas a T2 sequence showed no obvious artifacts as shown in Fig. X.6(c). The detectors were also tested while concurrently performing a MRI scan, and the RF pulses generated during the scan

induced electromagnetic interference in the electrical cable leading to the preamplifier circuit which caused saturation of the output signal.

## 6.4 Other detectors

It is worth mentioning at this point other detectors that were evaluated while searching for the best detector. Detectors from Hamamatsu and Excelitas were purchased and tested in a similar fashion to the detectors discussed in this chapter. The table below provides a quick comparison of these detectors.

<b>Detector Type</b>	<b>Manufacturer</b>	<b>Size (mm<sup>2</sup>)</b>	<b>Min Sensitivity</b>	<b>Operate above 900nm</b>	<b>Price for 100 pieces (\$)</b>
SiPM	AdvansID	3x3	10pW	No	2,858
SiPM	Excelitas	6x6	1pW	No	20,800
SiPM	Hamamatsu	3x3	10pW	No	20,000
PD	Hamamatsu	10x10	1pW	Yes	24,000
PD	Advanced Photonix	8.8x9.8	10pW	Yes	2,674

**Table 6.2 Photodetector evaluated**

Aside from the price difference, the Hamamatsu SiPM detectors tested were much noisier than the Advanced Photonix counterpart.

## 6.5 Conclusion

This study focused on the feasibility of using PDs and SiPMs inside the MRI bore for development of a hybrid MRI/DOT system that efficiently and cost-effectively covers the tissue of interest with an easily adaptable profile. Although the primary use of SiPM detectors has focused on photon burst counting in PET [119], the results indicate that these detectors are also suitable for light detection in the CW regime.

As can be seen from Fig. X.5(a), the SiPM dynamic range is controlled by the applied bias voltage, with internal gain increasing with the setting. Higher bias voltages result in an increase in dark current as indicated in Fig. X.5(a) with a bias of 30.5V. Also, Fig. X.6(a) shows the response of the SiPM to two different laser wavelengths, confirming that it is less sensitive to longer wavelengths. This outcome agrees with the photon detection efficiency (PDE) of the SiPM detector where, similarly to PMT detectors, the SiPM PDE drops off rapidly in the NIR wavelengths. This feature is unfortunate for applications where spectroscopy of water or lipids may be valuable.

Cable length did not affect the sensitivity or dynamic range of the SiPM measurements which agrees with an earlier study by Kang et al. [119] investigating the photon counting behavior (energy resolution and timing) of the detector. This insensitivity to cable length can be explained, in part, by the operational behavior of the SiPM detector in which each photon generates an avalanche of electrons that can be easily identified and measured, and by the high impedance cables used.

The dynamic range of the PDs depends on the feedback resistor value, and as can be seen in Fig. X.6(b), extends from  $\sim 1$  pW up to  $\sim 100$   $\mu$ W. Furthermore, connecting the photodiode directly to the preamplifier circuitry produced results that were the same

as those obtained when using the long cable to connect the detector to the amplifier. Feedback resistor values greater than  $100\text{M } \Omega$  resulted in saturation of the circuit due to line voltage AC noise, and could possibly be limited by further pre-filtering. The AC noise was apparent with all feedback resistor values greater than  $10\text{M } \Omega$  but dominated the measurements for resistor values greater than  $100\text{M } \Omega$ . For resistor values between  $10\text{M } \Omega$  and  $100\text{M } \Omega$ , the average DC value was linearly correlated with the light signal despite the presence of a strong AC signal. Although higher feedback resistor values would yield better sensitivity below  $1\text{ pW}$ , large gains would not be functional for long separations between the detector unit and the preamplifier circuit. This problem was not evident with the SiPM detector since the feedback gain resistor was much lower ( $100\text{K } \Omega$ ).

T1 and T2 images with the detectors mounted on a silicon phantom were acquired to observe their effects on MRI image quality. The T1 scan showed negligible artifacts when the SiPM detector was present whereas a T2 scan showed no artifacts as indicated in Fig. X.6(c). However, the artifacts observed are attributed to the SiPM socket into which the detector was mounted. The detectors were also operated concurrently with the MR scan, and the resulting RF pulses were picked up by the long cable and amplified causing preamplifier saturation during the RF pulse generation. Synchronization of the optical acquisition to activate the detectors between the RF-pulses generated during an MRI scan would be possible in order to avoid signal saturation. Another possibility is to properly shield the cables in order to minimize interference.

Finally, the response of the detectors for light traveling through a tissue mimicking silicon phantom yielded the same behavior for the  $661\text{ nm}$  laser light. For

comparison, we acquired data with our current MR-compatible system which uses long fiber optic cables and PMT detectors in order to validate and compare the results for all detectors. Since the PMT response drops off rapidly for wavelengths longer than 850nm, only the 661 nm laser data was evaluated in this comparison. As shown in Fig. 6.6(a), the three detectors have essentially an identical response. At 948 nm, however, the data in Fig. 6.6(b) indicates that the PD provides greater sensitivity which was also evident from the dynamic range results presented in Fig. 6.5(b).

An advantage of the PD is its higher sensitivity at longer wavelengths which is ideal for recovery of water and lipids with DOT, since the spectral features of these absorbers are more prominent at longer wavelengths. However, the SiPM has better response time allowing laser modulation for frequencies up to 10MHz compared to around 1Mz for the PIN type PD. In either case, the detectors would not allow frequency domain NIRST techniques since modulation frequencies greater than 50 MHz are required. Frequency domain or time-resolved DOT techniques have some advantage over their CW counterparts because the data are able to separate the effects of the scattering and absorption of light in tissue.

No cooling of the detectors was necessary and the circuits used to control and amplify the signals were simple and cost effective which would allow scale-up to large arrays of detectors. The sensitivity limits of both detectors are essentially identical if one were to consider the size of each sensor.

## CHAPTER SEVEN

### Design of a multichannel MRI compatible tomography system

#### 7.1 Introduction

Diffuse optical tomography (DOT) is being investigated for a potential clinical and pre-clinical imaging tool for breast cancer characterization. A number of hybrid systems have been developed that combine DOT with other imaging modalities including x-ray mammography [120], ultrasound [121] [122], and MRI [123] [124] where anatomical details are combined with the function information obtained from DOT. However, it is common in most of these systems that there is a limited data set, due to the small number of sources and detectors that can be placed on the surface of the tissue, and so this renders image reconstruction quality to be very limited in terms of spatial resolution and accuracy. Furthermore, DOT imaging is limited by breast coverage issues, which means most systems only cover part of the breast, leaving out areas not imaged from the field of view. Use of large detector arrays would improve the image reconstruction as well as the ability to provide more comprehensive 3D coverage if a creative way to cover the tissue was found.

In order to obtain the largest data set possible, a large number of sources and detectors must be used for imaging. This can present a problem if adding sources and detectors will drive the cost of the system beyond a reasonable level. This is especially true for systems that use frequency-domain or time-domain techniques for DOT, where each channel is bulky and expensive. The problem is complicated even further by the imaging speed; more sources and detectors require more imaging time. Therefore, it is

essential to have a system that can acquire a large data set at fast imaging speeds yet is able to maintain a low cost to allow the system to be clinically practical.

The problem becomes more complicated when coupled to a different modality, where both modalities need to be co-registered and ideally acquisition is simultaneous from both modalities, preserving the shape and geometry of the breast and simplifying the co-registration process.

Simultaneous acquisition puts a burden on the type of DOT detectors used. For example, MRI-coupled DOT will require detectors that have no crosstalk with the large magnetic field of the MRI, X-ray mammography coupled DOT will require detectors that are insensitive to the X-ray radiation, etc. In this chapter, an MRI-coupled DOT prototype based on photodiode detectors which were evaluated in the previous chapter was designed and built. The design and characterization of the 64-channel prototype is described in detail. Finally, ink-based and blood-based phantom experiments were performed to test the system's performance.

## **7.2 System Design**

The 64-channel photodiode-based system consisted of photodiode detectors, programmable amplifiers, data-acquisition (DAQ) board, and shielded electrical cables. A description of each of the units follows.

### **7.2.1 Detectors**

The previous chapter compared the setup of two MRI-compatible detectors: a photodiode and a silicon photomultiplier. While both detectors have very similar characteristics, a major advantage of the photodiode detector is its higher sensitivity at longer wavelengths which is crucial for the recovery of water and lipid contents with

DOT, since the spectral features of these absorbers are more prominent at longer wavelengths. Also, adding light sources at longer wavelengths would be a benefit in the ill-posed reconstruction problem, since this issue is complicated further by using steady-state DOT rather than frequency or time-domain DOT techniques. Therefore, photodiode detectors were chosen for the design of the in-magnet multichannel prototype.

The photodiode in the previous chapter was a custom made variation of an already existing photodiode produced by Hamamatsu: S5107 shown in Figure 7.1. The custom made version, S5107-1369, is a ferromagnetic-free design rendering the detector compatible with the MRI, as supplied by Hamamatsu. Unfortunately the price of this custom detector was more than 10 times the price of the off-the-shelf version (\$37 vs \$416), prohibiting large purchases for a low-cost multichannel system.

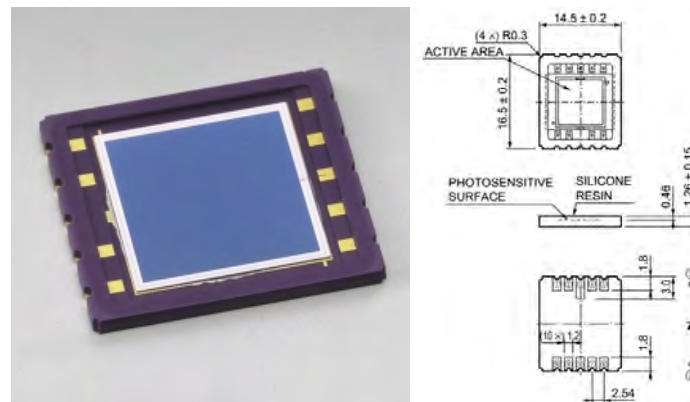


Figure 7.1: S5107 Hamamatsu Photodiode Detector is shown with design schematics of the packaging.

Our major challenge was to ensure the detector chosen had no ferromagnetic parts. Depending on the manufacturing process, photodiode manufacturers do not explicitly state the types of materials used in the fabrication process. Therefore several potential alternatives to the Hamamatsu detector were bought and tested. The detectors bought either had glass packaging or no packaging at all. After trying several different potential

detectors (PDB-C613-2-ND, PDB-C10-ND, 475-1429-ND, PDB-C156-ND), we found a Single-Element Silicon Pin Photodiode detector (PDB-V609-3) manufactured by API Advanced Photonix, Inc that meet the needs. These are red-enhanced photodiodes that come in buss wire leads and without any packaging material. The photodiode active area is  $6 \text{ mm}^2 \times 7 \text{ mm}^2$  with a cut-off frequency of around 100 KHz and an NEP value of  $\sim 1 \times 10^{-13} \text{ W/Hz}^{1/2}$ . The sole distributor of these detectors is Digi-key Corporation, and a photo of one of these photodiodes is shown in Figure 7.2.

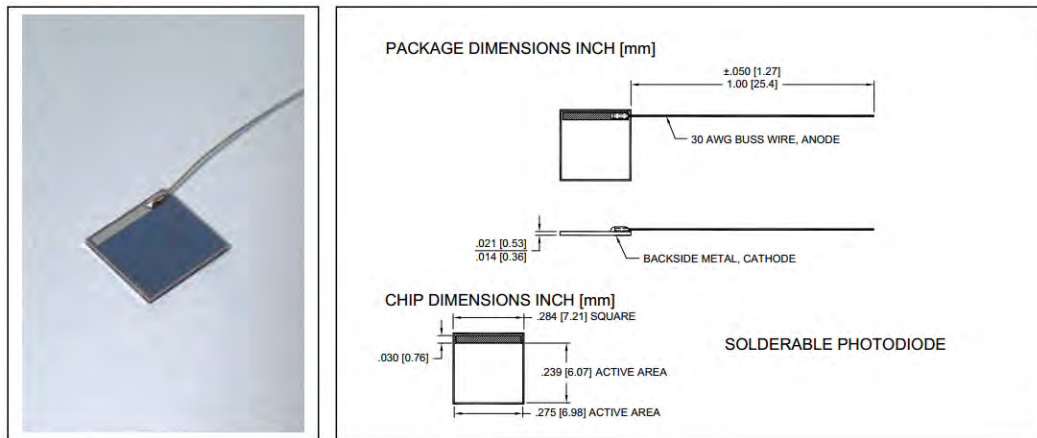


Figure 7.2: PDB-V609-3 Photodiode by API Advanced Photonics, Inc, along with package schematic at right.

MRI images of both detectors were acquired using the four MRI sequences that are typically used during a breast MRI examination. The detectors were mounted on top of a water-filled bottle that is routinely used for MRI calibration. Figure 7.3 (a – d) shows 3D surface rendered images of the MRI results whereas Figure 7.3 (e – f) shows the coronal view. These figures show that the API detector has less MRI artifacts as compared to the Hamamatsu detector. Also, it is important to note that MRI compatibility does not always mean no presence of artifacts as can be explicitly shown in both figures. Both detectors are MRI compatible, however, the MRI sequences that are

used in breast examination are sensitive to these detectors and do exhibit a slight artifacts, as is discussed later. The depth of the artifacts seen here was 12 – 15 mm for the Hamamatsu detector and 6 – 9 mm for the API detector.

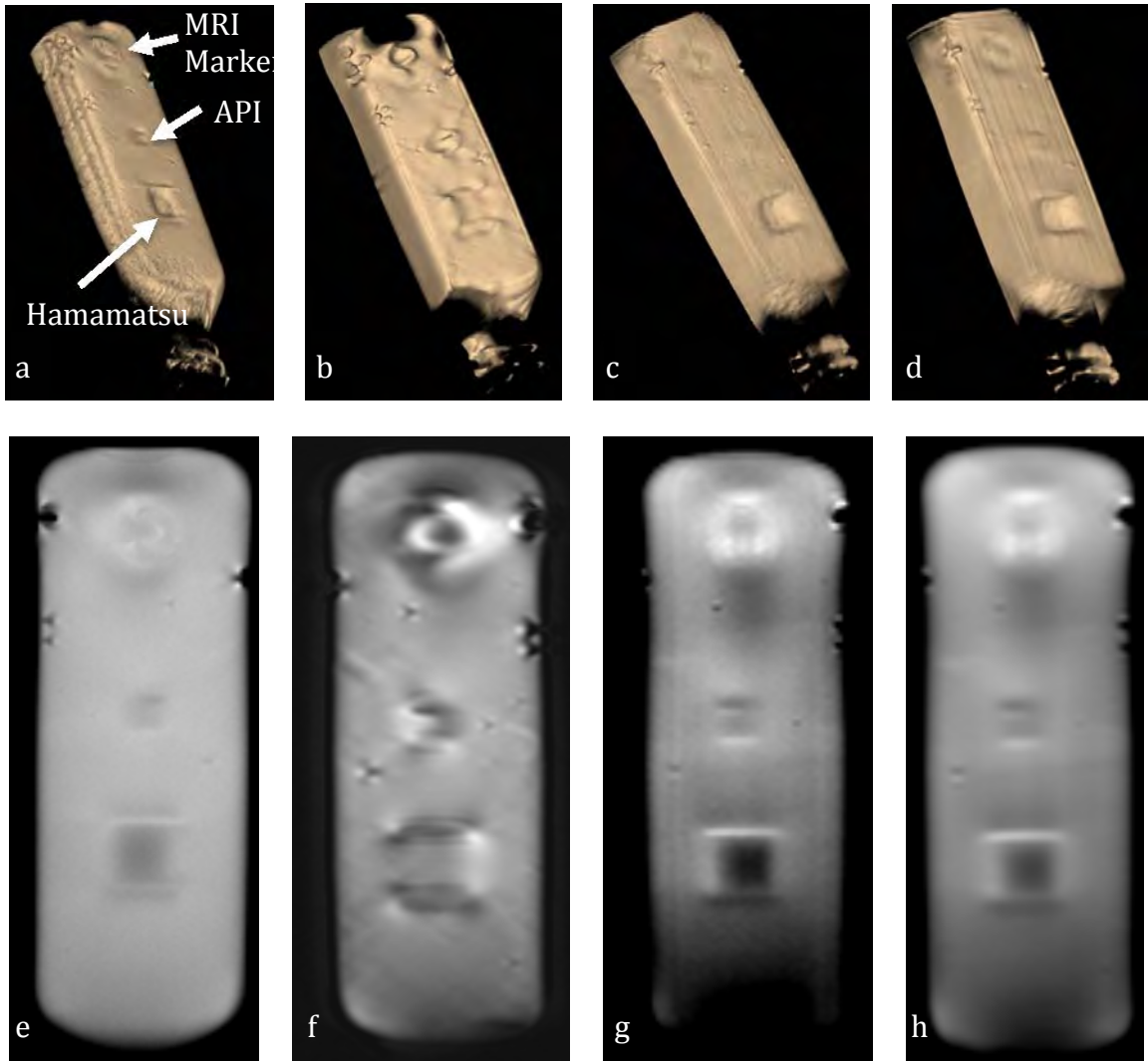


Figure 7.3 (top row) 3D MRI surface rendered images of the API and Hamamatsu detectors using (a) thrive MRI sequence, (b) FFE MRI sequence, (c) T2 – TSE MRI sequence, (d) T1 – TSE MRI sequence, (bottom row) MRI coronal view of the API and Hamamatsu detectors using (e) thrive MRI sequence, (f) FFE MRI sequence, (g) T2 – TSE MRI sequence, (h) T1 – TSE (MRI sequence).

Finally, the Hamamatsu detector has an NEP value of  $\sim 1 \times 10^{-14} \text{ W/Hz}^{1/2}$  while the API detector has an NEP value of  $\sim 1 \times 10^{-13} \text{ W/Hz}^{1/2}$ . The higher NEP value of the Hamamatsu detector is in part explained by the slightly bigger size of the detector compared to that of the API ( $10 \times 10 \text{ mm}^2$  vs  $6 \times 7 \text{ mm}^2$ ), which is therefore able to collect more light. However, the NEP difference is not great one and similar results can be achieved with both detectors. Thus, the API detector has the advantage of being cheaper and causes less image artifact on the MRI images yet has a sensitivity close to the Hamamatsu detector. Therefore, we have chosen the API detector for building our multichannel prototype.

### **7.2.2 Photodiode Circuit**

Photon detection in DOT experiments demand high performance detectors as tissue absorption may reduce optical signals by approximately 10-fold per centimeter of tissue for light in the red to near-infrared part of the spectrum. The transmitted optical power through tissue in optical tomography depends on the tissue type, source strength, and source-detector separation and may range from milli-watts up to femto-watts giving a dynamic range of  $10^{12}$ .

The NEP value of the chosen photodiode was  $1 \times 10^{-13} \text{ W/Hz}^{1/2}$  and thus, this detector has a lower limit of detection of 0.1pW of input light after a half-second integration time. However, as discussed in chapter 1, photodiodes offer no gain mechanism and one needs to amplify the output of the detector in order to be able to record the signal. In the previous chapter, a transimpedance amplifier circuit was used to amplify the detector output where two different feedback resistors were used to maximize the dynamic range of the detector/amplifier combination:  $100\text{K}\Omega$  and  $100\text{M}\Omega$ . The  $100\text{K}$

$\Omega$  enabled a dynamic range from  $\sim 1$  nW to  $\sim 100$  uW while the  $100\text{M}\Omega$  enabled a dynamic range from around  $1$  pW to  $0.1$  uW. The full dynamic range of using these two feedback resistor values was  $10^8$  (160dB).

Different feedback resistor values are needed to extend the photodiode acquisition dynamic range. But since the same photodiode detector will experience light at different magnitudes, the feedback gain resistor could not be hard wired, and a programmable-gain TIA should be used that allows for different gains depending on the incident light level.

There are two approaches that can be used for the design of a programmable TIA: 1- the TIA can be followed by a programmable gain amplifier (PGA) stage as shown in in Figure 7.4 (a) or 2- the varying gain can be implemented directly from the TIA itself as shown in Figure 7.4 (b).

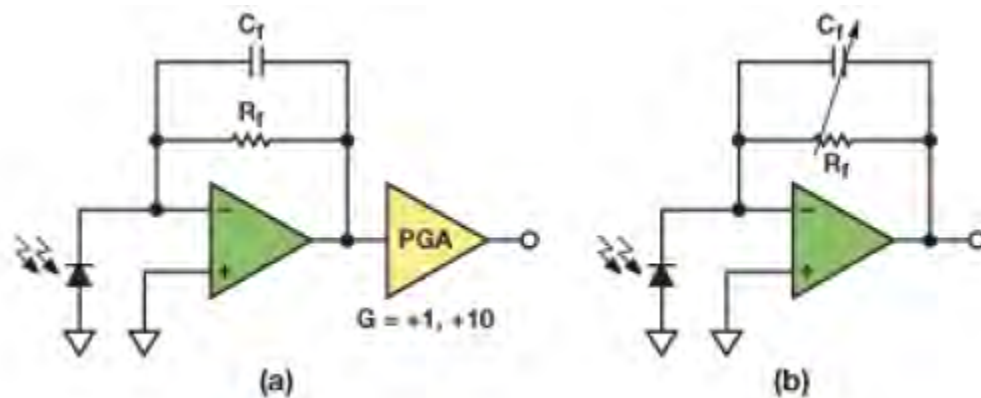


Figure 7.4 (a) programmable gain functionality implemented using a dedicated programmable gain amplifier (PGA), (b) or by varying feedback network ( $R_f$  and  $C_f$ ).

Incorporating the PGA stage directly right after the TIA has the advantage of simplifying the TIA design. This approach is necessary to optimize the performance of the analog-to-digital (ADC) converter that usually follows the PGA. However, any noise generated by the TIA will also be amplified with the PGA. On the other hand,

implementing the PGA directly from the TIA will increase the signal-to-noise ratio of the output signal by amplifying the signal from the detector directly. Any noise generated by the TIA itself will not be amplified.

The chosen design for our multichannel prototype is a combination of both types of amplifiers; a PGA was implemented directly on the TIA along with an additional PGA stage immediately after the photodiode TIA as shown in Figure 7.5. The PGA functionality on the TIA was implemented using a mechanical relay switch which alternated between the two feedback resistor values ( $100\text{K}\Omega$  and  $100\text{M}\Omega$ ). The relay switched only between two feedback resistors where the feedback capacitor remained constant for both feedback gain values.

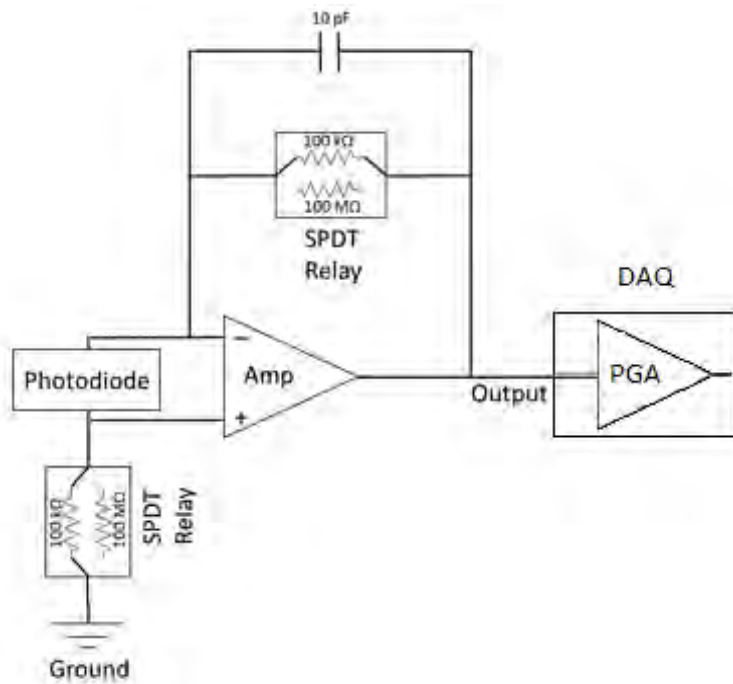


Figure 7.5: Schematic diagram of the photodiode circuit showing implementation of the gain changing mechanism via the SPDT relays.

The PGA amplifier stage following the TIA was implemented using the data acquisition (DAQ) card (PCI-6031E) which contained an on-board programmable gain instrumentation amplifier referred to as NI-PGIA. The NI-PGIA is a measurement and instrument class amplifier that guarantees minimum settling times at all gains. It is used to amplify an analog input signal to ensure that the maximum resolution of the analog-to-digital converter (ADC) is used. This amplifier delivers a 16-bit digital signal and can be programmed with a different polarity and range for each of the 64 analog input channels of the DAQ card. Table 7.1 below shows the input ranges and polarities that may be used with the NI-PGIA. The amplifier had a 1nA bias current and 2nA offset current.

(Software selectable per channel)

Analog Input Range	Gain	Polarity	Precision ( $\mu\text{V}$ )
0 to +10V	1	Unipolar	153
0 to +5V	2		76.3
0 to +2V	5		30.5
0 to +1V	10		15.3
0 to +500mV	20		7.63
0 to +200mV	50		3.05
0 to +100mV	100		1.53
-10 to +10V	1	Bipolar	305
-5 to +5V	2		153
-2 to +2V	5		61
-1 to +1V	10		30.5
-500 to +500mV	20		15.3
-200 to +200mV	50		6.1
-100 to +100mV	100		3.05

Table 7.1: Polarity and input ranges of the signals that can be used with the NI-PGIA of the PCI-6031E data acquisition card

A current-to-voltage transimpedance amplifier is extremely sensitive to external electrostatic and RF noise due to its very high resistance. Shielding and careful attention to ground is very important for applications requiring high sensitivity. The

transimpedance circuit shown in the previous chapter works well but was found to be sensitive to the 60 Hz ac signal caused by the power lines. The output of the circuit at high gain is shown in Figure 7.6 (a). The figure shows that the output of the circuit is saturated due to the sinusoidal AC signal. However, the circuit continued to work well for low light level signals and maintained linearity up to 1pW of DC light power. This was achieved by simply averaging the output despite saturation.

In order to protect the amplifier from saturation and extend its life further, a new design was used that exploits the differential input capability of the operational amplifier and reduces external noise caused by power line interference. Since the photodiode produces a signal in terms of current, the output current is available at both terminals of the sensor and can drive both inputs of the amplifier. By driving both inputs of the amplifier, external noise sources appear on both terminals of the amplifier. Since an amplifier functions by maintaining the same signal at both terminals, the noise will therefore effectively be eliminated.

The final design of the transimpedance amplifier circuit, shown in Figure 7.5 connects the cathode of the photodiode to the positive terminal of the amplifier as opposed to being connected directly to ground. The output of the circuit at high gain setting is shown in Figure 7.6 (b). The 60 Hz still exists but does not cause saturation of the amplifier circuit. Averaging the DC signal of the output continues to reflect an accurate reading of the input light signal.

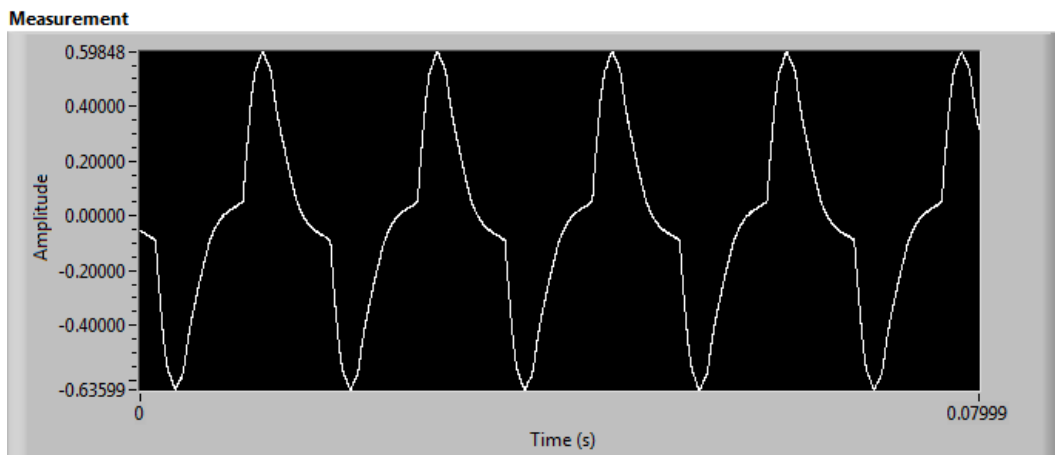
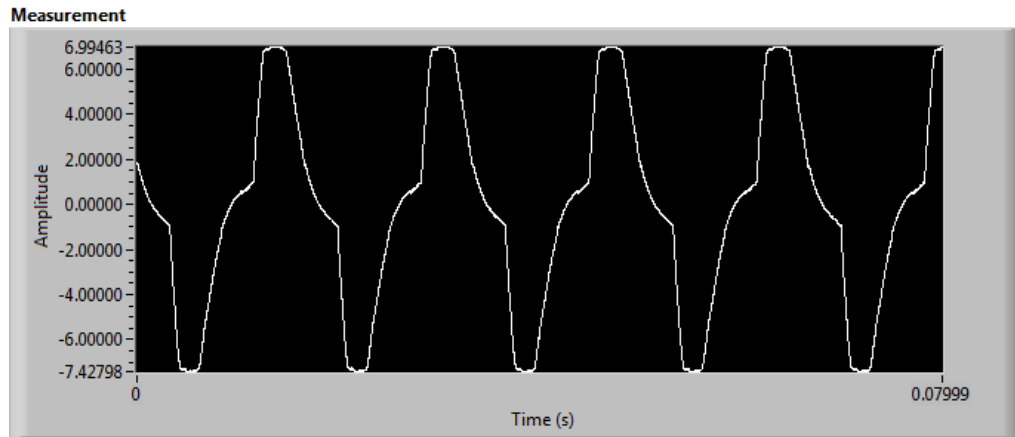


Figure 7.6 (a) Saturation of photodiode output at high gain setting due to the 60 Hz frequency signal caused by power line interference for the photodiode circuit shown in Figure 6.2, (b) Photodiode output at high gain setting for the same input signal but for the modified circuit shown in Figure 7.5.

Finally, the need for dual relays for each photodiode was evaluated by testing the circuit with only the main feedback resistor relay and using a constant resistor connected to the positive terminal as shown in Figure 7.7 (a), and then by using dual relays as shown in Figure 7.7 (b). The output of both circuits as a function of incident light power is shown in Figure 7.8. Light was incident on the photodiode where natural density

filters were used to attenuate the light level. As can be seen from figure 7.7, using dual relays enables a greater dynamic range than using a single relay alone.

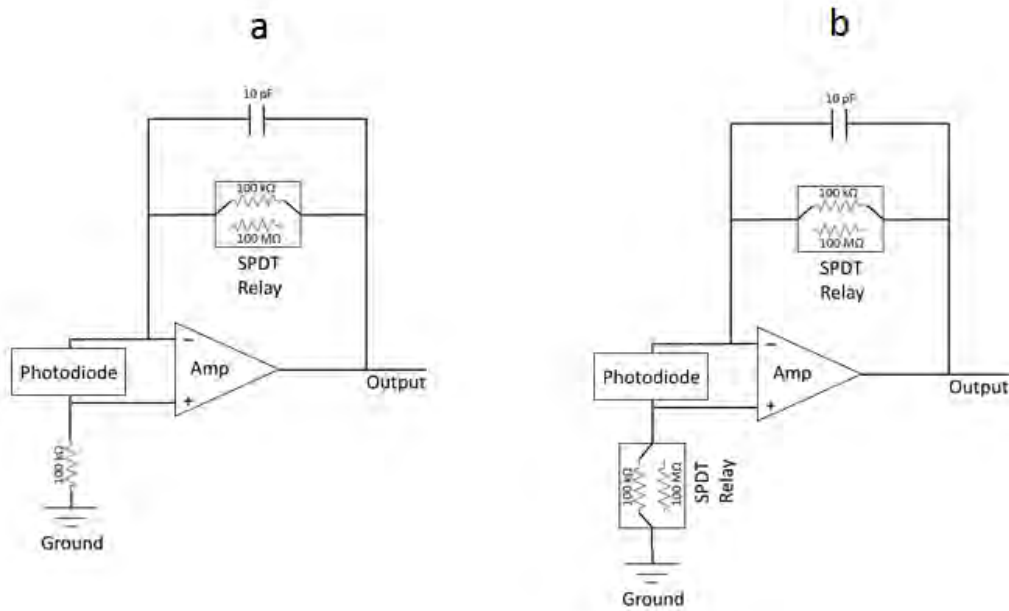


Figure 7.7: The design is shown for varying the gain of the photodiode transimpedance amplifier circuit using a single relay (a) and dual relays (b).

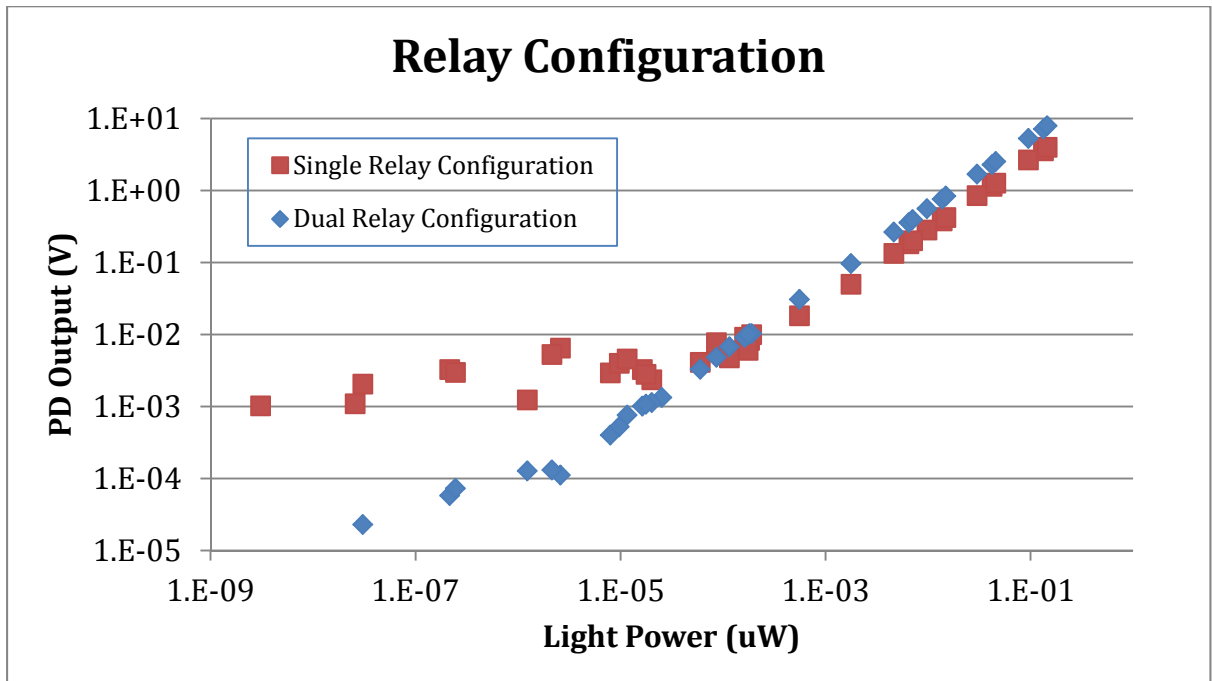


Figure 7.8: Photodiode performance characteristic is shown for a single relay (orange) and a dual relay (blue) configuration.

### 7.2.3 PCB Design

The prototype was designed to accommodate 64 photodiodes per layout. Four-layer printed circuit boards (PCB) were designed using CadSfot Eagle PCB Design software to build the prototype, which holds all the electronics needed to interface to the photodiodes including amplification and multiplexing circuitry.

A simple multiplexer circuit was designed and built in order to expand the number of digital outputs of the data acquisition card. The data acquisition card used was a National Instruments PCI-6031E which had 64 analog inputs and 8 digital inputs/outputs channels. Since each photodiode requires a digital signal to control the relays and thus the gain of each detector, 64 digital outputs are needed for the prototype. Therefore, the multiplexer circuit expanded the 8 digital output channels of the DAQ card to 64 digital outputs.

The 8-to-64 output multiplexer functionality was implemented using a 4-of-16 decoder (74L) and 16 D-type edge-triggered flip-flops (74LS374). The schematic of the circuit is shown in figure 7.9. Each flip-flop controlled 4 relays where each relay controlled the gain of a photodiode detector. As can be seen from Figure 7.9, the 8 available digital outputs from the DAQ device (D0 through D7) were routed such that 4 outputs were connected directly to the 4-of-16 decoder chip and the other 4 outputs were shared among the 16 flip-flops.

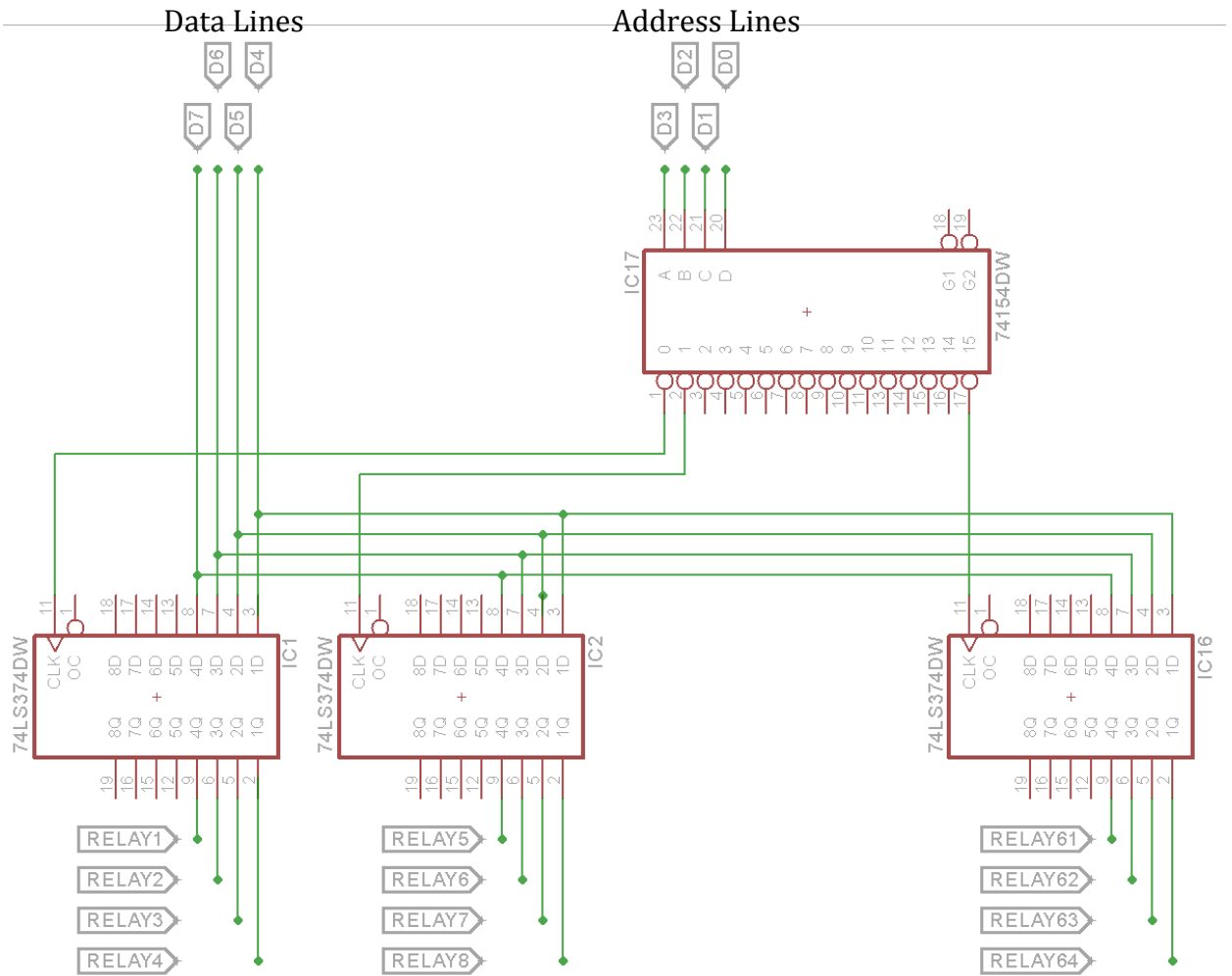


Figure 7.9: The schematic of the digital multiplexer circuitry used to expand the number of available outputs is shown, as needed to control the 64 photodiode relays.

The resulting 64 digital outputs each controlled the dual relays for each of the photodiode circuits. The relays were wired such that the photodiode circuit is set to low gain at default. When a digital high is applied to the relay through the multiplexer circuit, the relay switches to the 100 MΩ resistor thus setting the circuit for high gain acquisition.

The other circuit needed for completing the prototype PCB was the amplifier circuitry that was used to amplify the photodiodes outputs. In order to simplify prototyping, the 64 amplifier circuits were divided into 4 identical boards each with 16

amplifier circuitry. The finished results of the amplifier circuitry along with the multiplexer circuitry is shown in Figure 7.10. The multiplexer board shown enables a direct connection from the DAQ board to the multichannel system using the DAQ cable.

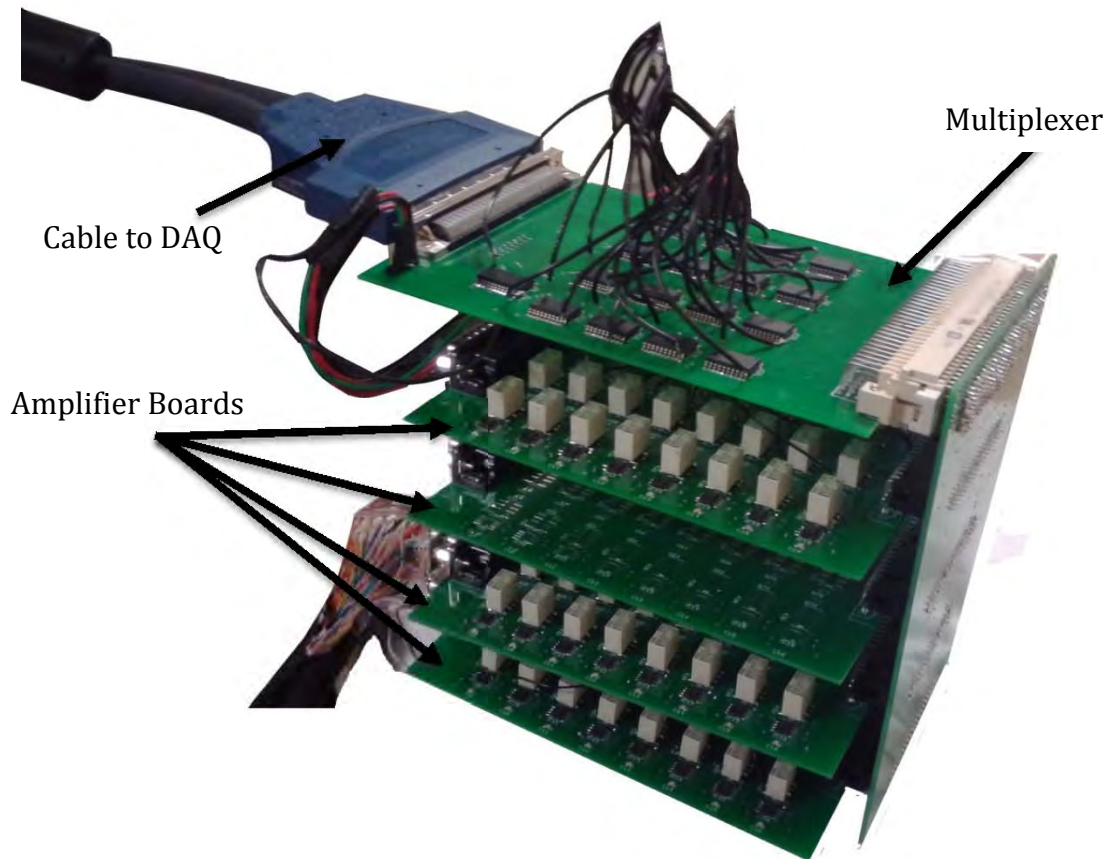


Figure 7.10: A photograph of the final electronic prototype is shown, as used to interface to the photodiode detectors via the ribbon cable (lower left), and coupling to the DAQ card (upper left).

#### 7.2.4 Phantom Interface

An interface that secures the tissue phantom and detectors was designed using Solidworks and 3D printed. The interface, shown in Figure 7.11, secures a phantom with a diameter of 87 mm and enables simultaneous acquisition of 4 planes separated by 1 cm.

Each plane accommodates 4 sources and 12 detectors. The sources were delivered via fiber optic bundle cables.



Figure 7.11: Diagram of interface built using Solidworks and used for testing the new multiple-detector array.

### **7.2.5 Photodiode packaging**

Photodiode packaging shown in Figure 7.12 (a) was custom designed using Solidworks and then built using a 3D printer. The packaging is used to secure the detector for safe handling. It also has a mechanism to attach the detector to the phantom interface. The packaging was designed to snap into two different types of interfaces; the first type uses the hollows in the packaging to secure the packaging onto the interface as shown in Figure 7.12 (b). The second type uses the wings of the photodiode packaging to snap into the interface type shown in Figure 7.12 (c).

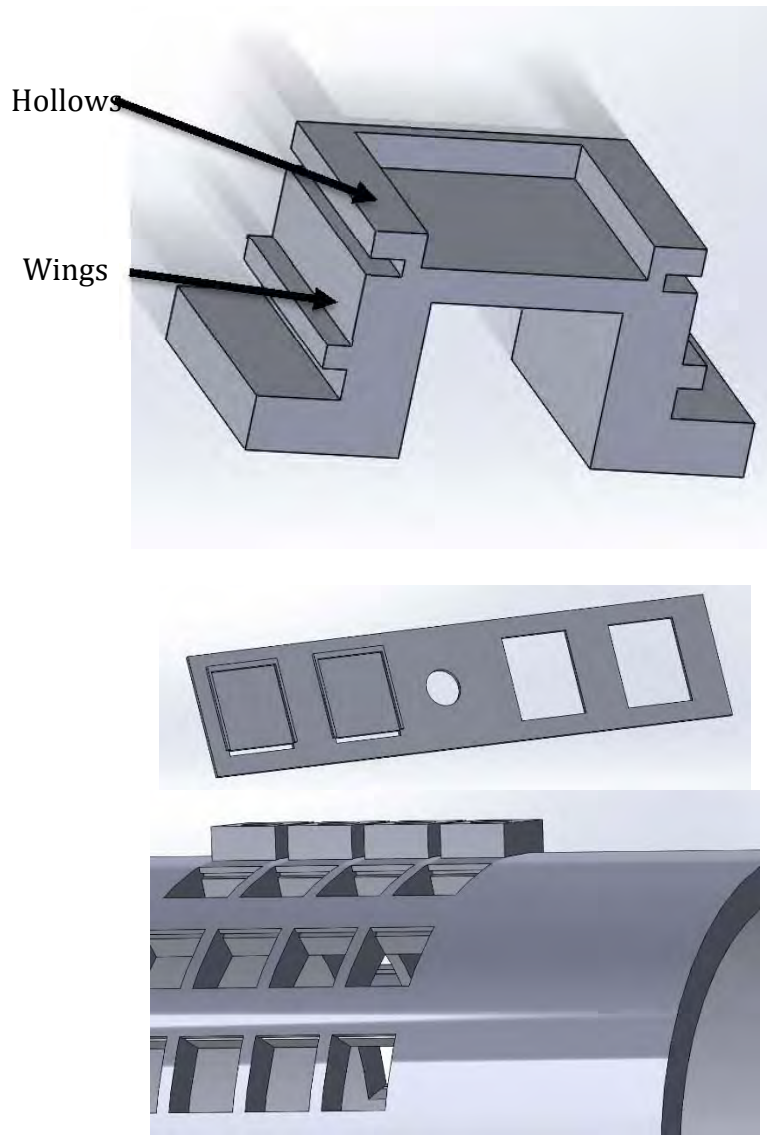


Figure 7.12 (a) photodiode detector packaging, (b) and (c) are two types of interfaces that are used to hold the detectors into contact with phantoms.

### 7.2.6 Calibration

The goal of the calibration process is designed to produce the same amplitude response for equivalent light input across the entire dynamic range of the detectors. It is an essential step that ensures proper function of the system. All detectors were calibrated in a similar fashion to the PMT and PD detectors described in the hybrid system chapter (chapter 4) where light was incident at the center of a homogenous phantom for the

purpose of distributing the light equally to all detectors. The homogeneous gelatin phantom had a diameter of 87 mm and was made by mixing intralpid (5 ml), water (500ml), and agar (5g) and allowing the mixture to solidify. A calibration phantom holder shown in figure 7.13 (a) was designed using SolidWorks and built using a 3D printer. The phantom holder had a connector at the center that allowed a fiber optics cable to deliver the laser light to the center of the phantom. Neutral density (ND) filters were used to attenuate the laser input. The output of the photodiode detectors was recorded while varying the laser input using the ND filters. Since the photodiodes can be operated at two different gain settings, the calibration was performed with both the high and the low gain settings.



Figure 7.13: The calibration phantom holder is shown, as designed with a laser fiber at the center of the holder and one photodiode detector snapped into one of the available slots.

Calibration was performed by placing 16 detectors at-a-time on the phantom holder and recording their output while varying the laser input with the ND filters. The process was repeated until the output of all detectors was recorded as a function of laser

power for the two different gain settings. Figure 7.14 below shows an example of the linearity for one of the photodiodes (photodiode #2).

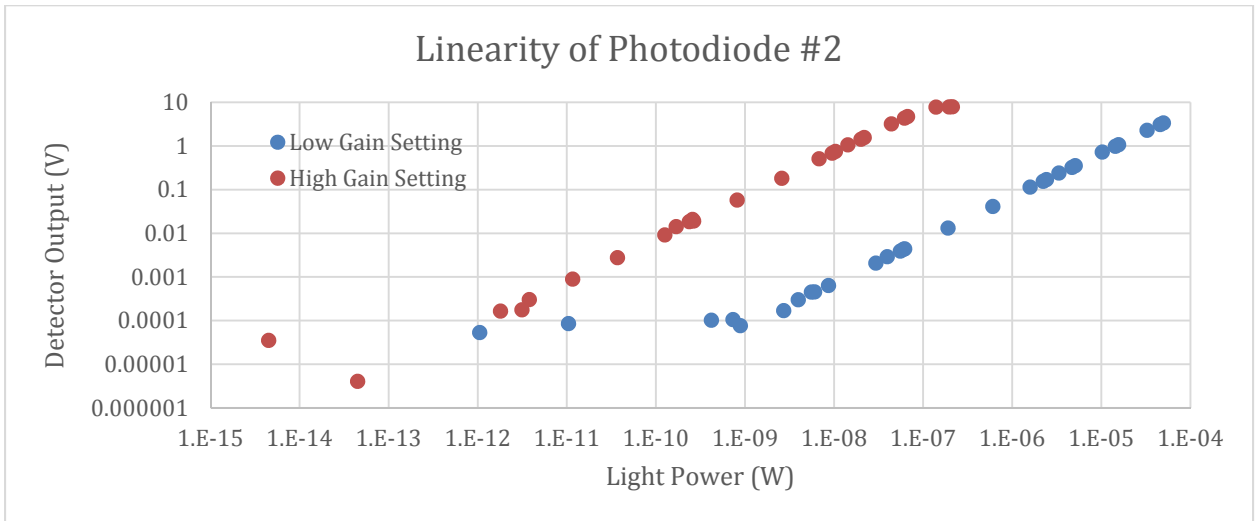


Figure 7.14: The response of the low and high gain settings of the photodiode amplifier are shown, for calibrated input light powers. Measureable signal was seen down to 1pW on the high gain, and 1 nW on the low gain.

As can be seen from the figure, photodiodes exhibit a great linearity and a large dynamic range. The dynamic range of the photodiode using the low gain setting (100 K $\Omega$ ) extends from ~ 1nW to ~100uW, whereas it extends from ~1pW to ~0.1uW using the high gain setting (100 M $\Omega$ ). The slope of the linear region of the two curves were recorded for each of the detectors in order to calibrate the response of each detector and convert a voltage output reading into an accurate light input power (values listed below).

Calibration is an essential step that ensures proper function of the detectors. However, photodiodes are extremely robust detectors. Since they are semiconductor based detector, they have the qualities of semiconductors which include long lifetimes, physical robustness, durability, low power requirements, easy to process, and, most

importantly, detectors made from the same wafers have identical behavior and properties. This can be clearly evident in Figure 7.15 below which shows the raw detector output voltage measured by the DAQ device (Figure 7.15 (a)) and the calibrated detector output (Figure 7.15 (b)) for a homogenous phantom experiment that is described in the next section. As can be seen from the two figures, the results are identical and calibration could in fact be skipped all together. In fact, the slope of the curves shown in Figure 7.14 above was nearly identical for all detectors ( $0.99 \pm 0.01$  for the low-gain setting and  $0.98 \pm 0.03$  for the high-gain setting). The greater error in the slope for the high gain setting is possibly due to differences in the variation in amplifier circuit electrical characteristics (amplifiers, resistors, capacitors, cable length, solder inconsistencies, etc.). The normalized raw and calibrated outputs shown in figure 7.15 (c) demonstrate that inter-detector calibration may not be an essential part of data acquisition for photodiodes due to their nature. This is a unique advantage compared to the hybrid system which required inter-detector calibration due to differences in the fiber optical cables used to carry the light signal to the PD/PMT detectors.

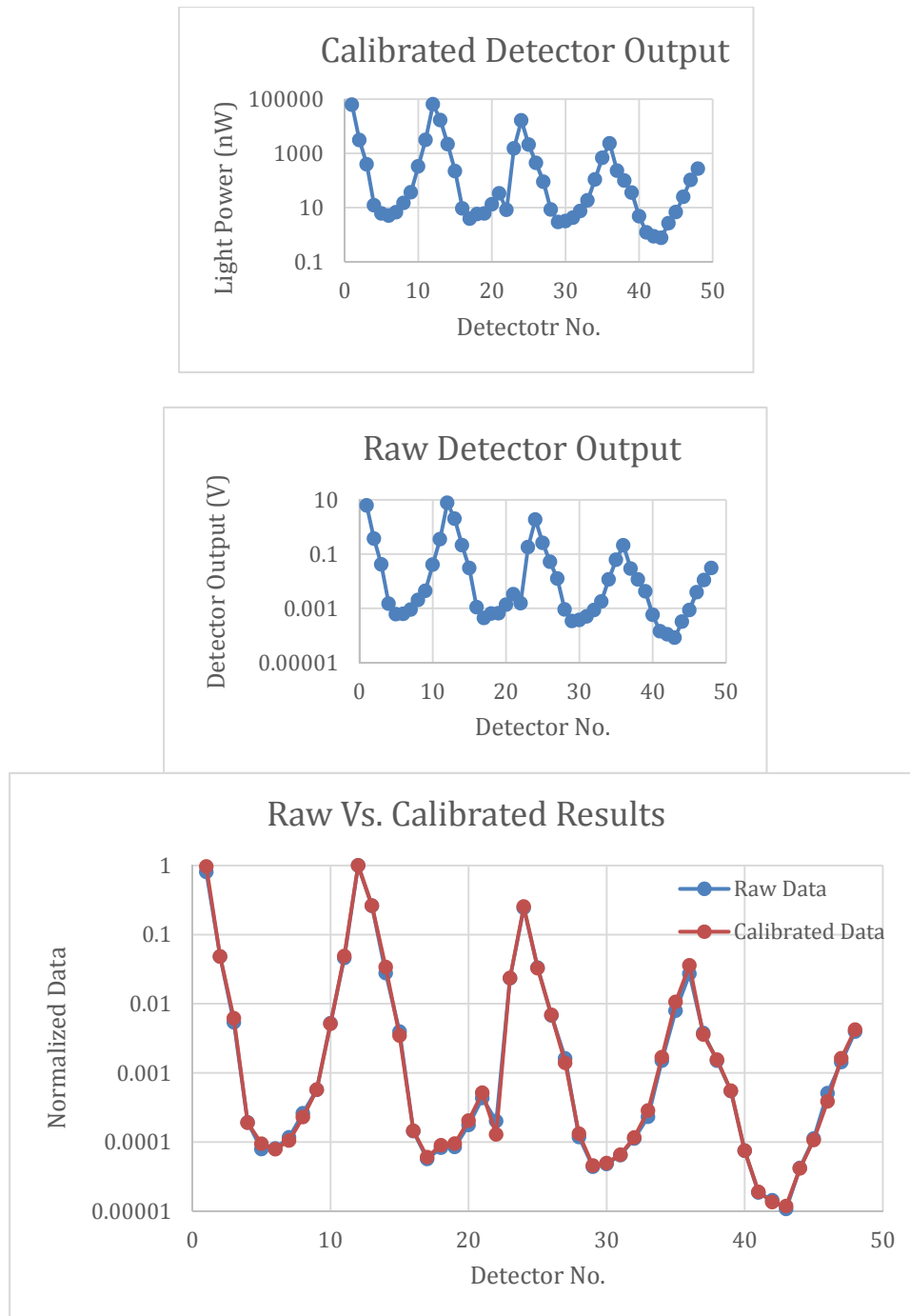


Figure 7.15 In (a) the calibrated output of a phantom experiment is shown, and (b) shows the raw output of the same phantom experiment, while (c) shows the normalized calibrated and raw output of the same phantom experiment, showing minimal need for calibration.

### 7.2.7 Cross talk

Crosstalk was evaluated in order to determine erroneous output that may appear where a signal from one channel effects neighboring channels. One detector was covered completely while a neighboring detector was subjected to the same calibration experiment as described previously. The signal was recorded as a function of the incident laser power, and Figure 7.16 shows that despite being neighboring channels, there was no apparent cross talk between the two channels.

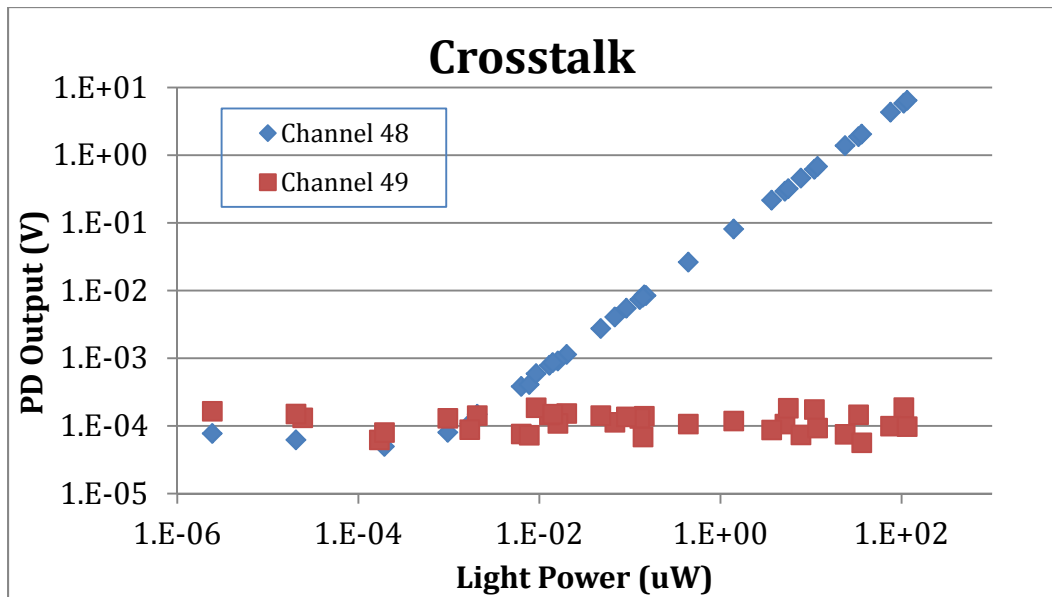


Figure 7.16: The crosstalk behavior of two neighboring channels is shown, with signal recorded in the blue data, and crosstalk in the orange data shown, exhibiting minimal increase over the noise floor.

### 7.2.8 Phantom Experiments

Tissue mimicking phantoms with a diameter of 87 mm and a length 150 mm in length were used to test the system. Two types of gelatin phantoms were used, with ink in one, and blood in the other, as absorbers. With both types, a homogeneous and a heterogeneous phantom of each type was tested. The homogenous type had no inclusions

whereas the heterogeneous type had an inclusion that was ~20mm in diameter which was filled with varying concentration of the same absorber as the background (ink for the ink phantom and blood for the blood phantom). In order to simplify phantom preparation, a fixture was designed with Solidworks and built using a 3D printer, which enabled a simple way of creating an inclusion. This piece, shown in Figure 7.17, enables an inclusion to be created with the same exact location with respect to the center of the phantom and exact size every time a phantom is created.



Figure 7.17: Phantom and phantom inclusion molds as printed, allowing a hole to be created for an inclusion in the gelatin phantom.

#### **7.2.8.1 Ink Phantom Results**

A homogenous and a heterogeneous ink phantom was used to test the new system. The phantom was constructed by mixing 1000 ml of water, 10g of Agar, 50 ml of 20% Intralipid, and 8ml of 2% Ink, in order to generate an absorption coefficient of approximately  $0.01\text{mm}^{-1}$ . The heterogeneous phantom had a 20 mm inclusion that was filled with an increasing concentration of ink ranging from 0 up to 5 times the ink concentration of the background. Figure 7.18 shows an image of the phantom and embedded inclusion.

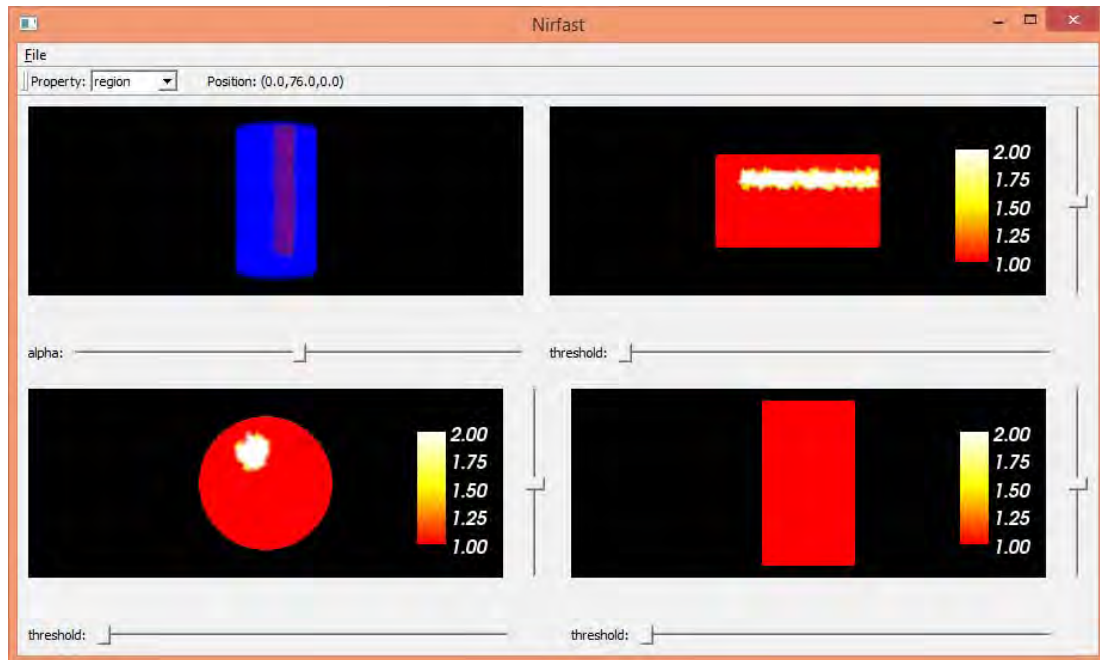


Figure 7.18 Image of phantom showing location of the inclusion as seen in the NIRFAST display.

The phantom was placed in the phantom holder and the photodiodes were snapped into their designated areas in contact with the phantom. A total of 48 detectors and 16 sources were used. Figure 7.19 (a) below shows the phantom holder and the detectors. The actual phantom used is displayed in Figure 7.19 (b) showing the inclusion. Figure 7.19 (c) is the mesh of the phantom showing the placement of sources and detectors.



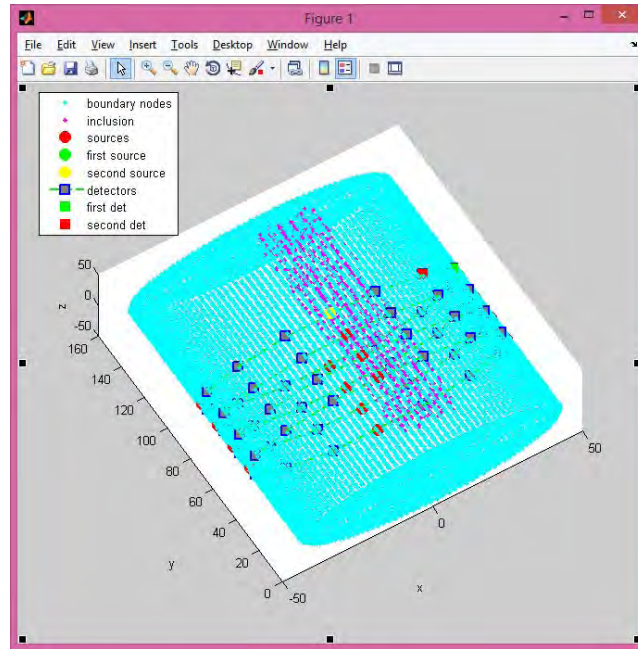


Figure 7.19 (a) image of the phantom holder showing the detector array, (b) image of the phantom showing an empty inclusion (c) mesh of the phantom showing the location of sources and detectors around the phantom.

As can be seen from the figure, all four source/detector planes intersect the inclusion. The inclusion was filled initially with a mixture of Intralid and water so as to match the scattering properties of the background. Then, ink was added to the mixture such that it would yield 1 up to 20 times the ink concentration of the background. Nirfast was used to reconstruct the images of the phantom and inclusion at each concentration. Figure 7.20 shows the reconstructed ink concentration  $\left(\frac{\text{Inclusion Ink Concentration}}{\text{Background Ink Concentration}}\right)$  for 0 up to 20 x. Contrast ratios from 1 to 5 are shown in the data in Figure 7.21, which is the linear recovery part of the data set. Above the contrast level of 5, it is expected that diffusion-based reconstruction cannot fully recover the true contrast, and biological contrast values are typically all well below a 5X contrast.

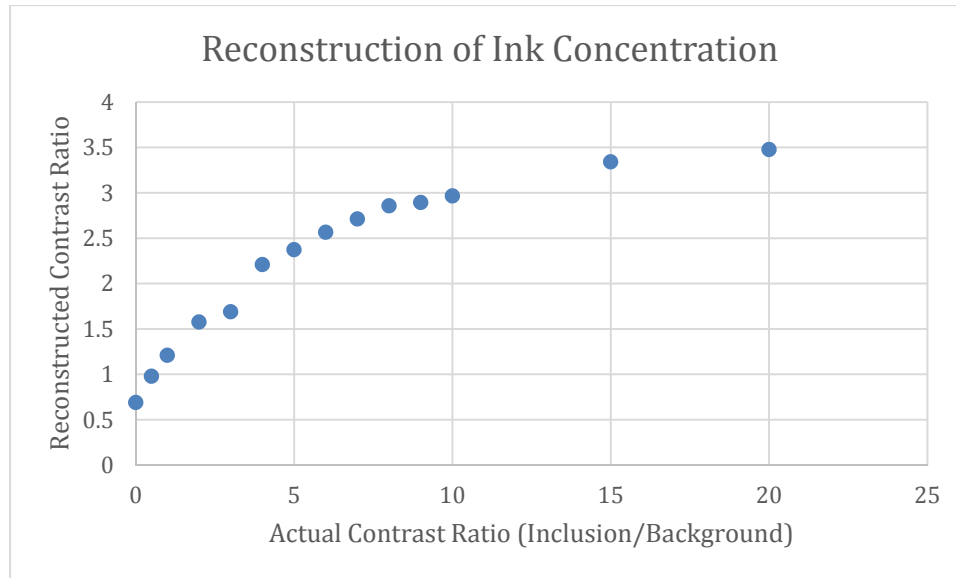


Figure 7.20 Reconstructed ink concentration of the phantom inclusion for a large range of contrasts recovered.

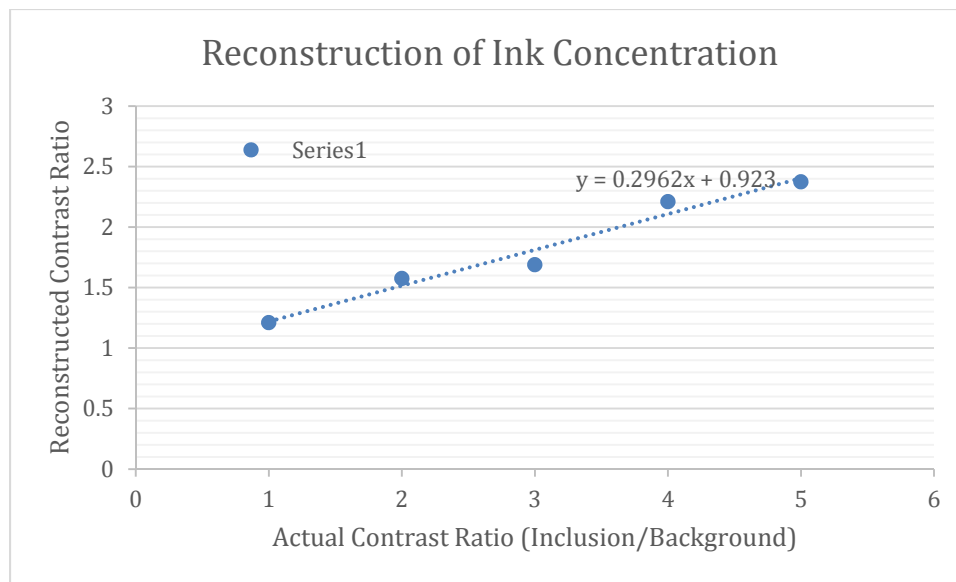


Figure 7.21 Reconstructed ink concentration of the phantom inclusion from 1 up to 5 times the background absorption value.

A similar ink phantom experiment was performed but with an inclusion that extends to the middle of the phantom. In this experiment, the inclusion intersected two out of the four source/detector planes as shown in Figure 7.22 (a). The idea behind this

experiment was to confirm the need for enough sources and detectors to map the entire phantom/tissue.

Reconstruction of the increasing ink concentration a similar behavior as the previous phantom. The results for contrast ratio between 1 and 5 is shown in Figure 7.22 (b).

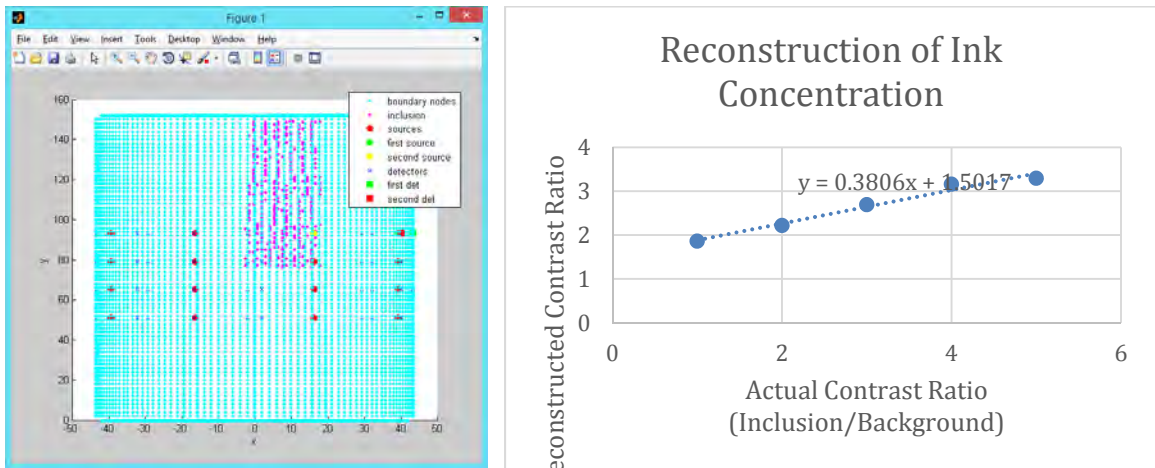


Figure 7.22: (a) mesh of the phantom showing the inclusion along with the location of sources and detectors around the phantom. This inclusion only intersected two out of the four source/detector planes used for data acquisition. (b) Reconstructed ink concentration of the phantom inclusion up to 5 times the background absorption value.

To demonstrate the importance of coverage, the data was reconstructed in 2 dimensions for each plane of acquisition indecently ignoring the data from other planes. Figure 7.23 shows the 2D reconstruction of the four planes of acquisition. As can be seen from the figure, the two planes that do not intersect the inclusion show no sensitivity to the increase of ink concentration inside the inclusion. The second plane which barely intersect the inclusion also shows a much lower sensitivity compared to first plane which completely intersects the inclusion.

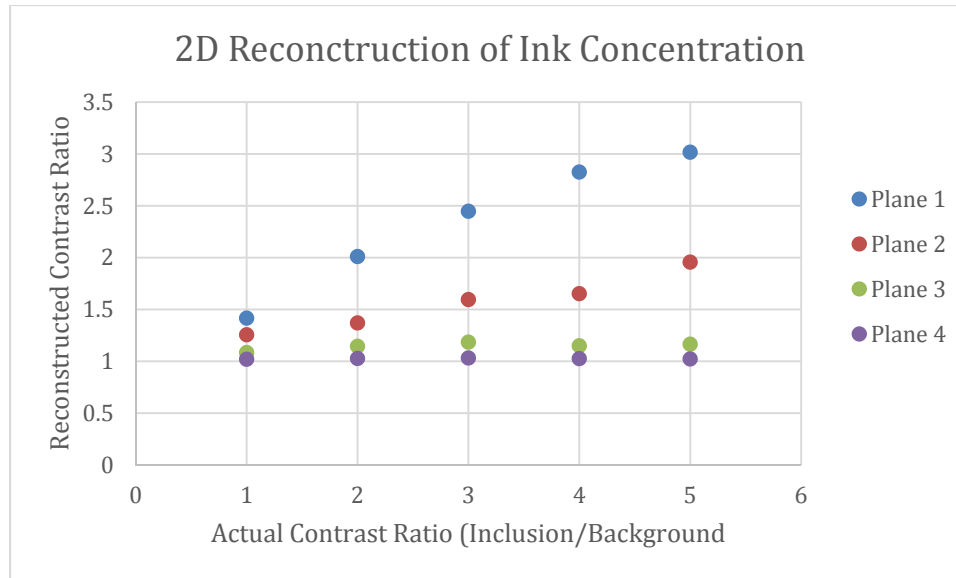


Figure 7.23 2D reconstruction of the four acquisition planes was done, and the recovered contrast is shown as a function of increasing input contrast in the inclusion.

#### 7.2.8.2 Blood Phantom Results

Finally, a blood phantom was created in order to thoroughly assess the performance of the prototype by using 9 different laser wavelengths (661, 735, 785, 808, 826, 849, 902, 912, and 948). The bulk optical properties of the phantom were similar to those of breast tissue. It was constructed using water, type 1 Agarose, 1% Intralipid, and whole porcine blood at a background concentration of 12 $\mu$ M. The hematocrit level of the blood was measured by a Hemocue device to be 10 g/dL of the blood. An inclusion was created in the phantom which was filled with varying concentrations of blood from 12 $\mu$ M up to 60  $\mu$ M in 12  $\mu$ M increments, in order to vary the absorption systematically. After each concentration, the phantom was imaged with all 9-wavelengths. The geometry of the phantom was identical to that of the ink phantom shown in Figure 7.18 and 7.19.

Images were reconstructed using Nirfast software to determine the accuracy in recovery of the blood concentration of each run as compared to the expected concentrations. The final results are shown in Figure 7.24.

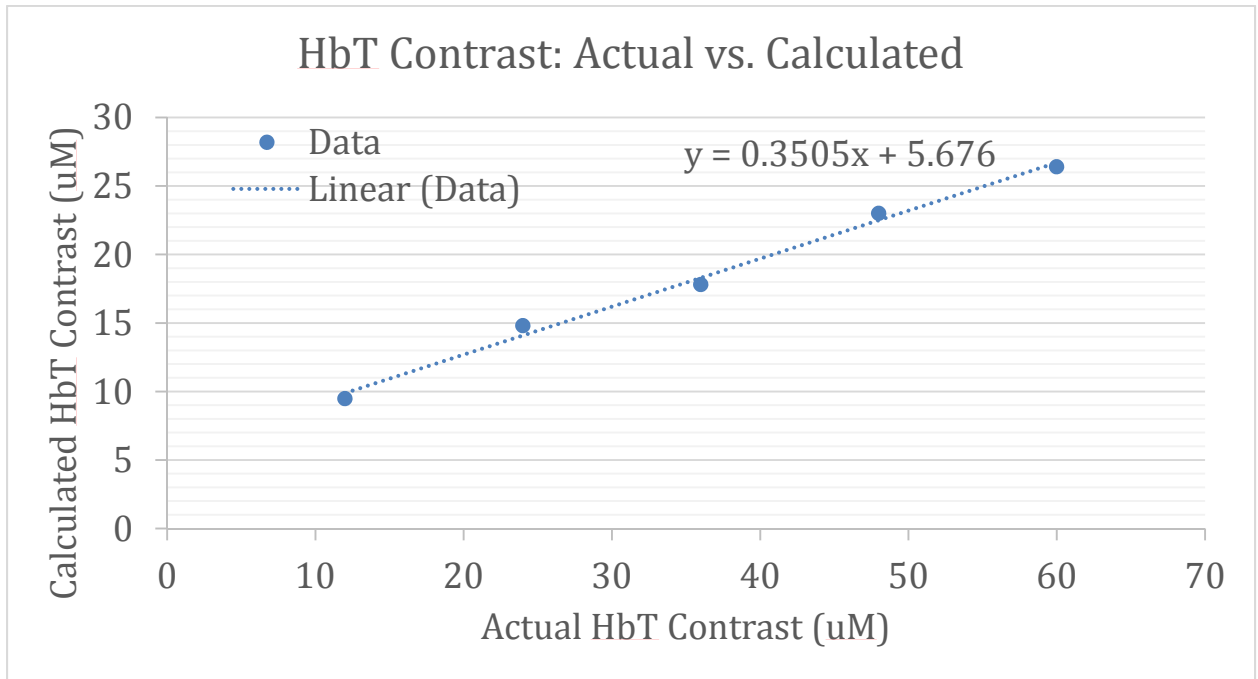


Figure 7.24 Total blood concentration reconstruction of the phantom inclusion from 1 up to 5 times the background absorption value.

## CHAPTER EIGHT

### Conclusion and Future Directions

#### 8.1 Completed Work

This thesis focused on instrumentation of systems used in optical tomography. Detectors used in near-infrared optical tomography were discussed in chapter 2 along with their pros and cons. A small animal imaging system was described in chapter 3 along with the work needed to calibrate and characterize the system. The time-correlated single photon counting (TCSPC)-based system demonstrated the complexity of time-domain systems as well as the advantage and high level of information content that be acquired from such system provided that TPSF data sets are measured at high accuracy and resolution.

Chapters 4 discussed a new hybrid system utilizing frequency-domain and continuous-wave measurements to image breast tissue using wavelengths ranging from 661 up to 948nm. The system improved data quality and accuracy in the recovery of the breast chromophores and was able to image phantoms/patients in ~12 minutes. The results of phantom testing along with healthy volunteers were discussed in chapter 5. The system was also used in a breast cancer clinical trial at Xi'an, China where 61 patients were imaged. The system demonstrated the advantage of combining MRI along with NIRS where the combined MRI/NIRS of MR-identified regions correlated to the histopathological findings of that region. The system also demonstrated that sensitivity of NIRS is greatly affected by breast coverage and that full breast coverage is essential for proper diagnosis.

In order to provide full breast coverage of NIRS, a technological solution which places sources and detectors directly on the tissue and utilizes electrical (rather than optical) signal transfer on MRI compatible wires was tested. Two optical detectors, photodiodes and silicon photomultipliers, which can potentially be used inside the magnet of the MRI for breast tomography experiments were evaluated. The dynamic range and sensitivity of both detectors was examined and yielded identical behavior. However, a major advantage of using photodiodes is their spectral responsivity which extends to 1100nm and is ideal for recovery of water and lipids with DOT, since the spectral features of these absorbers are more prominent at longer wavelengths.

The results found from chapter 6 are used in the design and development of a new optical tomography prototype that places detectors directly on the breast tissue while the patient is in the MRI. In chapter 7, a 64-channel photodiode prototype was designed and built that has the ability to cover the entire breast volume and perform NIRS scan while inside the MRI, thus, eliminating the use of bulky and expensive fiber optic cables used with the hybrid FD/CW system. The system was cost effective and robust. Characterization of the prototype along with phantom experiments were also discussed in the same chapter.

The prototype presented in the chapter 7 has shown a great potential for acquiring NIRS data when the patient is inside the MRI while providing full breast coverage. While the prototype works, there are few changes that can improve the prototype and prepare it for use in a clinical setting. These improvements are discussed further in the next section.

## **8.2 Future Directions**

The prototype presented in the previous chapter has shown a great potential in providing near-infrared spectroscopic information that can be coupled to clinical MRI while providing full breast coverage. Some changes which can improve the performance and aesthetics of the prototype as well as prepare it for use in a clinical settings are discussed next.

### **8.2.1 EMI Interference**

One of the areas of improvements includes minimizing electromagnetic interference (EMI). It is essential to minimize EMI due to the nature of the system and the sensitivity requirements of the electronics used in NIRS experiments. One method of minimizing EMI is on the PCB board itself by placing the ground plane on the top and bottom layers of the printed circuit boards used to house electronics. Housing the entire PCB in a protective aluminum case and connecting the PCB ground planes to this case turns the entire apparatus into a protective shield that will minimize EMI.

One issue that was apparent with the previous prototype is the lack of a dedicated ground plane which caused some unwanted noise characteristics. The signal ground for the electronic components in the previous prototype had a single copper trace that connected the ground of each component to the next as shown in Figure 8.1 (a). The same is also true for the copper trace which provided power to the integrated chips. The problem with this approach is that when a chip is activated, it will draw slightly more current from the power and ground terminals. This, in process will slightly diminish the current going to the next chip. The process repeats and will cause the ground of each chip to be at a slightly different ground. This is known as virtual ground where even

though the chips are connected to the same ground trace, they are in fact at a different ground points compared to the true ground of the system.

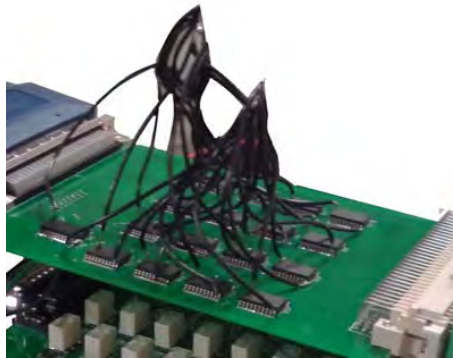
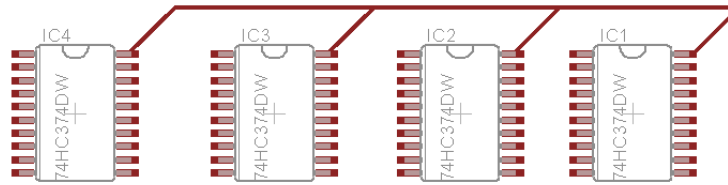


Figure 8.1: (a) An example of a single trace connecting different points on a circuit board  
(b) star connection implementation is shown where wires (black) shown in the figure are connected to IC circuits on one end and soldered together on the end

In this prototype, this was solved by connecting the grounds together using external wires in what is called a star ground as shown in Figure 8.1 (b). External wires were soldered to the ground of each integrate chip and then the other end of the wires where brought together to from a single junction which was soldered and connected to the true ground.

While this method works, it is certainly aesthetically unprofessional. Furthermore, this approach would have not worked for high frequency designs since adding such wires increases the impedance leading to undesired circuit characteristics. The correct approach to solving this issue is by dedicating a full layer in the PCB to the ground and power signals

### 8.2.2 Cables

In order to carry the signal from the photodiodes to the amplifier circuitry, 10 ft. flat ribbon-type cables were used to tether the detectors inside the MRI room to the electronics located outside the MRI room. A PVC jacketed flat cable with expanded copper shielding was used for this purpose. The cable had 36 conductor wires each with a wire gauge of 28 AWG.



Figure 8.2: 3M™ Shielded/Jacketed, Flat Cable used to transport the photodiode signals to the amplifier circuitry outside the MRI room

It is possible to use a cable with even a smaller gauge wires. Using smaller wires will decrease the size of the cables used to carry the signals in and out of the MRI room and will make the design easier to transport and setup. The original intent of the shielding was to protect against RF interference caused by AC power lines and RF interference caused by the MRI. The AC interference was diminished by the new amplifier design which attenuated the power line frequency interference as was discussed in chapter 7. However, the RF interference could not be eliminated. While the cable was shielded and protected from external interference, the photodiodes placed inside the MRI bore were not shielded from this RF interference. In fact, the RF at the MRI bore leaked

into the unshielded sections of the photodiode and solder joints which connected the photodiodes to the cable. This RF interference is very difficult and may be impossible to shield against. Therefore, it is possible and recommended to go with smaller wires in order to keep the system light, portable, and ready for clinical applications.

### 8.2.3 Synchronizing MRI/NIRS Acquisition

One of the draw backs of the current prototype is that we are unable to run both MRI and NIRS experiment simultaneously due to the RF interference caused by the MRI scan. An MRI scan uses RF pulses to disturb the protons in tissue/phantoms that are aligned with the magnetic field in order to image these protons as they go back to their default state when the RF pulse is turned off. These RF pulses are very strong in the center of the bore where the photodiodes are present and it is therefore extremely difficult to shield the detectors from the RF pulses. Figure 8.3 shows an example of one of the photodiodes output during a simultaneous NIRS and MRI acquisitions. The figure shows the effects of the RF pulses on the output of a photodiode set at high gain.

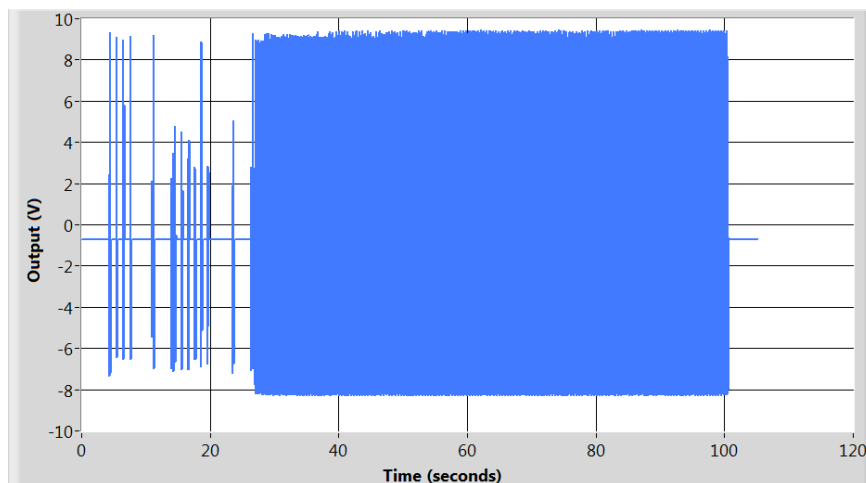


Figure 8.3: An example of a photodiode output dominated by RF pulses of the MRI during a simultaneous MRI/NIRS acquisition

As can be seen from the figure, the signal appears to be dominated by spikes caused by the MRI RF pulses. A potential solution to running both systems simultaneously is to synchronize the MRI scan with the NIRS acquisition such that the NIRS data is being acquired between the RF pulses. Figure 8.4 below shows a photodiode output during a T1-TSE MRI sequence acquisition. The figure on the right shows a zoomed in version of the T1 acquisition. Individual RF pulses can be seen in this plot. It can be seen that there are 5 to 20 ms intervals where there are no RF pulses present. It is possible to synchronize the NIRS acquisition with RF pulses of the MRI in order to acquire both data sets simultaneously by acquiring data during such intervals.

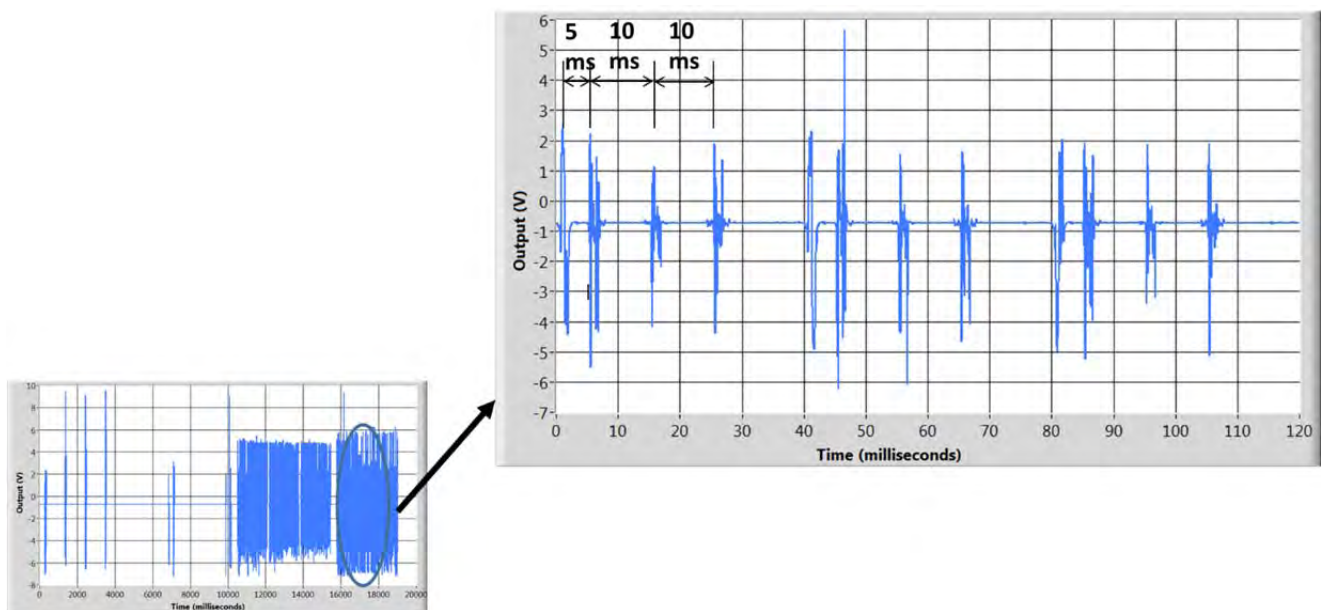


Figure 8.4: An example of a photodiode output during a simultaneous MRI/NIRS acquisition showing intervals that can be used to collect NIRS data after the MRI RF pulses settle

One advantage of the above approach is that we don't need to physically wire or interface to the MRI system as these RF pulses can be simply read from our NIRS

prototype. Therefore, this approach can work with any MRI without the need to build dedicated circuits that can explicitly read the RF pulses.

The data shown above was taken when the photodiode was set to low gain setting which is able to acquire light input from 1 nW up to 0.1mW. At high gain setting, the photodiode circuit response time is diminished by orders of magnitude and therefore would require more time until the effect of the MRI RF pulses are settled as can be shown from Figure 8.5.

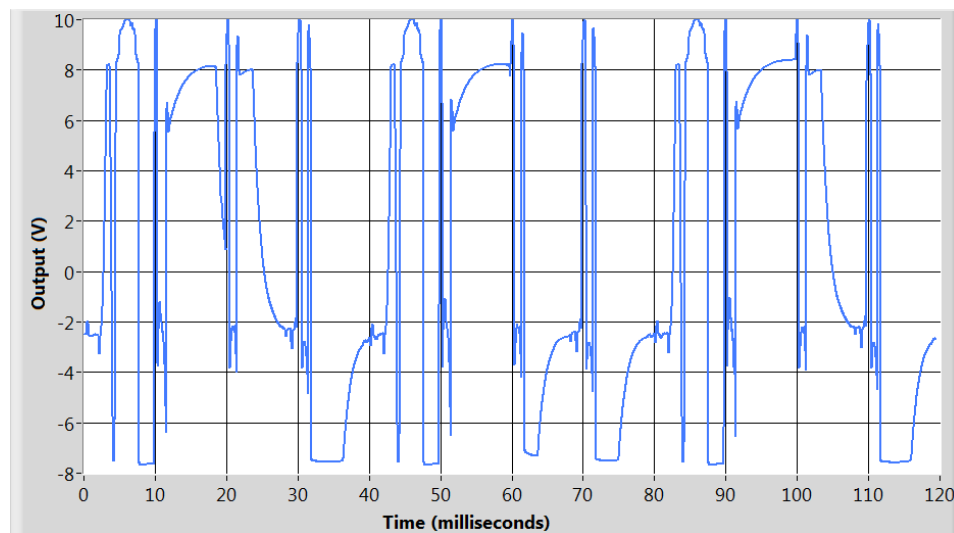


Figure 8.5: An example of a photodiode output under high gain setting during a simultaneous MRI/NIRS acquisition showing no intervals for acquitting NIRS data during MRI imaging

In this setting, it is no longer possible to acquire MRI and NIRS data simultaneously. In practice, however, during an MRI scan, there are several time instants where there are no RF pulses present such as the time when switching between different MRI sequences or at the beginning of each sequence where the system emits warm-up pulses as shown in Figure 8.6.

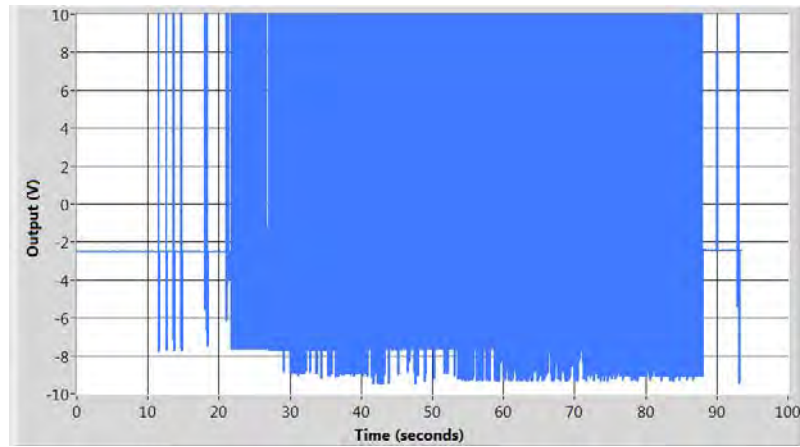


Figure 8.6: An example of a photodiode output under high gain setting during a simultaneous MRI/NIRS acquisition showing possible NIRS acquisition intervals during the beginning or an MRI sequence

Therefore it is possible to run simultaneous MRI and NIRS acquisition provided that the NIRS data is acquired between RF pulses at low gain setting of the photodiode and during warm-up pulses or sequence changes for high gain setting of the photodiodes. Synchronization can be implemented using hardware triggering by simply connecting the output of one of the photodiodes to a DAQ board capable of hardware triggering and setting a simple threshold.

#### **8.2.4 Patient Interface**

Another area of improvement is the patient interface. The patient interface used with the hybrid system which was discussed in chapter 5 worked very well. The new pentagonal design enabled different breast sizes to be imaged. However, since the interface only allows for a single plane of acquisition, the idea is to use the same working design but to redesign the interface to adapt to the new detectors as well as to enable sources and detector to be placed at multiple planes. An example of the interface is shown in figure 8.7. This interface was designed using Solidworks and 3D printed using

our 3D printing facility at Thayer. The detectors were able to snap into the interface with ease. The only draw back of the current design is that it uses large fiber optic cables to deliver the laser light which imposes a limit on the number of detectors that can be used. This particular interface allows for 3 planes of detectors and two planes of sources as can be seen giving a total of 30 detectors and 20 sources. Using smaller fiber optic cables to deliver the light will enable additional detectors to be used.

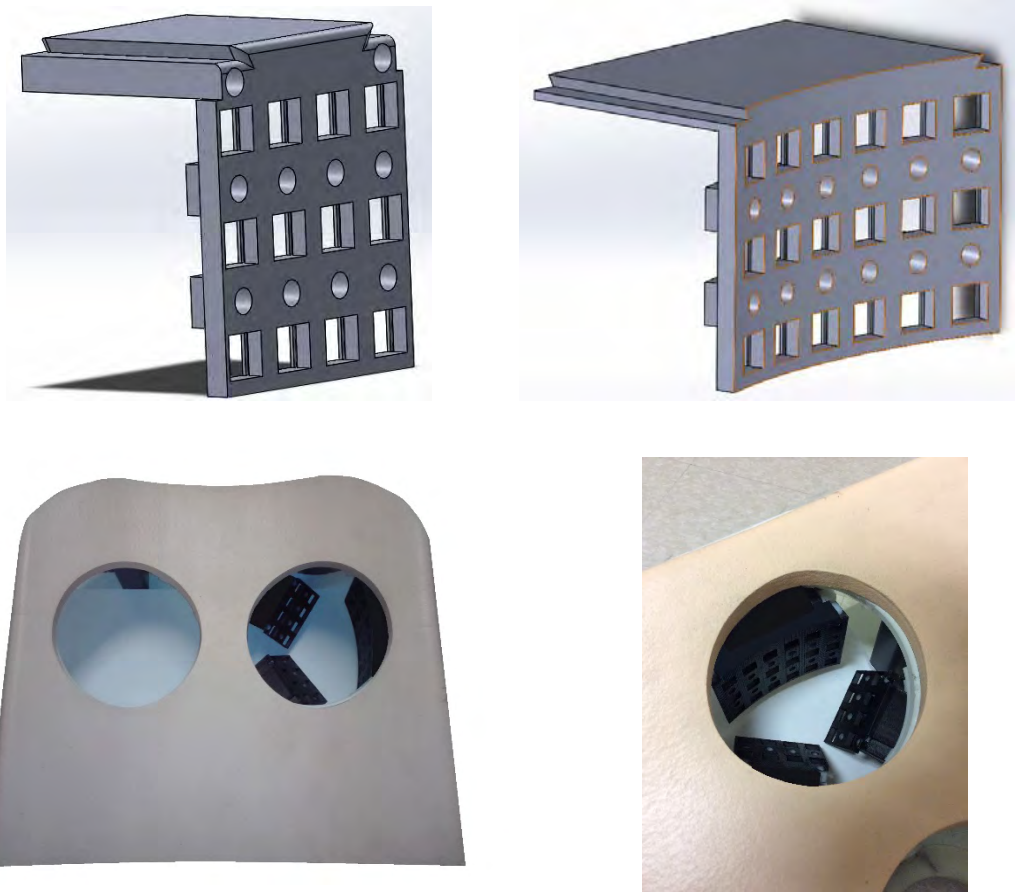


Figure 8.7 Possible breast interface for full breast coverage based on previous breast interface design

### 8.2.5 Simultaneous Breasts Acquisition

The prototype showed a great potential to perform MRI-coupled NIRS acquisition at a very low cost of less than \$50 per detection channel for a 64-channel system. Due to

its low cost, it is possible to build a system to acquire NIRS images of both breasts simultaneously. This has the advantage of being able to compare optical information from both breasts which can aid in distinguishing between a healthy and unhealthy breasts.

### **8.2.6 Scattering and absorption information**

One of the draw backs of the current prototype is that it uses continuous-wave measurements only. Using continuous-wave measurements alone may not provide full scattering and absorption information. However, studies have demonstrated that CW methods with multiple wavelengths information may in fact have the potential to decouple scattering and absorption information and therefore, our 9-wavelength system may be able decouple these effects.

Different possibilities exist in order to provide further decoupling of scattering and absorption. For example, it may be possible to obtain such information directly from the MRI. Another possible approach is to use fast detectors such as PMT detectors for frequency domain measurements which are able to separate the effects of scattering and absorption. One can use a fiber optic cable approach that is similar to the hybrid system. Instead of using fiber optic cables, one can use fast PIN type photodiodes which may possibly be used inside the MRI bore similar to the way the PD prototype works. The disadvantage of such approach is that PIN type photodiode detectors that can record FD type measurements are usually small in size ( $<5\text{mm}^2$ ). This approach may yield benefits but requires some engineering in order to be able to deliver the RF signal from the photodiode to the data acquisition electronics. Finally, while the approaches above focused on getting scattering information while the patient is inside the MRI, it is also

possible to use NIRS systems to get an estimate of scattering while the patient is outside the MRI provided that one is only interested in an average measure of scattering.

## Appendices

### Appendix A: Noise Sources

The signal of interest is often obscured by noises. Noise is composed of undesirable components that arise from various sources. Understanding of the noise sources in a measurement is critical to achieving the highest signal-to-noise ratio in any system. Noise can be divided into fundamental and external noise. External noise includes unwanted background illumination which may find its way to the detector, thermal EMF, or inductive pick-up noise. Fundamental noise sources are noise sources caused by the physics of particles and therefore cannot be eliminated. Such sources include shot noise, Johnson (thermal) noise, and 1/f noise.

- **Shot Noise**

Light, as well as electrical charge, are quantized. They are produced in discrete numbers and are subject to statistical fluctuations. For a given interval, there will be random fluctuations in the number of electrons or photons generated. These fluctuations will follow Poisson statistics where the uncertainty in the number of events in a given interval is simply the square root of the number of events. For example, if 100 photons are generated in a given time interval, the standard deviation of a series of counts over the same time interval is  $\sqrt{100} = 10$ . Therefore  $100 \pm 10$  are detected during that time interval. This random statistical fluctuation is the most fundamental type of noise in a measurement. Photons and electrical

charge shot noise will cause a slight noise in the signal readout regardless of how sensitive is the detector.

- **Johnson Noise**

In addition to shot noise, electrons are also subject to random motion which increases with temperature. This random fluctuation of the electrons will generate a noise known as Johnson noise. For example, a resistor has an RMS noise voltage value equal to:

$$V_{Johnson,rms} = \sqrt{4KTR \Delta f}$$

, where

K = Boltman's Constant [J/K]

T = temperature [K]

R = resistance [ $\Omega$ ]

$\Delta f$  = bandwidth [Hz]

For a 1 Hz bandwidth, this yields:

$$V_{Johnson,rms}(per \sqrt{Hz}) = 0.13nV \times \sqrt{R}$$

The current equivalence is:

$$I_{Johnson,rms}(per \sqrt{Hz}) = \frac{130pA}{\sqrt{R}}$$

From the above two expressions, if the signal of interest is delivered to a voltage amplifier, a small resistor value must be used in order to keep the additional Johnson noise due to the resistor small. However, if the signal is delivered to a current amplifier, small value resistors should be avoided.

- **Flicker Noise**

This noise is sometimes known as pink, low-frequency, or  $1/f$  noise. The mechanism that produces such noise is not well understood. This type of noise has a spectral density equal to  $1/f$  and may dominate when the bandwidth of interest contains frequencies below 1 KHz.

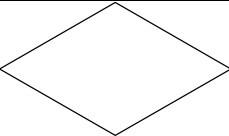
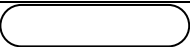
- **External Noise Sources**

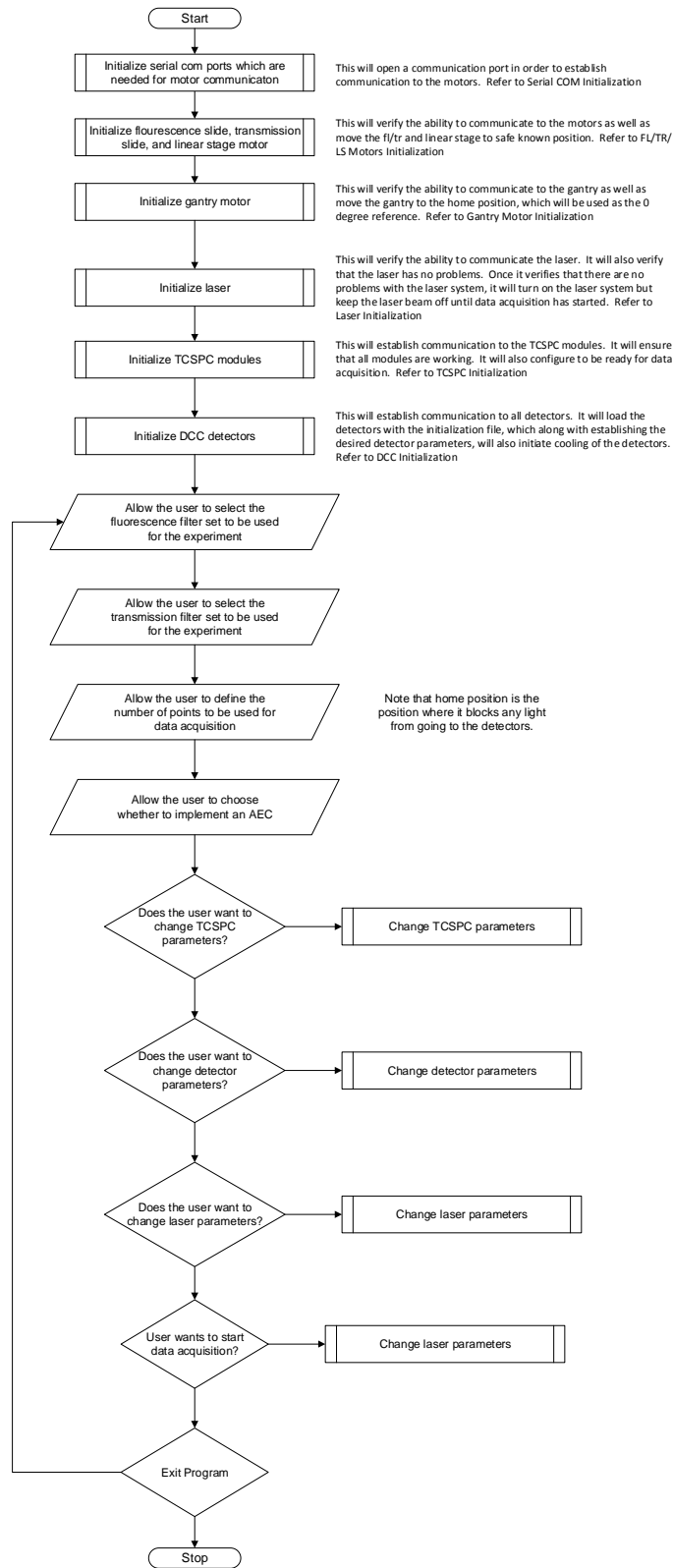
In order to make reliable low-level light measurements, external noise sources must be avoided. Some methods for avoiding external noise sources include shielding, using of differential inputs to reject common mode noise, limiting amplifier bandwidth to match the bandwidth of the signal of interest, modulation of the input signal, and synchronous triggering.

## Appendix B: Programs flow chart

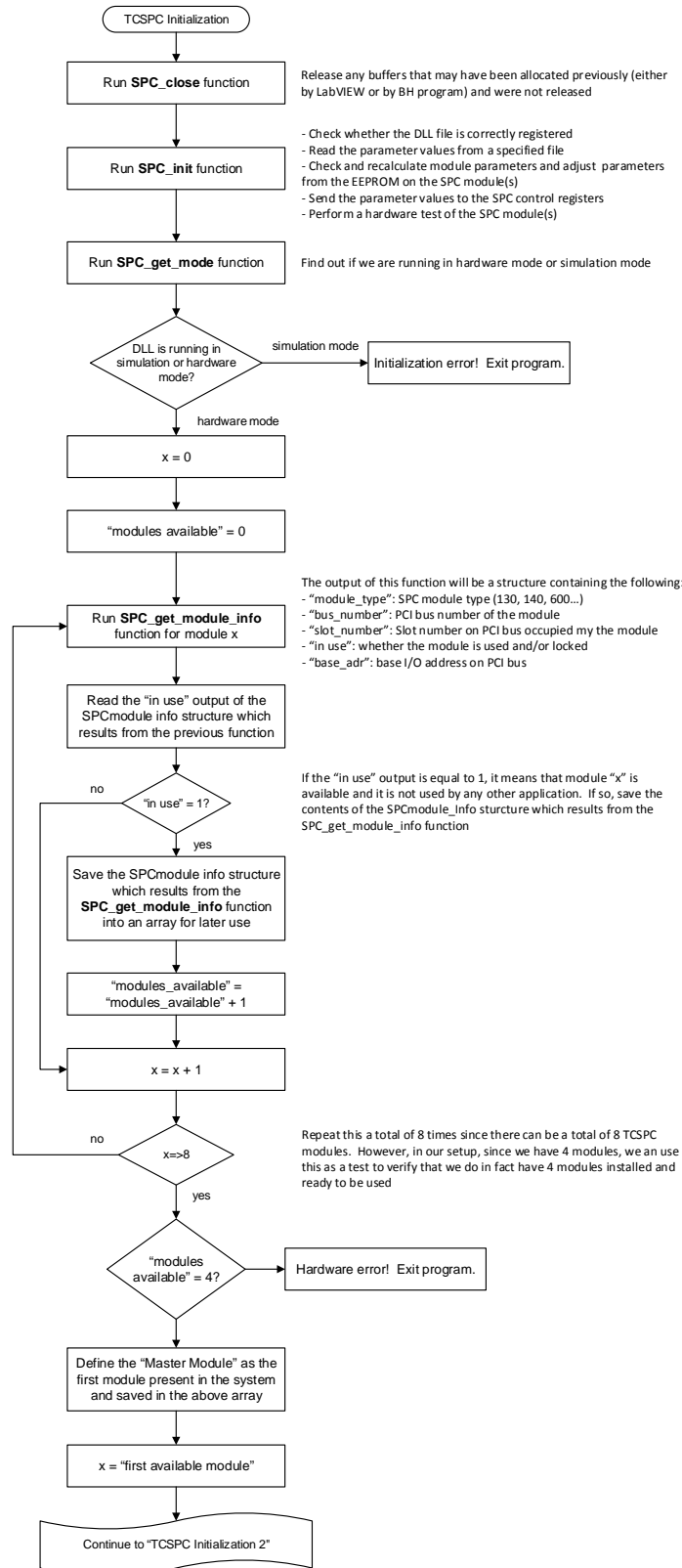
All programs in this thesis to control and automate data acquisitions were written in the LabVIEW programming language. In this programming language, software engineering practices have been followed, for the most part, to build scalable, readable, and maintainable VI's. In order to write such code, flowcharts are used to build and document the steps involved in programming each VI. Flowcharts are a powerful way to organize ideas and are able to provide a good understanding of the application flow. Furthermore, flowcharts are easy to understand and program since the LabVIEW block diagram paradigm is very similar to a flowchart.

There are two projects that were automated using LabVIEW: the small-animal tomography system and the hybrid breast imaging system. Since it is very difficult to show the actual graphical code of these programs, the flowcharts of the programs used in both systems are shown below instead. The VI programs are all zipped and stored in the Thayer Research Folder.

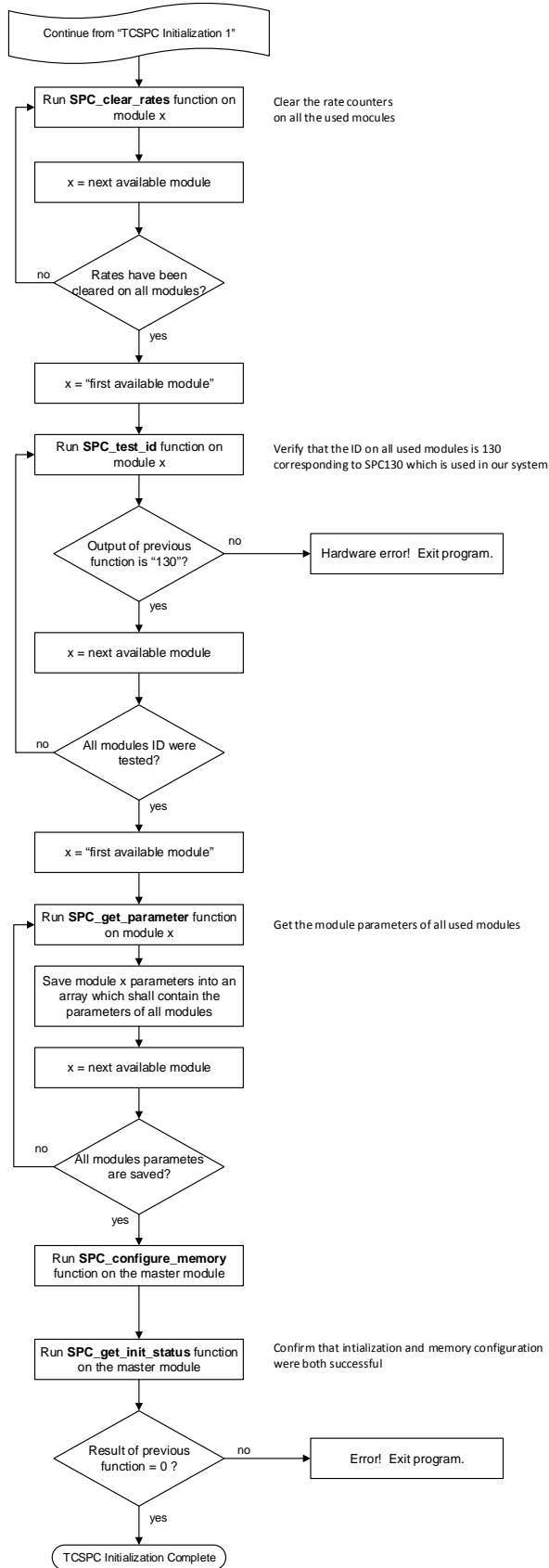
	Refers to a subvi
	Refers to
	
	
	



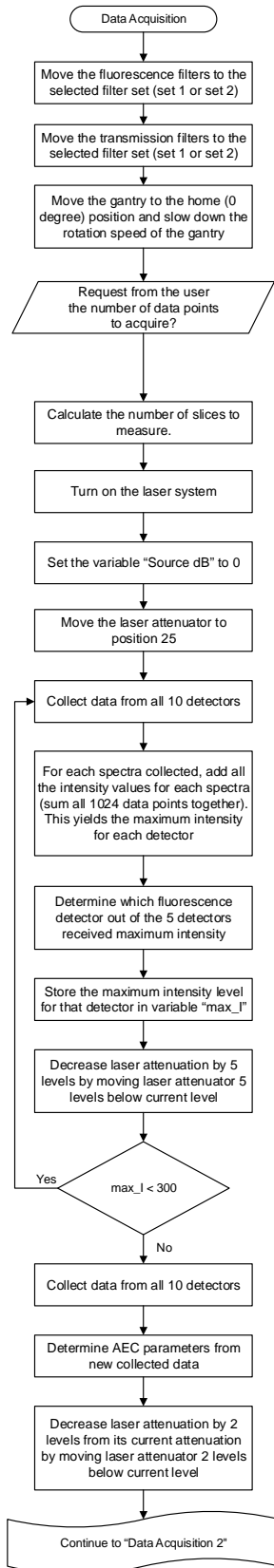
**Main Graphical User Interface Flowchart**



## TCSPC Initialization (1 out of 2)



## TCSPC Initialization (2 out of 2)



Most common are 16, 32, and 64 corresponding to 22.5, 11.25, and 5.625 degree separation between each data point. The user shall define a number of points between 1 and 360 which corresponds to a max of 360 degree and a minimum of 1 degree separation between each measurement

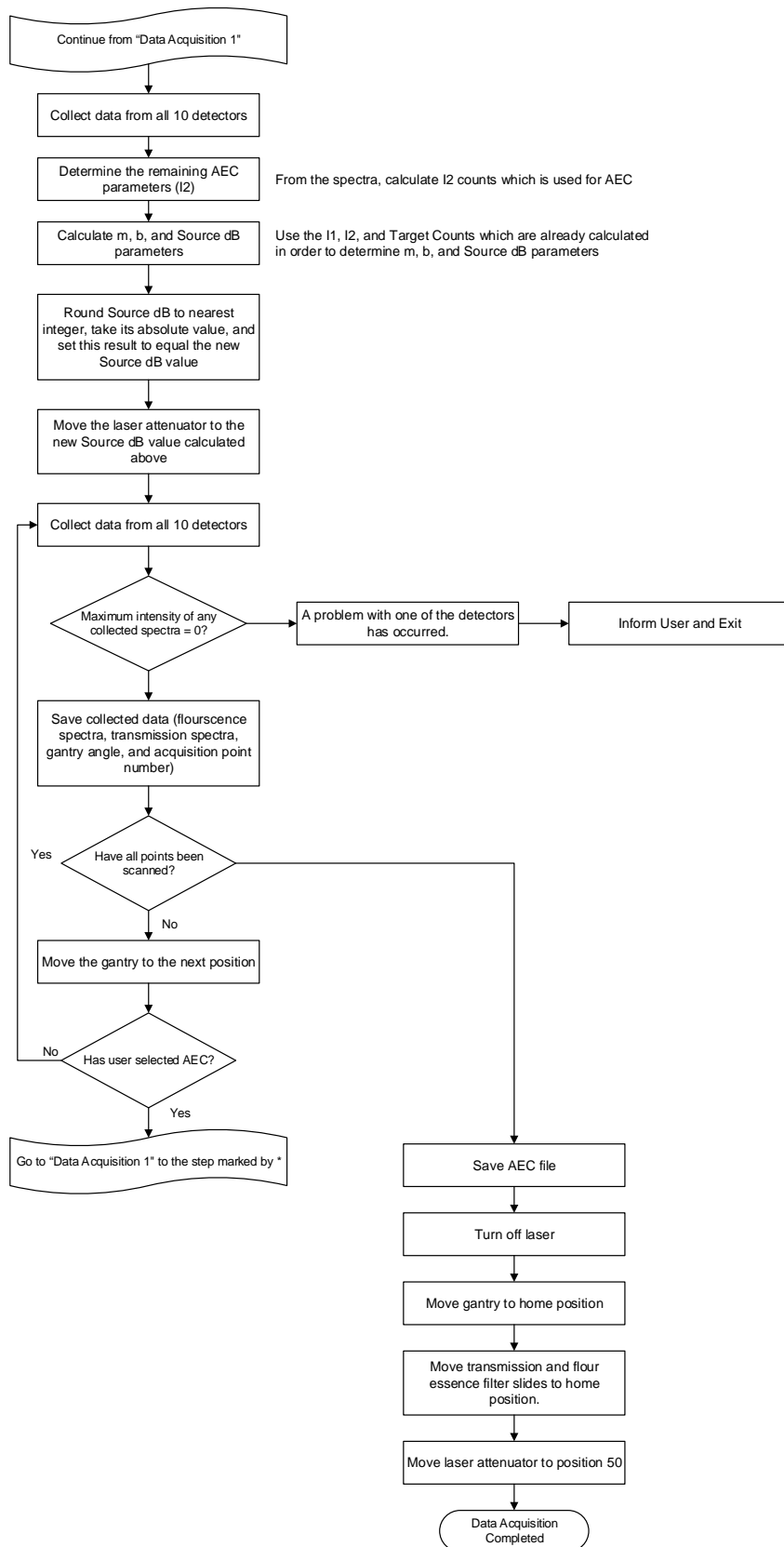
The number of slices = (ROI size in mm rounded to nearest integer) / (slice thickness in mm), where the result is rounded to the nearest integer

Note that each spectra contains 1024 data points

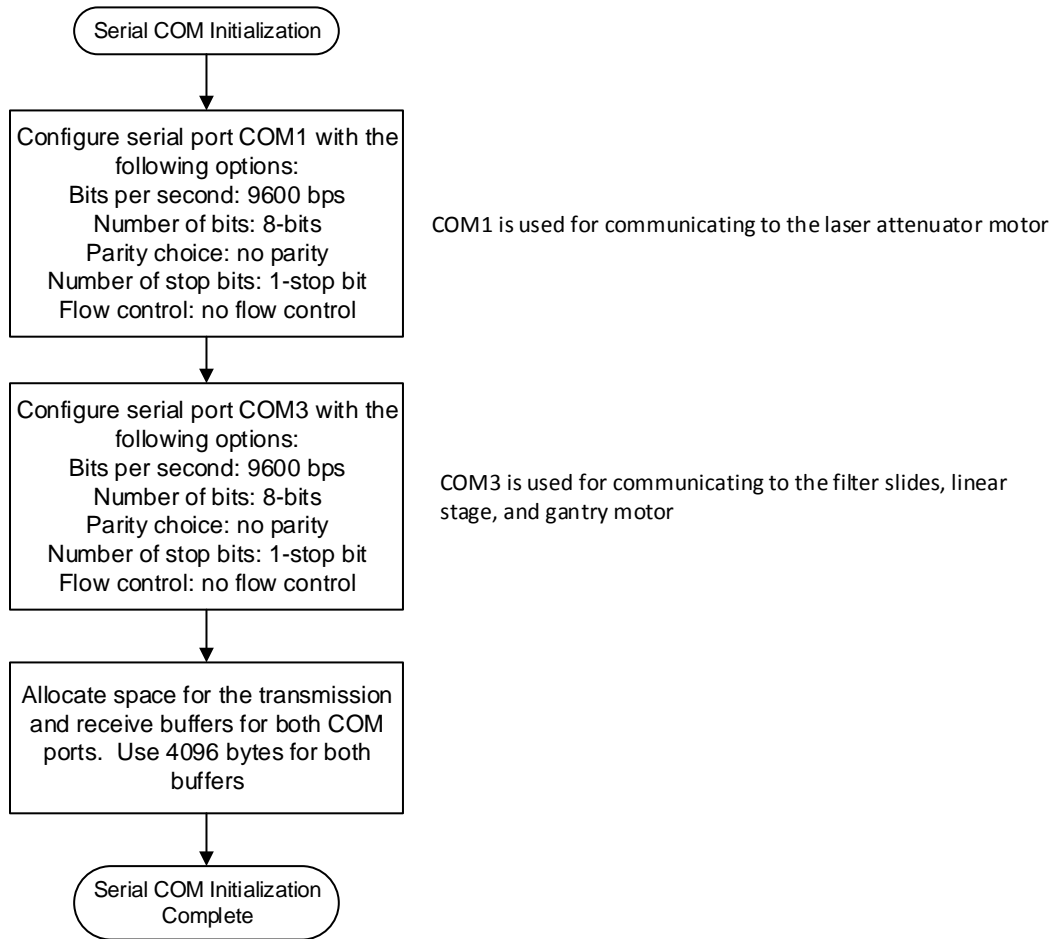
According to Dax, these steps are used to determine the initial source strength of the most sensitive detector (I don't understand this!)

From the spectra, calculate Target Counts, Target Channel, and 11 counts which are used for AEC

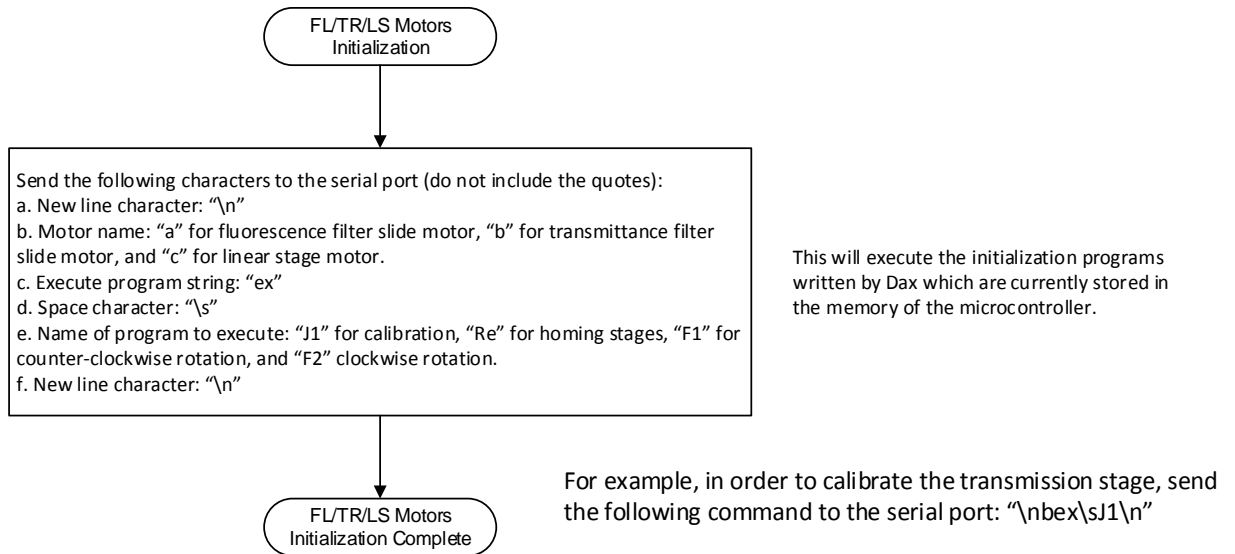
## Data Acquisition (1 out of 2)



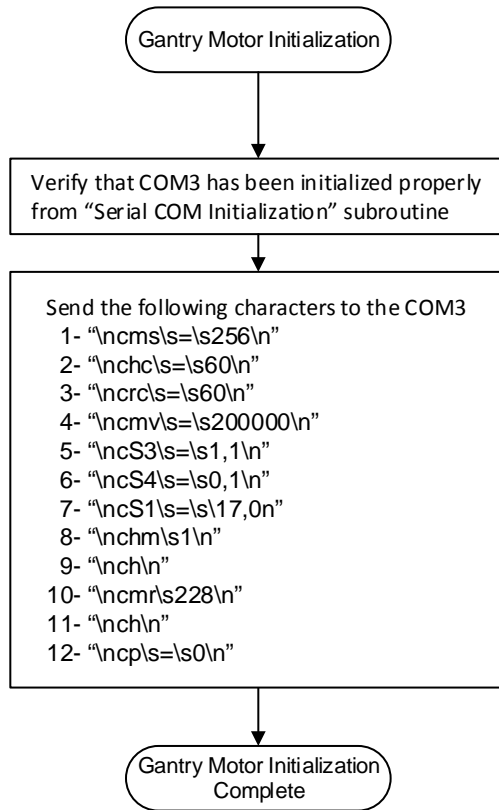
## Data Acquisition (2 out of 2)



## Serial COM Initialization



## FL/TR/LS Motor Initialization



These instructions will move the gantry to the home switch and then will move CCW by 228 steps. We can't use DaX's code because there is an error in his programming. The 228 steps, however, come from his code!

### Gantry Motor Initialization

## **Appendix C: PCB Circuits**

## **Appendix D: Detectors**

### **Introduction**

#### **Detectors Overview**

The main two categories for photon detectors are photoelectric and thermal detectors. Manufacturers have more or less followed common international standards in describing their detectors. Detectors will be compared according to their quantum efficiency, collection efficiency, responsivity, gain, noise equivalent power (NEP), specific detectivity, response time, bandwidth, energy resolution, and excess noise factor (ENF). Noise sources will also be introduced in order to understand some of the limitations of photon detectors. Therefore, before going any further, common definitions that are shared by all detectors will be explained.

- **Quantum Efficiency**

One of the important keys in selecting a detector is its quantum efficiency. Quantum efficiency of a photodetector, defined by the symbol  $\eta$ , is the probability that a single photon will generate a charge carrier that will contribute to the detectors' current. Not every photon will generate a charge carrier which would contribute to the detectors' output current. Absorption is a stochastic process and some photons will not be absorbed by the detector. A fraction of photons will be reflected from the surface of the detector. Finally, some of the charge carriers produced by photon absorption will fail to contribute to the detector output. For examples, in semiconductor detectors, some charge carriers will recombine at the surface of the detector instead of contributing to the final output. These effects are shown in Figure

D.1 below. Quantum efficiency takes into account all these variables and is defined as:

$$\eta \equiv \frac{\text{Number of emitted photoelectrons}}{\text{Number of incident photons}} = (1 - \mathcal{R})\zeta(1 - e^{-\alpha(\lambda)d})$$

, where:

$\mathcal{R}$  = optical power reflectance

$\eta$  = efficiency

$\zeta$  = fraction of charge carriers that avoid recombination and contribute to the output

$\alpha$  = absorption coefficient [1/length]

$d$  = detector depth [length]

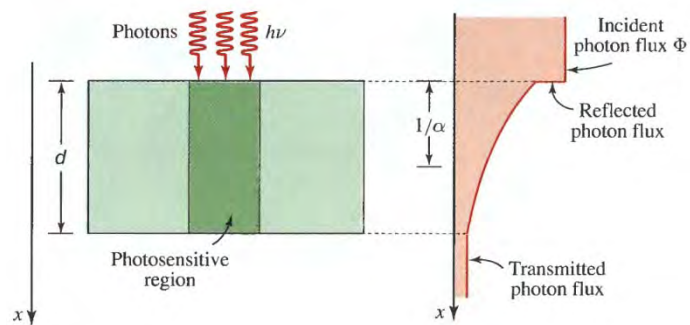


Figure D.1: Effect of reflection and incomplete absorption on the quantum efficiency [34]

The  $(1 - \mathcal{R})$  represents the number of photons that have avoided reflection and carried on towards the light-sensitive part of the detector. The  $\zeta$  represent the fraction of charge carriers that avoid recombination and contribute to the final detector output. Finally, the  $(1 - e^{-\alpha(\lambda)d})$  term represents the fraction of the photon flux that are absorbed in the light-sensitive part of the detector.

It is important to note that the dependence of the efficiency of a detector on wavelength is due to the dependence on the absorption coefficient  $\alpha(\lambda)$ , which is wavelength dependent.

- **Collection Efficiency**

Collection efficiency is another important term that must be considered while selecting a photon detector. It is a measure of how efficient the detector is in transferring the primary photoelectrons or electron-hole pair charge carriers to the output terminal. While an absolute measurement for collection efficiency is not easy, relative comparisons between detectors can easily be made.

- **Responsivity**

Responsivity, defined by the symbol  $\mathfrak{R}$ , is a measure of the sensitivity of a detector. It is equal to the ratio of the root mean square (rms) output current measured in amperes (or output voltage, measured in volts) produced by the detector to the incident light power measured in watts. The higher the responsivity, the more sensitive is the detector. Responsivity can be calculated from the following:

$$\mathfrak{R} \left[ \frac{\text{Amp}}{\text{Watt}} \right] = \frac{i_p}{P} = \frac{i_p}{h \nu \Phi_e} = \frac{\eta G e \Phi_e}{h \nu \Phi_e} = \frac{\eta G e}{h \nu} = \frac{\eta G e}{h \left( \frac{c}{\lambda} \right)} = \eta G \frac{\lambda_o}{1.24}$$

$\mathfrak{R}$  = responsivity [amp/watts]

$i_p$  = rms current output of the detector [Amperes]

$P$  = incident radiation power [watts]

$h$  = Plank's constant [joule-second]

$\nu$  = light frequency [Hz]

$\Phi_e$  = photon flux [photons/second]

$\eta$  = efficiency of detector

$G$  = gain of detector

$e$  = electron charge [coulombs]

$c$  = speed of light [m/s]

$\lambda$  = light wavelength in [m]

$\lambda_o$  = light wavelength in [ $\mu\text{m}$ ]

- **Gain**

Some photon detectors have a gain mechanism which amplifies the charge carriers that contribute to the output current. For example, as will be discussed later in this chapter, a photon absorbed in a PMT detector will initially generate few electrons. These electrons will be amplified further through dynode elements that eject more electrons as they themselves are bombarded with electrons. A single photon in the PMT case may generate up to  $10^6$  electrons or even more. This gain mechanism is essential for single photon detection where detectors are able to respond and detect single photons.

- **Noise Equivalent Power**

A detector produces an output signal even if it does not get any input light due to different noise sources that are inherent to each detector. The noise

equivalent power (NEP) is defined as the input radiant power that produces a signal value equal to the noise value produced in the detector. It is not easy to find a clear mathematical definition of NEP in the literature. The previous definition results in NEP measured in units of Watts. However, since this definition does not take into consideration the bandwidth of the detector, other authors define NEP to be the input radiant power that produces a signal value equal to the noise value produced in the detector in a one hertz output bandwidth [125]. An output bandwidth of one hertz is equal to half a second of integration time. Therefore, NEP is the radiant power which gives a signal-to-noise ratio of one during a 500ms integration time. In this case, NEP has the units of  $W/\sqrt{Hz}$ . A detector with an NEP of  $10^{-9} W/\sqrt{Hz}$  can detect a signal power of one nanowatt ( $10^{-9} W$ ) with a signal-to-noise ratio (SNR) of one after one half second of averaging. In such case, the NEP is simply found by the ratio of the noise current to the photosensitivity (NEP  $[W/Hz^{1/2}] =$

$$NEP \left[ \frac{W}{Hz^{1/2}} \right] = \frac{\text{Noise Current} \left[ \frac{A}{Hz^{1/2}} \right]}{\text{Photosensitivity} \left[ \frac{A}{W} \right]}$$

In either case, this measurement is valid only when the dark-current noise dominates the noise level as will be discussed later in the chapter.

- **Specific Detectivity**

The NEP value provides a great insight into the sensitivity of the detector.

However, it introduces a bias in the detector comparison since NEP depends

on the area of the detector. Another figure of merit that is used to characterize the performance of a detector while removing the dependence on the area is the specific detectivity,  $D^*$ . It is defined as the reciprocal of the NEP value normalized by the area of the detector.  $D^*$  provides a great method for comparing different detectors and is defined as:

$$D^* = \frac{\sqrt{(A_d \Delta f)}}{NEP}$$

, where:

$$D^* = \text{specific detectivity} \left[ \frac{\text{cm} \cdot \sqrt{\text{Hz}}}{\text{W}} \right]$$

$$A_d = \text{area of the photosensitive region of the detector} [\text{cm}^2]$$

$$\Delta f = \text{signal bandwidth} [\text{Hz}]$$

$$NEP = \text{noise equivalent power} [W/\sqrt{\text{Hz}}]$$

The higher the  $D^*$  the lower the noise in a system [126]. Finally, it is important to note that detectivity is different from specific detectivity.

Detectivity is simply the inverse of the NEP ( $D = 1/NEP$ ) and thus,

$$D^* = D \sqrt{(A_d \Delta f)}$$

- **Response Time**

Response time is another important aspect that measures a detectors performance. It is the time required for a detector to respond to an optical input and is expressed as the time required for a photodetector to go from 10% to 90% of its final response state. The two main variables that determine the response time of a detector are the transit-time spread and the RC time constant. The transit-time spread is the time required to collect the

charge carriers which contribute to the output of the detector. The RC time constant is a delay imposed by the inherent resistance and capacitance of any detector. Both resistance and capacitance increase the response time by integrating the current output of the detector. Other variables may also control the response time of a detector such as diffusion time and avalanche build-up time but to a lesser extent. The response time in such cases is equal to the root mean square sum of all the variables.

- **Bandwidth**

Bandwidth of a detector is a measure of the maximum frequency that can be measured. It is related to the response time. However, more common definitions relate the bandwidth to the time constant of the system,  $\tau$ , which is the time it takes a detector output to reach  $\left(1 - \frac{1}{e}\right) \approx 63\%$  of its final steady state value and is defined as:

$$\Delta f = \frac{1}{2\pi\tau}$$

, where  $\tau$  is the time-constant of the system.

- **Energy Resolution**

Energy resolution is a measurement typically used in nuclear medical applications to determine the ability of a detector to accurately measure the energy of the incoming radiation. It is expressed as a percentage of the energy of the incoming photons. For example, if a system has an energy resolution of 10% and only 140 KeV photons are striking the camera, the

system will record photons ranging from 133 KeV to 147 KeV; it can determine the incoming energy within 10% of the actual energy.

Energy resolution is defined

$$\frac{\sigma}{E} = \frac{\sqrt{N_\gamma}}{N_\gamma} = \sqrt{\frac{1}{N_\gamma}}$$

, where

$N_\gamma$  is the number of incident photons

A more accurate definition is given by

$$\frac{\sigma}{E} = \sqrt{\frac{ENF}{N_\gamma \eta C_{ol}} + \left(\frac{ENC}{N_\gamma \eta C_{ol} G_p}\right)^2}$$

, where

$N_\gamma$  = number of incident photons

$\eta$  = quantum efficiency

$C_{ol}$  = collection efficiency

ENF = excess noise factor

ENC = the equivalence noise charge (readout noise)

This measurement is used to measure the overall performance of a camera responding to high energy photons (i.e. gamma, x-ray, etc.) and since the primary focus of this thesis is NIR light detection, energy resolution will not be covered any further.

- **Excess noise factor (ENF)**

The excess noise factor (ENF) is simply the noise added to the signal due to the inherent internal gain mechanism of a detector. Different noise

mechanisms contribute in different ways to the detector gain and these will be discussed further with each detector.

### **Thermal Detectors**

Thermal detectors convert photon energy into heat. The photons are absorbed in the detector material which causes the temperature of the detector to change. The temperature change in the material causes a change in the properties of the detector material (i.e. thermoelectric voltage, resistance, pyroelectric voltage, etc.). For example, pyroelectric detectors change their electrical polarization; bolometers change their electrical resistance; etc. Thermal detectors are approximately wavelength independent. First approximations assume that the photon absorption mechanism of thermal detectors is independent of the photon wavelength, and thus, these detectors do not depend on the nature or spectral features of the photons, but rather respond directly to the radiant power (watts). Thermal detectors include thermoelectric, bolometric, etc. Table 2.1 below shows different thermal detectors along with the detector property that is measured which correlates to the light radiant power. These detectors are typically used for wavelengths from the IR up to sub-mm wavelength.

<b>Detector</b>	<b>Method of operation</b>
Bolometer	Change in electrical conductivity
Thermocouple/Thermopile	Voltage generation caused by change in temperature of the junction of two dissimilar materials
Pyroelectric	Changes in spontaneous electrical polarization
Golay cell/Gas microphone	Thermal expansion of a gas
Absorption edge	Optical transmission of a semiconductor

Pyromagnetic	Changes in magnetic properties
Liquid crystal	Changes of optical properties

Table D.1: Thermal Detectors and their method of operation [127]

The highest possible  $D^*$  value for thermal detectors operated at room temperature is  $\sim 2 \times 10^{10} \text{ cmHz}^{1/2}\text{W}^{-1}$  [127]. While this value may be improved by cooling, it remains a problem for thermal detectors. Thermal detectors have few shortcomings including their intermediate sensitivity and slow response due to the relatively slow process of heating and cooling of the detector material. However, with advances in technology, these detectors have improved drastically and may one day become the leading choice of detectors.

### **Photoelectric detectors**

The other type of photodetector, photoelectric detectors, absorbs photons and produce electrons. Unlike thermal detectors which depend on the optical power, these detectors depend on the photon flux (photons/second) [34]. Photoelectric detectors are based on the photoeffect where photons interact with the electrons (electrons bound to the lattice atoms, electrons that are bound to impurity atoms or with free electrons). Absorption of photons by atoms causes electrons to transition to higher energy levels resulting in mobile charge carriers. These electrons would quickly recombine unless an electric field is applied through the material. An external electric field that is applied causes the free electrons to move and produce an electric current. Photoelectric detectors are further divided into two categories depending on what happens to the mobile charge carriers generated through photon absorption. The first category is the external photoeffect-based detectors where the generated electrons escape the material. This category includes

photomultiplier tubes (PMT), microchannel plate – PMTs (MCP-PMT), and streak cameras. The second category, which is the basis of most modern photon detectors, is the internal photoeffect based detectors where mobile charge carriers remain inside the material. For such detectors, the application of an electric field applied causes changes in the conductivity of the material. Unlike thermal detectors, detectors based on the photoeffect (internal or external) are wavelength dependent, with the majority of detectors showing sensitivity to a small window in the electromagnetic spectrum.

**Photomultiplier tube (PMT) detectors**

To this day, PMT detectors are the gold standard among the most sensitive detectors. A single photon striking a PMT detector generates anywhere between  $10^6 - 10^9$  electrons. With the proper resistor terminated at the output of the PMT, this current pulse is converted to voltage in the mV range which can easily be measured. A simplified schematic of a typical PMT is shown in Figure D.2 below.

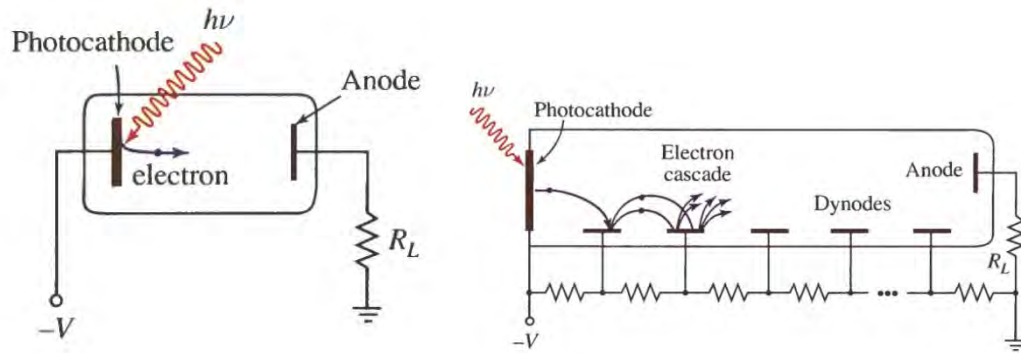


Figure D.2 the detection of light in an electron-vacuum tube is illustrated at left, where electrons are generated from a photocathode and travel through vacuum to the anode where current is generated. On the right, the electron multiplication is illustrated by sequential collision at each of the charged dynodes in a photomultiplier tube [34]

As shown in Figure 2.2, a PMT consists of a photoemissive cathode (photocathode), focusing electrode(s), electron multiplier (dynodes) and electron collector (anode). The entire apparatus is housed inside a vacuum tube. When a photon strikes the photocathode, an electron is generated (photoelectron). The focusing electrodes direct the photoelectron to the dynode chain where each dynode is then used to multiply the number of electrons through the process of secondary emission. The first conversion process, the photoelectron conversion, has a rather poor efficiency (typically below 30%). In fact, some of the emitted photoelectrons do not find their way to the first dynode and thus cannot be multiplied. This is the reason why collection efficiency is an important parameter when dealing with detectors as some of the produced charge carriers are unable to contribute to the final output.

Collection efficiency for a PMT is defined as:

$$C_{ol} = \frac{\text{Number of photoelectrons captured by first dynode}}{\text{Total number of photoelectrons emitted from the cathode}}$$

The collection efficiency of a PMT varies with wavelength and is between 60 and 90%. The remaining electron multiplication activity after the first dynode has very little noise associated with this process and is usually very efficient.

As the electrons are multiplied by each consecutive dynode in the chain, the number of electrons grows larger and larger until all the electrons are collected at the anode. The output signal therefore is a current signal consisting of a large number of electrons. By connecting the anode to the ground through a resistor, the current signal induces a voltage drop across the resistor which can be measured by electronic circuitry.

Each dynode in the dynode chain contributes to the electron multiplication. The multiplication due to each dynode is not constant and exhibits some variance. Therefore, one considers only the mean value of the secondary emission factor for each dynode ( $\delta$ ). In an n-dynode chain PMT, a single electron is multiplied by  $\delta^n$  and results in a pulse at the anode. This gain mechanism associated with the photomultiplier tube detectors makes it one of the most sensitive devices to date. Due to the variance of secondary emission, the generated output pulse has a large variance. Thus, for the same number of photons striking the PMT, output pulses with varying heights are generated. Figure D.3(a) shows an example of PMT output pulses with varying heights that may result from the same number of incident photons. Figure D.3(b) shows a histogram of the pulse height distribution. As expected, the pulse height distribution shows a Poisson characteristic except for a slight deviation at the low pulse heights side of the curve due to dark counts which will be explained later in this chapter.

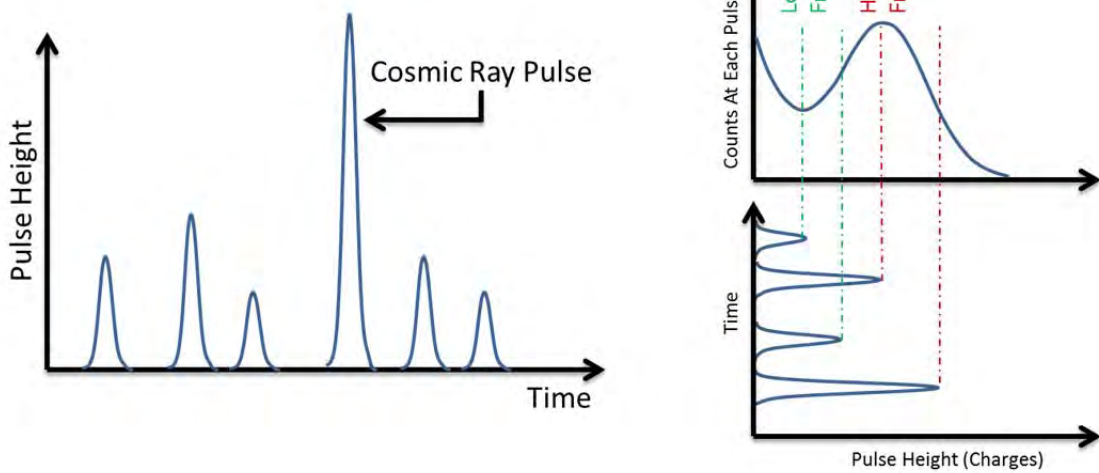


Figure D.3: a. Diversity of PMT output pulse heights (b) PMT output pulses and pulse height distribution of the pulses

A PMT detector may be operated in an analog (DC) or digital (photon counting) mode. In an analog mode, the detector is unable to resolve the effect of individual photons due to the large number of photons striking the detector. The contribution of individual photons cannot be measured, but rather the sum of contributions of all photons is summed. This mode is depicted in Figure D.4(a).

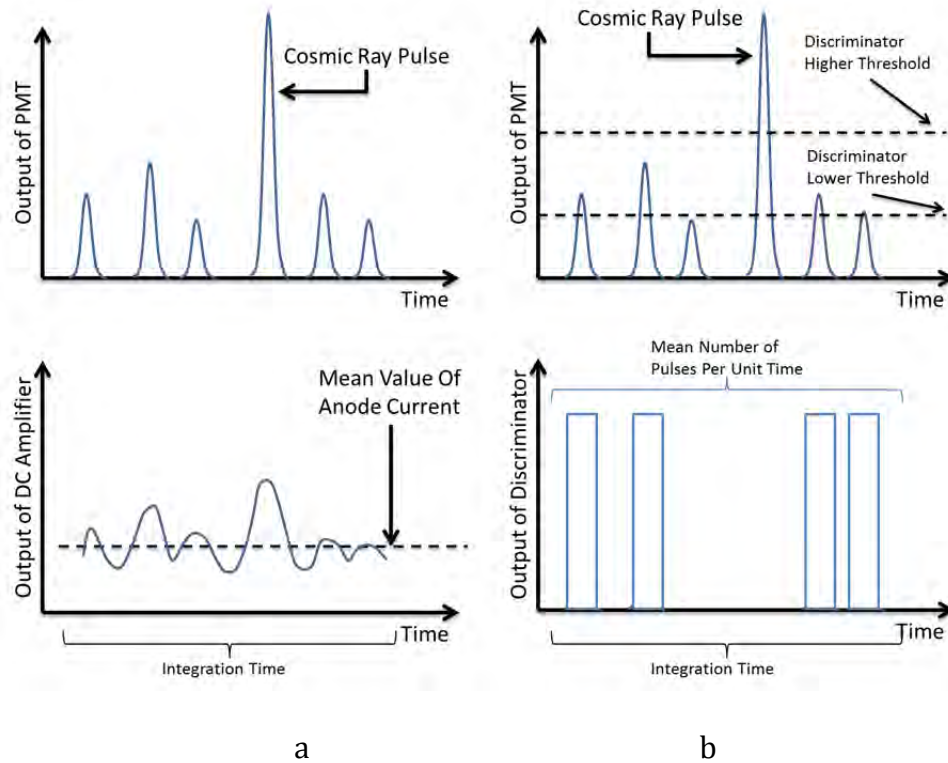


Figure D.4: PMT operation modes: (a) analog (b) photon counting

As shown in part a, even though photons generate pulses, the pulses end up overlapping each other. In this mode, the mean value of the analog current, which is proportional to the intensity of the light flux input, is measured. Due to the statistical characteristics and variance of the amplitude of the output pulses, the noise of the mean value of the anode current is larger than the photon (shot) noise. SNR is lower in the analog mode than photon counting operation mode.

In digital (photon counting) mode, the detector receives photons that are separated from each other by at least the width of the single electron response (SER) of the detector. This mode allows the individual pulses to be counted and summed, regardless of the pulse amplitude. The number of pulses counted per unit time is proportional to the light flux intensity. An immediate advantage can be seen here

where the noise associated with the output pulse variation no longer contributes to the noise of the output signal. There are several advantages to using PMTs in digital (photon counting) mode instead of the analog mode. These benefits are discussed in more detail in the photon counting section in this chapter.

The ENF of a PMT is defined as:

$$ENF = 1 + \frac{1}{\delta_1} + \frac{1}{\delta_1\delta_2} + \dots + \frac{1}{\delta_1\delta_2 \dots \delta_n}$$

This value is around 1.4 for a PMT detector and decreases with increasing gain.

The analysis below demonstrates how to calculate the signal-to-noise ratio for a PMT. The signal-to-noise is expressed in root mean square (r.m.s). For the waveform shown in Figure D.5, the signal-to-noise is defined as:

$$\frac{S}{N} = \frac{I_{mean.signal}}{I_{rms.signal+rms.background}} = \frac{I_{mean.signal+mean.background} - I_{mean.background}}{I_{rms.signal+rms.background}}$$

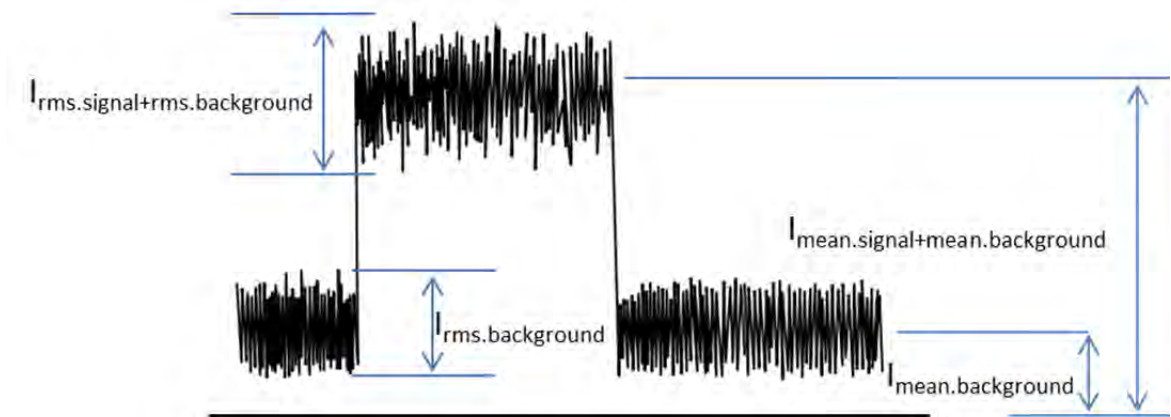


Figure D.5

The signal to noise ratio of a PMT depends on the operation mode. For analog measurements, in order to calculate the SNR, we have to consider the noise sources. In analog mode, the noise sources include shot noise due to the input light, shot

noise due to background, shot noise due to dark current, and finally noise due to the amplifier circuit. The signal-to-noise ratio for a photomultiplier tube is calculated

as:

$$\frac{S}{N} = \frac{I_{anode\_photocurrent}}{I_{rms.noise}}$$

Thus:

$$I_{noise(r.m.s)}[A] = \sqrt{I_{backgroundshotnoise}^2 + I_{darkcurrentshotnoise}^2 + I_{photocurrentshotnoise}^2 + I_{amplifiernoise}^2}$$

, where

$$I_{rms.backgroundshotnoise}[A] = \mu \sqrt{2e ENF I_{meanbackgroundcurrent} \Delta f}$$

, where:

$\mu$  = detector gain

$e$  = electron charge [coulombs]

ENF = excess noise factor

$I_{meanbackgroundcurrent}$  = the average cathode current produced by unwanted background light [A]

$\Delta f$  = the noise bandwidth of the photodiode [Hz]

$$I_{rms.darkcurrentshotnoise}[A] = \mu \sqrt{2e ENF I_{meandarkcurrent} \Delta f}$$

, where:

$I_{meandarkcurrent}$  = the average dark current resulting from the photocathode (thermionic emission, leakage current between electrodes, and field emission current from residual gases inside the tube)

$$I_{rms.signalshotnoise} [A] = \mu \sqrt{2e ENF I_{meancathodphotocurrent} \Delta f}$$

, where:

$I_{meancathodphotocurrent}$  = the photocathode current generated by the incident light.

$$I_{amplifiernoise} [A] = \sqrt{\frac{4k T \Delta f F}{R_{eq}}}$$

Since the PMT gain is sufficiently large, the amplifier noise can generally be ignored [128].

Thus, the signal to noise ratio can be found as follows:

$$\begin{aligned} \frac{S}{N} &= \frac{I_{meananodephotocurrent}}{I_{rms.noise}} \\ &= \frac{\mu I_{meancathodphotocurrent}}{\sqrt{I_{rms.backgroundshotnoise}^2 + I_{rms.darkcurrentshotnoise}^2 + I_{rms.photocurrentshotnoise}^2}} \\ &= \frac{\mu I_{meancathodphotocurrent}}{\mu \sqrt{2e ENF \Delta f (I_{meancathodphotocurrent} + 2(I_{meandarkcurrent} + I_{meanbackgroundcurrent}))}} \\ &= \frac{I_{cathodmeanphotocurrent}}{\sqrt{2e ENF \Delta f (I_{meancathodphotocurrent} + 2(I_{meandarkcurrent} + I_{meanbackgroundcurrent}))}} \end{aligned}$$

The anode signal current,  $I_{meananodephotocurrent}$ , defined above as

$\mu I_{meancathodphotocurrent}$  can also be calculated from the incident light power P and the anode radiant sensitivity  $S_p$  which can be found from the PMT spec sheets:

$$I_{anodemeanphotocurrent} = S_p P.$$

For light power greater than the NEP value of the PMT, the signal-to-noise ratio can be approximated as

$$\frac{S}{N} |_{\text{Lightpower} \gg \text{NEP}} = \sqrt{\frac{I_{\text{cathodmeanphotocurrent}}}{2e ENF \Delta f}}$$

Photon counting regime offers a different and a higher signal-to-noise ratio. For photon counting measurements, in order to calculate the SNR, we also have to consider the noise sources as well, which include shot noise resulting from the signal light, shot noise resulting from the background light, and shot noise resulting from the dark counts:

$$n_{ph} = \sqrt{N_{ph}} \quad n_b = \sqrt{N_b} \quad n_d = \sqrt{N_d}$$

, where:

$n_{ph}$  = the shot noise resulting from the signal light

$N_{ph}$  = the number of counts from the signal light

$n_b$  = the shot noise resulting from the background light

$N_b$  = the number of counts from the background light

$n_d$  = the shot noise resulting from the dark counts

$N_d$  = the number of counts from the dark counts

For photon counting mode, the signal-to-noise ratio can then be calculated as:

$$\frac{S}{N} = \frac{N_{ph}}{N_{total}} = \frac{N_{ph}}{\sqrt{N_{ph} + 2(N_b + N_d)}}$$

The number of counts/sec,  $N'$ , can be found using the formula  $N' = N/t$ . Therefore, the signal-to-noise ratio expressed in counts/sec using the above formula yields:

$$\frac{S}{N} = \frac{N_{ph}}{N_{total}} = \frac{N'_{ph} \sqrt{t}}{\sqrt{N'_{ph} + 2(N'_b + N'_d)}}$$

As can be seen from the equation above, the signal-to-noise ratio can be improved as the measurement time is made longer.

Comparing both analog and photon counting operations, the signal-to-noise ratio of analog and photon counting for a signal with 1 Hz bandwidth signal is:

$$\frac{S}{N}(\text{analog}) = \frac{I_{\text{meancathodephotocurrent}}}{\sqrt{2e ENF (I_{\text{meancathodephotocurrent}} + 2(I_{\text{meandarkcurrent}} + I_{\text{meanbackgroundcurrent}}))}}$$

$$\frac{S}{N}(\text{photoncounting}) = \frac{N_s}{\sqrt{2(N_s + 2N_d)}}$$

As can be seen, the signal-to-noise ratio of the photon counting regime is better than the analog regime by the factor ENF. Furthermore, using a discriminator increases the signal-to-ratio in photon counting mode through elimination of dark counts and random cosmic pulses that cannot be removed in the analog regime. The discriminator is discussed in detail in chapter 3. Setting a lower discriminator level can suppress most of the dark counts ( $N_d$ ) while setting an upper discrimination level can suppress spurious counts caused by cosmic radiation, as shown in figure 2.4(b), which produce higher noise pulses and cause signal degradation that cannot be eliminated in analog mode.

NEP for a PMT can easily be found by setting the signal-to-noise ratio to 1. Ignoring the shot noise, the NEP can be simplified to:

$$NEP[W] = \frac{\sqrt{2e I_{\text{meananodedarkcurrent}} \mu \Delta f}}{S}$$

, where

$e$  = electron charge [ $1.6 \times 10^{-19}\text{C}$ ],

$I_{\text{meananodedarkcurrent}}$  = anode dark current in amperes [A],

$\mu$  = detector gain,

$\Delta f$  = bandwidth of the system in hertz [Hz],

$S$  = anode radiant sensitivity in amperes per watt at the wavelength of interest [A/W].

Typical NEP values for a bandwidth of 1 Hz for a PMT are between  $10^{-15}$  and  $10^{-16}$  Watts [35]. This translates to detection of 400 to 4000 photons per second for a 800 nm photons. Cooling the PMT can improve the NEP value by reducing dark current. Cooled PMT detectors are able to reach NEP values of  $10^{-21} \text{ W/Hz}^{0.5}$  [36]. Including shot noise in the calculation above will reduce the NEP value slightly. The difference, however, will increase with increasing bandwidth.

Finally, the electron multipliers, dynodes, of a PMT consist of 8 up to 19 stages. These stages are arranged in different configuration where each configuration yielding certain over other configurations. Figure D.6 shows different types of configurations that are commonly found with PMT detectors and table D.2 below shows some of the properties for different PMT dynode configurations.

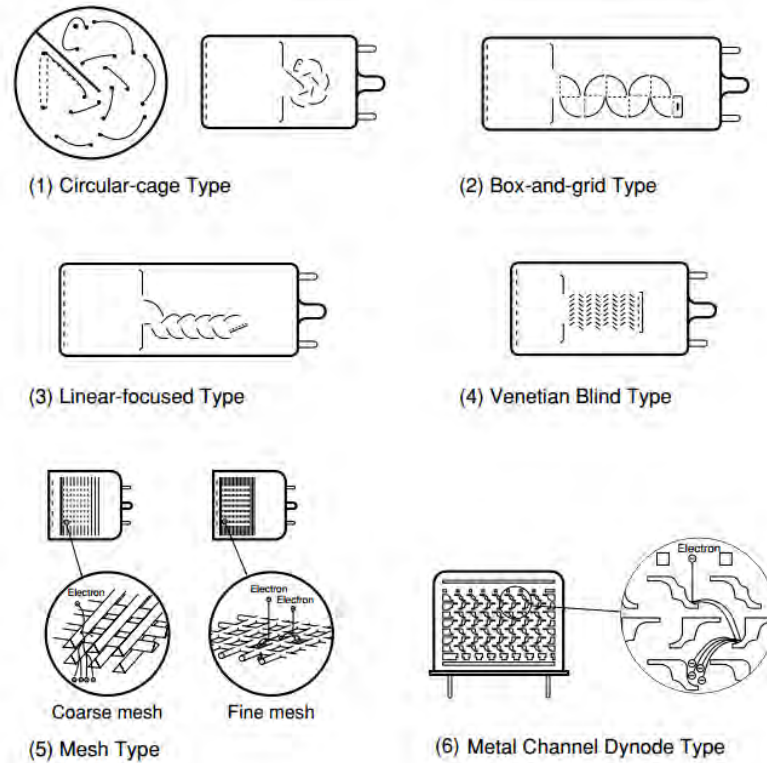


Figure D.6 Types of electron multiplier structures used with PMT detectors [35]

Dynode Type	Rise Time (nS)	Collection Efficiency	Features
Circular	0.9 to 3	Good	Compact, high speed
Box-and-grid	6 to 20	Very good	High collection efficiency
Linear focused	0.7 to 3	Good	High speed, high linearity
Venetian Blind	6 to 18	Poor	Suited for large diameter
Fine Mesh	1.5 to 5.5	Poor	Higher magnetic field immunity (up to 1.5T for magnetic field parallel to tube axis)
Metal Channel	0.65 to 1.5		Compact, high speed

Table D.2 Typical characteristics of dynode types [35]

### Microchannel Plate PMT (MCP-PMT) Detectors

The second type of photoelectric based detectors is the microchannel plate PMT (MCP-PMT). The MCP-PMT is similar to the conventional PMT except it replaces the

dynodes with an array of high number (millions) of capillaries (channels) in a glass plate as shown in Figure D.7. The faces of both sides of the plate are coated with thin metal films that act as the electrodes. Applying a voltage across these electrodes creates an electric field that causes the electron to accelerate from one electrode (anode) to the other electrode (cathode). The channels, whose inner diameter is  $\sim 10\mu\text{m}$ , are coated with a material that emits secondary electrons. Therefore, each channel acts as independent-continuous dynode multiplying the electrons as they hit the walls.

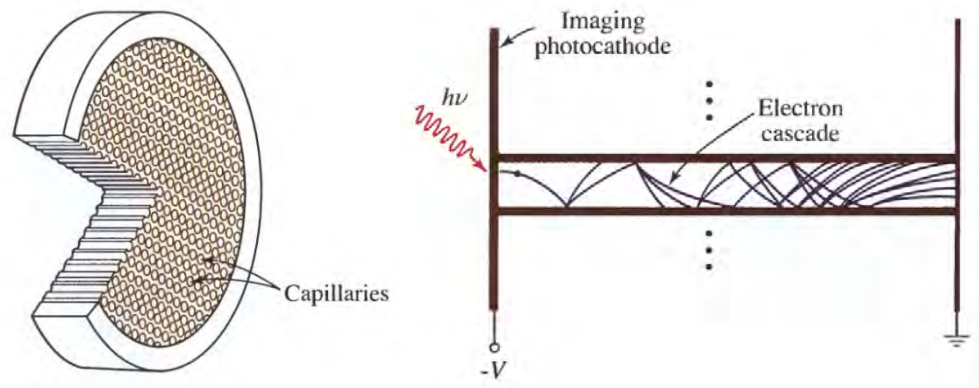


Figure D.7: (a) Cutaway view of Microchannel-plate PMT, (b) electron multiplication in a single capillary of a microchannel plate [34]

The MCP-PMT offers timing improvement over the PMT (down to the ps level) as well as low-light level detection at the photon counting mode. Furthermore, they exhibit better immunity to magnetic fields due to their construction.

### Streak Cameras

A streak camera is a two-dimensional detector that is able to record ultra-short light events. It transforms the temporal profile of an input pulse into a spatial profile on the detector by use of a time-varying electric field. Streak cameras offer a superior

temporal resolution that can reach as low as 100s of femtoseconds compared to other detectors [129].

Figure D.8 shows the schematic of a streak camera [130]. Four pulses that vary in time, position, and intensity are shown at the input. As these pulses enter the streak camera, they first pass through a slit. Optical lenses are used to focus the light input on the photocathode. The incident light is then converted into electrons proportional to the intensity of the light. The electrons are then accelerated towards a micro-channel plate (MCP). On their way to the MCP, the electrons pass between a pair of electrode plates which are used to deflect the electrons so that photoelectrons that arrive at different times hit the detector at a different position. The electrons are deflected via a time-varying electric field applied to the electrodes that is synchronized to the incident light. As the electrons pass through the MCP, they are multiplied several thousand times and then the electrons are converted to light after they hit a phosphor screen. A detector, such as a charged-couple device (CCD) detector, is used to measure the streak pattern on the phosphor screen, and thus one can infer the temporal profile and intensity of the input light pulse.

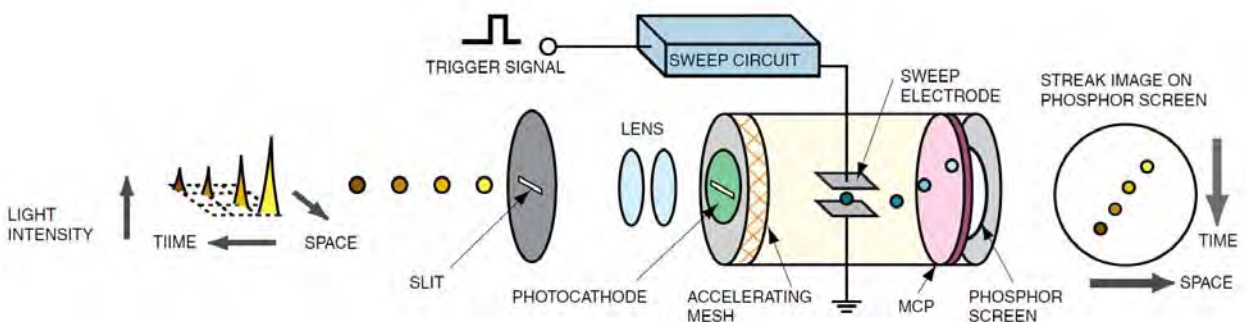


Figure D.8: Operating principle of a streak tube [130]

A streak camera, therefore, is used to transform changes in the temporal and spatial light intensity input into a 2D streak image where one dimension carries spatial information and the other dimension carries time information. The intensity of the input light is directly proportional to the intensity of the output image. Thus, every point in the streak image provides information representing intensity, location, and time. For example, a single flash on a streak camera would look like a streak along the temporal axis. The length of the streak on the image is directly related to the duration of the flash that it represents.

### **Internal photoeffect detectors**

The second type of photoeffect-based detectors is the internal photoeffect detectors where electrons remain inside the material. Most modern detectors are based on semiconductor technologies that rely on the internal photoeffect where a photon is absorbed in the material resulting in a free excited electron. If an electric field is applied, the electron drifts towards the positive side of the field. An electron leaving its valance band creates an unoccupied state where other electrons in the valance band attempt to occupy. In the absence of an electric field, the free electron would find an unoccupied state and fill it up, thus, emitting a photon in the process.

However, in the presence of an external electric field, the unoccupied state is filled up with a valance electron, creating another unoccupied state which itself gets occupied by another valance electron and the process continues to repeats.

Therefore, the electrons in the valance band move to fill in the unoccupied state, which may be regarded as a movement of electrons in the opposite direction of the hole that was created by the free electron. The hole may be thought off as an

electron but with a positive charge. This electron-hole pair is responsible for the electric current in the device.

Semiconductors are crystalline or amorphous materials with electrical conductivity that is between conductors and insulators. The properties of a semiconductor can be tailored to fit specific applications simply by controlled addition of impurities. These devices are the foundation of modern solid state electronics.

Semiconductors can be divided into intrinsic and extrinsic semiconductors.

Intrinsic semiconductors are pure semiconductors with no embedded impurities with a structure similar to the one shown in Figure D.9.a. Extrinsic semiconductors have impurities added to the semiconductor in a process known as doping. An example of an extrinsic semiconductor is shown in Figure D.9.b. In both types of semiconductors, current conduction occurs via free electrons and holes, collectively known as charge carriers. The advantage of doping is that it increases the number of charge carriers.

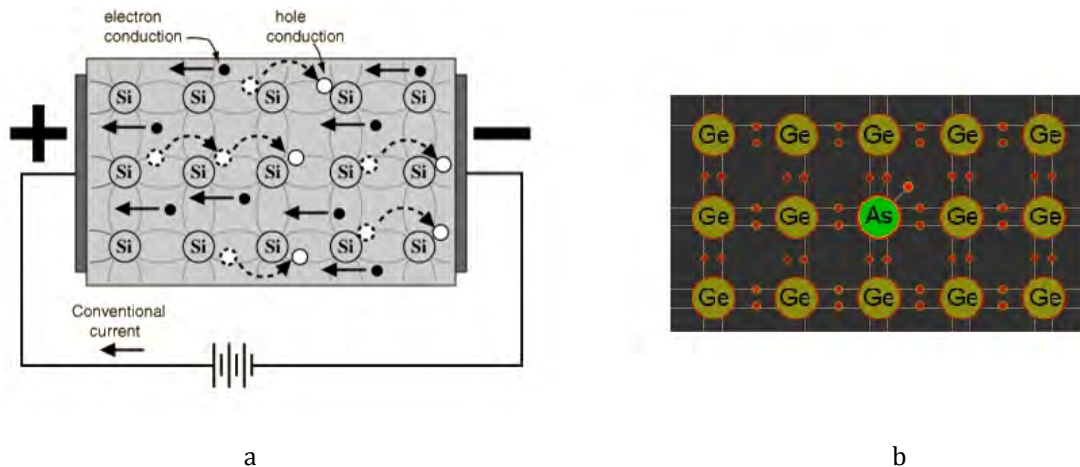


Figure D.9: (a) intrinsic (pure) semiconductors (b) extrinsic semiconductor

Extrinsic semiconductors are of two types: n-type and p-type. A p-type semiconductor contains a larger holes concentration than electrons whereas an n-

n-type semiconductor contains larger electron concentration than holes. N-type semiconductors are obtained by doping an intrinsic semiconductor with donor impurities whereas P-type semiconductors are obtained by doping an intrinsic semiconductor with acceptor impurities.

Intrinsic semiconductors have limited uses in photon detection. Examples of photon detectors that are based on this type are photoresistors which are identical to Figure 2.9(a). While these detectors are able to detect photons, they have low sensitivity and are not suitable for low light level detection.

Photons absorbed in the p-n junctions have a quantum efficiency approaching 100%, but the intrinsic noise of these devices limit the detection of low light signals[117]. Besides, it is totally immune to magnetic fields[117].

The spectral range of operation for these types of detectors is limited. The upper limit of operation depends on the band gap energy of the detector. The photovoltaic effect cannot occur for photons with energy below the band gap energy of the detector. For example, the band gap energy of silicon photodetector is 1.12 eV. The cut-off wavelength for these detectors can be found via the formula:  $\lambda_c [nm] = \frac{1240}{E_g}$ .

For example, the cut-off wavelength for a silicon based semiconductor photon detector is around 1100nm. Table 2.3 below shows the energy band gap and the corresponding cut-off wavelength for the three most common materials used in semiconductor photon detectors.

(T=300K)	$E_{gap}$ (eV)	$\lambda_{gap}$ (nm)
----------	----------------	----------------------

Ge	0.66	1880
Si	1.11	1150
GaAs	1.42	870

Table D.3: Energy band gap and corresponding cut-off wavelength for common semiconductor detectors

The lower wavelength limit is determined by the degree of photon absorption. Short wavelength photons are immediacy absorbed on the surface of the material and any hole-electron pairs would simply recombine at the surface and not contribute to any output current. Devices can be designed with thin layers, which can improve the short-wavelength response of the detectors.

### **Photoresistor**

A photoresistor, also known as a photoconductor, light dependent resistor, or a Cadmium sulfide (CdS) cell, is an undoped semiconductor with no semiconductor junctions (i.e. P-N, P-I-N, etc) as shown in Figure D.10 below.

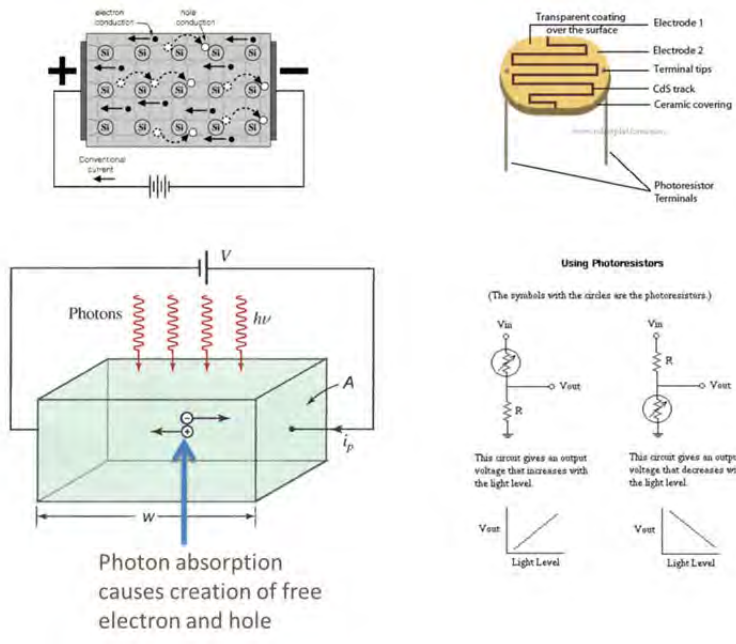


Figure D.10: Photoresistor [34]

It is essentially a resistor whose resistance decreases with increasing incident light intensity. Remarkably, these detectors provide an internal gain mechanism. The output current generated is a function of the incident light power, quantum efficiency of the device, and the ratio between the excess-carrier recombination lifetime and the electron transit time across the detector:

$$i_p \approx \eta \left( \frac{\tau}{\tau_e} \right) e\Phi$$

, where:

- $i_p$  = electric current [A]
- $\eta$  = detector efficiency
- $\tau$  = excess-carrier recombination lifetime [s]
- $\tau_e$  = electron transit time across the sample [s]

$e$  = electron charge [C]

$\Phi$  = photon flux [photons/sec]

The detector has internal gain since the recombination lifetime  $\tau$  and the transit time  $\tau_e$  differ. For example, referring to Figure 2.10(c), if the electrons travel faster than the holes and the recombination lifetime of the electrons and holes is long, as the electrons and holes travel to the opposite sides of the photoconductor, the electron will complete its trip before the hole, which forces the external circuit to provide an additional electron. The process may repeat many numbers of times until the electron recombines with the hole.

Photoresistors have a zigzag pattern as shown in Figure 2.10(b) in order to maximize the exposed area as well as enhance the gain of the detector.

Photoresistors, however, cannot be used to determine precise light levels. They have a limited bandwidth and limited sensitivity. The NEP of photoresistor does not typically exceed  $3 \times 10^{-9} \text{ W/sm/Hz}^{1/2}$ .

### **Photodiodes/PIN photodiodes**

A Photodiode is a fast, highly linear photon detector with high quantum efficiency.

It is a semiconductor device where a P-layer and N-layer regions form a p-n junction which is the basic element of a photodiode. By controlling the thickness of these layers as well as the dopant concentration in the layers, the spectral and frequency response of the photodiode can be controlled to fit various applications. Figure 2.11 shows a schematic of the cross section of a typical photodiode.

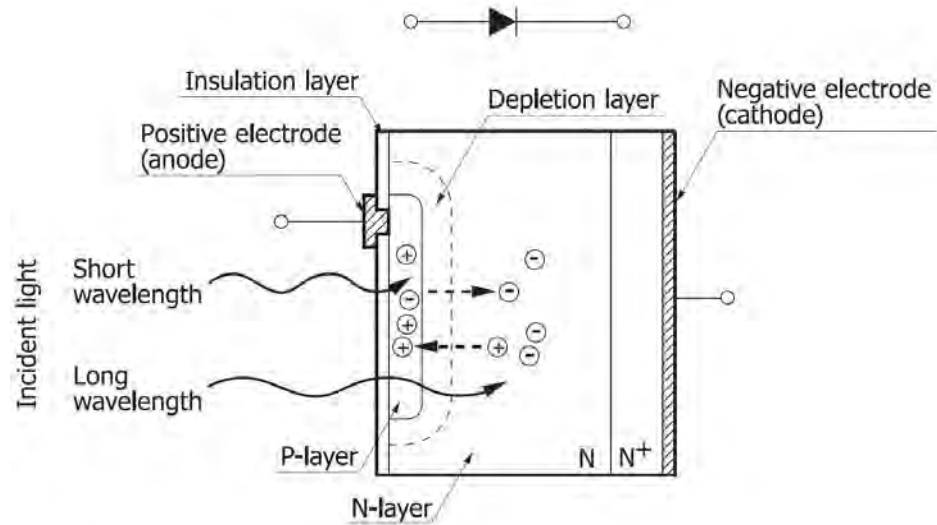


Figure D.11: Schematic of Si Photodiode Cross Section [37]

Light (with sufficient energy) incident on a photodiode generates electron-hole pairs throughout the photodiode in proportion to the light level. Due to the dopant concentration which offers excess electrons in the n-layer and excess holes in the p-layer, the electron-hole pairs distribute themselves in such a manner which results in an accumulation of positive charge in the P-layer and a negative charge in the N-layer. If connected to a circuit, electrons will flow away from the N-layer side and holes will flow away from the p-layer type resulting in an electric current in the circuit.

While the electrons and holes rearrange themselves in the PN junctions, a depletion region that is free of excess carriers (no holes or electrons) is created. Adding a voltage potential across the PN junction of the device creates an additional electric field which in turn, enables a larger depletion region and aids in transporting the carriers to their respective terminals; holes are transported to the anode side (p-layer) and electrons are transported to the cathode side (n-layer).

A PIN photodiode, shown in Figure D.12(b), is similar to an ordinary photodiode except it has an additional intrinsic (un-doped) layer sandwiched between the p and n layers and is thus called p-i-n or PIN photodiode. This region provides better and smoother depletion region which has advantages over ordinary photodiodes and will be discussed later in this section.

When light is incident on the photodetector, photons that are absorbed in the depletion region or the intrinsic region in a PIN photodiode create electron-hole pairs, most of which contribute to the photocurrents. These electron-hole pairs are swept from the junction by the electric field where holes move toward the anode and electrons move toward the cathode, thus, generating a photocurrent.

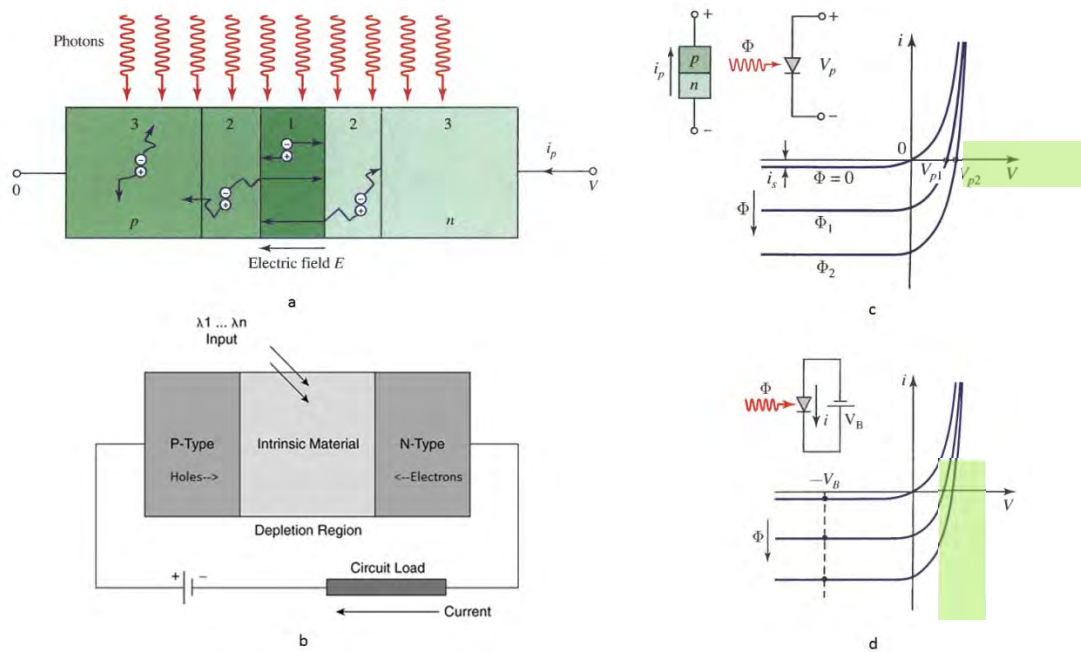


Figure D.12: (a) photons illuminating an ideal reverse-biased p-n photodiode, (b) PIN photodiode operation, (c) forward-biased (photovoltaic) operation of a photodiode, (d) reverse biased operation of a photodiode

A p-n junction allows current to flow easily in one direction (forward biasing) but hardly at all in the other direction (reverse biasing). In forward biasing mode depicted in Figure D.12(c), also may be known as zero-bias mode, the detector generates current as light is absorbed by the detector. This mode of operation requires no biasing voltage and it is said that the detector is operating in the photovoltaic region. This mode has the advantage that the dark current is kept at a minimum. However, the maximum speed is not achieved.

In reverse biasing mode, as shown in Figure D.12(d) an external reverse voltage bias is applied, which increases the width of the depletion region, resulting in an increase in responsivity and a decrease in junction capacitance which leads to an increase in the response time of the detector. Detectors operating in reverse bias mode are said to operate in the photoconductive mode. The output signal in this mode is highly linear. The dependence of the photocurrent on the light power can be very linear over six or more orders of magnitude of the light power, e.g. in a range from a few nanowatts to tens of milliwatts for a silicon p-i-n photodiode with an active area of a few  $\text{mm}^2$  [48]. However, this mode has a higher dark current contribution to the output signal resulting in a slightly less sensitive detector compared to the forward (zero) biased mode.

Junction capacitance and shunt resistance are both important properties of a photodiode. Junction capacitance is the capacitance caused by storage of charge across the PN junction. It depends mainly on the thickness of the depletion region. Increasing the reverse bias voltage increases the thickness of this region which in turn reduces the junction capacitance resulting in an increase of the detector's

response time. The junction capacitance is also a function of the resistivity of the silicon and the active area size of the detector. Shunt resistance is the resistance of the zero-biased photodiode. Although an ideal photodiode has an infinite shunt resistance, actual values range from 10 ohm up to  $10^9$  ohms [131].

The advantage of a PIN photodiodes over ordinary photodiodes is that the intrinsic region between the pn junctions provides several advantages:

- 1- Increasing the width of depletion layer increases the light sensitive area of the detector.
- 2- Increasing the width of depletion layer reduces the junction capacitance and thereby improves the RC time constant

One of the disadvantages of photodiodes is that they provide no internal gain mechanism. One photon generates a single electron-hole pair. Therefore, these detectors must use an amplifier circuit in order to amplify the output signal and detect low light levels. Furthermore, in order to detect a signal, the incident light must be larger than the inherent noise of the detector. With photodiode, noise limits the sensitivity of these detectors in room-temperature to several hundred photons [38].

Photodiodes are fabricated with different materials, each of which results in different photodiode characteristics. Table D.4 below shows some of the most common materials used in building photodiode detectors along with some of their basic characteristics.

Material	Dark Current	Speed	Sensitivity	Cost
Silicon (Si)	Low	High Speed	400 - 1000 nm	Low
Germanium (Ge)	High	Low Speed	900 - 1600 nm	Low

Material	Dark Current	Speed	Sensitivity	Cost
Gallium Phosphide (GaP)	Low	High Speed	150 - 550 nm	Moderate
Indium Gallium Arsenide (InGaAs)	Low	High Speed	800 - 1800 nm	Moderate
Indium Arsenide Antimonide (InAsSb)	High	Low Speed	1000 - 5800 nm	High
Extended Range Indium Gallium Arsenide (InGaAs)	High	High Speed	1200 - 2600 nm	High
Mercury Cadmium Telluride (MCT, HgCdTe)	High	Low Speed	2000 - 5400 nm	High

Table D.4: Different photodiode materials and their properties [131]

A photodiode noise is equal to the sum of the thermal (Johnson) noise of the detector, shot noise due to the dark current, and shot noise due to the photocurrent:

$$I_{rms.noise} [A] = \sqrt{I_{rms.thermal}^2 + I_{rms.darkcurrentshotnoise}^2 + I_{rms.photocurrentshotnoise}^2}$$

, where

$$I_{rms.thermal} [A] = \sqrt{\frac{4kTB}{R_{sh}}}$$

, where:

k = the Boltzmann's constant [J/K],

T = the absolute temperature of the photodiode [K],

B = the noise bandwidth of the photodiode [Hz]

$R_{sh}$  = is the shunt resistance of the photodiode at zero bias

$$I_{rms.darkcurrentshotnoise} [A] = \sqrt{2eI_{meandarkcurrent}B}$$

, where:

e = the electron charge,

$I_{meandarkcurrent}$  = the photodiode dark current,

$$I_{rms.signalshotnoise} [A] = \sqrt{2eI_{meanphotocurrent}B}$$

, where:

$I_{\text{meanphotocurrent}}$  = the current generated by the incident light.

When  $I_{\text{meanphotocurrent}} \gg I_{\text{meandarkcurrent}}$ , then the photocurrent shot noise dominates over the dark current shot noise.

For an unbiased photodiode, there is no dark current contribution and the signal-to-noise ratio can be calculated from:

$$\frac{S}{N} = \frac{I_{\text{meanphotocurrent}}}{I_{\text{rms.noise}}} = \frac{I_{\text{meanphotocurrent}}}{\sqrt{\frac{4kTB}{R_{sh}} + 2eI_{\text{meanphotocurrent}}B}}$$

For light levels greater than the NEP, the signal-to-noise ratio can be approximated as:

$$\frac{S}{N} |_{\text{Lightpower} \gg \text{NEP}} = \sqrt{\frac{I_{\text{meanphotocurrent}}}{2eB}}$$

, which is very similar to the case of PMT detectors.

NEP for a photodiode at zero bias can be calculated from the following equation:

$$\text{NEP} = \frac{\sqrt{\frac{4kTB}{R_{sh}}}}{\mathfrak{R}}$$

, where  $\mathfrak{R}$  is the photo sensitivity in Amperes/Watt

For a 1 cm<sup>2</sup> active area detector, a typical value of NEP is around 10<sup>-12</sup> W/Hz<sup>-0.5</sup> [36].

The NEP value is a strong function of temperature due to the direct temperature dependence and due to the dependence of the shunt resistance  $R_{sh}$  on the

temperature. Also, smaller area detectors can reach a higher NEP value of around

10<sup>-15</sup> W/Hz<sup>-0.5</sup>.

Adding a bias voltage may slightly increase the sensitivity of the photodiode but will also increase the dark current, thus, decreasing the NEP value.

The response time of a photodiode is the time required for the output signal to change from 10% to 90% of the peak output and is governed by the 1)  $t_1$ : time constant of the capacitance and load resistance of the detector, 2)  $t_2$ : time needed for carriers generated outside depletion region to diffuse through depletion region and contribute to the generated output (diffusion time), 3)  $t_3$ : time needed for carriers to travel through the device and contribute to the current output. The total rise time is thus:

$$tr = \sqrt{t_1^2 + t_2^2 + t_3^2}$$

The smaller the photodiode, the smaller the rise time. Typical rise times for a regular photodiodes are about  $\sim 1 \mu\text{s}$  whereas rise times as fast 1 ns can be found for small-area PIN type photodiodes.

### **Avalanche photodiodes**

Avalanche photodiode detectors (APDs) are another type of semiconductor based detectors. These detectors are similar to photodiodes except that they improve the detectors' performance by utilizing a gain mechanism that amplifies the number of electron-hole pairs created from photons.

APD are PIN photodiodes with an additional p-layer sandwiched between the i-n junctions as shown in Figure D.13. A very high electric field is created when a high reverse bias voltage is applied across the junction. Electron-hole pairs are created as photons are absorbed in the depletion region. As the electrons are transported to one terminal of the junction, they collide with the atomic lattice. Since the electric

field is so large, the electron gains enough energy that collisions with the lattice causes it to release additional electrons via secondary (or impact) ionization. This multiplication process creates an avalanche of electron-hole pairs. The original charge is amplified by a factor of 20 to 1000 depending on the magnitude of the reverse voltage applied. The charge multiplication is called the avalanche effect and hence the name of the detector.

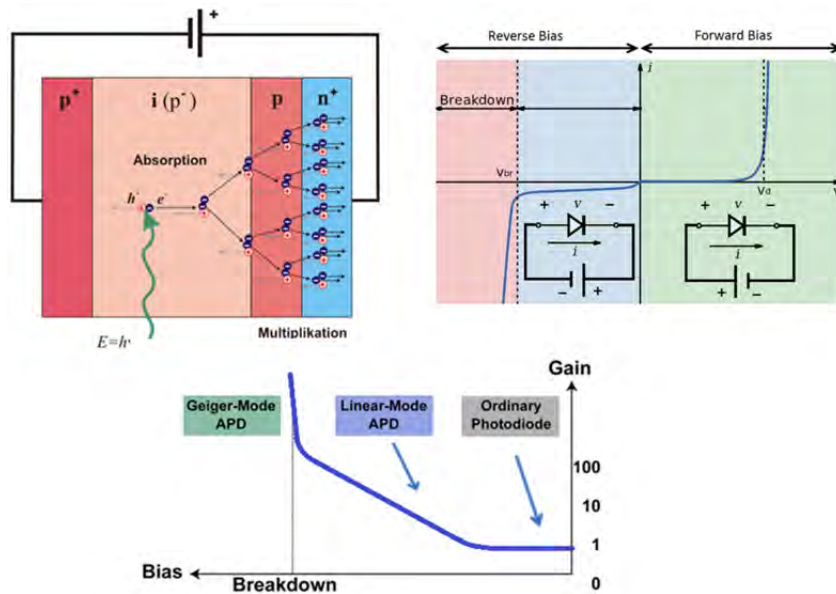


Figure D.13: (a) Avalanche photodiode (b) i/V photodiode relation showing breakdown region (c) Gain vs. bias voltage for photodiodes

This mode of operation is called the non-Geiger mode where the avalanches are limited by the reverse voltage. Another mode of operation that is discussed in more detail with single photon avalanche diode detectors increases the reverse voltage to such a level that a self-sustaining avalanche is created. This mode of operation is referred to as Geiger mode.

In both modes of operation, the sudden increase and the self-amplifying current can easily damage the device. Therefore, precautions have to be taken in order to avoid high currents which would damage the device.

In non-Geiger mode, the APD output is proportional to the incident light. APDs however have a limited dynamic range and are mainly used in very low light level applications. They have good quantum efficiency with a spectral range between 300 nm to 1,000 nm.

One of the issues that plague APDs is the issue of afterpulsing. Afterpulsing is a phenomenon where phantom pulses are generated some time after the generation of the primary pulse. This is due to electron charges being trapped in the semiconductor dopant during the avalanche caused by the primary pulse. These trapped charges themselves cause an avalanche which results in a false pulse which may be regarded as a true pulse. While cooling the APD may result in a decrease in the dark current, afterpulsing becomes more apparent at low temperatures.

Therefore, the operation of an APD, which is usually operated at -50 C, requires one to find the sweet spot between a minimum dark count and a minimum afterpulse.

APD detectors offer a better sensitivity than PIN photodiodes while still providing the advantage of high quantum efficiency, robustness, and insensitivity to magnetic fields. The NEP value of APD's can reach  $10fW/\sqrt{Hz}$ . Even though APDs are very sensitive detectors, they are not able to detect single photons. A minimum of 10-20 photons are needed for a detectable signal. Also, APD detectors have a high excess noise factor due to the stochastic nature of the avalanche multiplication process.

The excess noise factor associated with APDs is greater than 2 [42]. Figure 2.14 shows the excess noise factor as a function of gain.

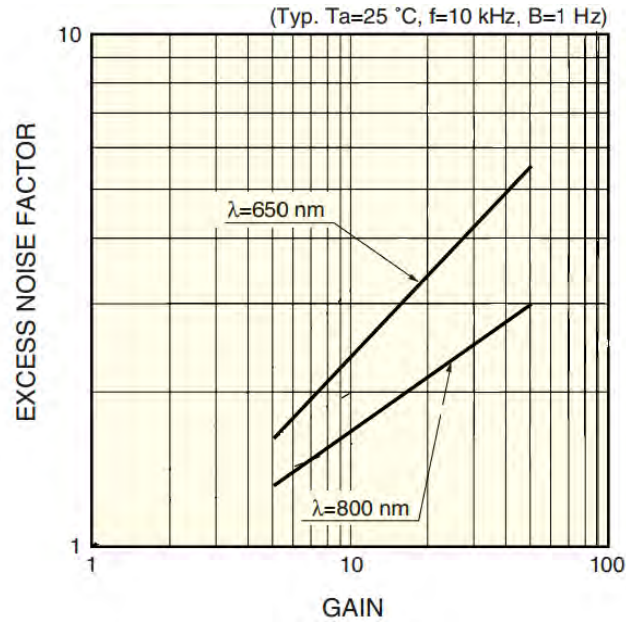


Figure D.14: Excess noise factor for APD detectors as a function of gain [132]

Another drawback of using APD detectors is the need for low noise amplifiers for readout due to the limited detector gain (20-1000). Also, as the area of the detector increases, the capacitance of the junction increases which increases the transit time of the charge carriers implying a tradeoff between noise and timing and thus, the larger the APD, the slower the response time. Making a large area, yet stable APD is not trivial [117].

The response time of an APD is governed by the time constant of the capacitance and load resistance of the detector (CR time constant) and time needed for carriers to travel through the device and contribute to the current output which is usually

dictated by the CR time constant. Depending on their size, APD detectors are able to achieve a high bandwidth than can reach up to 1GHz.

The major noise contribution in an APD is due to excess noise which is the noise due to statistical fluctuations of the ionization rate during the APD multiplication process.

The APD sensitivity is limited by the shot noise (due to random statistical fluctuations of the dark current) and by the APD leakage current. The APD shot noise is larger than that of a typical PD or PIN photodiode:

$$\begin{aligned}
 I_{shotnoise(r.m.s)}[A] &= \\
 &= \sqrt{I_{photoncurrentshotnoise}^2 + I_{bulkdarkcurrentshotnoise}^2 + I_{surfaceleakagedarkcurrentshotnoise}^2} \\
 &= \sqrt{2e I_{meanphotocurrent} B M^2 F + \{2e I_{surfacecurrent} B + 2e I_{bulkdarkcurrent} B M^2 F\}} \\
 &= \sqrt{2eB I_{surfacecurrent} + 2eB M^2 F (I_{meanphotocurrent} + I_{bulkdarkcurrent})}
 \end{aligned}$$

, where

$e$  = the electron charge,

$I_{meanphotocurrent}$  = photocurrent generated at  $M=1$  due to photons (prior to multiplication),  $I_{bulkdarkcurrent}$  = dark current component multiplied,

$B$  = bandwidth,

$M$  = multiplication ratio (gain),

$F$  = excess noise factor,

$I_{darkcurrent}$  = dark current components not multiplied.

Ignoring background shot noise, the signal to noise ratio can be calculated from:

$$\begin{aligned} \frac{S}{N} &= \frac{I_{\text{meanphotocurrent}}}{I_{\text{rms.noise}}} = \frac{I_{\text{meanphotocurrent}}}{\sqrt{(I_{\text{shotnoise}}^2 + I_{\text{rms.Johnsonnoise}}^2)}} \\ &= \frac{I_{\text{meanphotocurrent}}}{\sqrt{(I_{\text{photoncurrentshotnoise}}^2 + I_{\text{bulkdarkcurrentshotnoise}}^2 + I_{\text{surfaceleakagedarkcur}}^2)}} \\ &= \frac{I_{\text{meanphotocurrent}}M}{\sqrt{\{2qB (I_{\text{surfacecurrent}}) + 2qB M^2 F (I_{\text{meanphotocurrent}} + I_{\text{bulkdarkcurrent}})\}}} \end{aligned}$$

In most cases, the lower limit of light detection is determined by the thermal (Johnson) noise due to the load resistor connected to the APD detector. From the equation above, and figure 2.15 below, a signal can be multiplied without increasing the total noise until the shot noise reaches a level equal to the thermal noise [35].

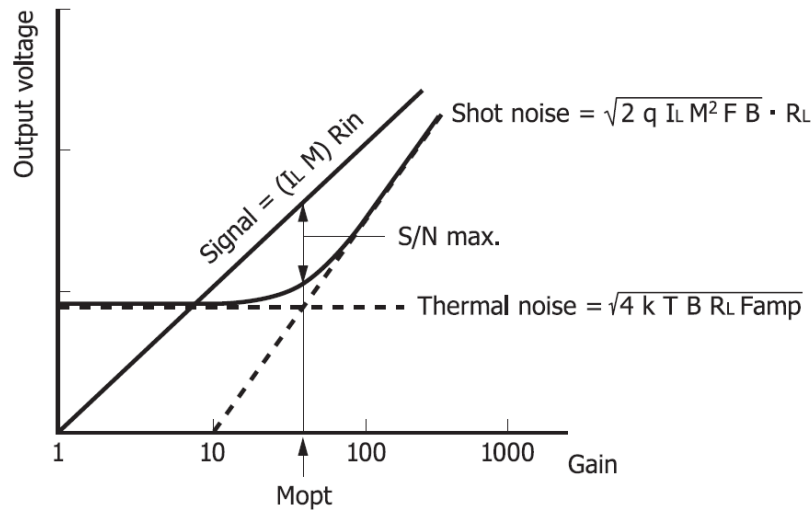


Figure D.15. APD noise characteristics [35]

APDs are characterized by high detection efficiency (80%) and typical dark count rate for an APD at room temperature is below 1000 counts/sec. Cooling the detector reduces the dark counts exponentially. However, cooling will also increase the after-pulsing of the detector and a balance must be established between dark

count rates and after-pulsing. Excess noise factor for APD's is rather very large (larger than 2 and increases with higher gain). The table below shows excess noise factor for different types of APD.

Detector Type	Typical Gain (M)	Excess Noise Factor (ENF)
Silicon (reach through structure)	150	4.9
Silicon (SLiK™ structure)	500	3
Germanium	10	9.2
InGaAs	10	5.5

Table 2.5: Excess noise factor for different APD detectors

The typical size of an APD is below  $1 \times 1 \text{ mm}^2$ . Such detectors can reach a cutoff frequency of around 1 GHz. APD's as large as of  $10 \times 10 \text{ mm}^2$  can be found but with a much slower response ( $<10\text{MHz}$ ). Figure 2.16 shows a typical APD circuit. The main components of the circuit are a power supply to apply the reverse biasing, a load resistor that limits the current in the circuit in order to avoid damaging the detector, and an amplifier circuit to amplify the detector output further.

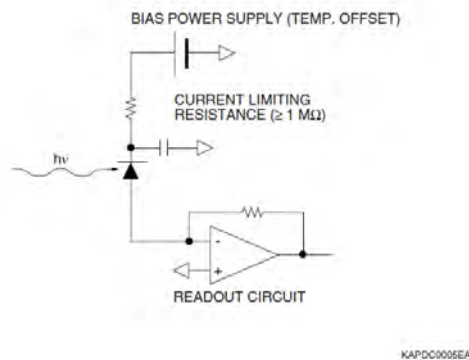


Figure D.16 [132]

## Single photon Avalanche Photodiodes

Single photon avalanche photodiodes (SPADs), also known as Geiger-mode APD, are semiconductor based photon detectors that can detect low intensity signals down to the single photon level. These detectors are essentially APD detector except that they are biased above the breakdown voltage as shown in Figure D.17. Biasing above the breakdown voltage causes a photon to trigger a self-sustaining avalanche multiplication throughout the volume of the detector which breaks the semiconductor junction and essentially transforms the detector into a conductor. Thus, a single photon is transformed into a macroscopic current flow. In APDs, only the electrons participate in the avalanche process. In the Geiger-mode, however, both electrons and holes are involved in the multiplication process. This inherent gain mechanism enables detection of single photons.

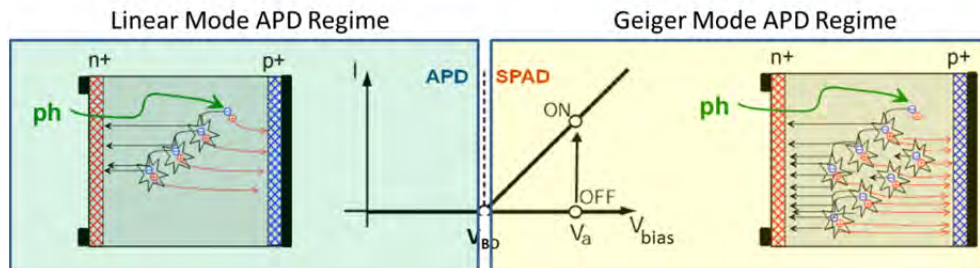


Figure D.17: Linear mode and Geiger mode photodiode operation modes

A detector that is triggered once is not a very useful detector and therefore, a reset mechanism is needed to stop the avalanche and avoid any detector damage.

Stopping the avalanche is called avalanche quenching, which plays an important role in the operation speed of the detector.

Quenching basically consists of lowering the bias voltage below the breakdown voltage for a period of time in order to stop the Geiger discharge. Three different

quenching approaches are available with SPAD detectors. The simplest and most cost effective approach is to place a resistor in series with the detector. Once the detector is triggered, the large current would flow through the resistor resulting in a voltage drop across both the resistor and detector, thus quenching the detector. This is referred to as passive quenching and is shown in Figure 2.18 below. A quenching resistor connected to a SPAD configures the circuit to output a pulse at a constant level when it detects a photon. Also, the dead time is very well defined. The disadvantage of this approach is that it limits the count rate to around  $10^5$  counts/second.

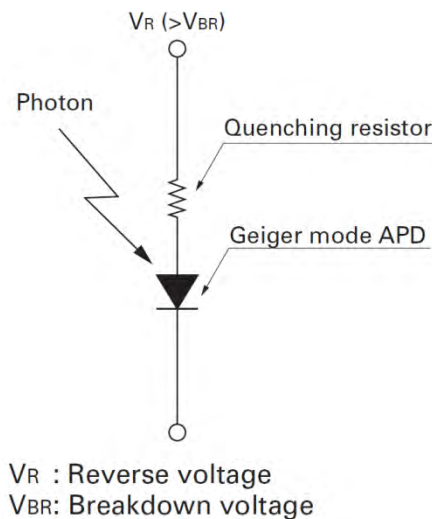


Figure D.18: SPAD operating circuit with passive quenching resistor

The second quenching approach, referred to as active quenching, uses dedicated electronic circuits to lower the bias voltage below the breakdown voltage for a certain period of time until the detector is quenched. This approach improves timing accuracy as well as it reduces dead time of the detector recovery, thus, enabling higher count rates exceeding  $10^6$  counts/sec. Figure D.19 shows examples of active quenching. As can be seen from these circuits, active quenching is more

complicated and requires careful design to avoid issues such as circuit oscillations, improver timings,

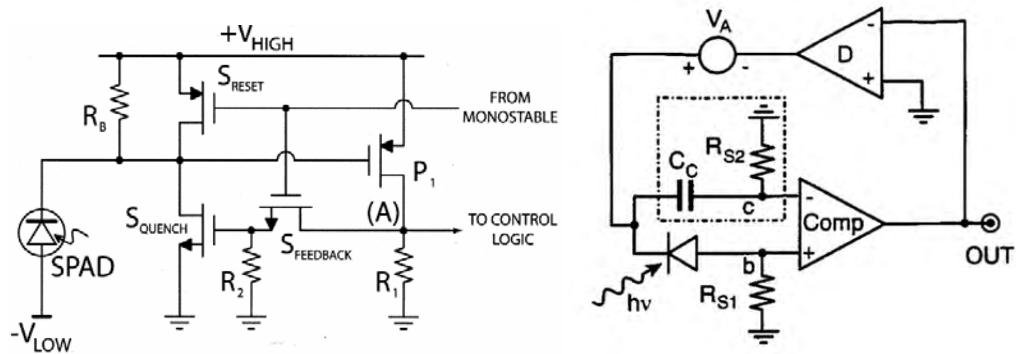


Figure D.19: Examples of SPAD active quenching circuits

SPAD detectors are essentially binary detectors: they are either 'on' or 'off'. They cannot distinguish between a single photon and multiple photons that arrive simultaneously on the detector – they cannot be used to measure magnitude of light intensity (photon flux) directly. These detectors can be used with photon counting techniques at very weak light levels as they have very fast rise time. However, the recovery time of these detectors is usually slow and extend from few nanoseconds up to 100's of nanoseconds.

In order to calculate the efficiency of SPAD detectors, a measure other than quantum efficiency (QE) is used that takes the probability of forming an avalanche into consideration. Photon detection efficiency is defined as the product of the quantum efficiency (probability to produce an electron-hole pair) times the probability of the electron-hole pair triggering an avalanche in the detector material:  $PDE = QE * PA$

SPAD detectors have a high PDE and low dark counts. Cooling the detector reduces the dark count exponentially and allows the detector to be used for photon counting

applications. After-pulsing caused by trapped carriers remains a problem, and overall, these detectors are limited to count rates in the tens of MHz.

SPAD detectors are only useful for very small area detectors (100 – 10,000  $\mu\text{m}^2$ ) since dark counts caused by thermal generation can reach up to  $6 \times 10^8$  per second per  $\text{cm}^2$  for a 450  $\mu\text{m}$  thick fully depleted silicon [42] [12]. In fact, a typical PMT with an active area of 2.5cm produces around 1000 electrons/s at room temperature whereas a SPAD with an active area of around 200 $\mu\text{m}$  is required to produce the same dark count. The density of dark counts for a PMT detector is < 200 electrons/ $\text{cm}^2$  s while this number is <  $4 \times 10^6$  electrons/ $\text{cm}^2$  s for a typical SPAD detector. The small detector size is acceptable for applications which can focus the light into the detector area.

Noise in SPAD is due to statistics of dark counts and photons. The inherent high gain of these detectors enables the use of low gain amplifiers which adds very little noise to the process, thus, making these detectors great for photon counting applications.

NEP for SPAD detectors can be found using the equation[133]:

$$NEP [W \text{ Hz}^{-1/2}] = \frac{h\nu}{PDE} \sqrt{\frac{N_{dark}}{t}}$$

, where:

$h$  = Planck's constant

$\nu$  = the frequency of the light

PDE = the photon detection efficiency

$N_{\text{dark}}$  = the number of dark counts/second

$t$  = the integration time.

Typical NEP values for SPAD detectors can reach as high as  $10^{-15}$   $\text{WHz}^{-0.5}$ . [134]

[135]

### Silicon PMT

The silicon photomultiplier is a novel semiconductor detector which consists of an array of SPAD detectors in parallel as shown in Figure D.20. Each SPAD represents one pixel (also referred to as a microcell) of the SiPM detector that is capable of detecting single photons. SiPM detectors are known by many names in the literature where some of the common ones include multipixel photon counter (MPPC), pixelized photon detector (PPD), multipixel Geiger-mode avalanche photodiode (MPGM APD), Geiger-mode avalanche photodiode (G-APD), solid state photomultiplier (SSPM), etc. These detectors overcome the weakness of the smaller size of SPAD detectors

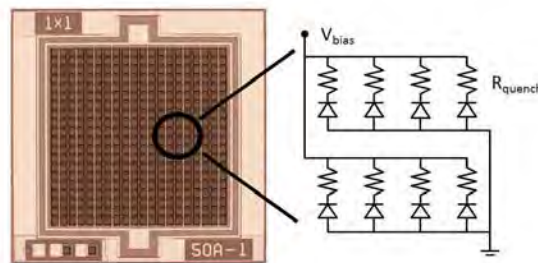


Figure D.20: SiPM detector showing SPAD array

When the photon flux is low and photons arrive at intervals longer than the recovery time of a pixel, the output of a SiPM detector will be pulses that are equal to a single photoelectron and photon counting can be used to count the number of

photons and deduce the intensity of light. Note that all the pixels are connected to a single readout channel. When the photon flux is high or the photons arrive in short pulses with intervals less than the recovery time of a pixel, the output pulses from the pixels will overlap each other and create a larger pulse as shown in figure D.21 below for 2 and 3-photoelectron pulses [40]. This pseudo-analog output can measure the number of photons per pulse which is not possible with SPAD detectors. By measuring the height or by integrating the area of each pulse, the number of photons detected can be estimated and the photon flux can be measured.

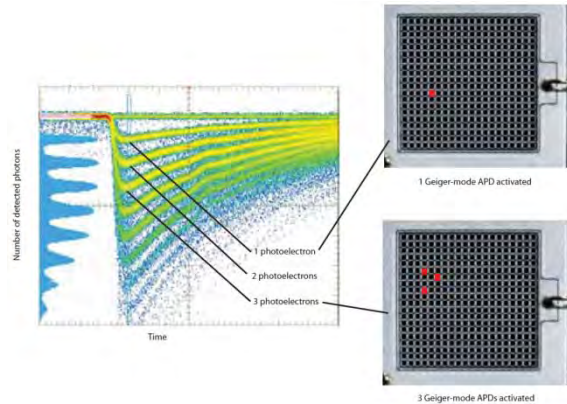


Figure D.21: Pulse waveform for different number of photoelectrons

In order to calculate the efficiency of SiPM detectors, the photon detection efficiency takes the fill factor into consideration and is defined as:

$$PDE(\lambda, V) = QE(\lambda)\epsilon(V)GE$$

, where

QE = the quantum efficiency,

$\epsilon$  = the avalanche initiation probability,

GE = the geometrical efficiency (fill factor) which reflects the fraction of

photosensitive surface of the device due to the fact that each pixel is surrounded by some strip of insensitive material separating the pixels from each other.

The PDE of three similar SiPM detectors but with different fill factor is shown in the figure below.

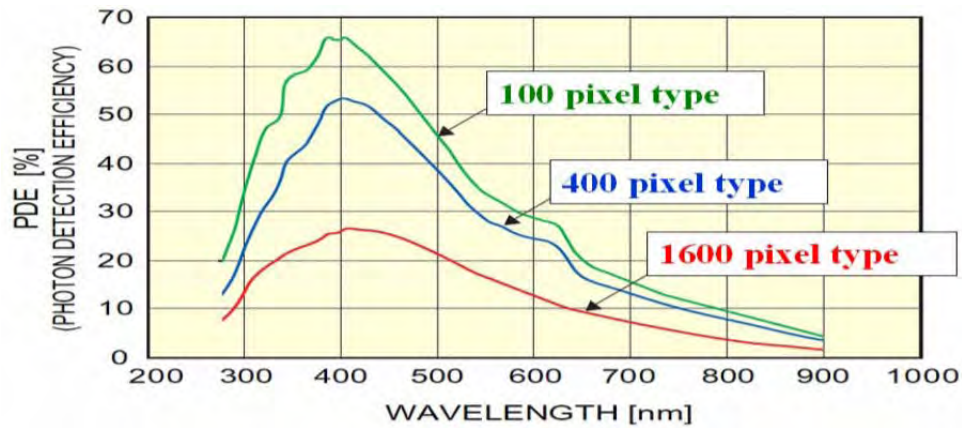


Figure D.22: PDE curve for SiPM detectors with different pixel numbers [REF]

Typical pixel size varies between 20-100 $\mu$ m with a pixel density between 100 and 1000 per  $\text{mm}^2$  (highest density achieved so far is around 1600 pixel per  $\text{mm}^2$ ).

Typical active areas range between 1x1 to 3x3  $\text{mm}^2$ . SiPM detectors have numerous advantages: they are solid state devices, compact, rugged, durable, require low bias voltage (<100V) and low power consumption, low cost (<\$300), easy to use, high photon detection efficiency (PDE  $\sim$  20% and increasing with a potential of reaching 70%), high gain ( $10^5 \sim 10^6$ ), good speed response (300 – 900 nm), good time resolution, have a wide spectral response range, have no burn in phenomena that might occur due to light saturation, they tolerate accidental illumination, and can be used for photon counting. Also, these detectors are insensitive to magnetic fields up to 15 Tesla. Another distinguishing feature of these detectors is their ability to resolve the number of photons striking the detector. The pulse height spectrum

(PHD) of a SiPM detector shows a resolution better than most photon detectors. An example PHD curve is shown in Figure 2.23.

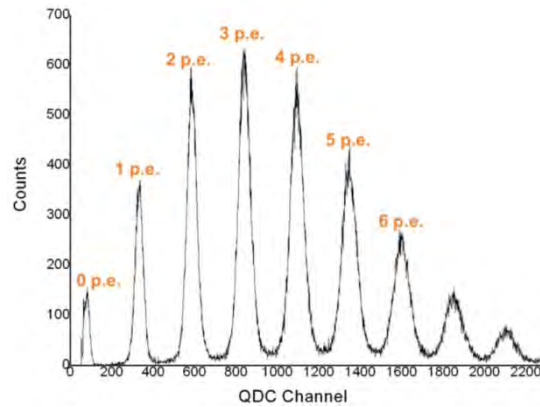


Figure D.23 [43]

These detectors, however, do have few drawbacks. Their dynamic range is limited by the number of available pixels – the output signal is proportional to the number of triggered pixels for as long as the number of incident photons in a pulse ( $N_{\text{photon}}$ ) times the PDE is smaller than the number of available pixels ( $N_{\text{Available}}$ )

$$N_{\text{triggered}} = N_{\text{available}} \left( 1 - e^{-\frac{\text{PDE} \cdot N_{\text{photon}}}{N_{\text{available}}}} \right)$$

Figure 2.24 shows simulation of the response for a 1000 and 3600 pixel SiPM detectors when uniformly illuminated with 50ns duration light pulses of increasing brightness. At low signal levels, the SiPM output is linear. After a certain point, the response becomes sub-linear since as the number of photons increase, and the probability of two or more photons interacting with the same pixel at the same time increases. As the number of photons increase, the output will then saturate.

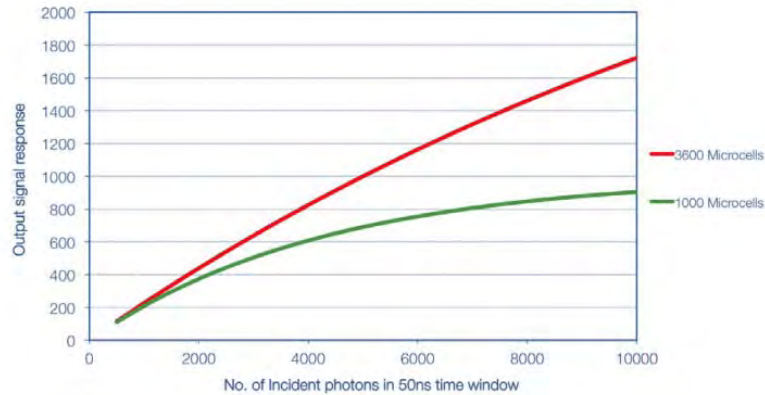


Figure D.24: Linearity for SiPM detectors with 3600 and 1000 pixels [43]

Also, their dark count rate is high. Dark counts are caused by thermally generated electrons afterpulsing, and optical cross talk where thermally generated electrons are the dominant contributor for SiPM detectors. At room temperature, typical dark count rates are  $10^5$ - $10^6$  counts per second per  $\text{mm}^2$  [42] [42]. The dark pulses have a Poisson distribution in time and so the noise contribution is the square root of the dark count rate. Reducing the volume of the detector or cooling the detector will reduce the dark counts significantly. Another method that combats dark counts is to use a discriminator and set its threshold value above the single electron level which improves the dark count rate substantially. Figure D.25 below shows effect of setting different discriminator threshold values

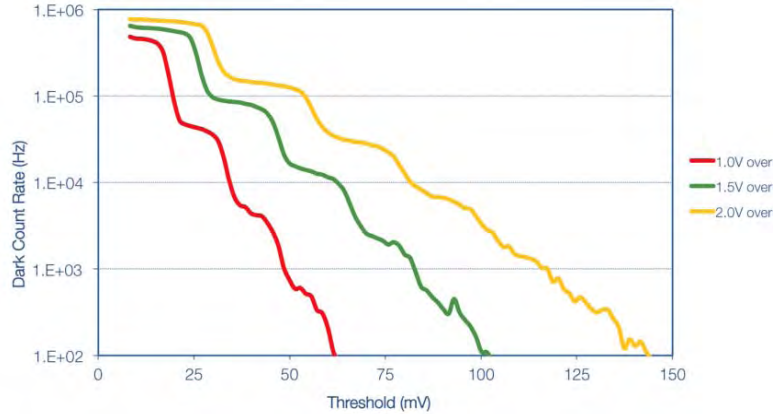


Figure D.25. Dark count rate of a 1mm, 35um microcell SPM as a function of discriminator threshold for different over-voltage levels [43].

However, reducing the temperature further may enhance dark counts caused by afterpulsing. Afterpulsing was discussed with APD and SPAD detectors and it is virtually the same as in SiPM detectors.

Optical cross talk is another issue that plagues SiPM detectors where an avalanche in one pixel will initiate another avalanche in a neighboring pixel. During avalanche multiplication, carriers near the junction emit photons as they are accelerated by the high electric field. Three photons with energy higher than 1.14 eV are emitted for  $10^5$  carriers during an avalanche breakdown [44]. Increasing the discriminator threshold reduces the dark count rate including dark counts due to optical cross talk. The breakdown voltage and the dark count rate are both a function of temperature. Temperature stabilization may be required for some applications using these detectors. Finally, NEP values for SiPM can reach as low as  $0.5 \times 10^{-15} \text{W/Hz}^{0.5}$  [45]

### CCD and ICCD

Charged-coupled devices (CCDs) are a silicon-based semiconductor consisting of a dense matrix of biased-photodiodes. The electrons generated from photons striking

the detector material are stored in potential wells and are transferred across the chip through registers to amplifiers that convert the charge into a voltage signal which is directly related to the photon flux hitting the pixels.

There are different architectures to transfer the electrons from the wells to the amplifier such as frame transfer CCDs (FT CCDs), full frame transfer CCDs (FFT CCDs), interline transfer CCDs (IT CCDs), and frame interline transfer CCDs (FIT CCDs). All these techniques utilize registers in order to store and/or move the stored charges from a pixel to the amplifier. Different architectures have different advantages. The architectures are beyond the scope of the thesis and will not be discussed here.

The main sources of noise in a CCD detector include:

- 1- fixed pattern noise ( $N_{\text{fixedpatternnoise}}$ ) due to pixel non-uniformities. This noise appears as blemishes on the captured image.
- 2- Photon shot noise ( $N_{\text{photocurrentshotnoise}}$ ) due to the inherent statistical variation of the arrival of photons incident on the CCD:

$$N_{\text{photonshotnoise}} = \sqrt{\eta P}$$

, where:

$\eta$  = quantum efficiency,

$P$  = input photon flux

- 3- Background photons shot noise ( $N_{\text{photocurrentshotnoise}}$ ) due to contribution of unwanted backgrounds light photons that may find their way to the CCD:

$$N_{\text{photonshotnoise}} = \sqrt{\eta B}$$

, where:

$\eta$  = the quantum efficiency,

$B$  = the background photons flux

- 4- Dark current shot noise ( $N_{\text{darkcurrentshotnoise}}$ ) caused by the statistical variation in the number of electrons thermally generated within the silicon structure:

$$N_{\text{darkcurrentshotnoise}} = \sqrt{Dt}$$

, where:

$D$  = the dark current in electrons/pixel/sec

$t$  = the exposure time in seconds

- 5- Readout noise ( $N_{\text{readoutnoise}}$ ): This is the error produced during the process of quantifying the electronic signal on the CCD. It is caused by the conversion of charges into a voltage signal via the on-chip preamplifier as well as spurious charges arising in the CCD.

The total noise can be expressed as

$N_{\text{rms.noise}}$

$$= \sqrt{N_{\text{fixedpatternnoise}}^2 + N_{\text{photocurrentshotnoise}}^2 + N_{\text{darkcurrentshotnoise}}^2 + N_{\text{darkcurrentshotnoise}}^2 + N_{\text{readoutnoise}}^2}$$

Thanks to advances in semiconductor manufacturing processes, the fixed pattern noise can be ignored and the signal to noise ratio can be calculated as:

$$SNR = \frac{N_{\text{photons}}}{N_{\text{rms.noise}}} \frac{P \eta t}{\sqrt{(P\eta t) + (B\eta t) + (Dt) + (N_r^2)}}$$

Figure D.26 below shows the characteristics of these noise sources as a function of exposure time. Both the dark current shot noise and readout noise are not affected

by the exposure time, i.e. regardless of the number of incident photons or the acquisition time, these noise sources are constant.

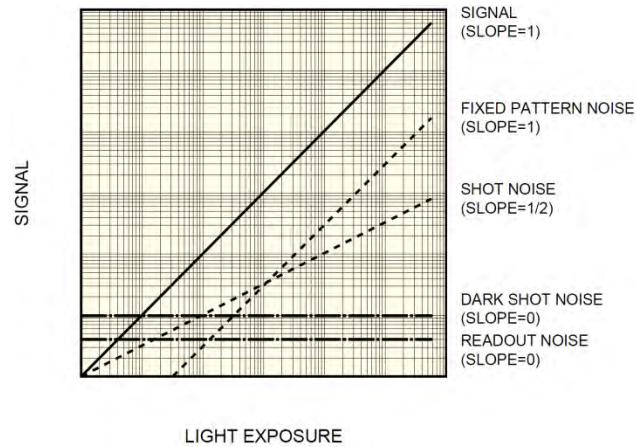


Figure D.26: Characteristics of the noise sources for a typical CCD sensor [136]

At very low exposure levels and short exposure times, the noise is dominated by the readout noise of the detector and the signal to noise ratio can be simplified to:

$$SNR = \frac{P \eta t}{N_r}$$

In a steady-state signal, the detected photon signal increases with longer exposure times. At high exposure levels, the noise is dominated by the fixed pattern noise. At room temperature, the detection limit is mostly affected by the dark current. The dark current shot noise can be dramatically reduced by cooling the CCD detector leaving the readout noise as the limiting factor in low exposure signal detection in cooled CCD detector types. By integrating over a longer period of time, the photon shot noise dominates over the readouts as well as the dark count noise, leaving an image that is said to be “photon limited”.

The signal-to-noise ratio will vary with different operating conditions such as temperature and integration time. Another means of increasing the SNR is via

binning. Binning combines the charges from adjacent pixels in a CCD during readout into a single “super-pixel”. This method enables CCD’s to reach photon-noise-limited conditions more quickly at the expense of spatial resolution. For M binned pixels, the signal-to-noise ratio can be rewritten as:

$$SNR = \frac{MP \eta t}{\sqrt{(MP\eta t) + (MB\eta t) + (MDt) + (N_r^2)}}$$

CCD cameras do not have a very large speed response with a typical response below 1MHz. The limiting factor in the speed response of the CCD camera is the on-chip charge amplifier. In order to allow for a high speed operation, the bandwidth of the amplifier must be very wide. However, the noise scales with the bandwidth of the amplifier, and hence, higher speed amplifiers result in higher noise.

Various technical innovations have been implemented on the CCD detector in order to allow for extremely low light level detection. For example, detecting a signal level below the readout noise of the CCD can be done by cooling the detector to suppress dark current noise and by integrating over a long time until the signal accumulates and becomes greater than the readout noise [137]. Employing multipinned phase (MPP) technology is able to reduce the dark current even further. The limiting factor of CCD cameras is their readout noise which is especially true at high speed rates where it becomes unacceptable.

In order to allow for low light level detection, different CCD technologies have used a different mechanisms to overcome the CCD readout noise limitations. These include: intensified CCD (ICCD), EB-CCD, and EM-CCD.

In an ICCD camera, also known as proximity-focused image intensifier, an intensifier is placed in front the CCD camera in order to enhance its light detection. The main components in an ICCD camera include a photocathode, a microchannel plate (MCP) detector and a phosphor screen as shown in Figure D.27 [138].

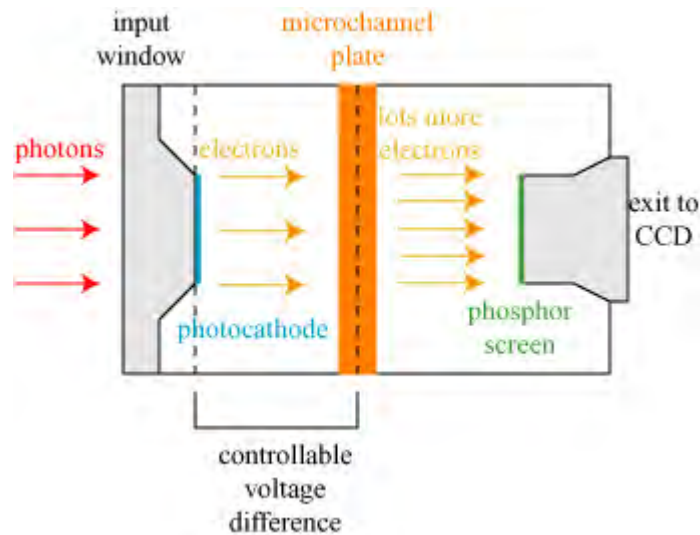


Figure D.27: Cross section of an ICCD camera.

Photons in an ICCD camera strike the photocathode generating electrons. These electrons are multiplied using the MCP detector which has been discussed earlier in this chapter. The number of electrons generated from a single electron depends on the user controllable voltage applied to the MCP. The resulting electrons strike a phosphor screen that converts these electrons back to photons which are then incident on a CCD sensor. The phosphor screen is coupled to the CCD using a fiber optic bundle or a high numerical aperture coupling lens [138].

The intensifier part of the camera directly amplifies the input light, thereby supplying the CCD sensor with a light intensity far above the thermal noise level.

Therefore, these cameras do not require strong cooling as compared to conventional CCD cameras or to EM-CCD cameras.

The EM-CCD camera is a new generation camera allowed by recent advances in technology where electrons are multiplied within the CCD detector itself. Instead of using an intensifier to amplify the light input as in the ICCD camera, the EM-CCD amplifies the electron-hole charge carriers that are generated from photons striking the detector. An EM-CCD uses an electron multiplying structure that is inserted between the shift register and the on-chip preamplifier to amplify the generated charge carriers. Thus, when a photon hits the CCD and is converted into an electron, once the pixel charge is transferred to the shift register for reading, it is inserted into an electron multiplication register. In this register, electrons are multiplied via impact ionization principle; the same principle that is responsible for multiplication in an avalanche photodiode. Figure D.28 shows the main difference between CCD and EM-CCD cameras

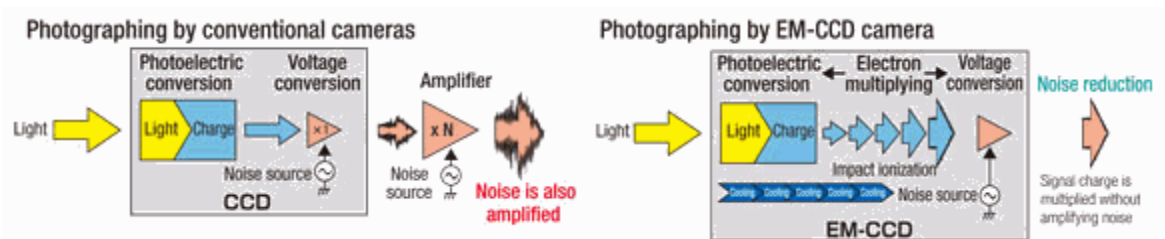


Figure D.28: Difference between CCD and EM-CCD cameras

The main advantage of EM-CCD is that the gain mechanism renders the readout noise negligible and permits the detection of single photon-generated electrons. While single photon detection is implemented with detectors such as PMT, SPAD, and SiPM detectors, it has never been available with the high quantum efficiency,

large area and convenience of a CCD. In this mode, a threshold is set above the amplifier readout noise and all events are counted as single photons. A high fraction of photons (>90%) can be counted without being effected by the ENF noise factor in this mode.

Another advantage of EM-CCD over a typical CCD camera is the operation speed. Since the electron charge is multiplied prior to the amplifier stage in an EM-CCD, the readout noise is effectively by-passed and would no longer be the limit on the sensitivity, thus, allowing for higher speed amplifiers with minimum readout noise. The multiplication involved in an EM-CCD is similar to that of APD detectors. As with APD, a single photo-electron striking the detector can give rise to a wide range of output signals. This statistical spread gives rise to the multiplication noise which manifests itself as an excess noise factor (ENF) in signal-to-noise ratio calculations, and can be approximated as  $\sqrt{2}$ . The main sources of noise in an EM-CCD detector, thus, are:

- 1- Photon shot noise ( $N_{\text{photocurrentshotnoise}}$ ) due to the inherent statistical variation of the arrival of photons incident on the CCD:

$$N_{\text{photonshotnoise}} = FG\sqrt{\eta P}$$

, where:

F = excess noise factor

G = electron gain

$\eta$  = quantum efficiency,

P = input photon flux

- 2- Background photons shot noise ( $N_{\text{photocurrentshotnoise}}$ ) due to contribution of unwanted backgrounds light photons that may find their way to the CCD:

$$N_{\text{photonshotnoise}} = FG\sqrt{\eta B}$$

, where:

$\eta$  = quantum efficiency,

$B$  = background photons flux

- 3- Dark current shot noise ( $N_{\text{darkcurrentshotnoise}}$ ) caused by the statistical variation in the number of electrons thermally generated within the silicon structure:

$$N_{\text{darkcurrentshotnoise}} = FG\sqrt{(D + S)t}$$

, where:

$D$  = dark current in electrons/pixel/sec

$S$  = the spurious charge generated when electrons are created during shifting of charges to the multiplication register and is approximately equal to one electron per 10 pixel transfers. This type of noise is not found in typical CCD cameras. This noise source is also referred to as the clock-induced charge.

$t$  = exposure time in seconds

- 4- Readout noise ( $N_{\text{readoutnoise}}$ ) caused by the conversion of charges into a voltage signal via the on-chip preamplifier

The total noise can be expressed as

$N_{\text{total}}$

$$= \sqrt{N_{\text{photocurrentshotnoise}}^2 + N_{\text{darkcurrentshotnoise}}^2 + N_{\text{backgroundshotnoise}}^2 + N_{\text{readoutnoise}}^2}$$

An EM-CCD camera can be run in conventional mode where there is no gain mechanism, in electron-multiplication mode where electrons are multiplied through the avalanche multiplication process, and in photon counting mode. In conventional mode, the signal-to-noise ratio is identical to that of a conventional CCD camera. In electron multiplication mode, the signal-to-noise ratio can be found using:

$$SNR = \frac{P \eta t}{\sqrt{(F^2 G^2 P \eta t) + (F^2 G^2 B \eta t) + (F^2 G^2 (D + S) t) + (N_r^2)}}$$

$$= \frac{P \eta t}{\sqrt{(F^2 t \eta (P + B) + F^2 t (D + S) + \left(\frac{N_r^2}{G^2}\right)}}$$

In cases where the background counts are eliminated and the camera is cooled below -100C thus eliminating the dark current, the signal to noise ratio can be approximated as:

$$SNR = \frac{P \eta t}{\sqrt{(F^2 t \eta P)}} = \frac{\sqrt{P \eta t}}{F} \approx \frac{\sqrt{P \eta t}}{1.4}$$

, assuming a typical excess noise factor of 1.4. This is remarkably close to the ideal SNR ratio one would expect from a perfect system ( $SNR = \sqrt{P \eta t}$ )

Comparing the SNR equations for the CCD and EM-CCD cameras, it can be seen that when the readout noise is greater than the photon shot noise ( $P < N_r^2$ ), then, the  $SNR_{EM-CCD} > SNR_{CCD}$  whereas the  $SNR_{CCD} > SNR_{EM-CCD}$  when the photon shot noise is greater than the readout noise. Thus, the EM-CCD gain benefits SNR in situations where the shot noise of the incoming photon signal is less than or equal to the readout noise generated for the given pixel read rate. This can also be shown from figure x.27 below which shows the probability distribution of the number output

electrons for 1, 2, 3, 4, and 5 electrons for an EM-CCD gain of 100. From the figure, an output signal of 300 electrons could have been generated either from either 3 or 4 electrons with equal probability. The overall effect is to double the variance of the signal which is statistically equivalent to halving the quantum efficiency of the camera [139].

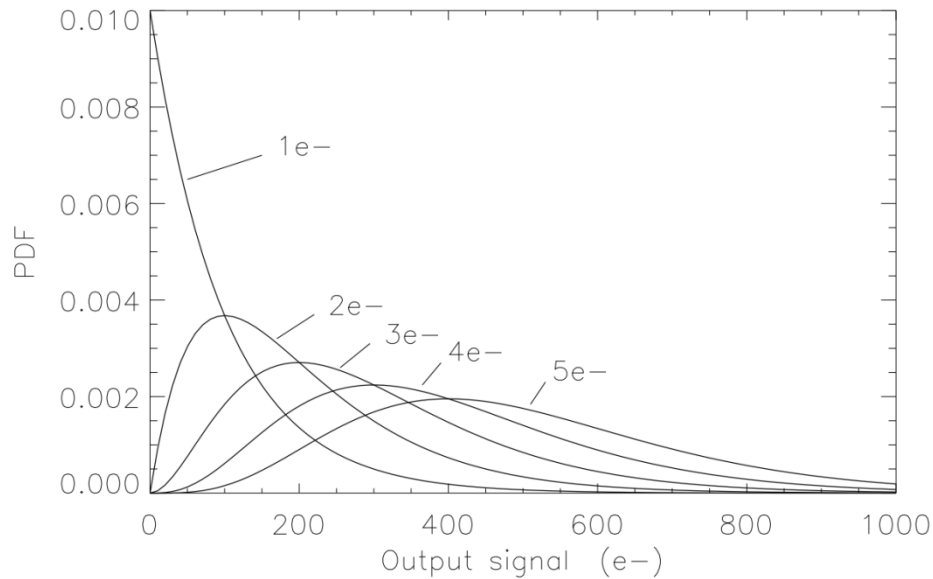


Figure D.29. Output of an EM register with  $gA = 100$  in response to a range of inputs from 1 to 5 electrons. The y-axis shows the probability density function (PDF) of the output signal, i.e. the fraction of pixels lying within a histogram bin [139]

Therefore, conventional CCD mode will result in a higher performance when photon shot noise dominates the , while EM-CCD module will result in a higher performance in readout noise dominated regime.

In photon counting mode, when the input signal is very weak and the probability of detecting two or more photons is very low, photon counting provides a signal-to-noise ratio that is very close to an ideal detector. More information about photon counting is provided at the end of this chapter.

In an ideal detector, including the effects of coincidence losses, the signal to noise ratio is given by:

$$SNR = \frac{M}{\sqrt{e^M - 1}}$$

, where M is the number of photons [139].

Since photon counting uses a threshold value in order to ignore counts not caused by photons, the signal to noise ratio maybe a bit complicated to calculate. However, for a threshold of 0.1 electron, the signal to noise can be derived according to Tulloch [139] and is found via the following equation:

$$SNR = \frac{0.9M}{\sqrt{e^{\frac{0.9(M+D+B)}{\delta} + 0.23 \ln(G)S} - 1}}$$

, where:

M = number of photons generated from the input signal

D = number of photons generated from the dark current

B = number of photons generated from the unwanted background

G = gain of the EM-CCD

S = number of spurious electrons generated when electrons are created during shifting of charges to the multiplication register

$\delta$  = number of frames acquired

From the above equation, it appears that photon counting provides means for eliminating the multiplication noise. The maximum possible SNR in a single photon counting frame is around 0.8 and therefore, it becomes necessary to average many

frames to arrive at a usable image where the SNR is greater than 3 for example [139]. It is also important to note that this technique only works for low frame rates. In order to maximize the signal-to-noise ratio, one has to carefully select the mode of operation for an EM-CCD camera. Figure D.30 below shows the signal-to-noise ratio of the three modes of operation for a given signal strength.

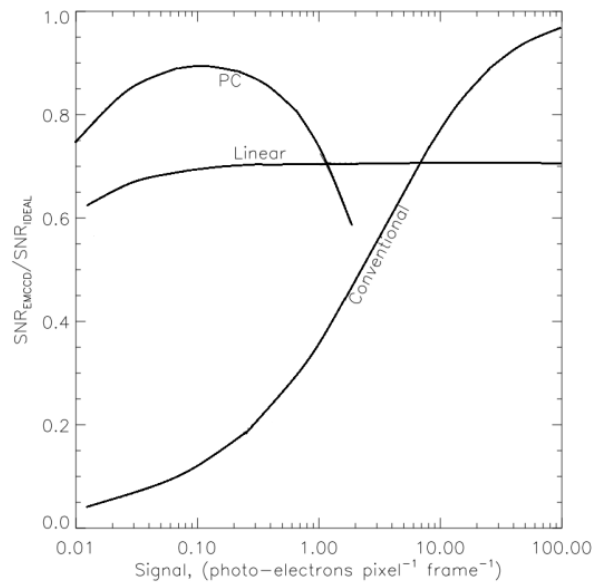


Figure D.30 [139].

## References

1. Solovey, E.T., et al. *Sensing cognitive multitasking for a brain-based adaptive user interface*. in *Proceedings of the SIGCHI Conference on Human Factors in Computing Systems*. 2011. ACM.
2. Hebden, J.C., et al., *Three-dimensional optical tomography of the premature infant brain*. *Physics in medicine and biology*, 2002. **47**(23): p. 4155.
3. Bluestone, A., et al., *Three-dimensional optical tomography of hemodynamics in the human head*. *Optics Express*, 2001. **9**(6): p. 272-286.
4. Culver, J.P., et al., *Volumetric diffuse optical tomography of brain activity*. *Optics letters*, 2003. **28**(21): p. 2061-2063.
5. Hebden, J.C., et al., *Monitoring recovery after laser surgery of the breast with optical tomography: a case study*. *Applied optics*, 2005. **44**(10): p. 1898-1904.
6. Fantini, S., et al., *Assessment of the Size, Position, and Optical Properties of Breast Tumors *in Vivo* by Noninvasive Optical Methods*. *Applied optics*, 1998. **37**(10): p. 1982-1989.
7. Cerussi, A., et al., *In vivo absorption, scattering, and physiologic properties of 58 malignant breast tumors determined by broadband diffuse optical spectroscopy*. *Journal of biomedical optics*, 2006. **11**(4): p. 044005-044005-16.
8. Choe, R., et al., *Diffuse optical tomography of breast cancer during neoadjuvant chemotherapy: a case study with comparison to MRI*. *Medical physics*, 2005. **32**: p. 1128.
9. McBride, T.O., et al., *Spectroscopic diffuse optical tomography for the quantitative assessment of hemoglobin concentration and oxygen saturation in breast tissue*. *Applied optics*, 1999. **38**(25): p. 5480-5490.
10. Fantini, S. and A. Sassaroli, *Near-infrared optical mammography for breast cancer detection with intrinsic contrast*. *Annals of biomedical engineering*, 2012. **40**(2): p. 398-407.
11. Dehghani, H., et al., *Near infrared optical tomography using NIRFAST: Algorithm for numerical model and image reconstruction*. *Communications in numerical methods in engineering*, 2009. **25**(6): p. 711-732.
12. Hebden, J.C., S.R. Arridge, and D.T. Delpy, *Optical imaging in medicine: I. Experimental techniques*. *Phys Med Biol*, 1997. **42**(5): p. 825-40.
13. Jermyn, M., et al. *A user-enabling visual workflow for near-infrared light transport modeling in tissue*. in *Biomedical Optics*. 2012. Optical Society of America.
14. Arridge, S.R., *Optical tomography in medical imaging*. *Inverse problems*, 1999. **15**(2): p. R41.

15. Gibson, A., J. Hebden, and S.R. Arridge, *Recent advances in diffuse optical imaging*. Physics in medicine and biology, 2005. **50**(4): p. R1.
16. Chance, B., *Functional Mapping with Near Infrared*. NEUROIMAGE, 1998. **7**: p. P-0689.
17. Luker, G.D. and K.E. Luker, *Optical imaging: current applications and future directions*. Journal of Nuclear Medicine, 2008. **49**(1): p. 1-4.
18. Contag, C.H., et al., *Photonic detection of bacterial pathogens in living hosts*. Mol Microbiol, 1995. **18**(4): p. 593-603.
19. Weissleder, R. and V. Ntziachristos, *Shedding light onto live molecular targets*. Nat Med, 2003. **9**(1): p. 123-8.
20. Chance, B., et al., *Hypoxia/ischemia triggers a light scattering event in rat brain*. Advances in experimental medicine and biology, 1997. **428**: p. 457.
21. Chance, B., et al., *Effects of solutes on optical properties of biological materials: models, cells, and tissues*. Analytical biochemistry, 1995. **227**(2): p. 351-362.
22. Van de Ven, S., et al., *Optical imaging of the breast*. Cancer Imaging, 2008. **8**(1): p. 206.
23. Eriksson, B. and R. Nowak. *Maximum likelihood methods for time-resolved imaging through turbid media*. in *Image Processing, 2006 IEEE International Conference on*. 2006. IEEE.
24. Ishimaru, A., *Wave propagation and scattering in random media*. Vol. 2. 1978: Academic press New York.
25. Bohren, C.F. and D.R. Huffman, *Absorption and scattering of light by small particles*. 2008: Wiley. com.
26. Arridge, S.R. and W.R. Lionheart, *Nonuniqueness in diffusion-based optical tomography*. Opt Lett, 1998. **23**(11): p. 882-4.
27. Enfield, L.C., et al., *Optical tomography of breast cancer-monitoring response to primary medical therapy*. Target Oncol, 2009. **4**(3): p. 219-33.
28. Gao, F., H. Zhao, and Y. Yamada, *Improvement of image quality in diffuse optical tomography by use of full time-resolved data*. Applied optics, 2002. **41**(4): p. 778-791.
29. Gao, F., et al., *A linear, featured-data scheme for image reconstruction in time-domain fluorescence molecular tomography*. Optics express, 2006. **14**(16): p. 7109-7124.
30. McBride, T.O., *Spectroscopic Reconstructed Near Infrared Tomographic Imaging for Breast Cancer Diagnosis*. 2001, Thayer School of Engineering, Dartmouth College.
31. Brooksby, B., et al., *Spectral priors improve near-infrared diffuse tomography more than spatial priors*. Optics letters, 2005. **30**(15): p. 1968-1970.

32. Srinivasan, S., et al., *Spectrally constrained chromophore and scattering near-infrared tomography provides quantitative and robust reconstruction*. Applied optics, 2005. **44**(10): p. 1858-1869.
33. Masciotti, J.M., et al. *Design of a frequency domain instrument for simultaneous optical tomography and magnetic resonance imaging of small animals*. in *Biomedical Optics (BiOS) 2007*. 2007. International Society for Optics and Photonics.
34. Saleh, B.E., M.C. Teich, and B.E. Saleh, *Fundamentals of photonics*. Vol. 22. 1991: Wiley New York.
35. Hamamatsu Photonics, K. and E. Committee, *Photomultiplier tubes-basics and applications*. Edition 3a, 2006.
36. Kleinfeld, D., *Noise and signal-to-noise in photodetector systems* 1979, UC San Diego.
37. Hamamatsu, *OPTO-SEMICONDUCTOR HANDBOOK*.
38. Beringer, J., et al., *Review of particle physics*. Physical Review D, 2012. **86**(1).
39. Solutions, K.-C.D. *SiPM Technology » Working Principle*. 2014; Available from: <http://www.ketek.net/products/sipm-technology/working-principle/>.
40. *MPPC Multi-Pixel Photon Counter*. 2008; Available from: [http://www.hamamatsu.com/resources/pdf/ssd/mppc\\_techinfo\\_e.pdf](http://www.hamamatsu.com/resources/pdf/ssd/mppc_techinfo_e.pdf).
41. Lares, E.H.a.M., *APD Arrays: Geiger-mode APD arrays detect low light*, in *Laser Focus World*. 2008.
42. Otte, N. *The Silicon Photomultiplier-A new device for High Energy Physics, Astroparticle Physics, Industrial and Medical Applications*. in *Proceedings to SNIC symposium (SLAC, Stanford, 2006)*. 2006.
43. *An Introduction to the Silicon Photomultiplier*. [Technical Note] 2011 [cited 2013; Available from: <http://www.sensl.com/downloads/ds/TN%20-%20Intro%20to%20SPM%20Tech.pdf>.
44. Lacaita, A.L., et al., *On the bremsstrahlung origin of hot-carrier-induced photons in silicon devices*. Electron Devices, IEEE Transactions on, 1993. **40**(3): p. 577-582.
45. Technologies, E., *LynXTM Silicon Photomultiplier Module User Guide*.
46. Becker, W., *Advanced time-correlated single photon counting techniques (Series in chemical physics, Vol. 81)*. 2005: Springer-Verlag.
47. Kalytis, R., *Photon Counting in Astrophotometry. Fundamentals and Some Advices for Beginners*. Turkish Journal of Physics, 1999. **23**(335-346): p. 48.
48. Inc., J.Y., *Photon-Counting Means Sensitivity*. 2000.
49. Donovan, D., J. Whiteway, and A.I. Carswell, *Correction for nonlinear photon-counting effects in lidar systems*. Applied optics, 1993. **32**(33): p. 6742-6753.

50. Gandjbakhche, A.H., et al., *Time-dependent contrast functions for quantitative imaging in time-resolved transillumination experiments*. Appl Opt, 1998. **37**(10): p. 1973-81.
51. Cubeddu, R., et al., *Imaging with diffusing light: an experimental study of the effect of background optical properties*. Appl Opt, 1998. **37**(16): p. 3564-73.
52. Grosenick, D., et al., *Time-domain optical mammography: initial clinical results on detection and characterization of breast tumors*. Appl Opt, 2003. **42**(16): p. 3170-86.
53. Faris, G.W. and M. Banks, *Upconverting time gate for imaging through highly scattering media*. Opt Lett, 1994. **19**(22): p. 1813.
54. Watson, J., et al., *Imaging in diffuse media with ultrafast degenerate optical parametric amplification*. Opt Lett, 1995. **20**(3): p. 231-3.
55. J. REINTJES, M.B., M.D. DUNCAN, R. MAHON, L.L. TANKERSLEY, J.A. MOON, C.L. ADLER, AND J.M.S. PREWITT, *Time-gated imaging with nonlinear optical raman interactions*. Optics and Photonics News, 1993. **4**(10): p. 28-32
56. Yoo, K.M., Q. Xing, and R.R. Alfano, *Imaging objects hidden in highly scattering media using femtosecond second-harmonic-generation cross-correlation time gating*. Opt Lett, 1991. **16**(13): p. 1019-21.
57. Yan, C. and J.C. Diels, *Imaging with femtosecond pulses*. Appl Opt, 1992. **31**(32): p. 6869-73.
58. Kirkby, D.R. and D.T. Delpy. *Measurement of tissue temporal point spread function (TPSF) by use of a cross-correlation technique with an avalanche photodiode detector*. in *Photonics West'95*. 1995. International Society for Optics and Photonics.
59. Behin-Ain, S., T. van Doorn, and J.R. Patterson, *First photon detection in time-resolved transillumination imaging: a theoretical evaluation*. Phys Med Biol, 2004. **49**(17): p. 3939-55.
60. Wahl, M., *Time-Correlated Single Photon Counting*. PicoQuant GmbH, Technical Note, 2009.
61. Patterson, M.S., B. Chance, and B.C. Wilson, *Time resolved reflectance and transmittance for the non-invasive measurement of tissue optical properties*. Appl. Opt, 1989. **28**(12): p. 2331-2336.
62. Branco, G., *The development and evaluation of head probes for optical imaging of the infant head*. 2007, University of London.
63. Arridge, S.R., M. Cope, and D. Delpy, *The theoretical basis for the determination of optical pathlengths in tissue: temporal and frequency analysis*. Physics in medicine and biology, 1992. **37**(7): p. 1531.
64. Schweiger, M. and S. Arridge, *Optical tomographic reconstruction in a complex head model using a priori region boundary information*. Physics in Medicine and Biology, 1999. **44**(11): p. 2703.

65. Kepshire, D., et al., *A microcomputed tomography guided fluorescence tomography system for small animal molecular imaging*. Rev Sci Instrum, 2009. **80**(4): p. 043701.
66. Kepshire, D.S., et al., *Imaging of glioma tumor with endogenous fluorescence tomography*. J Biomed Opt, 2009. **14**(3): p. 030501.
67. Kepshire, D.L., et al., *Automatic exposure control and estimation of effective system noise in diffuse fluorescence tomography*. Opt Express, 2009. **17**(25): p. 23272-83.
68. Hebden, J.C. and D.T. Delpy, *Enhanced time-resolved imaging with a diffusion model of photon transport*. Opt Lett, 1994. **19**(5): p. 311-3.
69. Book, S.P., *Handbook of Optical Biomedical Diagnostics*. 2002: p. 407.
70. Schmidt, F.E.W., *Development of a time-resolved optical tomography system for neonatal brain imaging*. 2000, University of London.
71. Yang, Y., et al., *Low-cost frequency-domain photon migration instrument for tissue spectroscopy, oximetry, and imaging*. Optical Engineering, 1997. **36**(5): p. 1562-1569.
72. Fantini, S. and M.A. Franceschini, *Frequency-domain techniques for tissue spectroscopy and imaging*.
73. Chance, B., et al., *Phase measurement of light absorption and scatter in human tissue*. Review of scientific instruments, 1998. **69**(10): p. 3457-3481.
74. Madsen, S.J., et al., *Portable, high-bandwidth frequency-domain photon migration instrument for tissue spectroscopy*. Optics letters, 1994. **19**(23): p. 1934-1936.
75. Gulsen, G., et al., *Design and implementation of a multifrequency near-infrared diffuse optical tomography system*. Journal of Biomedical Optics, 2006. **11**(1): p. 014020-014020-10.
76. Sevick, E., et al., *Quantitation of time-and frequency-resolved optical spectra for the determination of tissue oxygenation*. Analytical biochemistry, 1991. **195**(2): p. 330-351.
77. Fishkin, J.B. and E. Gratton, *Propagation of photon-density waves in strongly scattering media containing an absorbing semi-infinite plane bounded by a straight edge*. JOSA A, 1993. **10**(1): p. 127-140.
78. Yu, Y., et al., *Near-infrared, broad-band spectral imaging of the human breast for quantitative oximetry: applications to healthy and cancerous breasts*. Journal of Innovative Optical Health Sciences, 2010. **3**(04): p. 267-277.
79. Wang, J., et al., *Spectral tomography with diffuse near-infrared light: inclusion of broadband frequency domain spectral data*. Journal of biomedical optics, 2008. **13**(4): p. 041305-041305-10.

80. Taroni, P., *Diffuse optical imaging and spectroscopy of the breast: a brief outline of history and perspectives*. Photochem Photobiol Sci, 2012. **11**(2): p. 241-50.
81. Nissila, I., et al., *Instrumentation and calibration methods for the multichannel measurement of phase and amplitude in optical tomography*. Review of scientific instruments, 2005. **76**(4): p. 044302-044302-10.
82. McBride, T.O., et al., *A parallel-detection frequency-domain near-infrared tomography system for hemoglobin imaging of the breast in vivo*. Review of Scientific Instruments, 2001. **72**(3): p. 1817-1824.
83. Culver, J., et al., *Three-dimensional diffuse optical tomography in the parallel plane transmission geometry: evaluation of a hybrid frequency domain/continuous wave clinical system for breast imaging*. Medical physics, 2003. **30**: p. 235.
84. Wang, J., et al., *In vivo quantitative imaging of normal and cancerous breast tissue using broadband diffuse optical tomography*. Medical physics, 2010. **37**: p. 3715.
85. Taroni, P., et al., *Seven-wavelength time-resolved optical mammography extending beyond 1000 nm for breast collagen quantification*. Opt Express, 2009. **17**(18): p. 15932-46.
86. Bevilacqua, F., et al., *Broadband absorption spectroscopy in turbid media by combined frequency-domain and steady-state methods*. Applied Optics, 2000. **39**(34): p. 6498-6507.
87. Wang, J., et al., *Near-infrared tomography of breast cancer hemoglobin, water, lipid, and scattering using combined frequency domain and cw measurement*. Optics letters, 2010. **35**(1): p. 82-84.
88. Mastanduno, M.A., et al., *Remote positioning optical breast magnetic resonance coil for slice-selection during image-guided near-infrared spectroscopy of breast cancer*. J Biomed Opt, 2011. **16**(6): p. 066001.
89. Mastanduno, M., El-Ghoussein F, Jiang, S, Diflorio-Alexander, R, Xu, J, Pogue, BW, Paulsen, KD, *Adaptable near infrared spectroscopy fiber array for improved coupling to different breast sizes during clinical MRI*. In Preperation, 2013.
90. Dehghani, H., et al., *Three-dimensional optical tomography: resolution in small-object imaging*. Applied Optics, 2003. **42**(16): p. 3117-3128.
91. Srinivasan, S., et al., *In Vivo Hemoglobin and Water Concentrations, Oxygen Saturation, and Scattering Estimates From Near-Infrared Breast Tomography Using Spectral Reconstruction*. Academic radiology, 2006. **13**(2): p. 195-202.

92. Carpenter, C.M., et al., *Methodology development for three-dimensional MR-guided near infrared spectroscopy of breast tumors*. Optics express, 2008. **16**(22): p. 17903.
93. Brooksby, B., et al., *Combining near-infrared tomography and magnetic resonance imaging to study in vivo breast tissue: implementation of a Laplacian-type regularization to incorporate magnetic resonance structure*. Journal of biomedical optics, 2005. **10**(5): p. 051504-051504-10.
94. Pogue, B.W., et al., *Near-infrared characterization of breast tumors in vivo using spectrally-constrained reconstruction*. Technology in cancer research & treatment, 2005. **4**(5).
95. Poplack, S.P., et al., *Electromagnetic breast imaging: results of a pilot study in women with abnormal mammograms*. Radiology, 2007. **243**(2): p. 350-9.
96. Pogue, B.W., et al., *Image analysis methods for diffuse optical tomography*. Journal of Biomedical Optics, 2006. **11**(3).
97. Cerussi, A., et al., *In vivo absorption, scattering, and physiologic properties of 58 malignant breast tumors determined by broadband diffuse optical spectroscopy*. J Biomed Opt, 2006. **11**(4): p. 044005.
98. Jiang, S., et al., *Evaluation of breast tumor response to neoadjuvant chemotherapy with tomographic diffuse optical spectroscopy: case studies of tumor region-of-interest changes*. Radiology, 2009. **252**(2): p. 551-60.
99. Brooksby, B., et al., *Imaging breast adipose and fibroglandular tissue molecular signatures by using hybrid MRI-guided near-infrared spectral tomography*. Proceedings of the National Academy of Sciences of the United States of America, 2006. **103**(23): p. 8828-8833.
100. Srinivasan, S., et al., *Near-infrared characterization of breast tumors in vivo using spectrally-constrained reconstruction*. Technol Cancer Res Treat, 2005. **4**(5): p. 513-26.
101. Orel, S.G., *MR imaging of the breast*. Radiologic Clinics of North America, 2000. **38**(4): p. 899-913.
102. Sauter, A.W., et al., *Combined PET/MRI: one step further in multimodality imaging*. Trends in molecular medicine, 2010. **16**(11): p. 508-515.
103. de Langen, A.J., et al., *Monitoring Response to Antiangiogenic Therapy in Non-Small Cell Lung Cancer Using Imaging Markers Derived from PET and Dynamic Contrast-Enhanced MRI*. Journal of Nuclear Medicine, 2011. **52**(1): p. 48-55.
104. El-Ghoussein, F., et al., *Hybrid photomultiplier tube and photodiode parallel detection array for wideband optical spectroscopy of the breast guided by magnetic resonance imaging*. J Biomed Opt, 2014. **19**(1): p. 11010.
105. Ntziachristos, V., et al., *Concurrent MRI and diffuse optical tomography of breast after indocyanine green enhancement*. Proc Natl Acad Sci U S A, 2000. **97**(6): p. 2767-72.

106. Carpenter, C.M., et al., *Image-guided optical spectroscopy provides molecular-specific information in vivo: MRI-guided spectroscopy of breast cancer hemoglobin, water, and scatterer size*. Optics letters, 2007. **32**(8): p. 933-935.
107. Mastanduno, M.A., et al., *Adaptable Near-Infrared Spectroscopy Fiber Array for Improved Coupling to Different Breast Sizes During Clinical MRI*. Acad Radiol, 2014. **21**(2): p. 141-150.
108. Boas, D.A., et al., *Twenty years of functional near-infrared spectroscopy: introduction for the special issue*. NeuroImage, 2014. **85**: p. 1-5.
109. Steinbrink, J., et al., *Illuminating the BOLD signal: combined fMRI-fNIRS studies*. Magnetic resonance imaging, 2006. **24**(4): p. 495-505.
110. Mastanduno, M.A., *Combined MRI and Near-Infrared spectroscopy for increased specificity of breast cancer imaging*. 2013, Dartmouth College.
111. Mastanduno, M.A., et al., *Adaptable Near-Infrared Spectroscopy Fiber Array for Improved Coupling to Different Breast Sizes During Clinical MRI*. Academic radiology, 2014. **21**(2): p. 141-150.
112. Schlyer, D., et al. *Preliminary studies of a simultaneous PET/MRI scanner based on the RatCAP small animal tomograph*. in *Nuclear Science Symposium Conference Record, 2006. IEEE*. 2006. IEEE.
113. Judenhofer, M.S., et al., *Simultaneous PET/MR images, acquired with a compact MRI compatible PET detector in a 7 Tesla magnet*. Radiology, 2007. **244**(3): p. 807-814.
114. Schlemmer, H.-P.W., et al., *Simultaneous MR/PET imaging of the human brain: feasibility study*. Radiology, 2008. **248**(3): p. 1028.
115. *Preamplifier Introduction*. [www.ortec-online.com](http://www.ortec-online.com).
116. Flyckt, S. and C. Marmonier, *Photomultiplier tubes: principles and applications*. Photonis, Brive, France, 2002: p. 84.
117. Arisaka, K., *New trends in vacuum-based photon detectors*. Nuclear Instruments and Methods in Physics Research Section A: Accelerators, Spectrometers, Detectors and Associated Equipment, 2000. **442**(1): p. 80-90.
118. Linga, K.R., et al., *Dark current analysis and characterization of In x Ga 1-x As/InAs y P 1-y graded photodiodes with x > 0.53 for response to longer wavelengths (> 1.7 μm)*. Lightwave Technology, Journal of, 1992. **10**(8): p. 1050-1055.
119. Kang, J., et al., *A feasibility study of photosensor charge signal transmission to preamplifier using long cable for development of hybrid PET-MRI*. Medical physics, 2010. **37**: p. 5655.
120. Fang, Q., et al., *Combined optical imaging and mammography of the healthy breast: optical contrast derived from breast structure and compression*. IEEE Trans Med Imaging, 2009. **28**(1): p. 30-42.

121. Chen, N.G., et al., *Simultaneous near-infrared diffusive light and ultrasound imaging*. Appl Opt, 2001. **40**(34): p. 6367-80.
122. You, S.S., et al., *US-guided diffused optical tomography: a promising functional imaging technique in breast lesions*. Eur Radiol, 2010. **20**(2): p. 309-17.
123. Ntziachristos, V., X. Ma, and B. Chance, *Time-correlated single photon counting imager for simultaneous magnetic resonance and near-infrared mammography*. Review of Scientific Instruments, 1998. **69**(12): p. 4221-4233.
124. Brooksby, B., et al., *Magnetic resonance-guided near-infrared tomography of the breast*. Review of Scientific Instruments, 2004. **75**(12): p. 5262-5270.
125. Richards, P., *Bolometers for infrared and millimeter waves*. Journal of Applied Physics, 1994. **76**(1): p. 1-24.
126. Brooker, G., *Introduction to sensors for ranging and imaging*. 2009: The Institution of Engineering and Technology.
127. Ciupa, R. and A. Rogalski, *Performance limitations of photon and thermal infrared detectors*. OPTOELECTRONICS REVIEW, 1997: p. 257-266.
128. Hamamatsu Photonics, K., *Photon counting using photomultiplier tubes*. Technical note TPHO9001E04, 2005.
129. Takahashi, A., et al. *New femtosecond streak camera with temporal resolution of 180 fs*. in *OE/LASE'94*. 1994. International Society for Optics and Photonics.
130. Photonics, H., *Guide to Streak Cameras*. Hamamatsu City, 2002.
131. *Photodiode Tutorial*  
Available from: <http://www.thorlabs.com/tutorials.cfm?tabID=31760>.
132. Hamamatsu, *Characteristics and use of SiAPD, Technical Information SD-28*. 2004.
133. Karve, G.V. and J.C. Campbell, *Avalanche photodiodes as single photon detectors [electronic resource]*. 2006.
134. Gu, Y., et al. *Single-photon avalanche photodiode with improved structure using an innovative current bias scheme*. in *Integrated Optoelectronic Devices 2008*. 2008. International Society for Optics and Photonics.
135. Eraerds, P., et al., *Photon counting OTDR: advantages and limitations*. Journal of Lightwave Technology, 2010. **28**(6): p. 952-964.
136. Photonics, H., *Characteristics and use of FFT-CCD area image Sensor*. 2003.
137. Hamamatsu, *EM-CCD Technical Note*. 2009.
138. Dussault, D. and P. Hoess. *Noise performance comparison of ICCD with CCD and EMCCD cameras*. in *Optical Science and Technology, the SPIE 49th Annual Meeting*. 2004. International Society for Optics and Photonics.

139. Tulloch, S. and V. Dhillon, *On the use of electron-multiplying CCDs for astronomical spectroscopy*. Monthly Notices of the Royal Astronomical Society, 2011. **411**(1): p. 211-225.